

**Bacteria-Enabled Autonomous Drug Delivery Systems:
Biomanufacturing, Characterization of Intratumoral Transport and
Modelling**

SeungBeum Suh

Dissertation submitted to the faculty of the Virginia Polytechnic Institute and State University in
partial fulfillment of the requirements for the degree of

Doctor of Philosophy
in
Mechanical Engineering

Chair: Behkam, Bahareh
Battaglia, Francine
Dervisis, Nikolaos
Scharf, Birgit
Tafti, Danesh

Blacksburg, VA
June 7, 2017

Keywords: Tumor targeting bacteria, Cancer treatment, Bio-hybrid microrobotics

Copyright © 2017 SeungBeum Suh

Bacteria-Enabled Autonomous Drug Delivery Systems: Biomanufacturing, Characterization of Intratumoral Transport and Modelling

SeungBeum Suh

Abstract

Systemic chemotherapy is a major therapeutic approach for nearly all types and stages of cancer. Success of this treatment depends not only on the efficacy of the therapeutics but also on the transport of the drug to all tumor cells in sufficient concentrations. Intratumoral drug transport is limited by characteristics of the tumor microenvironment such as elevated interstitial pressure and sparse, irregular vascularization. Moreover, poor tumor selectivity, leads to systemic toxicity. Bacteria possess a host of characteristics that address the aforementioned challenges in conventional drug delivery approaches including tumor selectivity, preferential tumor colonization, effective tumor penetration, which can be augmented via genetic engineering. However, in clinical trials conducted to date, bacteria have rarely been able to inhibit tumor growth solely by their presence in the tumor. The overall goal of this doctoral dissertation is to develop a novel tumor treatment system based on *Salmonella* Typhimurium VNP20009 (genetically modified for preferential tumor colonization and attenuation) coupled with biodegradable copolymer, poly(lactic-co-glycolic acid) nanoparticles, hereafter referred to as NanoBEADS (Nanoscale Bacteria Enabled Autonomous Drug Delivery System). To this end, a NanoBEADS fabrication procedure that is robust and repeatable was established and a microfluidic chemotaxis-based sorting platform for the separation NanoBEADS from unattached nanoparticles was developed. The transport efficacy of NanoBEADS compared to the commonly used passively-diffusing nanoparticle was investigated *in vitro* and *in vivo* and the intratumoral penetration of the therapeutic vectors was quantified using a custom image processing algorithm. The mechanism of intratumoral penetration was elucidated through 2D

and 3D invasion assays. Lastly, we developed a biophysical model of intratumoral transport of NanoBEADS based on the intratumoral penetration experimental results towards the theoretical evaluation of the drug transport profile following the administration of NanoBEADS.

Bacteria-Enabled Autonomous Drug Delivery Systems: Biomanufacturing, Characterization of Intratumoral Transport and Modelling

SeungBeum Suh

General Audience Abstract

Currently, the transport of chemotherapeutic drugs into tumors is limited by numerous characteristics of the tumor microenvironment. This problem is exacerbated by poor tumor selectivity, leading to severe side effects to patients. Bacteria possess a host of characteristics that address the aforementioned shortcomings in conventional drug delivery approaches including preferential tumor colonization and anti-tumor effects, which may be mediated naturally or enhanced via genetic engineering. The overall goal of this doctoral dissertation is to develop a novel tumor treatment system based on genetically modified bacteria for safety and efficiency, *Salmonella* Typhimurium VNP20009 coupled with a polymeric nanoparticles, hereafter referred to as NanoBEADS (Nanoscale Bacteria Enabled Autonomous Drug Delivery Systems). To this end, a NanoBEADS fabrication procedure that is robust and repeatable was established and a microfluidic chemotaxis-based sorting platform for the separation NanoBEADS from unattached nanoparticles was developed. The transport efficiency of NanoBEADS compared to the commonly used nanoparticle was investigated *in vitro* and *in vivo* and the intratumoral penetration of the therapeutic vectors was quantified using a custom image processing algorithm. The mechanism of intratumoral penetration was elucidated through 2D and 3D invasion assays. Lastly, we developed a biophysical model of intratumoral transport of NanoBEADS based on the intratumoral penetration experimental results towards the theoretical evaluation of the drug transport profile following the administration of NanoBEADS.

Acknowledgement

Foremost, I would like to sincerely thank my advisor and mentor, Dr. Bahareh Behkam, for giving me the opportunity to work in her lab and for her relentless support of my Ph.D. work through her insightful advice, patience, understanding, and enthusiasm. The conversations we have had, both work-related and unrelated, have been stimulating and challenging, encouraging me to become a better research scientist. I am also very grateful to my committee members. Dr. Birgit Scharf deserves special recognition – her advice, encouragement, training, and relentless support have greatly helped me during my intellectual journey as a graduate student. Dr. Francine Battaglia, Dr. Danesh Tafti, and Dr. Nikolaos Dervisis deserve many thanks for their helpful discussions, support, and encouragement along the way.

I would also like to thank all the members and alumni of the MicroN BASE laboratory, especially Zhou Ye, Carolyn Mottley, Apratim Mukherjee, Ying Zhan, Carmen Damico, AhRam Kim, Ali Sahari, and Mahama Aziz Traore for making the lab an enjoyable working place and for their support and intellectual input. Eric Leaman deserves special recognition for countless constructive discussions and help with proof reading. I would also like to acknowledge Katie Broadway and Ami Jo for their help and discussions during my research, which led to joint paper publications.

Virginia Tech has been a wonderful place for me to complete my Ph.D. studies. I would like to acknowledge financial support from the Robert E. Hord, Jr. Mechanical Engineering Graduate Fellowship and the Graduate Research Development Program. I would also like to thank KIST (Korea Institute of Science & Technology) to grant the wonderful opportunity for me to continue on staying in the research field.

On a more personal note, I would like to thank my very special friends, Jaeung Kim, Seungmo Kim, Dongseok Shin, Seunghwan Kim, and Hyungil Kim, whom have helped me along the way and I consider more than friends. I am grateful for their friendship and moral support throughout all my years in graduate school.

I would like to thank my family for their unwavering support, encouragements, and, above all, their unconditional love. Words cannot express how grateful I am to the love of my life, Soojin Huh for all of the sacrifices that you've made on my behalf of me to take care of our family, raising our lovely children, Yunsu Joanna Suh and Yunuk Joshua Suh. I also wish to thank my parents and parents-in-law so much for your unfailing support throughout all these years without losing belief in me. Your prayer and support for me were what sustained me thus far.

Throughout all the sleepless nights with fear that I might not be able to finish this journey, God helped me to remember the words of promise "Even though I walk through the darkest valley, I will fear no evil, for you are with me; your rod and your staff, they comfort me" from Psalm 23:4. I would like to give thanks to God for providing the strength to go through with it and holding my hands to walk on with him.

Table of contents

Abstract.....	ii
General Audience Abstract	iv
Acknowledgement.....	v
List of Figures	xi
List of Tables	xvi
Chapter 1. Introduction.....	1
1.1 Motivation and problem statement	1
1.2 Background.....	5
a. Challenges of Conventional Chemotherapy	5
b. Bacteria-mediated Drug Delivery System.....	7
1.3 Organization of the Thesis	10
Chapter 2. Image Processing Algorithm Development for 3D map Construction of Fluorescent Objects	15
2.1 Introduction.....	15
2.2 Methods.....	16
a. Overview.....	16
b. Image pre-processing	17
c. Filtering algorithm	18
d. Quantification of the size of a single agent.....	20
e. Construction of 3D agent distribution map with compensation algorithm.....	20
2.3 Results.....	23
a. Filtering Algorithm.....	23
b. Compensation algorithm	24
c. Application Study	26
2.4 Conclusion.....	27
2.5 Supplementary Information	28
Chapter 3. Optimizing the restored chemotactic behavior of anticancer agent <i>Salmonella enterica</i> serovar Typhimurium VNP20009	33
3.1 Abstract	33
3.2 Introduction.....	34
3.3 Materials and methods.....	36
a. Bacterial strains and growth conditions	36
b. Mutant construction.....	36

c.	Quantitative swim plate assay.....	37
d.	Microfluidic device fabrication and testing.....	37
e.	Imaging and data analysis of the chemotaxis response within microfluidic device	38
f.	Image and data analysis of bacterial swimming speed.....	39
g.	Flagella labeling, fluorescence microscopy and image acquisition	39
h.	Immunoblotting	40
3.4	Results.....	41
a.	Chemotactic ability is significantly increased by restoring <i>msbB</i> in VNP20009 <i>cheY</i> ⁺ 41	
b.	Swimming speed is increased by restoration of <i>msbB</i>	42
c.	A subpopulation of non-motile cells exists in VNP20009 <i>cheY</i> ⁺ and is mitigated by restoration of <i>msbB</i>	43
d.	Flagellation is unaffected by <i>msbB</i>	44
e.	The presence of <i>msbB</i> increases the performance of VNP20009 <i>cheY</i> ⁺ in microfluidic chemotaxis assays.....	45
3.5	Discussion	47
3.6	Acknowledgments.....	51
Chapter 4. Robust Biomanufacturing of the Nanoscale Bacterial Enabled Autonomous Delivery Systems (NanoBEADS) and Bacterial Chemotaxis Enabled Autonomous Sorting of NanoBEADS		52
4.1	Introduction.....	52
4.2	Materials and methods.....	56
a.	Bacteria culture.....	56
b.	NanoBEADS construction	57
c.	Fabrication of the microfluidic platforms	58
d.	Selective bacteria adhesion to nanoparticles	60
e.	Imaging and data analysis	62
4.3	Results and Discussion.....	63
a.	Quantification of nanoparticle loading in NanoBEADS	63
b.	Quantification of the bacterial chemotactic response	65
c.	Sorting of nanoparticles using bacterial chemotaxis.....	66
4.4	Conclusions	71
4.5	Appendix.....	73
Chapter 5. Intratumoral Transport of Nanoscale Bacteria-Enabled Autonomous Drug Delivery Systems (NanoBEADS)		80
5.1	Introduction.....	80
5.2	Materials and methods.....	83

a.	Mammalian cell culture	83
b.	Tumor spheroid formation	84
c.	2D <i>in vitro</i> invasion assay of bacteria and NanoBEADS through cancer cells	84
d.	Quantification of bacterial intra/inter-tumoral penetration through <i>in vitro</i> tumor spheroids	86
e.	Intratumoral penetration of particles, bacteria, and NanoBEADS through <i>in vitro</i> tumor spheroids	87
f.	Histology and image acquisition	88
g.	Image processing for data analysis	88
h.	Structure Compactness Measurement of Multicellular Tumor Spheroids	88
i.	Animal experiment	89
j.	Tissue collection and processing	90
5.3	Results and discussions.....	90
a.	Role of chemical and mechanical treatment and nanoparticle loading on bacteria invasiveness	90
b.	Role of chemical and mechanical treatment and nanoparticle loading on intratumoral penetration of infecting agents through <i>in vitro</i> tumor spheroids.....	92
c.	Intracellular and intercellular penetration of bacteria	97
d.	Cell Packing Density of Multicellular Tumor Spheroids	99
e.	In-vivo experiment results	100
5.4	Conclusions	101
5.5	Appendix.....	104
Chapter 6. Mathematical Modeling of NanoBEADS Penetration into <i>In vitro</i> Tumor Spheroids		106
6.1	Introduction.....	106
6.2	Methods.....	109
a.	Computational Modeling of the Intratumoral Penetration.....	109
b.	Experimental Measurement of the Intratumoral Penetration of the Infecting Agents..	113
c.	Experimental setup for Hypoxic study	113
d.	Bacterial growth rate assay in Hypoxia	115
e.	Bacterial Invasiveness in Hypoxia.....	115
f.	Cell Viability assay in Hypoxia	116
g.	Statistical analysis.....	116
6.3	Results.....	117
a.	Model Validation	117

b. Bacterial Phenotype Assay (Growth rate, Invasiveness, and Cell Viability) in Hypoxia	121
6.4 Discussion	122
6.5 Conclusion	127
Chapter 7. Conclusions and future directions	129
7.1 Concluding remarks	129
7.2 Future Directions	133
References	135

List of Figures

Figure 1.1. Schematic of bacteria-enabled drug delivery system (NanoBEADS) for tumor treatment.....	6
Figure 2.1. General flow chart for image processing for construction of a 3D object distribution map.....	17
Figure 2.2. Image processing procedure. (A) Fluorescent microscope images, (B) Cropped image based on the user-defined boundary, (C) Conversion of greyscale image to binary image, and (D) Filtering algorithm for thresholding based on local fluorescent intensities.....	18
Figure 2.3. Size quantification for the single agent based on the microscope image. (A) Original greyscale image, (B) Filtered Binary Image, (C) Single agent-based segmented image using connected component segmentation, and (D) Size distribution of detected fluorescent objects from segmentation	19
Figure 2.4. Calibration curve fitting for fluorescent intensity dissipation over distance. (A) z-stack images of single agent acquired for calibration, (B) Selected point for demonstration, (C) Fluorescent intensity dissipation over distance in z direction, and (D) Compensation process based on the calibration curve fitting.....	21
Figure 2.5. A 3D agent distribution map is constructed using a compensation algorithm comparing consecutive images acquired from z-stack microscopy images. (A) Acquired z-stack images, (B) 2D projected distribution map for the number of fluorescent objects, and (C) The resulting 3D agent distribution map.....	22
Figure 2.6. Filtering algorithm performance for a locally noisy region. (A) Fluorescent microscope images contain signals from out-of-focus objects and (B) A processed image after filtering noisy signals using a locally defined threshold.....	23
Figure 2.7. Construction of a 3D agent distribution map from bacterial colonization of tumor spheroids. (A) Zoomed-in microscope images at different z-depths, (B) Processed images, (C) Projected distribution map for quantifying the number of fluorescent objects, and (D) Number of fluorescent objects quantification results using <i>3DCONFO</i> vs. manual counts.....	25
Figure 2.S1. Size quantification of single bacteria of different strains based on the microscope images in selected regions of interest. (A) <i>Salmonella</i> Typhimurium 14028, (B) <i>Escherichia coli</i> RP437, and (D) <i>Salmonella</i> Typhimurium VNP20009	28
Figure 2.S2. Representative fluorescent microscope image of infecting fluorescent objects, nanoparticles, bacteria, and bacteria-nanoparticle complex in tumor spheroids (HCT-116 (colon cancer)), the definitions of efficacy indices, and experimental data showing penetration index and colonization index of each infecting fluorescent objects.....	29
Figure 2.S3. <i>3DCONFO</i> estimates the distribution of bacteria within a microfluidic channel to quantify chemotaxis via the chemotaxis partitioned coefficient (CPC) over time.....	30
Figure 2.S4. Construction of a 3D agent distribution map. (A) Fluorescent microscope images of biofilm forming bacteria at different z-positions and (B) The 3D agent distribution map created by <i>3DCONFO</i>	31
Figure 2.S5. Cell packing density profile estimation. (A) Fluorescent microscope images sliced samples from nuclei-stained tumor spheroids (HCT-116 colon cancer), (B) Processed binary image, and (C) Cell packing density profile vs. radial dimension (Scale bar is 100 μm)	32

Figure 3 1. Chemotactic performance of *S. Typhimurium* wild-type and mutant strains on swim plate. All swim ring diameters were normalized to the average of 14028, with data representing the average of 6 experiments, each in triplicate and error bars representing standard deviations. The behavior of all strains is statistically different from each other, as determined by a one-way analysis of variance (ANOVA), using the Tukey-Kramer HSD test for means comparison, with a significance level of 0.05. All strains are significantly different from each other ($p < 0.01$).40

Figure 3.2. Swimming speed of *S. Typhimurium* wild-type and mutant strains. The average swimming speed was assessed by 2-D bacterial cell tracking for 14028 ($n=95$), VNP20009 *cheY*⁺ ($n=67$), and VNP20009 *cheY*⁺ *msbB*⁺ ($n=81$) cells. Error bars represent standard error and statistical significance was determined by a one-way ANOVA followed by Tukey-Kramer HSD test. A p-value of 0.05 was used as the threshold for significance, with statistical differences between all tested strains being $p < 0.0001$42

Figure 3.3. Proportion of motile cells in *S. Typhimurium* wild-type and mutant strains. The percentage of motile bacteria in the whole cell population was assessed through manual tracking. Data is represented as averages of 3 independent experiments for each strain, and error bars represent standard error. Statistical significance was determined by a one-way ANOVA followed by Tukey-Kramer HSD test. A p-value of 0.05 was used as the threshold for significance with statistical differences between all tested strains being $p < 0.001$43

Figure 3.4. Representative fluorescence microscopy images of Cy3-labeled *S. Typhimurium* 14028 and VNP20009 *cheY*⁺ cells.44

Figure 3.5. Immunoblots probing flagellin expression in 14028, VNP20009 *cheY*⁺ or VNP20009 *cheY*⁺ *msbB*⁺. **A.** Whole cell lysates and **B.** culture supernatants were probed for presence of flagellin with anti-FliC/FliB antibody. Top: Representative immunoblots. Bottom: Average from 5 experiments, each in duplicate, with error bars denoting standard deviations. Statistical significance was determined by a one-way ANOVA, using the Tukey-Kramer HSD test for means comparison, with a significance level of 0.05. For the whole cell lysates, only the negative control sample, 14028 *fliC* significantly differed from all other strains tested (** $p < 0.01$). The culture supernatants were not significantly different between all strains tested.45

Figure 3.6. Chemotactic performance of *S. Typhimurium* wild-type and mutant strains to L-aspartic acid in a microfluidic device. Each strain was loaded into the attractant gradient established-microfluidic device and data was collected after 15 minutes. The CPC value was ascertained for the whole population and only the motile population of each strain, as indicated (the whole population is the motile population for 14028). At the peak attractant concentration, statistical analysis with one-way ANOVA, followed by Tukey-Kramer HSD test with a significance level of 0.05, was performed. For motile populations, all strains significantly differed from one another ($p < 0.001$), as well as when whole populations of all strains were compared ($p < 0.001$).47

Figure 4.1 Microfluidic device for sorting of similarly sized particles (A) A schematic of the PEG-DA microfluidic sorting platform with the $500 \times 4000 \mu\text{m}^2$ work area, marked by black dotted line. A mixture of freely diffusing particles (green) and particle (red)-bacteria assemblies are introduced in the left side of the work area. The outer channels contain a chemo-effector solution (yellow) and a buffer solution (white) to establish a chemoattractant gradient in the center channel and promote separation of the nanoparticles carried by chemotactic bacteria. Zoomed-in view of the work area (B) at the start of the sorting process, and (C) after 45 minutes.

Particles propelled by bacteria migrate up the chemoattractant concentration gradient and separate from the freely diffusing particles.54

Figure 4.2. Schematic of the chemotaxis assay platform. (A) The three-channel PEG-DA microfluidic device (bacteria not drawn to scale), (B) scanning electron micrograph of the porous PEG-DA gel structure.59

Figure 4.3. Optimization of NanoBEADS fabrication process parameters (A) Percentage of nanoparticle loading bacteria with respect to bacteria-nanoparticle ratio when the concentration of antibody (IgG) was 10 µg/ml and concentration of antibody (IgG) when the number ratio was set to 50 to 1, (B) The nanoparticle loading on each NanoBEADS agent as a function of the zeta potential of the nanoparticles (C) Scanning Electron Microscopy image of a NanoBEADS agent.62

Figure 4.4. Effect of chemo-effector concentration gradient on the chemotactic behavior of *E. coli* RP437. (A) Plot showing the chemotaxis partition coefficient (CPC) and chemotaxis migration coefficient (CMC) as a function of the chemo-effector gradient in the center channel. Distribution of bacterial cells in the center channel (B) in absence of a gradient (control), (C) at the optimal gradient of 5×10^{-4} g/ml/mm, (D) at the high gradient of 2.5×10^{-2} g/ml/mm.64

Figure 4.5. Mass transport within the microfluidic device. (A)-(C) COMSOL® simulation results show contour plots of the chemo-effector concentration field. (D) The simulated chemical concentration distribution within the center channel of the microfluidic sorting platform at $t = 0$ s (), $t = 900$ s (), $t = 1800$ s (▲), $t = 2700$ s (▼), $t = 3600$ s (), and $t = 4500$ s (◄).66

Figure 4.6. Representative microscopy images of the work area in the microfluidic sorting device. The bacteria carrying 390 nm particles are shown in red and the 320 nm particles are shown in green. (A) $t = 0$ minutes, 390 nm particle-bacteria assemblies and freely diffusing 320 nm particles reside in the left-half of the device center channel. (B) At $t = 35$ minutes, bacteria carrying 390 nm particles have migrated up the chemical gradient and reside in the right-half of the device center channel. (C)-(D) Representative SEM images of 390 nm particle-bacteria assemblies.68

Figure 4.7. Sorting efficiency of the bacteria-enabled microfluidic sorting platform. The chemotactic partition coefficient (CPC) for the 390 nm (solid black rectangle) and 1040 nm (solid red circle) particle-bacteria complexes formed by specific biotin-streptavidin interactions reach steady-state values of 0.57 and 0.63, corresponding to a sorting efficiency of up to 81%. The CPC value for the 1000 nm positively charged particle-bacteria assemblies (solid blue diamond) formed through non-specific electrostatic interactions reaches a steady state value of 0.49, corresponding to a sorting efficiency of 75%. The CPC of the freely diffusing 320 nm (open black rectangle) and 1000 nm (open red circle and open blue circle) particles remain at around 0.7.70

Figure 4.S1. (A) Representative micrograph images of 1040 nm streptavidin-coated particles (green), 1000 nm polystyrene particles (red), and biotinylated antibody coated *E. coli* MG1655m (false coloured in yellow). *E. coli* selectively attached on the surface of the 1040 nm particles via streptavidin-biotin binding. (B) Representative micrograph images of 1000 nm positively charged particles (yellow), 1000 nm neutrally charged polystyrene particles (red), and biotinylated antibody coated *E. coli* MG1655m (green). Negatively charged bacteria selectively attached on positively charged particle via electrostatic interactions, while neutrally charged particles remain unattached. All scale bars are 10 µm.73

Figure 4.S2 Representative images of the work area in the microfluidic sorting device. (A) At $t = 0$ minutes, the 1000 nm particle-bacteria assemblies (yellow) and the freely diffusing neutrally charged 1000 nm particles (red) reside in the left-half of the device center channel. (B) At $t = 35$ minutes, bacteria carrying 1000 nm particles have migrated up the chemical gradient and reside in the right-half of the device center channel. All scale bars are 100 μm73

Figure 4.S3. Sample bacterial trajectory in (A) absence of chemo-attractant and (B) in a chemo-attractant gradient environment with 0.4% (w/v) chemo-attractant as a point source. The blue solid circle on the bacterial path represents the starting point and the green diamond at coordinates (0,0,0) represents the location of the chemical attractant source.75

Figure 4.S4. Representative intensity size distribution plot of TIPS pentacene-loaded PLGA nanoparticles in PBS at a concentration of ~ 0.02 mg/ml.77

Figure 4.S5. Zeta potential versus time to track streptavidin-coating of nanoparticles for appropriate incubation period in coupling solution.....78

Figure 5.1. Schematic of nanoscale bacteria enabled drug delivery system compared to nanoparticle only strategy for tumor treatment.82

Figure 5.2. Bright-field microscopy images of HCT-116 (colon cancer) multicellular tumor spheroid after (A) 1-day, (B) 3 days, (C) 5 days, and (D) 7 days. (E) Tumor spheroid with a clearly defined viable rim consisting of live cells and a hypoxic core comprised of quiescent and dead cells.....85

Figure 5.3. Schematic of 3D *in vitro* multicellular tumor spheroid showing intercellular and intracellular penetrating bacteria86

Figure 5.4. Invasion assay results **(A)** Representative microscopy images of invaded HCT-116 (colon cancer) cells (scale bar is 10 μm) **(B)** Percentage of infected cell for each infecting agents and cell line. Each data point represents the mean \pm standard error91

Figure 5.5. Tumoral transport quantification, (A) Definitions of intratumoral penetration performance metric; Representative microscopic images of the penetration of infecting agents into tumor spheroids of (B) HCT-116 (colon cancer), (C) U87MG (brain cancer), and (D) 4T1 (breast cancer). Bacteria are shown in red and nanoparticles are in purple. All scale bar is 100 μm93

Figure 5.6. Intratumoral penetration results of infecting agents through *in vitro* tumor spheroids as indicated by the weighted penetration index.....95

Figure 5.7. Radial distribution of infecting agent with the tumor spheroids (A) & (B) HCT-116 (colon cancer with $n=10$ for bacteria, $n=9$ for NanoBEADS, and $n=7$ for nanoparticles), (C) & (D) U87MG (brain cancer with $n=7$ for bacteria, $n=7$ for NanoBEADS, and $n=7$ for nanoparticles), and (E) & (F) 4T1 (breast cancer with $n=7$ for bacteria, $n=4$ for NanoBEADS, and $n=3$ for nanoparticles).96

Figure 5.8. Fraction of infecting agents residing intra/intercellularly in HCT-116 (colon cancer) and 4T1 (breast cancer) tumor spheroids.....98

Figure 5.9. Results of tumor compactness analysis (A) Overall tumor compactness and (B) Cell packing density profile over the radial dimension of *in vitro* tumor spheroids, and “Histological staining of collagen in different tumor of (C) LS174T (colon carcinoma) and (D) U87 (Glioblastoma),” reproduced from [4] with permission.100

Figure 5.10. *In-vivo* experiment results, (A) Bacterial CFU enumeration in tumor, spleen, and liver, (B) Weighted penetration index (WPI) of infecting agents, and Representative microscopy

images of tumor tissue with (C) Nanoparticle injected, (D) Bacteria injected, and (E) NanoBEADS injected. (Scale bar is 1 mm)101
 Figure 5.S1. NanoBEADS growth effect on attached PLGA particles (A) Number of attached PLGA particles on NanoBEADS and the fraction of bacteria contains particles attached during the growth of NanoBEADS (B) SEM image of NanoBEADS during the binary fission. (Scale bar is 500 nm.)104

Figure 6.1. Normalized Oxygen Concentration $O^*(r)$, the Fraction of Necrotic Cells $f_{nec}(r)$, and Normalized Nutrient Concentration $s^*(r)$ vs. Radial Location. (A) Steady state simulation results for a 250 μm -radius tumor spheroid, and (B) Steady state simulation for a 500 μm -radius tumor spheroid. Note that the locations $r_{1\%}$ and r_{nec} are shown on each plot.....111

Figure 6.2. Schematic drawing of hypoxic gas infusion system (Top) and the experimental setup in hypoxic condition (Bottom) (red dotted box shows zoomed-in rotameter setting for each gas)114

Figure 6.3. Representative Parameter Fitting Results. (A) PB concentration curve shows a gradual decrease in the number of bacteria, (B) PB concentration curve exhibited a rise in the number of bacteria in the hypoxic region (concentration “bump”). This was observed in 2 out of the 3 experiments performed, (C) Characteristic NanoBEADS concentration curve, (D) Characteristic nanoparticles concentration curve.118

Figure 6.4. Parameter Fitting Results for Each of the Three Independent Experiments with PB. (A) DB , (B) τ_{min} , (C) Km^* , and (D) Y^* . Error bars show \pm standard deviation. Note that these results were obtained by averaging the fit of each imaged tumor slice from each experiment. There were 3 tumors for Experiment 1, 4 tumors for Experiment 2, and 3 tumors for Experiment 3. The minimum number of slices per tumor is 3.119

Figure 6.5. Average Effective Diffusion Coefficients of PEGylated Bacteria (PB), PEGylated NanoBEADS (PNBs), and PEGylated Nanoparticles (PNPs) as Determined by Fitting the Model to Experimental Data. Error bars show \pm standard deviation.120

Figure 6.6. Invasion assay results of *S. Typhimurium* VNP20009 into HCT-116 colon cancer at different oxygen concentration (1%, 5%, and 21%) ($p < 0.0001$).....121

Figure 6.7. Cell viability assay showing (A) all cell (blue) and dead cell (green) for HCT-116 colon cancer and (B) all bacteria (green) and dead bacteria (red) for *S. Typhimurium* VNP20009, and (C) Fraction of dead cell among the whole population. (Scale bar is 200 μm .)122

Figure 6.8. Sensitivity Analysis of the PB Colonization Profile with Respect to Fitted Parameters. (A) Sensitivity to DB with $DB = 0.033 \mu\text{m}^2/\text{s}$, (B) Sensitivity to τ_{min} with $\tau_{min} = 95 \text{ min}$, (C) Sensitivity to Km^* with $K^*m = 0.26$, and (D) Sensitivity to Y^* with $Y^* = 0.52$. Note that x indicates the average value. The arrows shown on each plot indicate trending direction of the curves with increase in the parameter of interest.123

Figure 6.9. Sensitivity of the Colonization Profile to Yield Y with $DB = 0.1 \mu\text{m}^2/\text{s}$, $\tau_{min} = 40 \text{ min}$, and $Km^* = 0.519$ 125

Figure 6.10. Results of 20 Simulations of STB with Parameters Randomly Selected from within Ranges Defined by Average Fit Values \pm Standard Deviation. Each curve represents a separate simulation.....126

List of Tables

Table 5.1. Complete growth medium for the cancer cell culture	84
Table 6.1. Constant Parameters and Boundary Conditions for All Simulations (* indicates normalized parameter)	112
Table 6.2. Deterministic Parameters and Boundary Conditions Derived from Experimental Data (* indicates normalized parameter)	117

Chapter 1. Introduction¹

1.1 Motivation and problem statement

Cancer is a leading cause of mortality worldwide, and a total of 1,688,780 new cancer cases and 600,920 deaths are expected in the U.S. in 2017 [1]. New treatment strategies are needed to address the shortcomings of conventional treatments such as chemotherapy or radiation, both of which have limited efficacy and present significant risk to healthy tissue. In the case of chemotherapy, the targeting of tumors is limited because the antitumor drugs delivered through the tumor vasculature, must cross the vessel wall, and penetrate into the tumor tissue. Thus, large doses are needed in order to adequately reach all viable tumor cells, which unavoidably causes systemic toxicity and severe side-effects [2], [3]. The inhibited transport of anti-tumor drugs is usually compounded by high interstitial pressure due to enhanced recruitment of fibroblasts and poorly functioning lymphatic drainage, leading to hypoxic and acidic conditions in the poorly vascularized regions of the tumor [4]-[5].

During the past decade, advances in nanotechnology have enabled a host of new treatment approaches, collectively termed “targeted drug delivery” [6]. While some of this research address the development of controlled release mechanisms for selective drug delivery to tumors via liposomes or other polymer-based carriers [7], the primary focus is on enhanced intracellular uptake by cancer cells, which occurs after majority of the particles has been lost to non-targeted areas of the body during blood circulation and cleared off by immune system. Thus, there exists a need to develop methods to enhance extravasation and delivery from tumor microvasculature into the tumor tissue. Additionally, the therapeutic agents must be engineered such that they are

¹ Excerpts from ‘Leaman, E., Suh, S., & Behkam, B. (2016) “Micro and Nano Robotics in Medicine”, Encyclopedia of Medical Robotics’ are included in this chapter.

able to overcome adverse outward fluid flow driven by the elevated interstitial pressure inside tumors.

An ideal targeted drug delivery system addressing transport limitations, would be one in which the individual agents of the system are introduced systemically, after which they are capable of autonomously targeting cancerous tissue in both primary and metastatic tumor sites. In addition to locomotion, an autonomous system requires that the agents are capable of sensing and responding to their environment. All of this must be built into a system with characteristic size of few microns or less, the upper limitation for a microrobot to reach tumor sites through capillaries.

Bacteria are one of the most promising and suitable drug carrier candidates [7]. Some bacterial strains have been genetically modified to evade the immune system resulting prolonged blood circulation allowing for larger tumor accumulation as well as preferential colonization [8], [9]. Certain bacterial species have also shown an invasive phenotype in tumor tissue and are capable of intratumoral penetration, which can enhance the interstitial transport efficacy [10], [11].

The overall goal of this doctoral dissertation is to quantitatively investigate the intratumoral transport enhancement of *Salmonella* Typhimurium VNP20009 coupled with biodegradable copolymer, poly(lactic-co-glycolic acid) nanoparticles, hereafter referred to as NanoBEADS (Nanoscale Bacteria Enabled Autonomous Drug Delivery Systems), compared to conventional passively diffusing nanoparticle based approach, and to identify mechanism of intratumoral transport in NanoBEADS. To this end, following specific aims were defined:

- Develop an image processing algorithm for precise and computationally inexpensive analysis of fluorescently labelled objects within the 3D tumor tissue
- Robust and repeatable biomanufacturing of NanoBEADS:

- Investigating the motility and chemotaxis of the *S. Typhimurium* VNP20009 bacteria used for biomanufacturing of NanoBEADS
- Optimizing the construction of NanoBEADS with respect to concentration of antibody, particle to bacteria assembly ratio, zeta potential of streptavidin coated PLGA particles, and removal of unbound particles after the assembly
- Developing a microfluidic sorting device for separation of similarly-sized particles via bacterial chemotaxis
- Evaluation of the intratumoral transport of NanoBEADS:
 - Quantification of the intratumoral penetration enhancement of NanoBEADS compared to passively diffusing nanoparticle
 - Investigating the crucial factors of intratumoral penetration of bacteria in different tumors *in vitro* (HCT-116 colon cancer, U87MG brain cancer, and 4T1 breast cancer) and *in vivo* (4T1 breast cancer)
 - Bacteria invasiveness
 - Intra/inter-cellular translocation
 - Tumor compactness
 - Effect of NanoBEADS processing steps (i.e. mechanical shear or PEGylation) on invasiveness
- Developing a biophysical model for intratumoral transport of infecting agents:
 - Investigating the impact of limited oxygen concentrations (1% and 5%) on bacteria and its interaction with cancer cells
 - Developing gas infusion system to realize the limited oxygen concentration environment

- Examining the impact of limited oxygen concentration on bacterial viability and growth, bacterial invasiveness into cancer cells, and cancer cell viability
- Development of a computational model of bacterial growth and transport within the tumor microenvironment
- Parametric sensitivity analysis of the transport model

1.2 Background

a. Challenges of Conventional Chemotherapy

Throughout human medical history, tremendous research effort has been made in a variety of respects related to symptoms, causes, pathophysiology, diagnosis, treatment, prevention, screening, management, and prognosis of cancer. Even though cancer-related research has advanced a great deal during the last several decades, the cure for cancer seems farfetched. This is because cancer is not a single disease. Rather, cancer is a group of diseases originating from various organs, which undergoes very different pathological time courses from its inception to its cure. More than 100 different types of cancer have been identified to date [12], [13]. Cancer is characterized by abnormal cell growth with the possibility of metastasis onto other organs. Untreated cancer leads to death. Six representative hallmarks of cancer have been identified [14]: 1) stimulation of growth factors, 2) inhibition of growth suppressors, 3) lack of compliance with the cell-cycle related to cell-death, 4) sustained, uncontrolled proliferation, 5) elevated angiogenesis, and 6) the stimulation of metastasis.

The tumor microenvironment especially possesses numerous characteristics, which make conventional treatments ineffective. Most notably, tumors are poorly vascularized due to rapidly dividing cells. This results limited oxygen and nutrient diffusion throughout the interstitium and causes the accumulation of biochemical products such as lactic and carbonic acid, byproducts of glycolysis during ATP production, which lowers the extracellular pH of tumoral sites [15]. Furthermore, limited oxygen diffusion leads to a hypoxic tumor microenvironment, which limits the effectiveness of traditional treatments such as radiotherapy [16]. A dense microenvironment due to the enhanced recruitment of fibroblasts, compacted structures of collagen, and space-filling glycosaminoglycan [17], and the lack of lymphatic drainage in tumor microenvironment, are additional degrading factors of efficacious chemotherapy, which requires drug delivery deep into hypoxic region of the tumor [18].

Conventional chemotherapy remains the most common form of therapy for all forms and stages of cancer [19]. Efficacious chemotherapy of primary solid tumors depends on transport of macromolecular antitumor drugs into the tumors [20]. Antitumor drugs travel to tumors through a sequence of transport modes: 1) circulation via blood vessels following intravenous administration, 2) transvascular transport into the tissue nearby, and 3) transport through interstitial spaces into the tumor [21]. Major reasons for poor drug delivery efficacy are twofold. Firstly, only a small portion of the chemotherapeutic drug is extravasated through the blood circulation. Although the extravasation of submicron-sized agents into tumors is thought to be

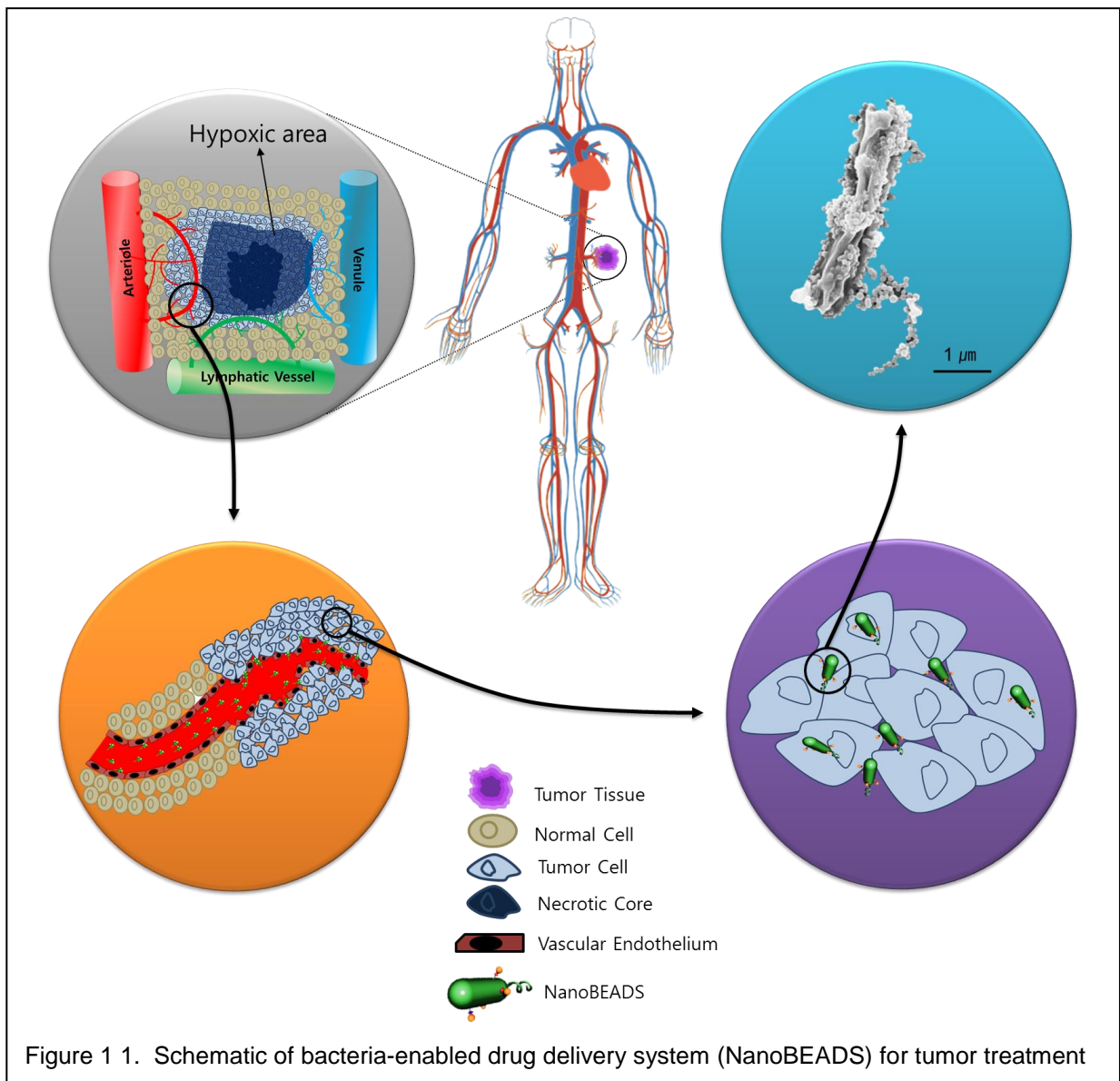


Figure 1 1. Schematic of bacteria-enabled drug delivery system (NanoBEADS) for tumor treatment

promoted by the so-called enhanced permeability and retention (EPR) effect, which is the enhancement of the accumulation of submicron-sized particles due to the leaky and fenestrated neovasculature [22], [23] as shown in Figure 1.1, more than 95% of nanoparticle-based chemotherapeutic drugs are cleared from the circulation and end up accumulating in organs such as the liver, spleen, and kidneys [6], [24].

The second major reason for poor drug delivery to tumors is the elevated interstitial pressure within the tumor microenvironment. Fast growing tumor cells within a confined volume increase the interstitial pressure and increase the distance ($>100\ \mu\text{m}$) between the blood vessels and tumor tissue [25]. Lack of lymphatic drainage causes additional accumulation of interstitial fluid, which results in elevated interstitial fluid pressure in the tumor microenvironment. Additional fluid pressure and osmotic gradients result in transvascular convection [26], [27] and a buildup of metabolic waste, which, together with limited oxygen diffusion, cause hypoxia and acidosis [28]. Diffusion of chemotherapeutic agents sized 60 nm or larger through the tumor microenvironment is greatly impeded due to the aforementioned reasons [21].

b. Bacteria-mediated Drug Delivery System

The afore-mentioned challenges of conventional chemotherapeutics underscore the need for an active targeting and alternative transport mechanism. The current state-of-the-art active targeting drug delivery systems rely on blood circulation and extravasation as passive transport mechanisms, followed by intracellular penetration by means of “active targeting”, i.e. specific ligand-receptor interactions between nanoparticle-based drug carriers and target cells [6]. [29]. Such a system is often misunderstood as a biological “missile tracking system” in which a drug carrier is guided from intravenous introduction into its target cell.

Advances in active targeting of nanomedicine has substantially improved specificity of drug delivery vectors; however, transport related issues described earlier remain unaddressed. Bacteria-mediated drug delivery systems possess unique characteristics that address many of

the shortcomings of conventional chemotherapy approaches. For example, various species of bacteria have been shown to preferentially colonize tumors over normal tissue [30], [31]. Moreover, bacteria are known to have an inherent therapeutic effect on cancer [7]. More than a century ago, William Coley, an early 20th century surgeon, intentionally infected cancer patients with bacteria after noting positive effects on a sarcoma patient and later developed a bacteria-derived cancer drug termed “Coley’s toxin” [8], [32]. While the mechanisms for innate tumor cell destruction are not entirely clear, it is hypothesized that a combination of several pathogenicity-related bacterial functions are at play [33]. Recent bacteria-related cancer research has shown that the numerous gram-negative and gram-positive species of bacteria are suited for therapeutics purposes. Strict anaerobes such as *Clostridium* [34] and *Bifidobacterium* [35] were used to target the hypoxic regions of solid tumors. Although the selective germination of *C. novyi*-NT spores in tumors imparts a degree of safety for the patient, the gene that encodes for the α -toxin was deleted to decrease bacterial toxicity. Subsequent administration of the spores to tumor-bearing mice resulted in good tumor colonization and prolonged the animals’ survival [36]. However, confinement of the strict anaerobes to the hypoxic region might have a negative effect on overall tumor colonization due to lack of growth in viable regions. In order to address this limitation, facultative anaerobes such as *Salmonella* Typhimurium [37], *Escherichia coli* [38], and *Listeria monocytogenes* [39] were studied and showed selective tumor colonization and antitumor effects. In particular, *S. Typhimurium* is widely recognized for tumor-targeting, preferentially colonizing primary tumor and metastatic cancer, and inhibiting the growth of tumors, which can be useful attributes for a therapeutic carrier [40], [41]. Most notably, *S. Typhimurium* VNP20009 was constructed by genetically modifying the highly-virulent and invasive wild-type strain *Salmonella enterica serovar Typhimurium* 14028, so as to retain a stable virulence attenuation without compromising its tumor targeting ability, anti-tumor effects, and antibiotic susceptibility [28]–[46]. A Phase I clinical trial in which human patients were intravenously injected with *S. Typhimurium* VNP20009 demonstrated the safety of this strain

(maximum-tolerated dose: 3×10^8 cfu/m²). Colonization within metastatic lesions was detected in only three out of 24 patients but no regression was observed. The results suggest that there is a need for an improved system to achieve more efficacious bacteria-mediated cancer treatment [9], [47].

We hypothesize that nanoparticle-bacteria complexes (i.e. NanoBEADS) address the shortcomings of bacteria-only and nanoparticle-only drug delivery systems and enable a more effective multimodal drug delivery approach by combining strengths of particle and bacteria-based drug delivery systems, particularly with respect to interstitial transport efficacy. Thus, this doctoral study focuses on developing a robust and repeatable biomanufacturing strategy for construction of NanoBEADS, followed by investigating the transport characteristics and mechanisms of the NanoBEADS system *in vitro* and *in vivo*.

1.3 Organization of the Thesis

The overall goal of this dissertation is to quantitatively investigate the intratumoral transport enhancement of *S. Typhimurium* VNP20009 coupled with biodegradable copolymer, poly(lactic-co-glycolic acid) nanoparticles compared to conventional passively diffusing nanoparticle based approach.

First, we have developed an image-processing algorithm, referred to as *3DCONFO (3D Map Construction for Fluorescent Objects)* in order to accurately analyze the distribution and concentration of fluorescently-labeled bacteria, nanoparticles, and NanoBEADS within the 3D tumor tissue. Then, we have investigated the correlation between the motility and chemotaxis of *S. Typhimurium* strain VNP20009 and the expression of *cheY* and *msbB* genes. We compared the results to the wild-type strain in order to better evaluate the performance of NanoBEADS with respect to the desirable characteristics of tumor-targeting bacteria, given that intrinsic bacterial characteristics such as motility and chemotaxis could be beneficial for efficacious intratumoral localization [48]–[51]. We have developed bacteria conjugated with a PEGylated polymer complex called NanoBEADS (Nanoscale bacteria-enabled autonomous drug delivery system). In order to optimize the fabrication of NanoBEADS, defined here as maximizing the nanoparticle load of each bacterium, the various experimental parameters have been studied: the particle to bacteria ratio, the zeta potential of streptavidin coated nanoparticles, and the pore size centrifugal filter for separating unoccupied nanoparticles from NanoBEADS that are made with non-chemotactic bacteria. Next, a high-throughput microfluidic sorting platform was developed to utilize the chemotaxis of bacteria through specific and non-specific types of nanoparticle attachment to bacteria in the extended work of separating unbound particles from NanoBEADS that are made with chemotactic bacteria. Subsequently, characterization of the intratumoral transport efficacy of NanoBEADS was carried out through quantitative analysis of the penetration into tumor spheroids *in vitro* and into tumors of tumor-bearing mice *in vivo*. The

results were compared to a nanoparticle-only-based approach and further investigations of the determining factors of transport efficacy. A biophysical model for intratumoral transport of infecting agents based on the intratumoral penetration experimental results was introduced along with a study of the impact that limited oxygen concentrations have on bacteria and tumor cells such as cytotoxicity, invasiveness, and growth rate. The remainder of this dissertation is organized as follows:

Chapter 2:

In this chapter, we present a novel semi-automated and computationally-efficient method to quantify and produce a 3D map of fluorescent objects in fluorescence images captured with either a confocal or wide-field microscope without the use of edge detection or other expensive algorithms by applying two calibration steps. First, the average size of the object of interest was calibrated. The grey level intensity for the fluorescent objects was also calibrated through the fitted analytical function using the distribution of fluorescence intensity along the z-axis for a series of representative z-stacked images. Conversion of the fluorescent intensity image into binary image was performed by dual-threshold filtering algorithm. Finally, 3D distribution map was constructed via employing the compensation algorithm. The robustness and accuracy of the method to analyze bacterial colonization of tissue, bacterial chemotaxis in a microfluidic channel, 3D architecture of bacterial biofilms, and the compactness of tumor tissue was also demonstrated.

Chapter 3:

In this chapter, constructed mutants (e.g. *S. Typhimurium* VNP20009 with *cheY* restored (denoted *cheY*⁺) and *S. Typhimurium* VNP20009 with *msbB* restored (denoted *msbB*⁺)) of

Salmonella Typhimurium VNP20009 with the *cheY* and *msbB* genes were used for motility and chemotaxis assays in order to determine if chemotaxis of VNP20009 can be optimized to enable future analysis of maximal tumor targeting potentially. The correlation between the restored genes and bacterial behavior with respect to the parental strain, *S. Typhimurium* 14028 was studied. Under normal function, CheY regulates the flagellar motor switch mechanism based on the relative rates of chemo-effector binding to and dissociation from transmembrane chemoreceptors, leading to a bias in flagellar rotation. The *msbB* gene is implicated in terminal myristoylation of the highly-immunogenic Lipid A component of LPS, thus its deletion results in altered outer membrane properties [38]. We reported that by restoring the gene which encodes a lipid A altering enzyme *msbB*, we significantly increased the performance of the strain in chemotaxis assays, including swim plates and a microfluidic device [52].

Chapter 4:

In this chapter, we described the fabrication of NanoBEADS (i.e. engineered bacteria coupled with a PEGylated polymer nanoparticles) and characterized their properties such as particle loading capacities, hydrodynamic size, zeta potential, and the pore size centrifugal filter for separating unbound nanoparticles from the NanoBEADS that are made with non-chemotactic bacteria. Lastly, we reported a simple and cost-effective sorting technique for the separation of similarly-sized particles of dissimilar surface properties within a diffusion-based microfluidic platform by utilizing chemotaxis in *Escherichia coli* (or any other chemotactic) bacteria. Differences in surface chemistry of two groups of similarly sized nanoparticles in a mixture were exploited to selectively assemble one particle group onto motile *E. coli*, through either specific or non-specific adhesion, which were separated from the remaining particle group via chemotaxis of the bacteria. The proposed sorting technique was also applicable to the separation of

NanoBEADS that are made with chemotactic bacteria from unbound nanoparticles, which are inevitable artifact of NanoBEADS fabrication. To enable optimal operation of the sorting platform, the chemotaxis behavior of *E. coli* bacteria in response to casamino acids, the chemo-effector of choice was first characterized. Sorting efficiency, throughput, and sensitivity of the system based on the size of particles were characterized under optimal operational conditions.

Chapter 5:

In this chapter, the intratumoral transport efficacy of the infecting agents (PLGA particles, bacteria, and developed NanoBEADS) into the *in vitro* tumor spheroids from colon (HCT-116), brain (U87MG), and breast (4T1) cancer tumor cell lines was determined. The results showed that bacteria conjugation strategy definitely enhance the interstitial transport efficacy. The mechanism for penetration with respect to intracellular invasiveness and intercellular translocation was also investigated. A discussion on intratumoral transport with respect to tumor compactness and the effects of treatments including mechanical shear and PEGylation on the transport performance was presented as well. To investigate the *in vivo* intratumoral transport efficacy of NanoBEADS, 4T1 breast tumor-bearing mice were used.

Chapter 6:

A biophysical model for intratumoral transport of the infecting agents (PLGA particles, bacteria, and developed NanoBEADS) based on the previous intratumoral penetration experimental results (chapter 5) was developed. In order to accurately describe intratumoral bacteria penetration within the hypoxic region, the impact of limited oxygen concentrations (1% and 5%) on bacteria viability and growth and tumor cell viability was examined. A parametric sensitivity analysis of the transport model was also carried out to determine the key factors affecting

bacterial transport and colonization of the tumor. The results showed that the model reproduce characteristic bacterial penetration profile, consistent with the experimental data.

Chapter 7:

This chapter describes the original contributions and the new knowledge developed through this Ph.D. dissertation. Future directions for expanding this research are also discussed.

Chapter 2. Image Processing Algorithm Development for 3D map Construction of Fluorescent Objects²

2.1 Introduction

Fluorescence microscopy has revolutionized biological research, enabling the development of a host of technologies and measurements across multiple scales, ranging from whole-cell tracking to the quantification of single molecules tagged with a fluorescent protein. One of its most significant advantages is the ability to image through otherwise opaque materials to locate and identify fluorescent objects in three dimensions. This is accomplished by acquiring a series of 2D images along the focal axis, which can then be used to computationally create a 3D representation of the entire sample [53].

As both microscopy and imaging technology improve, automated image processing becomes increasingly important for efficiently analyzing the large amounts of data collected. A number of approaches to automate or semi-automate the segmentation of discrete fluorescent objects in three dimensions have been presented in literature, usually consisting of a hybrid of several image processing techniques. For example, cell nuclei have been segmented in both 2D and 3D by quantifying intensity gradients and geometric distances, combined with a watershed algorithm, and followed by analysis of anatomical features to produce results that were up to 97% accurate relative to manual counts [54], [55]. Daims *et al.* [56] used thresholding combined with a watershed algorithm to segment colonies and aggregates of microbes in biofilms probed using FISH (fluorescent *in situ* hybridization). Their algorithm uniquely included a feature to correlate “biovolume” with actual cell numbers for quantification, rather than attempting to segment

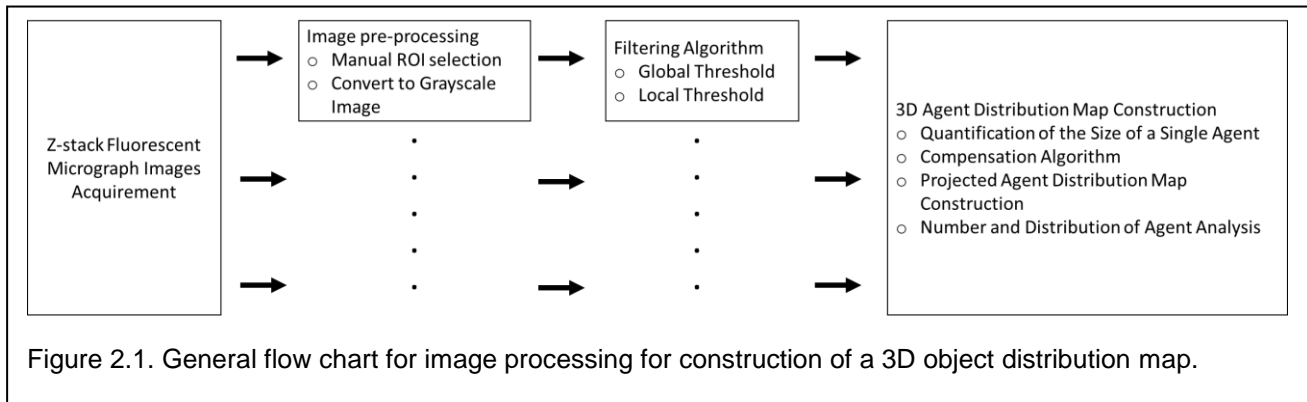
² Work done in collaboration with Eric Leaman (VT Mechanical Engineering)

individual microbes. More recently, Hodneland *et al.* [57] used an analogous approach for analysis of mammalian cells by implementing a minimum and maximum cell volume into the segmentation algorithm itself as part of their “CellSegm” program. Many of the published methods for segmenting, counting, and analyzing images of fluorescent cells have been implemented in freely-available software programs (reviewed in [58]).

The greatest challenge in accurate 3D fluorescent image analysis is proper filtering to eliminate signals from objects that are above or below the focal plane. This is of particular importance in conventional wide-field microscopy, as the excitation signal is applied throughout the height of the sample. Removal of this noise inherently increases the computational expense of image processing, as illustrated by the 3D edge detection and watershed algorithms employed in existing published methods [56]. In the present work, we present a novel semi-automated and computationally-efficient method to quantify and produce a 3D map of fluorescent objects in fluorescence images captured with either a confocal or wide-field microscope without the use of edge detection or other computationally-expensive algorithms. This is facilitated by conducting pre-image processing calibration of the data in prior to apply the image processing procedures. First, a sparsely-populated example image is input, from which the average object area is calculated. Next, an analytical function is fit to the distribution of fluorescence intensity along the z-axis for a series of representative z-stacked images. Together, this data provides the object size information needed to accurately create binary representations of the objects in space and quantify numbers. Our software quantifies fluorescent objects with an overall accuracy 98% across a variety of sample types.

2.2 Methods

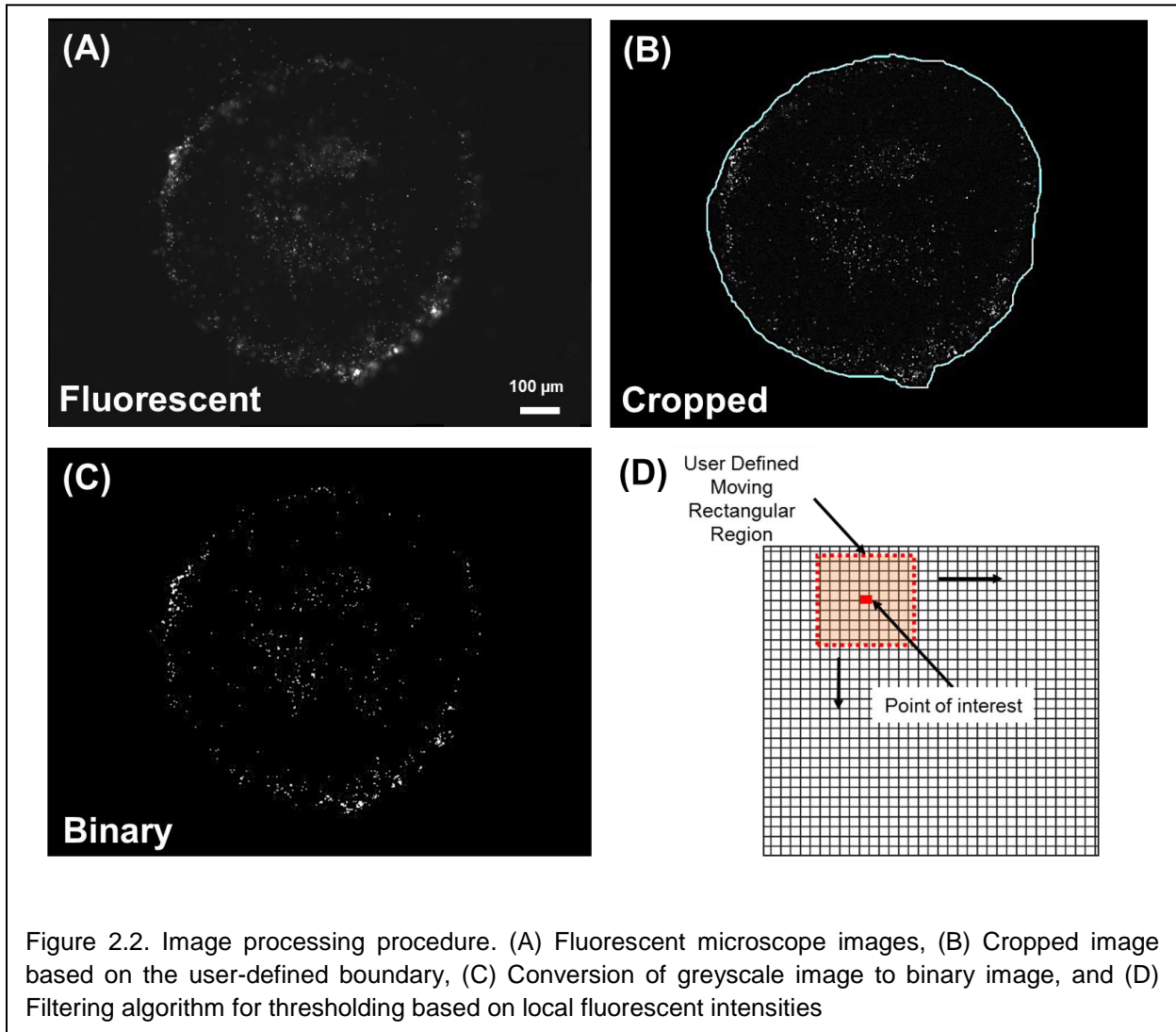
a. Overview



3DCONFO (3D Map Construction for Fluorescent Objects) automates the detection of fluorescent objects located in a 3D sample, constructs a 3D map of the fluorescent object distribution, and counts the number of objects. Briefly, the user loads a microscopy image and manually defines the region of interest (e.g. boundary of the sample). *3DCONFO* processes the image to identify the fluorescent objects and converts it to a binary image showing only the fluorescent objects according to optimal filtering parameters set by the user. These parameters are then used to analyze a series of z-stacked images to create a 3D distribution map. Throughout this process, *3DCONFO* generates files containing information about the spatial distribution of the objects and quantitative performance indices for selected applications (further described in Application Study). The MATLAB-based software tool is computationally efficient relative to comparable programs, and is extremely useful for performing enumerative analyses in a variety of applications, such as nanoparticle penetration or bacterial colonization of tissue samples, biofilm formation, and cell viability assays. General flow of the proposed image processing algorithm is described in Figure 2.1.

b. Image pre-processing

The user loads the grayscale image, separated from the acquired fluorescent images along the z-axis, which is orthogonal to the focal plane in order to investigate the distribution of fluorescent objects throughout the 3D sample. Before automated analysis begins, the user optimizes the filtering parameters to identify the infecting fluorescent objects within the manually-selected

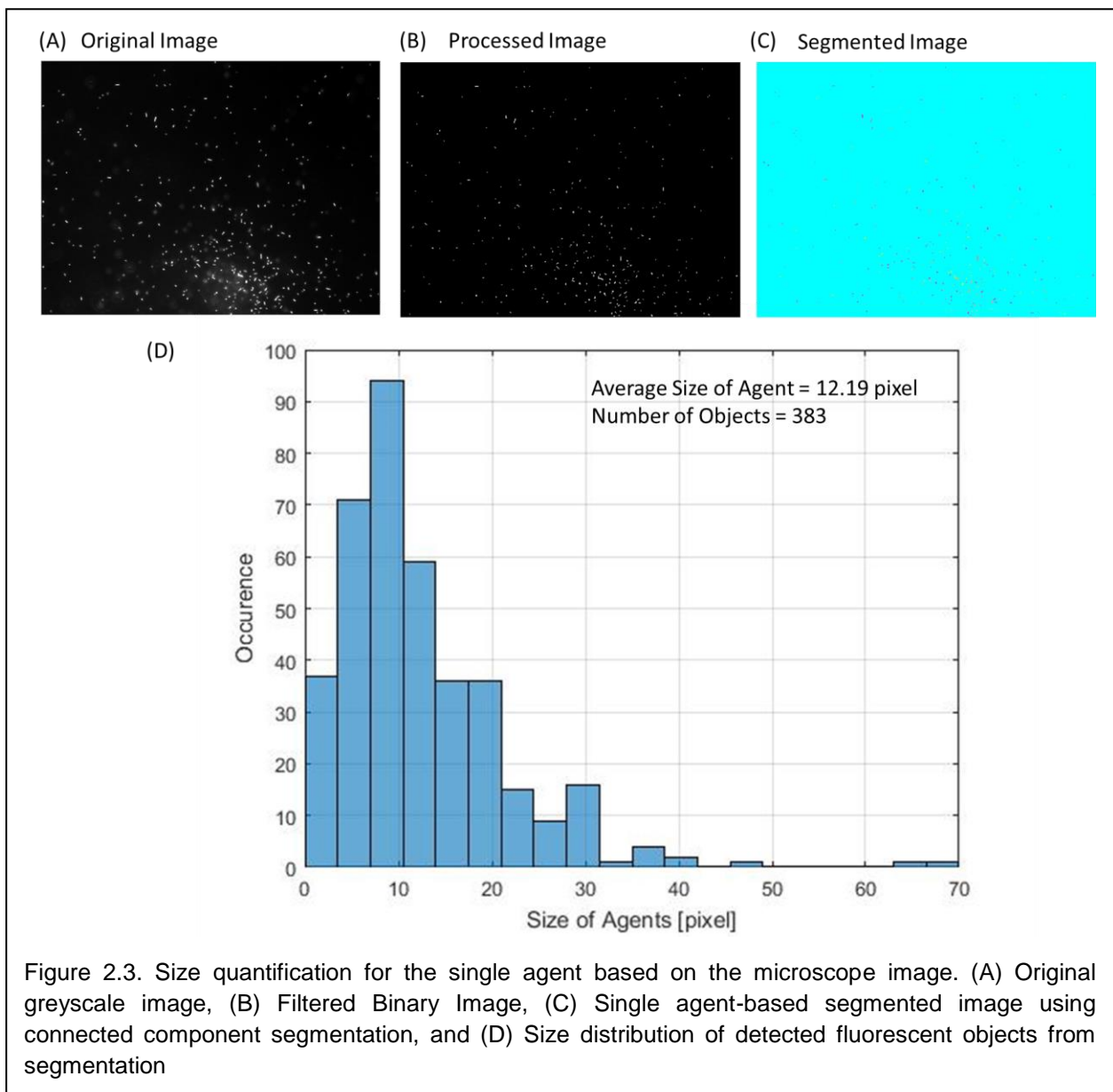


region of interest with a representative microscope image. Multiple images along the z-axis are then processed to build a 3D distribution map.

c. Filtering algorithm

In order to exclusively detect the fluorescent signals from fluorescent objects within the selected region of interest (ROI) of the image, a threshold filter based on the local and global greyscale intensity values was applied. We use rectangular bins of user-defined height and width to adaptively threshold each pixel. Different imaging modalities generate images with varying attributes such as signal-to-noise ratio, the average grayscale intensity value, etc., which present a challenge for obtaining consistent quantification results. We accommodate different

imaging modalities by allowing the user to manually set two threshold parameters. The first parameter sets a global greyscale intensity value ranging from 0 to 255, and the second parameter defines the acceptable percent variation from the mean greyscale intensity value inside any individual bin. Variable thresholds are then determined locally and used to assign any pixel with a raw greyscale intensity value greater than both the local and global thresholds in each bin a “1,” while all others are assigned a “0.” This procedure results in binary images with



false detection near locally bright or dark regions eliminated, showing only the locations of fluorescent objects within the sample as shown in Figure 2.2.

d. Quantification of the size of a single agent

Size quantification of individual fluorescent object presented a significant challenge in this work. When multiple fluorescent objects are located near one another, distinguishing a single agent requires computationally expensive segmentation algorithms, and random agent orientation causes the perceived size of each agent to vary greatly, especially for fluorescent objects with a high aspect ratio. Moreover, varying image resolution and excitation energy between different imaging modalities cause the signal-to-noise ratio to be inconsistent. In order to address these challenges and consistently and accurately quantify the number of fluorescent objects in imaged samples, the size of a single agent was incorporated into the analysis of each sample. *3DCONFO* includes this pre-analysis step for estimating the size of a single agent under different imaging conditions. The step also requires selecting a region of interest, which must be chosen from an area where fluorescent objects are sparsely distributed. Segmentation of connected components were identified for their size evaluation in order to determine the mean size of the single agent as shown in Figure 2.3. For example, the images of various bacterial strains were used to quantify the size of a single cell prior to enumeration of bacteria (Figure 2.S1).

e. Construction of 3D agent distribution map with compensation algorithm

Once the filtering parameters for the single image are optimized, a series of images along the z-axis are processed using the same parameters. The 3D agent distribution map is built based on the focal depth information of each frame. Simple piling up the multiple images, however, results in an overestimation of the number of fluorescent objects because the fluorescent signal from a single agent is present in neighboring frames. In order to filter signals such that final binary results only include at actual agent locations in 3D, a compensation algorithm was developed.

The repeating signal intensity profile throughout the z-stack images from a single agent is measured and fitted to a calibration curve (Figure 2.4 (C)). This curve, representing the light intensity as a function of distance along the z-axis, was modeled using the solution for 1D Fickian diffusion for a finite source placed between two semi-infinite bodies:

$$F = \text{erf}\left(\alpha\left(z + \frac{L}{2}\right)\right) - \text{erf}\left(\alpha\left(z - \frac{L}{2}\right)\right), \quad (2.1)$$

where fluorescent intensity is given by F , z is distance between the focal plane and the z

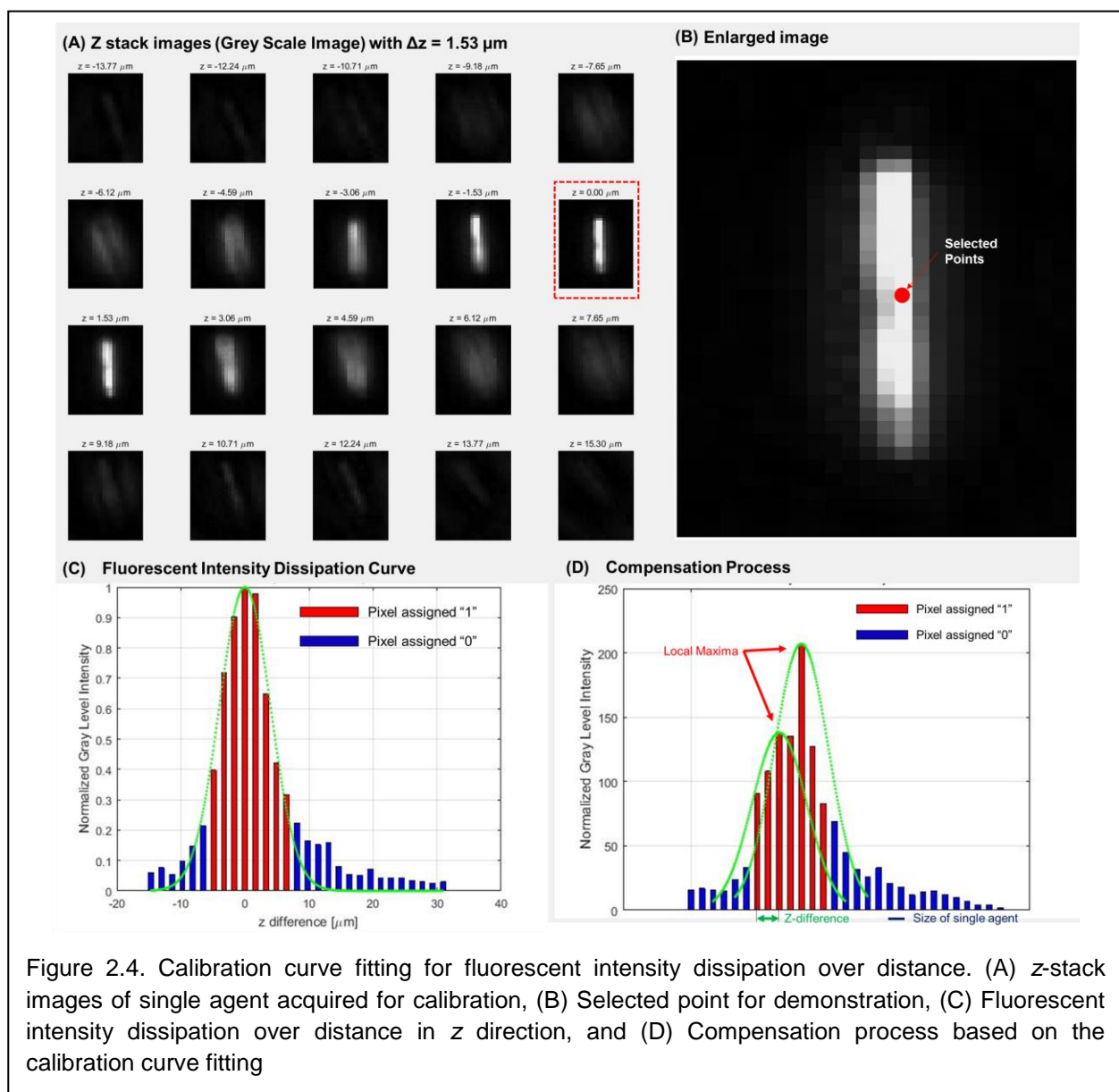
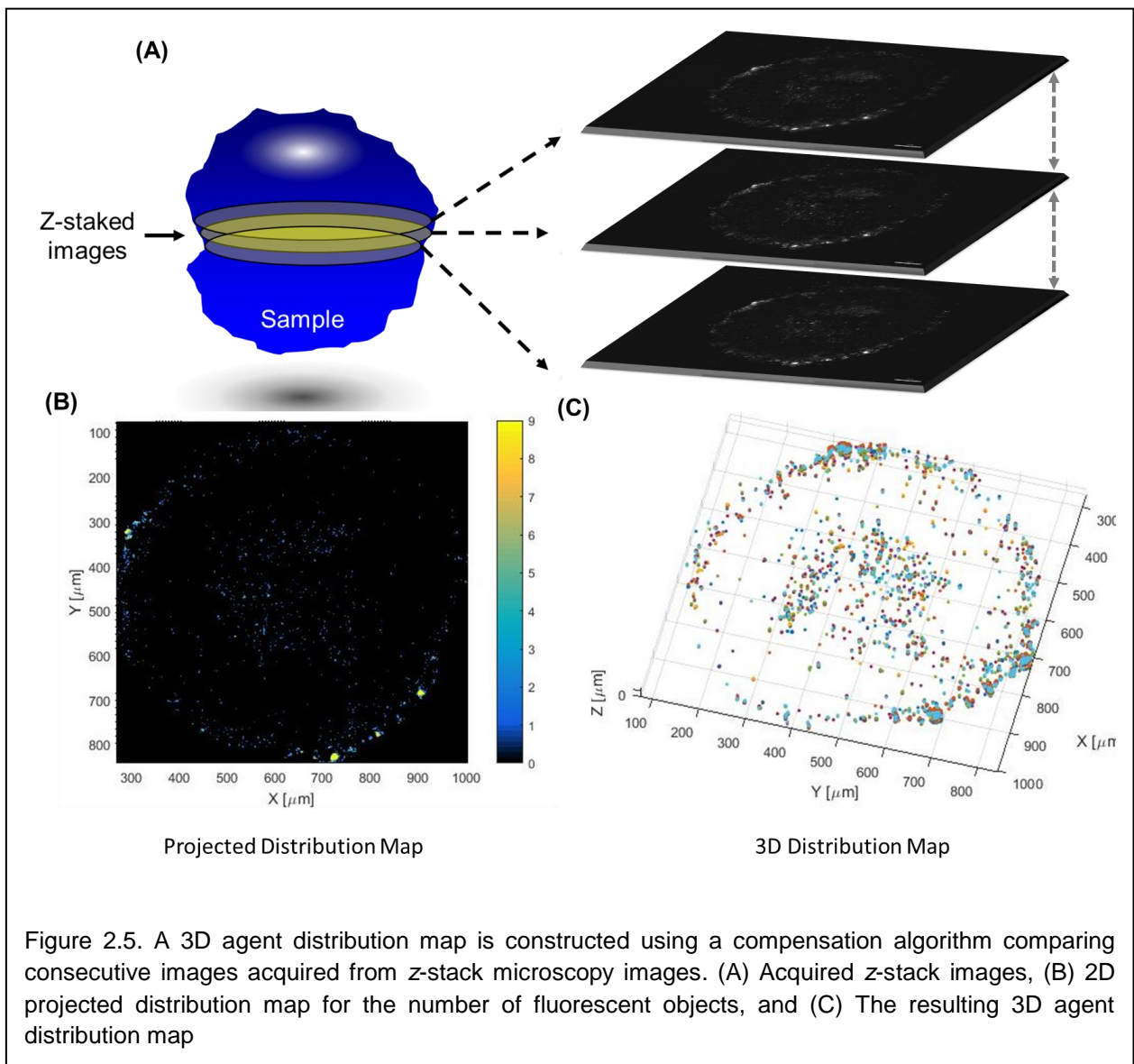


Figure 2.4. Calibration curve fitting for fluorescent intensity dissipation over distance. (A) z-stack images of single agent acquired for calibration, (B) Selected point for demonstration, (C) Fluorescent intensity dissipation over distance in z direction, and (D) Compensation process based on the calibration curve fitting

location of the fluorescent object, and L is width of the object. The constant, α , is solved through established model and experimental data from the library of sample images acquired with the equivalent imaging conditions. Once, the local maximum greyscale intensity values of multiple images throughout the z-axis are determined, the calibration curve, fitted at the local maximum is used to investigate whether the greyscale intensity value around the peaks are smaller than light dissipation curve to confirm that the signals are generated from the according local maxima. If distance between the peak and point of interest in an adjacent image from the z-stack

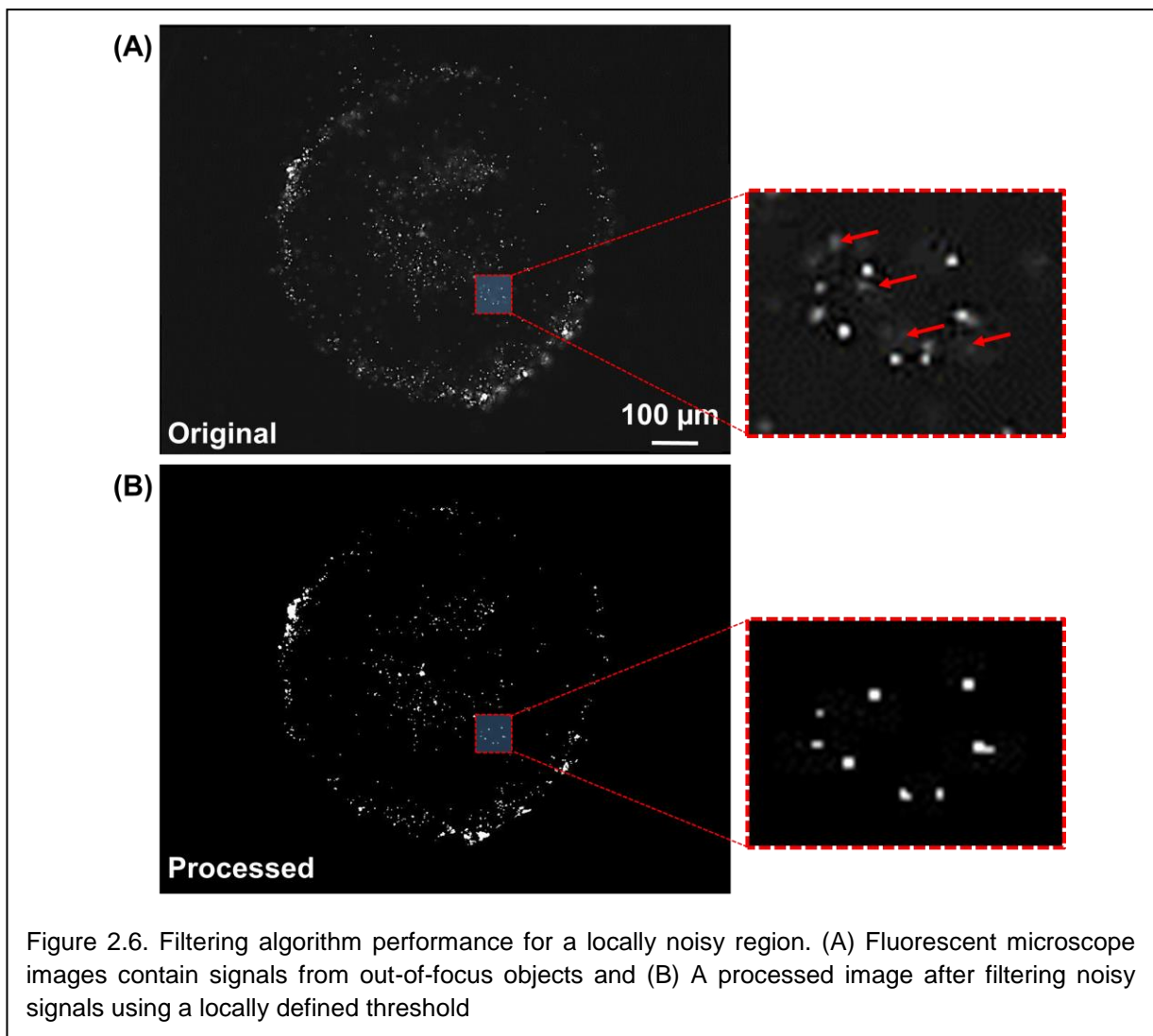


exceeds the size of single agent and the greyscale intensity value of the point is under the calibration curve, the point assigned “1” becomes “0” so as to exclusively detect the agent occupying locations. Figure 2.5 shows how the 3D agent distribution map is constructed applied with compensation algorithm.

2.3 Results

a. Filtering Algorithm

The filtering algorithm designed in this work utilizes a global threshold and a locally defined

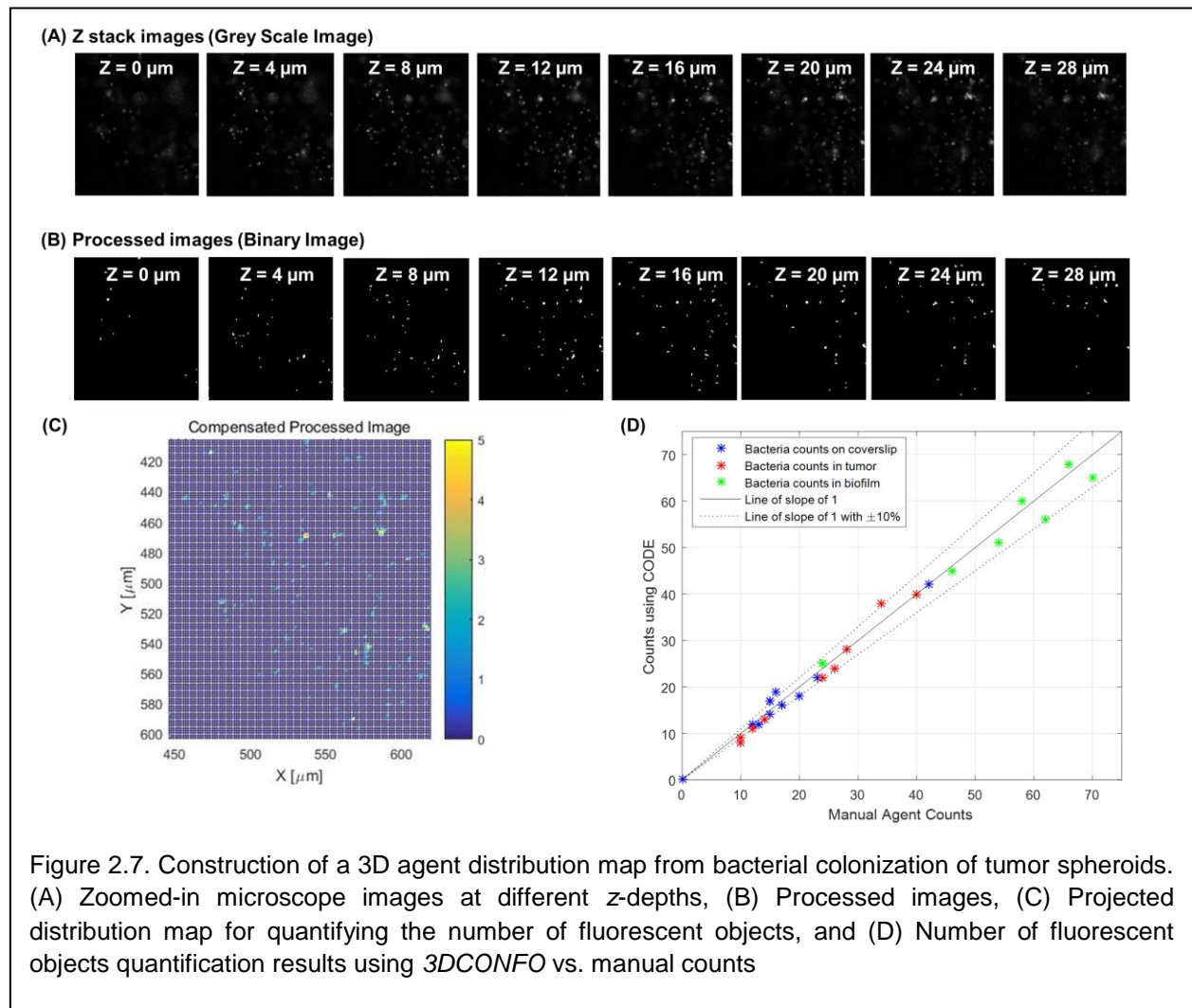


threshold, efficiently removing noise and fluorescent signals from objects above or below the focal plane as shown in Figure 2.2. However, many microscope images contain noisy signals originating due to auto fluorescence, inconsistent lighting conditions, etc., which may have a “cloudy” appearance. It is vital to distinguish and filter out the noise in order to quantify only the signals from infecting fluorescent objects. The filtering algorithm presented herein effectively excludes signals from noise as shown in arrows in Figure 2.6(A). Such signals may not be removed via the absolute threshold but are filtered by the local threshold. As shown in the resulting binary image in Figure 2.6(B), cloudy signals were excluded while distinctly brighter regions near the “cloudy” region were correctly detected as fluorescent objects.

b. Compensation algorithm

It is common that the fluorescent signals from one agent are detected in more than one slice of z-stack microscope images due to the light dissipation artifacts of fluorescent light. In order to accurately quantify the number of agent located within the sample without overestimating, it is crucial to resolve these limitations. To this end, the compensation algorithm was applied to interconnect multiple microscope images with determining if fluorescent signals originating from local maxima along the z-axis dissipate over adjacent 2D images from the z-stack. The algorithm removes signals when the greyscale intensity value surrounding a local maximum is lower than the calibrated dissipated light profile and the distance from the maxima to the point of interest is greater than the longest dimension (on average) of the fluorescent objects imaged. The culmination of the program is the creation of a projected agent distribution map, which can be used for analyzing the number of fluorescent objects and the distribution profile.

In order to determine the accuracy of the method for quantifying the number of fluorescent objects in a sample, we compared the number of fluorescent objects, bacteria on a coverslip, bacteria in tumor spheroids, or bacteria in a biofilm, detected by *3DCONFO* with the manual enumeration. The mean error was estimated to be $2.2 \pm 0.9 \%$ ($n = 27$). The majority of the error stemmed from the varying orientations of the fluorescent objects, which made the detected size of each vary significantly, thus skewing the enumeration of the fluorescent objects (Figure 2.7). Moreover, if the total number of fluorescent objects was too small, the results might not well represent the population and were more sensitive to deviations from average size measurements. Although higher magnification objectives and higher spatial resolution would



enhance the accuracy significantly, the major advantage of the proposed system is the quantification of fluorescent objects with the minimal computational power while providing highly accurate results given the appropriate conditions.

c. Application Study

Upon construction of 3D agent distribution map, *3DCONFO* converts the information from a number of pixels to a number of fluorescent objects. Depending on the application, the software can provide either the absolute number of fluorescent objects or the spatial density of agent accumulation. Spatial density of the agent accumulation is estimated from the sample size and focal depth of images. We have implemented *3DCONFO* to analyze the intratumoral penetration experiment using fluorescent bacteria *Salmonella* Typhimurium VNP20009 incubated with multicellular tumor spheroids (HCT-116 colon cancer). In order to analyze the intratumoral penetration performance of infecting fluorescent objects, i.e., bacteria, several indices were defined. The accumulation index (AI) quantifies the number of accumulating fluorescent objects that penetrated a given sample volume in units of number of fluorescent objects/ μm^3 :

$$\text{AI} = \frac{(n_{\text{agent}})_{\text{SAMPLE}}}{V_{\text{SAMPLE}}} \quad (2.2)$$

where V_{SAMPLE} is the volume of the sample and $(n_{\text{agent}})_{\text{SAMPLE}}$ is the number of fluorescent objects accumulated throughout the entire sample. In addition, the penetration index (PI) was defined to give a measure of the penetration depth of the infiltrating fluorescent objects with respect to the center of the sample:

$$\text{PI} = \frac{\sum_{i=1}^N r_i \cdot (n_{\text{agent}})_i}{R_{\text{max}} \cdot (n_{\text{agent}})_{\text{SAMPLE}}} \quad (2.3)$$

where r_i is the penetrating depth of each bin, $(n_{\text{agent}})_i$ is the number of the penetrating fluorescent objects within bin i , R_{max} is the maximum penetrating distance for the sample, and

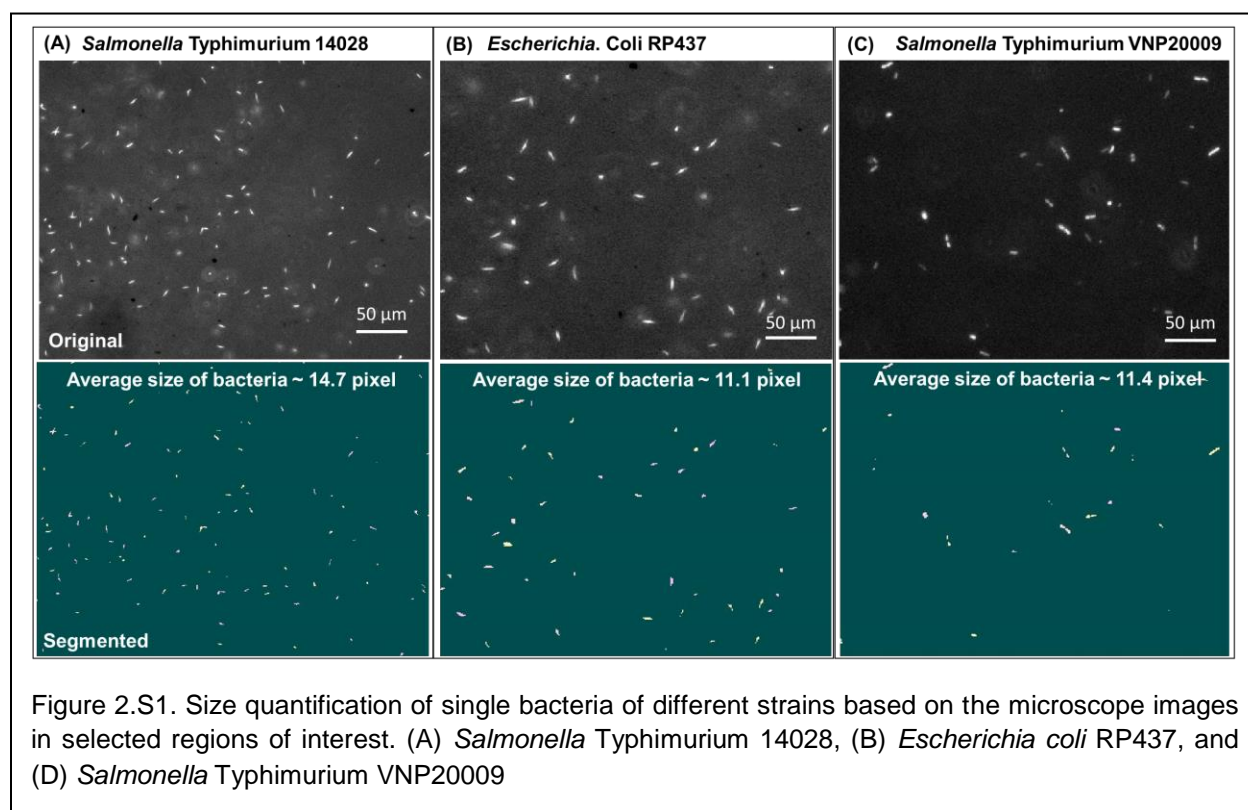
$(n_{\text{agent}})_{\text{SAMPLE}}$ is the total number of the fluorescent objects detected within the entire sample. The PI ranges from 0 to 1, where a value of 1 indicates that all of the fluorescent objects travelled to and ended up in the center of the sample and 0 indicates that all of the fluorescent objects remained in the periphery of the sample. The bacteria distribution map within tumor spheroids constructed using *3DCONFO* was used to precisely quantify penetration performance as well as the accumulation profile as shown in representative plot (Figure 2.S2). We also have utilized *3DCONFO* to precisely approximate the distribution of fluorescent bacteria in microfluidic device to quantitatively estimate bacterial chemotaxis [59]. The number and the location of bacteria were used to quantify chemotactic performance using indices such as the chemotaxis partition coefficient (CPC) [60] (Figure 2.S3). The bacteria that formed a thick biofilm on a glass substrate were imaged using fluorescence microscopy and *3DCONFO* generated the 3D agent distribution map (Figure 2.S4). It also quantified the number of bacteria deposited on the substrate, which was validated with manual counting of individual bacteria. Additionally, we used *3DCONFO* to assess the compactness of tumor spheroids by calculating the cell packing density, defined as the spatial fraction of cell nuclei [61]. This was done by fluorescently imaging slices of tumor spheroids with stained nuclei. *3DCONFO* was then used to quantify the spatial fraction of the size of cell nuclei and the average cell packing density profile along the radial dimension (Figure 2.S5).

2.4 Conclusion

We have developed a simple, semi-automated image processing paradigm for analyzing the distribution of fluorescent objects in microscope images, particularly useful for z-stacked sets. By using two manual pre-processing steps, the average size of the fluorescent objects is determined and used to accurately quantify the number of objects and produce a 3D map of the spatial distribution without the use of computationally expensive segmentation algorithms. We

demonstrated the robustness and accuracy of the method to analyze bacterial colonization of tissue, bacterial chemotaxis in a microfluidic channel, and the compactness of tumor tissue. This processing routine is widely useful in biomedical research applications. The method was implemented in a computationally efficient MATLAB program, which is available in the Supplementary Files.

2.5 Supplementary Information



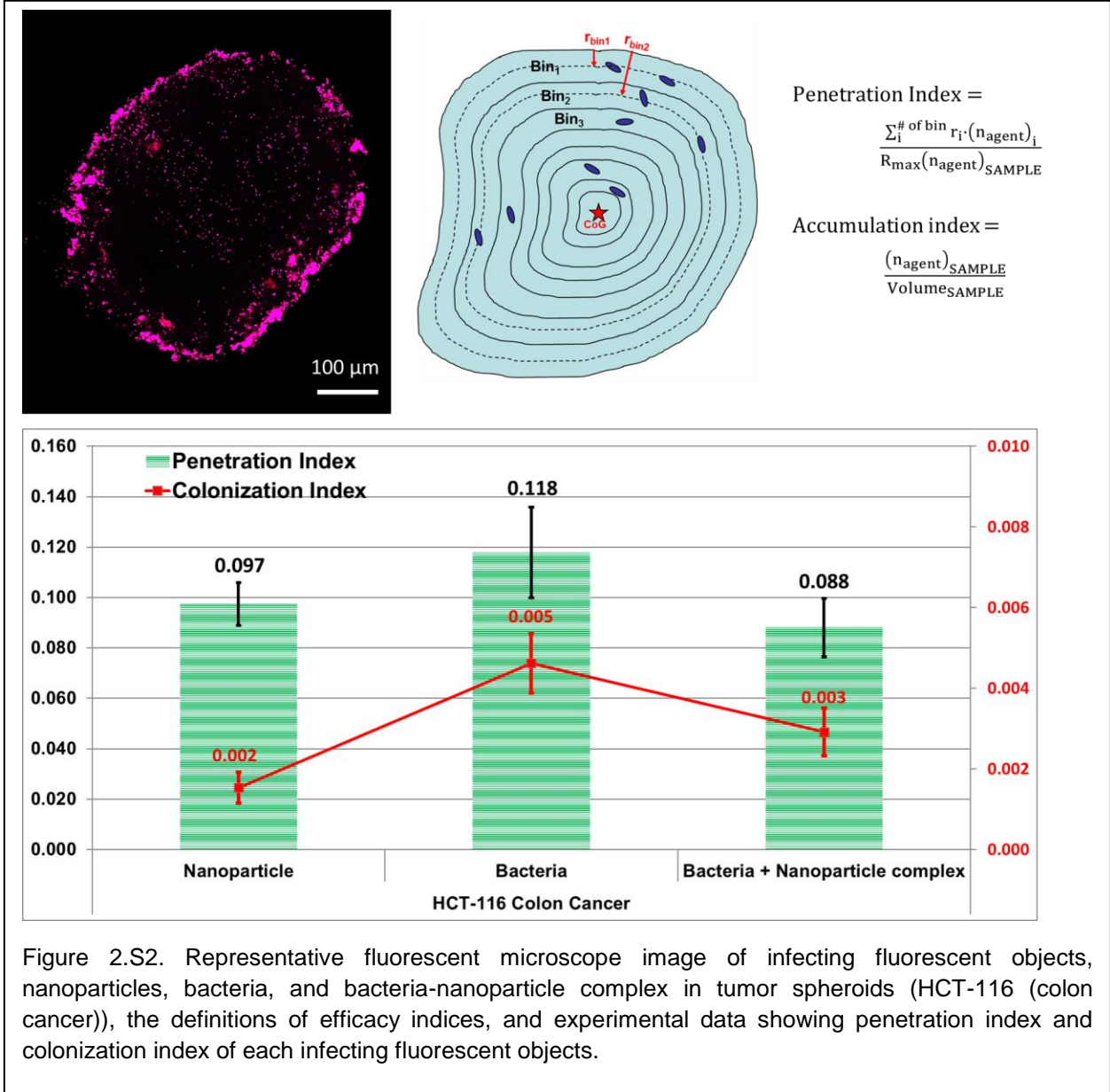
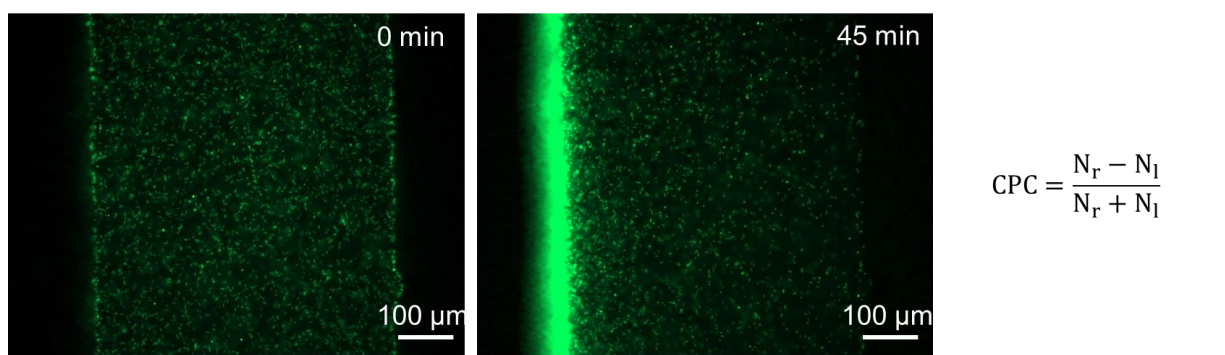


Figure 2.S2. Representative fluorescent microscope image of infecting fluorescent objects, nanoparticles, bacteria, and bacteria-nanoparticle complex in tumor spheroids (HCT-116 (colon cancer)), the definitions of efficacy indices, and experimental data showing penetration index and colonization index of each infecting fluorescent objects.



$$CPC = \frac{N_r - N_l}{N_r + N_l}$$

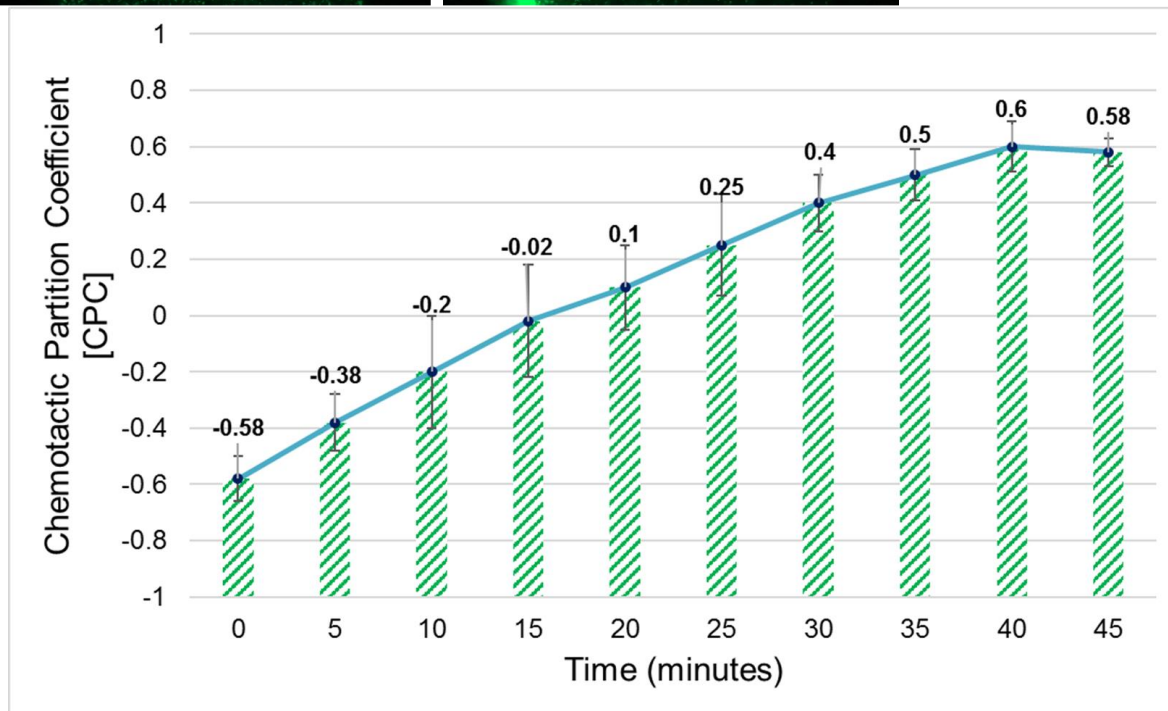
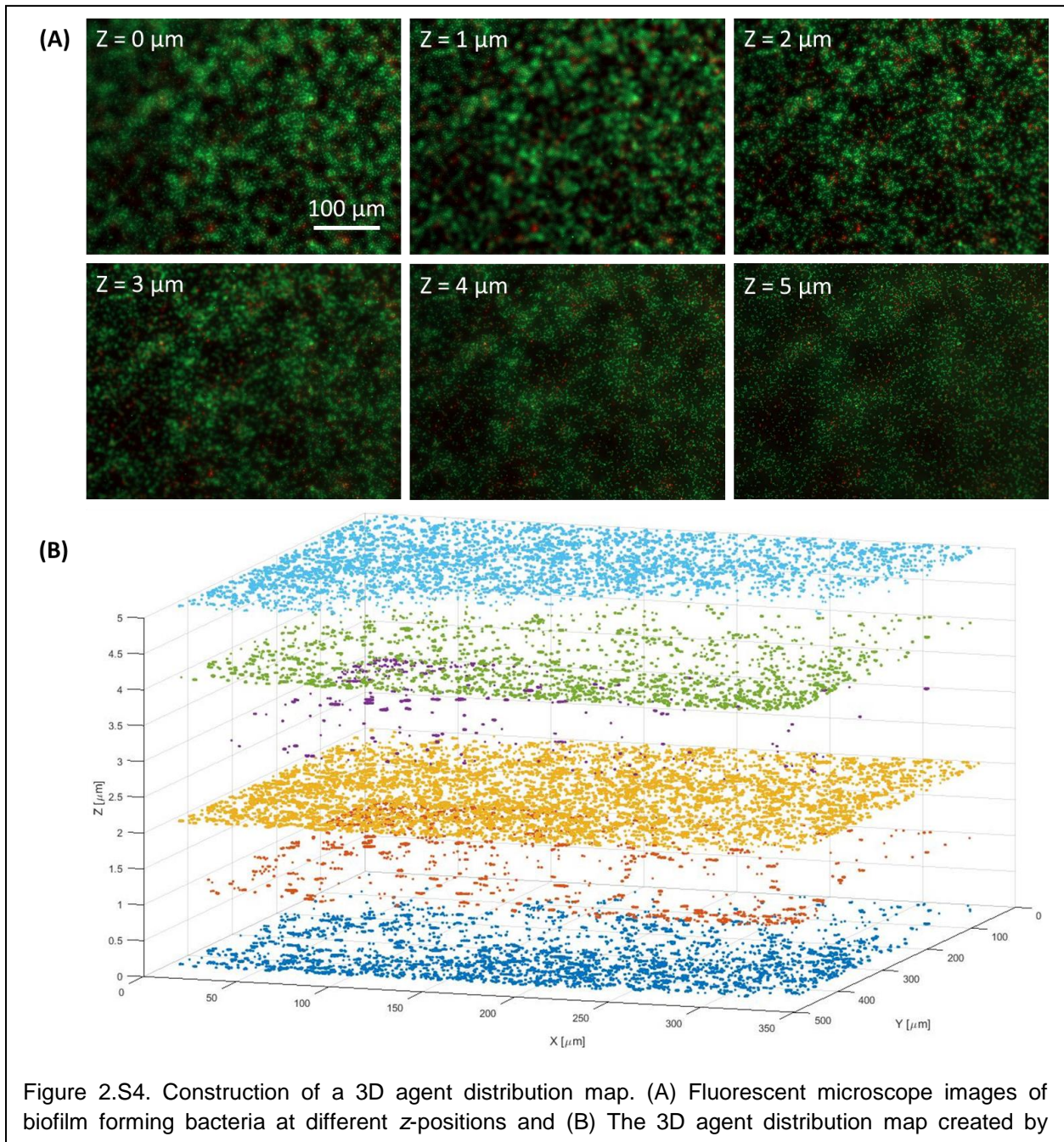
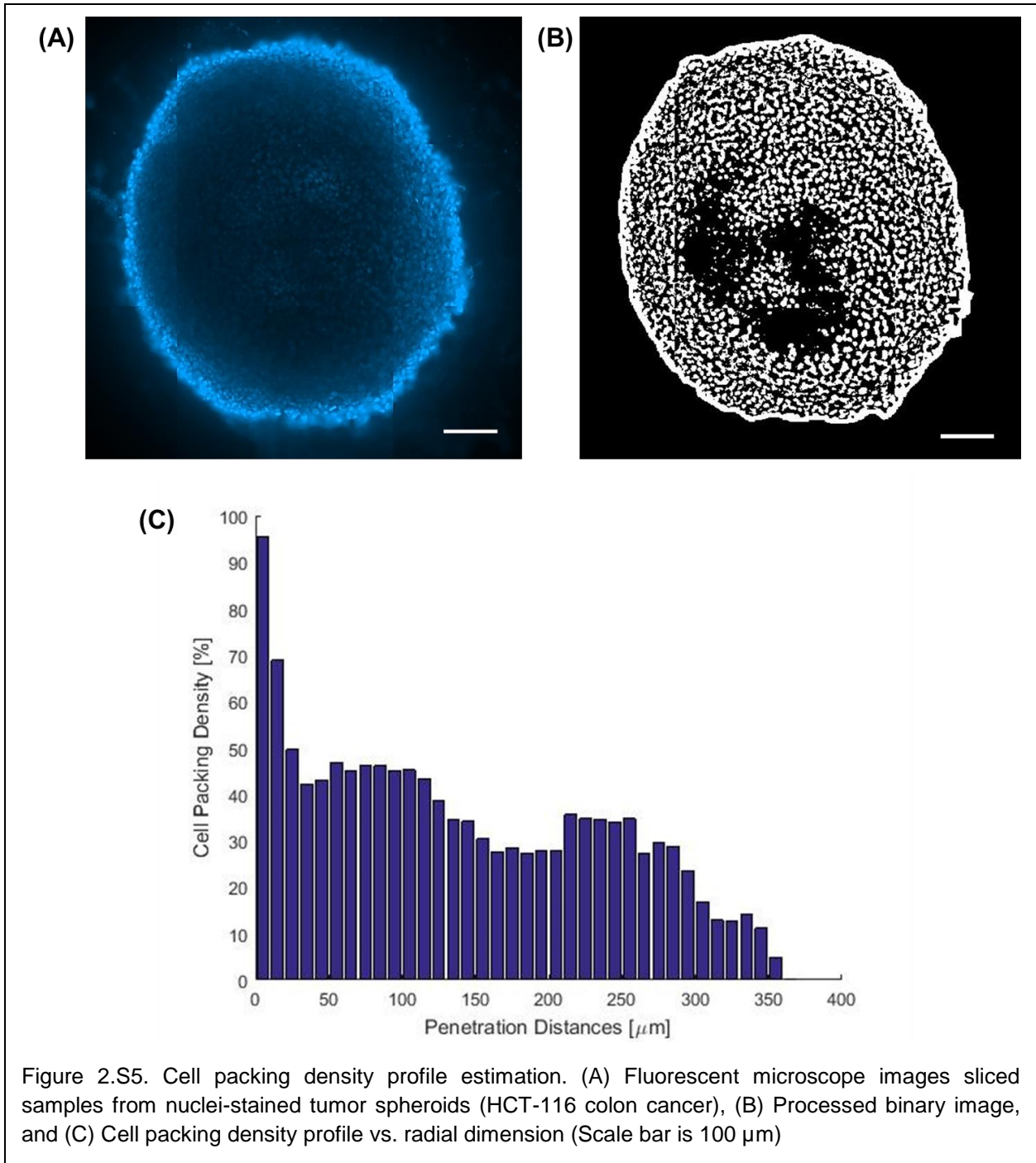


Figure 2.S3. 3DCONFO estimates the distribution of bacteria within a microfluidic channel to quantify chemotaxis via the chemotaxis partitioned coefficient (CPC) over time.





Chapter 3. Optimizing the restored chemotactic behavior of anticancer agent *Salmonella enterica* serovar Typhimurium VNP20009³

KEYWORDS

Bacterial anti-tumor therapy, chemotaxis, microfluidic chemotaxis assay, tumor-colonizing bacteria

3.1 Abstract

Bacteria, including strains of *Salmonella*, have been researched and applied as therapeutic cancer agents for centuries. *Salmonella* are particularly of interest due to their facultative anaerobic nature, facilitating colonization of differentially oxygenated tumor regions. Additionally, *Salmonella* can be manipulated with relative ease, resulting in the ability to attenuate the pathogen or engineer vectors for drug delivery. It was recently discovered that the anti-cancer *Salmonella enterica* serovar Typhimurium strain VNP20009 is lacking in chemotactic ability, due to a non-synonymous single nucleotide polymorphism in *cheY*. Replacing the mutated copy of *cheY* with the wild-type sequence restored chemotaxis to 70% of the parental strain. We aimed to investigate further if chemotaxis of VNP20009 can be optimized. By restoring the gene *msbB* in VNP20009 *cheY*⁺, which confers attenuation by lipid A modification, we observed a 9% increase in swimming speed, 13% increase in swim plate performance, 19% increase in microfluidic device partitioning towards the attractant at the optimum concentration gradient, and

³ Work done in collaboration with Katherine Broadway and Professor Birgit Scharf (VT Biological Sciences)

Note: The work presented in this chapter on the quantifications of chemotaxis and motility was done by SeungBeum Suh. Mutant construction, flagella labelling, and flagella quantification was done by Katherine Broadway.

Broadway, K, Suh. S, Behkam. B, Scharf. B, "Optimizing the restored chemotactic behavior of anticancer agent *Salmonella enterica* serovar Typhimurium VNP20009." Journal of Biotechnology 251 (2017): 76-83.

mitigation of a non-motile cell subpopulation. We conclude that chemotaxis can be enhanced further but at the cost of changing one defining characteristic of VNP20009. A less compromised strain might be needed to employ for investigating bacterial chemotaxis in tumor interactions.

HIGHLIGHTS

- A considerable subpopulation of non-motile cells exists in VNP20009 *cheY*⁺
- The *msbB* gene contributes significantly to the chemotaxis defect of VNP20009 *cheY*⁺
- VNP20009 cannot be made fully chemotactic without changing its core attributes

3.2 Introduction

Bacteria have been researched for their potential application as therapeutic agents for centuries. Specifically, the enterobacterium *Salmonella* is an attractive model for studying tumor targeting due to its facultative anaerobic nature, allowing for colonization of the differentially oxygenated necrotic and viable tumor regions [10], as well as large and small tumors [32]. In addition, *Salmonella* can be manipulated genetically with relative ease and possesses an intriguing facultative intracellular lifestyle [62]. Importantly, an attenuated, auxotrophic *Salmonella enterica* serovar Typhimurium strain has resulted in decreased tumor growth in mice bearing B16F10 melanoma and has been suggested to be able to colonize solid tumors up to a reported 9,000 times greater than the liver [63].

Several strains of *S. Typhimurium* have been constructed for the purpose of tumor targeting and chemotherapy delivery, most mentionable being: A1 [64]/A1-R [65]–[71], BRD509/BRD509E [72], [73], χ 4550 [74], CRC2631 [75], Δ ppGpp [76]–[78], LH340 [79]–[81], LVR01 [82], MvP728 [83]–[85], RE88 [86]–[88], SA186 [89], SB824 [90], SL3261 [91], [92], SL7207 [93]–[96], YB1 [97], [98], and VNP20009 [46]. VNP20009 was created by Low *et al.* [99] from strain 14028s

through selection for hyperinvasion by chemical/UV mutagenesis. The strain additionally contains two targeted deletions resulting in purine auxotroph (*purM*-), and attenuation by modification of lipid A (*msbB*-) [99]. VNP20009 was assessed in a variety of animal models, for acute toxic effects in cynomolus monkeys, yorkshire pigs and mice [100], as well as distribution in mice and nonhuman primates [46]. VNP20009 was found to preferentially target tumors in mice, with tumor:normal tissue colonization ratios of $\geq 1,000:1$ [46]. Finally, VNP20009 has been attributed to curing a dog with epitheliotropic lymphoma, in which the patient received two infusions of the bacteria, experienced a greater than 50% reduction of the tumor, and after five total infusions was disease free [101]. These studies culminated in a 2001 Phase 1 Clinical Trial, where VNP20009 was introduced as a treatment to patients with nonresponsive metastatic melanoma or renal cell carcinoma. Although colonization was observed for some patients, treatment with VNP20009 did not result in tumor regression [102]. The optimized balance of safe delivery and therapeutic efficacy remains a topic of interest for future use of *Salmonella* as a cancer therapy.

Many *S. Typhimurium* traits have been investigated for optimization of bacterial localization and retardation of tumor growth. These comprise components of virulence including pathogenicity islands SPI-1 and SPI-2, motility, chemotaxis, biofilm formation and metabolism [50], [103], [104]. Utilization of chemotaxis is particularly an interesting concept, because the machinery can be manipulated to facilitate bacterial colonization of specified regions of tumors based on the chemoattractant composition. Generally, it has been found that bacterial chemotaxis is favorable for tumor spheroid colonization *in vitro*, with specific chemoreceptors facilitating tumor microenvironment localization [49], [105]. In contrast, in immunocompetent mice, non-chemotactic or non-motile *Salmonella* strains colonized tumors with the same efficiency as the wild type [48]. Recently however, in a high-throughput screening of mutant *S. Typhimurium* strains, the presence of chemotaxis gene *cheY* and motility genes *motA* and *motB* was found to hold an advantage for tumor colonization [106]. Thus, due to different experimental conditions,

S. Typhimurium strains and cancer models, the role of chemotaxis *in vivo* is controversial, or perhaps greatly context dependent.

VNP20009 was recently discovered to be deficient in chemotaxis, due to a non-synonymous single nucleotide polymorphism (SNP) in the gene encoding the chemotaxis two-component response regulator, *cheY* [107]. Upon replacing the deficient copy of *cheY* with the wild-type copy, chemotaxis was recovered to 70% of the parental strain [107]. The overall objective of this study was to determine if chemotaxis of VNP20009 can be optimized to enable future analysis of maximal tumor targeting potentially through positive chemotaxis to metabolic byproducts of cancerous tissue. We report that by restoring the gene which encodes a lipid A altering enzyme *msbB*, we significantly increased the performance of the strain in chemotaxis assays, including swim plates and a microfluidic device, which establishes attractant gradients. We discovered that the enhancement in population scale chemotaxis performance was partially due to an increase in the motile cell population of VNP20009 *cheY+* upon curing the *msbB* defect. In conclusion, lack of modified lipid A due to the *msbB* deletion of VNP20009, which is a defining characteristic by the National Cancer Drug Dictionary [108], yielding the strain's safety as an anticancer therapy, also negatively impacts chemotaxis, which makes it a less ideal strain for exploring the impact of bacterial chemotaxis in cancer colonization.

3.3 Materials and methods

a. Bacterial strains and growth conditions

Bacterial cell cultures were routinely grown in MSB [109] media (1% tryptone, 0.5% yeast extract, 2 mM MgSO₄, 2 mM CaCl₂) at 37°C.

b. Mutant construction

Mutant strains were constructed using the lambda-red genetic engineering system [110], [111]. The *msbB* gene in VNP20009 *cheY+* was restored by replacing the mutated copy

with the parental copy. We were careful in this construction, not to alter the 3' extension of *pykA* in VNP20009, which resulted in 13 new codons [112]. This was ensured using primer pairs *msbB400dn* with *MID1dn*, and *msbB400up* with *MID2up*, with template chromosomal DNA from VNP20009 or 14028, respectively (see Supplemental Table 1). Each of the MID primers have overlapping regions, resulting in a DNA fragment approximately 1.7 kbps in size.

After deleting *msbB* in strain 14028, a mutant carrying the Suwvan deletion was selected for by plating on LB-0 plates (lysogeny broth [113] without NaCl) supplemented with 6 mM ethylene glycol-bis(β -aminoethyl ether)-N,N,N',N'-tetraacetic acid (EGTA). All mutations were confirmed by Sanger sequencing.

c. Quantitative swim plate assay

MSB swim plates (0.3% agar) were inoculated with 2.5 μ l of stationary phase cultures and incubated for approximately 12 hours at 37°C. Data was normalized to the average of 14028 and represents 6 experiments, except the negative control VNP20009 with 3 experiments, each in triplicate.

d. Microfluidic device fabrication and testing

The design and fabrication of the device was previously described in detail [52]. Briefly, polyethylene glycol diacrylate (PEG-DA, MW=700 Da, 10% (v/v) in phosphate buffered saline (PBS)) solution mixed with 0.5% (w/v) of the photoinitiator Irgacure® 2959 (Sigma-Aldrich, St. Louis, MO) was photo-polymerized by 15 seconds of UV treatment (365 nm, 18 W/cm², Omnicure S1000, Vanier, Quebec) within a polydimethylsiloxane (PDMS) enclosure on the glass slide. A three-channel pattern blocked the UV penetration to establish hydrogel wall around the channels. A PDMS layer with access ports for inlet and outlet tubing was placed on the PEG-DA hydrogel layer and the entire assembly was sandwiched between two plexiglass supports to ensure complete seal. Continuous flow of motility buffer (MB; 6.4 mM K₂HPO₄, 3.5 mM KH₂PO₄, 0.1 mM EDTA, 1 μ M L-

methionine, 10 mM _{DL}-lactate, 2 mM MgSO₄, 2 mM CaCl₂, pH 7.0) at 5 µl/min through the left outer channels and L-aspartic acid in MB in the right outer channel was maintained for 60 minutes using a syringe pump (PHD Ultra syringe pump, Harvard apparatus, Holliston, MA). Finite element analysis software package COMSOL® was used to evaluate the required diffusion time for L-aspartic acid transport through the hydrogel wall to establish a quasi-steady and linear chemical concentration gradients across the central channel. For instance, the optimum chemical concentration gradient of 1.54×10^{-5} M/mm was achieved within 60 minutes where the chemo-attractant channel was filled with the L-aspartic acid at a concentration of 10^{-4} M. For the computational model, the diffusion coefficient of L-aspartic acid was attained to be $D = 1.5 \times 10^{-6}$ cm²/s, from previous work using a Franz diffusion cell [52]. Once the chemical concentration gradient was established through the central channel, the bacteria suspended in MB were manually injected to the central channel. Bacterial biased distribution due to the chemotaxis reached steady state within 15 minutes.

e. Imaging and data analysis of the chemotaxis response within microfluidic device

Bacterial biased migration via chemotaxis within the microfluidic device was captured using a Zeiss AxioObserver Z1 inverted microscope equipped with an AxioCam mRM camera and a 20x objective. The images were analysed using an image processing algorithm developed in MATLAB to quantify the number of bacteria located either in the left or right half plane of the central channel. The chemotaxis performance was quantified using the chemotaxis partition coefficient (CPC) [52], a population-metric showing the chemotaxis responsiveness and is defined by

$$CPC = \frac{B_r - B_l}{B_r + B_l} \quad (3.1)$$

where B_r is the number of bacteria in the right half plane of the central channel, B_l is the number of bacteria in the left half plane of the central channel. When the chemo-effector

is located in the right side of a central channel, CPC values of +1 and -1 indicate the strongest attraction or repulsion, respectively. Data are representative of an average of 5×10^5 cells/experiment.

f. Image and data analysis of bacterial swimming speed

Bacterial movement was captured using a Zeiss AxioObserver Z1 inverted microscope equipped with an AxioCam Hsm camera and a 63 \times oil immersion objective at a spatial resolution of 0.31 $\mu\text{m}/\text{pixel}$ and temporal resolution of 30 fps. A minimum of 80 bacteria were tracked in each experiment and three independent set of experiments were carried out for each strain. All experiments were conducted at 37°C. The recorded images were analyzed in ImageJ using the Manual Tracking plug-in tool (NIH, Bethesda, MD). The instantaneous speeds were calculated by dividing the distances travelled during each time increment by the time increment. The average swimming speed was determined through averaging the instantaneous swimming speeds over independent experiments. The percentage of motile bacteria in the total population was quantified using an image processing algorithm developed in MATLAB, which detects the stationary (non-motile) subpopulation. The position of each bacterium was tracked at 30 second intervals, and bacteria with unchanged coordinates over two consecutive images were deemed non-motile. A total of 18 images (containing approximately 1,500 bacteria on average) were analyzed for each experiment, and three independent set of experiments were carried out for each strain.

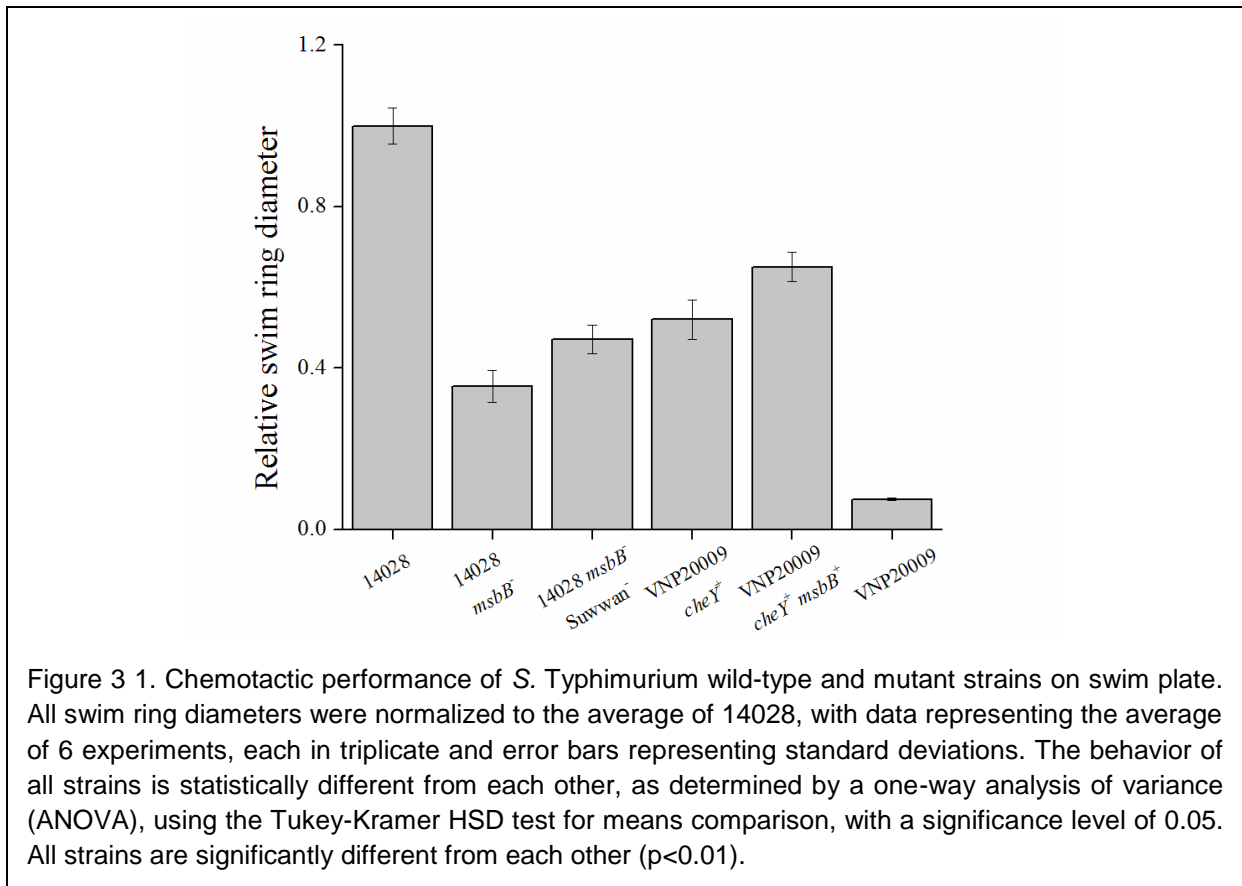
g. Flagella labeling, fluorescence microscopy and image acquisition

Cell cultures were grown to an OD_{600} of 1.0 in MSB media at 37°C with shaking at 100 rpm, and labeling was essentially performed as described elsewhere [114]. Cells were harvested at 1,500 $\times g$ for 5 minutes, washed 3 times in MB, with a final resuspension in 500 μl MB. One vial of Cy3 monofunctional dye was dissolved in 100 μl MB with 0.0001% Tween-20 (MBT) and divided amongst *S. Typhimurium* 14028 and VNP20009 *cheY*⁺. Cells were labeled by incubation at room temperature with gentle shaking for 60 minutes. Cells were washed 3 times in MB to

remove excess dye, diluted 10 fold in MBT, and 5 μ l sample aliquots added to poly-L-lysine treated glass slides. Fluorescently labeled cells and filaments were then observed on an Olympus IX71 microscope with Applied Precision SoftWorx image program, using a 100x objective. Fluorescence signal was detected using a TRITC filter.

h. Immunoblotting

Bacterial cell cultures were grown to an OD_{600} of 1.0 in MSB at 37°C with shaking at 100 rpm. Culture aliquots of 25 μ l, as well as 25 μ l supernatant aliquots of a 1 ml sample centrifuged for 10 minutes at 13,000 \times g, were prepared by the addition of 15 μ l loading buffer with β -mercaptoethanol and boiling at 95°C for 5 minutes. Samples were separated in 12.5 % SDS polyacrylamide gel and transferred to a nitrocellulose membrane. The membrane was probed with polyclonal rabbit antibody for *Salmonella* anti-FliC/FliB (Difco™) at a dilution of 1:50,000.



After removal of residual unbound antibody, blots were incubated with donkey anti-rabbit horse radish peroxidase conjugated antibody at a dilution of 1:2,500. After removal of unbound antibody, detection was achieved by enhanced chemiluminescence (Amersham ECL Western Blotting Detection Kit) using Hyperfilm ECL (GE Healthcare). Films were scanned with an Epson Perfection 1640SU and scans were analyzed using ImageJ.

3.4 Results

a. Chemotactic ability is significantly increased by restoring *msbB* in VNP20009 *cheY*⁺

We first aimed to determine the contribution of *msbB* to the remaining chemotaxis defect observed in VNP20009 *cheY*⁺. We therefore restored the *msbB* gene in VNP20009 *cheY*⁺ using the lambda red protocol [111]. Swim plates were inoculated with bacterial strains and the chemotactic response was measured. We determined that a restoration of *msbB* in the VNP20009 *cheY*⁺ background increased the relative swim plate phenotype by 13% (Figure 3.1). VNP20009 also carries a *Suwwan* deletion, which suppresses certain phenotypes caused by the *msbB* deletion such as its sensitivity to the chelator ethylene glycol-bis(β-aminoethyl ether)-N,N,N',N'-tetraacetic acid (EGTA) [115]. To differentiate between the contribution of the *msbB* and the *Suwwan* deletion to the chemotaxis phenotype, we created two mutant strains of the parental strain 14028, one carrying a deletion in *msbB* and one that is additionally lacking the *Suwwan* region. We found an *msbB* deletion alone had a severe effect on bacterial chemotaxis, with the average phenotype only reaching 34% of the parental strain. However, when the *Suwwan* region was deleted additionally, we found a significant increase (by 12%) in the chemotaxis phenotype on swim plate (Figure 3.1). We hypothesize that the compensating effect of the *Suwwan* deletion for several physiological characteristics observed in VNP20009 is also associated with its effect on chemotaxis and motility. Interestingly, there is only a small (5%) but significant difference between 14028 *msbB*⁻ *Suwwan*⁻ and VNP20009 *cheY*⁺ of 5% (Figure 3.1),

with the only genomic differences between the two strains being the *purM* disruption and SNPs inherently present in VNP20009 [112]. Therefore, *msbB* and Suwvan deletions majorly contribute to the chemotaxis defect discovered in VNP20009 *cheY*⁺.

b. Swimming speed is increased by restoration of *msbB*

To determine the effect of *msbB* on motility, a factor playing into the chemotactic response on swim plates, we measured the swimming speed of 14028, VNP20009 *cheY*⁺ and VNP20009 *cheY*⁺ *msbB*⁺ (Figure 3.2). The instantaneous speeds from the distances travelled during each time increment were defined as $\frac{\|\Delta\vec{d}\|}{\Delta t}$, where Δd is distance travelled and Δt is time increment.

The average speed of the strain was computed as $\frac{\sum_{i=1}^N \frac{\|\Delta\vec{d}_i\|}{\Delta t}}{N}$, where N is the total number of

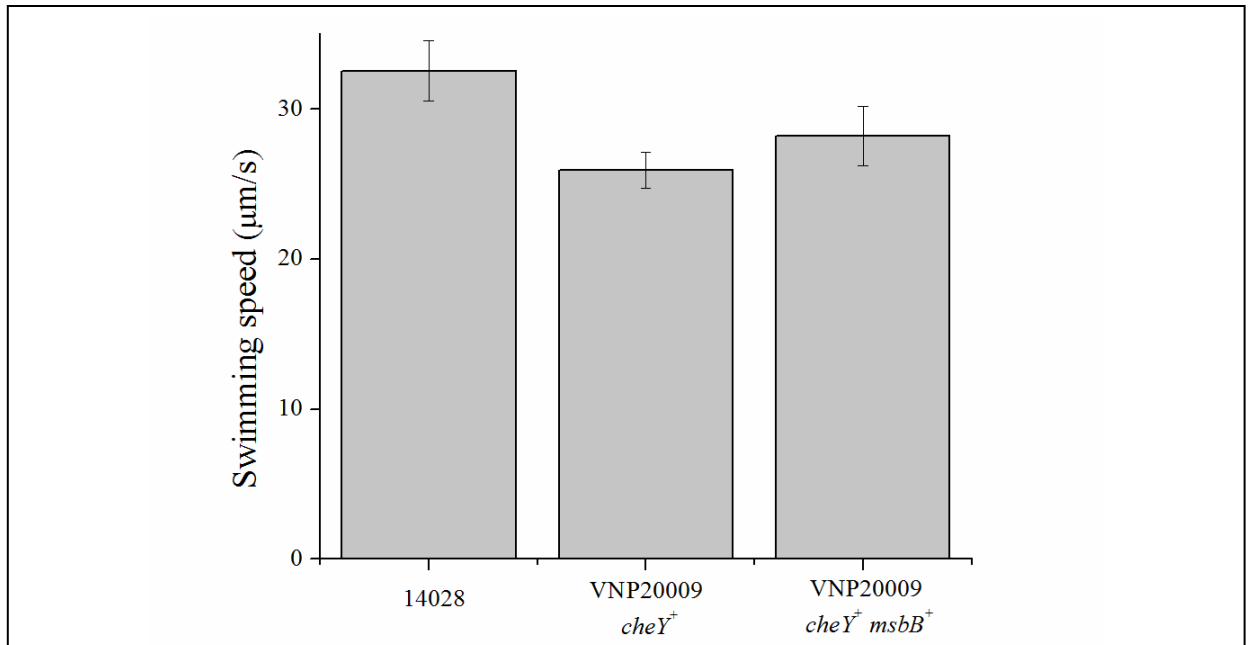


Figure 3.2. Swimming speed of *S. Typhimurium* wild-type and mutant strains. The average swimming speed was assessed by 2-D bacterial cell tracking for 14028 (n=95), VNP20009 *cheY*⁺ (n=67), and VNP20009 *cheY*⁺ *msbB*⁺ (n=81) cells. Error bars represent standard error and statistical significance was determined by a one-way ANOVA followed by Tukey-Kramer HSD test. A p-value of 0.05 was used as the threshold for significance, with statistical differences between all tested strains being p<0.0001.

time steps. The average speed of strains 14028, VNP20009 *cheY*⁺, and VNP20009 *cheY*⁺ *msbB*⁺ were 32.5 μm/s, 25.9 μm/s, and 28.2 μm/s, respectively (Figure 3.2), with the measured swimming speed of 14028 being in agreement with the literature [116]. There is a 20% difference in the average swimming speed between 14028 and VNP20009 *cheY*⁺ (p<0.0001). Notably, the swimming speed increased by 10% with the restoration of *msbB* (p<0.0001). Therefore, swimming speed might contribute to the reduced chemotaxis proficiency observed in VNP20009 *cheY*⁺.

c. A subpopulation of non-motile cells exists in VNP20009 *cheY*⁺ and is mitigated by restoration of *msbB*

While tracking bacteria for swimming speed measurements, we observed a substantial subpopulation of non-motile VNP20009 *cheY*⁺ cells, which were not included in the swimming speed calculations. To determine the percentage of motile cells within populations, motile and

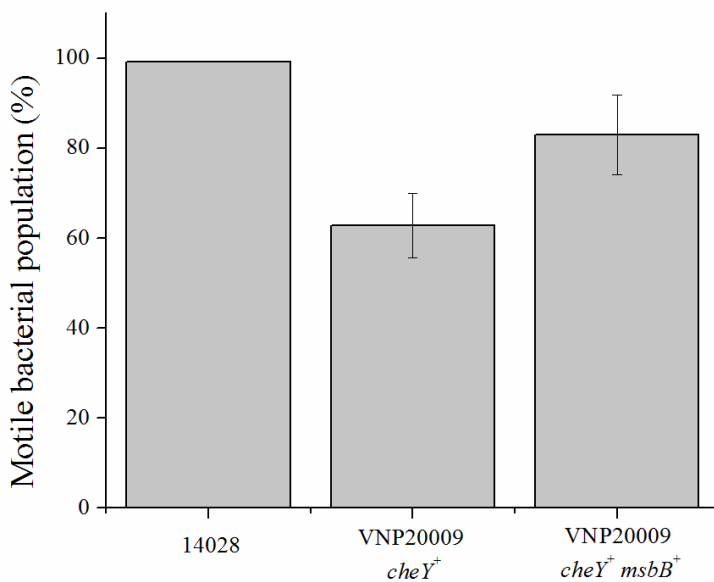
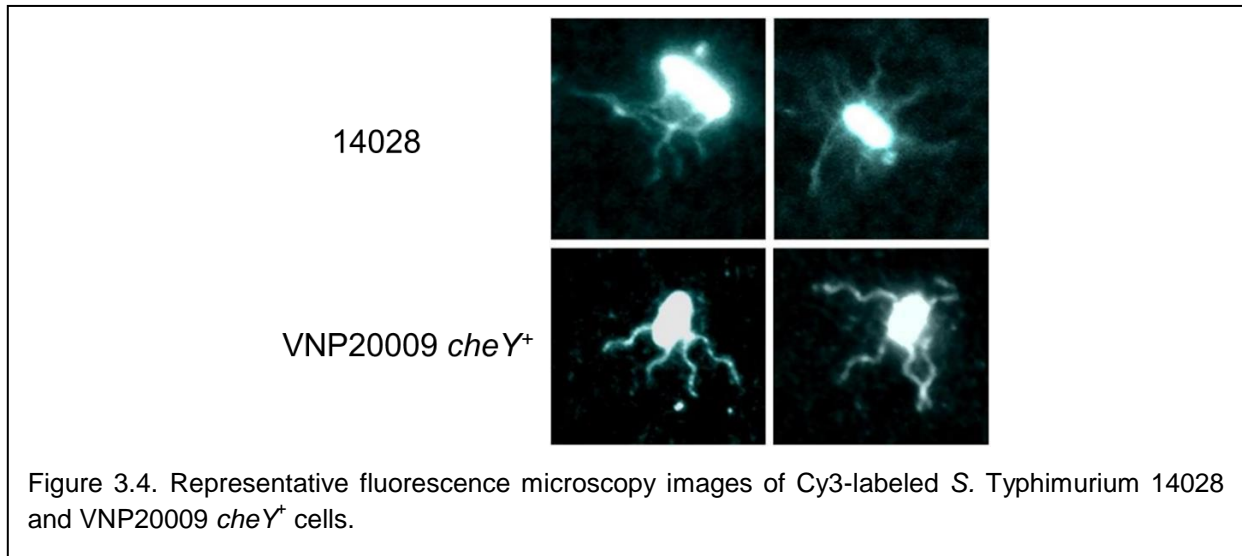


Figure 3.3. Proportion of motile cells in *S. Typhimurium* wild-type and mutant strains. The percentage of motile bacteria in the whole cell population was assessed through manual tracking. Data is represented as averages of 3 independent experiments for each strain, and error bars represent standard error. Statistical significance was determined by a one-way ANOVA followed by Tukey-Kramer HSD test. A p-value of 0.05 was used as the threshold for significance with statistical differences between all tested strains being p<0.001.



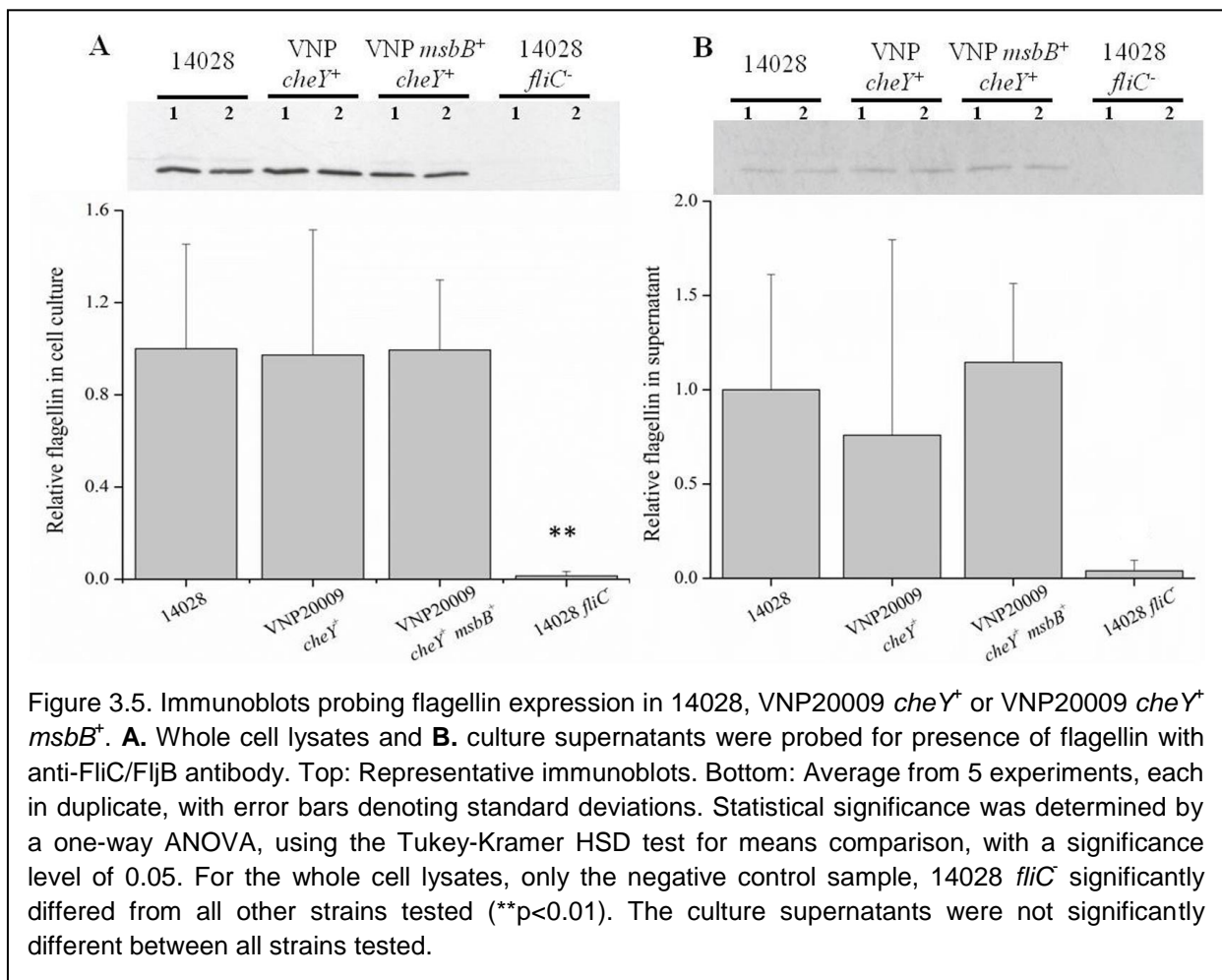
non-motile cells were manually counted, with bacterial 2-D tracking (Figure 3.3). While the whole population of 14028 is motile, only 63% of the VNP20009 *cheY*⁺ cells exhibited motility. Interestingly, the restoration of *msbB* resulted in a greater than 20% increase of the motile population to 83% in VNP20009 *cheY*⁺ *msbB*⁺. Thus, the presence of *msbB* considerably affects cell population motility.

d. Flagellation is unaffected by *msbB*

The deletion of the *msbB* gene could potentially affect flagellation and therefore influence the swimming speed and motility of VNP20009 *cheY*⁺. We labeled motile cells with Cy3 fluorescence dye to observe flagella quality for VNP20009 *cheY*⁺ and 14028. Specifically, we aimed to compare relative number, length, and helical pitch of flagellar filaments. No differences in these three parameters were observed between the two strains (Figure 3.4). However, we noted the presence of free flagellar filament fragments in VNP20009 *cheY*⁺ preparations more frequently than in 14028, which could have been a result of the extensive washing steps required during sample preparation (data not shown). Next, we quantified the amount of flagellin expressed, by probing cell extracts with an antibody against *Salmonella* FliC/ FliB, compared to a *fliC* strain as the negative control. We did not find any differences between 14028, VNP20009 *cheY*⁺, and VNP20009 *cheY*⁺ *msbB*⁺ (Figure 3.5). The observation of free filaments in the

fluorescently labeled VNP20009 *cheY*⁺ preparations prompted the hypothesis that the *msbB* deletion in VNP20009 could result in incomplete support of the flagella through alteration of the LPS/L-ring anchorage system, which might lead to greater flagella shearing. We therefore isolated the culture supernatant after removing bacteria by centrifugation and assayed for presence of flagellin. No differences in the flagellin amounts present in culture supernatants were detected. In fact, statistically, the amount of detected flagellin was not distinguishable between the negative control and test strains. In conclusion, deletion of *msbB* does not negatively affect flagellation.

e. The presence of *msbB* increases the performance of VNP20009 *cheY*⁺ in microfluidic chemotaxis assays



To investigate the chemoattractant sensitivities of 14028, VNP20009 *cheY*⁺, and VNP20009 *cheY*⁺ *msbB*⁺, we used a microfluidic device. Various concentration gradients ranging from 0 M/mm (control) to 3.0×10^{-5} M/mm of L-aspartic acid were established across the central channel of the device to characterize the bacterial response in the presence of the chemo-effector. Continuous flow of L-aspartic acid in MB in the right channel and MB in the left channel was maintained to generate static, linear concentration gradients of L-aspartic acid via diffusion through the hydrogel walls separating the central channel from the flow channels. The chemotactic partition coefficient (CPC) was computed and shown as a function of concentration gradient, where a value of 1 would indicate the strongest response of bacteria to the chemoattractant (Figure 3.6). In control experiments with 14028, VNP20009 *cheY*⁺, and VNP20009 *cheY*⁺ *msbB*⁺, bacterial migration did not show a biased distribution, as expected ($|CPC| < 0.05$). The attractant concentration gradient eliciting the strongest response was determined to be 1.5×10^{-5} M/mm. As expected, the non-chemotactic parental strain VNP20009 showed no response. While VNP20009 *cheY*⁺ showed a weak response at peak concentration, restoration of *msbB* resulted in an enhanced response of VNP20009 *cheY*⁺ *msbB*⁺ (Figure 3.6). Since 37% and 17% of the VNP20009 *cheY*⁺ and VNP20009 *cheY*⁺ *msbB*⁺ cell populations are non-motile, respectively, we analyzed the microfluidic chemotaxis data eliminating non-motile cells. At the optimum concentration gradient, data for the motile population of 14028 and VNP20009 *cheY*⁺ *msbB*⁺ mirror the data acquired for the mixed populations. In contrast, after factoring out the non-motile subpopulation for VNP20009 *cheY*⁺, sensitivity increased by 47%. Thus, the non-motile subpopulation contributes significantly to the chemotactic performance of VNP20009 *cheY*⁺ in the microfluidic device.

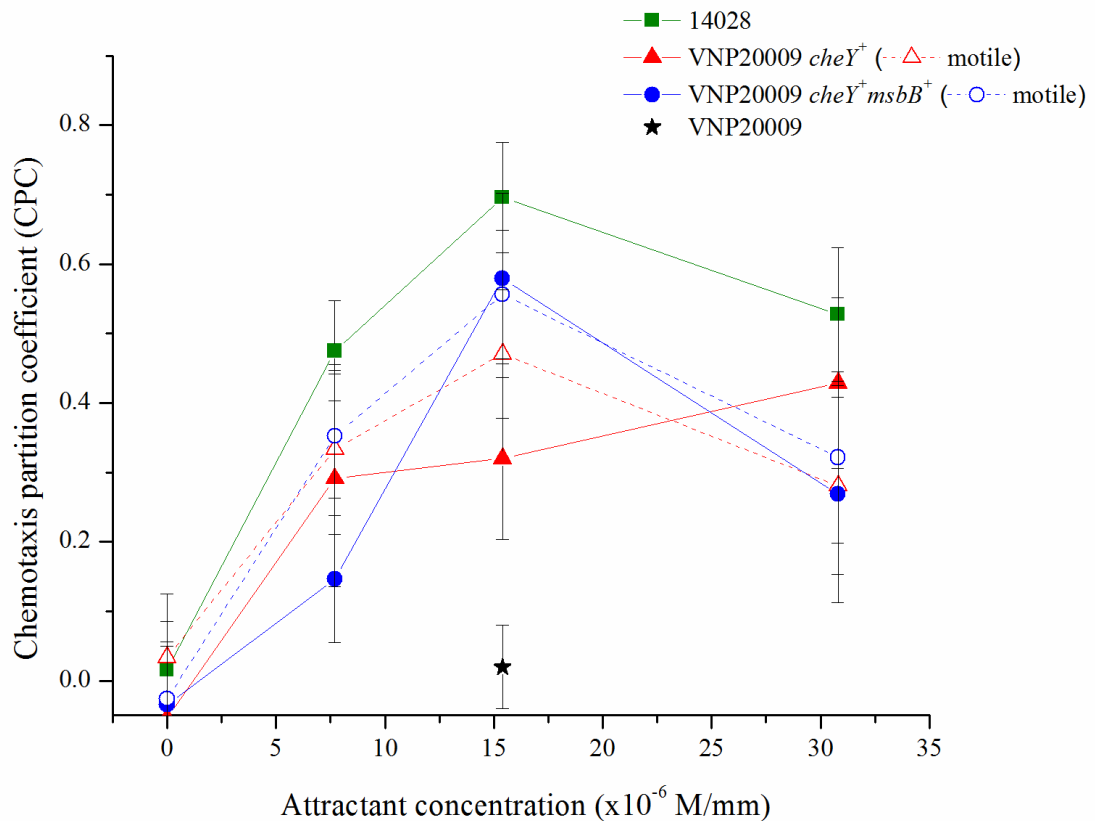


Figure 3.6. Chemotactic performance of *S. Typhimurium* wild-type and mutant strains to L-aspartic acid in a microfluidic device. Each strain was loaded into the attractant gradient established-microfluidic device and data was collected after 15 minutes. The CPC value was ascertained for the whole population and only the motile population of each strain, as indicated (the whole population is the motile population for 14028). At the peak attractant concentration, statistical analysis with one-way ANOVA, followed by Tukey-Kramer HSD test with a significance level of 0.05, was performed. For motile populations, all strains significantly differed from one another ($p < 0.001$), as well as when whole populations of all strains were compared ($p < 0.001$).

3.5 Discussion

Recent literature has witnessed a comeback for the potential use of bacterial therapy against cancer. Published work on bacterial therapy has increased two fold every 2.5 years since the mid-1990s through 2010 [8], where engineered strains of *Salmonella Typhimurium* have been most extensively studied for decades. Success of attenuated *S. Typhimurium* strains is well established in diverse tumor and animal models, ranging from immunodeficient to

immunocompetent mice; xenograft and syngeneic derived tumors; orthotopic, intravenous, and subcutaneous injection of cancer cells; route of bacterial delivery being intravenous, subcutaneous and oral; with outcomes ranging from tumor growth reduction, metastasis reduction, prolonged survival of mice and even being synergistically with cancer compromising the health of the animal. Efficacy of bacterial strains have been evaluated in preclinical and clinical trials, where the recent 2014 Phase 1 Clinical Trial of *S. Typhimurium* χ 4550 expressing IL-2 was orally administered to patients with unresectable hepatic metastases from a solid tumor [117]. Despite these impressive strides towards the use of bacteria as anticancer biotherapeutics, optimal targeting and anticancer effects of bacterial strains are yet to be achieved beyond preclinical studies.

Previously, we established that the anticancer agent VNP20009 is deficient in chemotaxis, due to a SNP in *cheY*, the gene coding for the response regulator in the two component chemotaxis system. Upon replacing the mutated copy of *cheY* with the 14028 parental copy, chemotaxis was restored to almost 70%, determined using traditional capillary assays [107]. Here, we explored several factors to explain the remaining differences in chemotaxis between VNP20009 and the parental strain, including swimming speed, flagellation, attractant sensitivity, and the contribution of *msbB* and *Suwwan* deletion to the remaining defect. The gene *msbB* encodes an enzyme that adds terminal myristyl groups to lipid A [118]. Without the LPS modifying enzyme, strains of *Salmonella* are known to possess growth defects as well as EGTA and galactose-MacConkey media sensitivity [109]. In strain *S. Typhimurium* 14028s, these effects are partially suppressed by the *Suwwan* deletion, a spontaneous recombination event causing the excision of a 108-kilobase region of the genome [119]. We tested the contribution of this region in conjunction with *msbB*, through the construction of 14028 *msbB* *Suwwan*⁻. Its chemotaxis performance on swim plates was only slightly lower (5%) than VNP20009 *cheY*⁺, which also has the genotype *msbB* *Suwwan*⁻ (Figure 3.1). This result allows the conclusion that the major contributors to the chemotaxis phenotype of VNP20009 *cheY*⁺ result from the *msbB* and

Suwwan deletions. This result is contrary to previously reported chemotaxis assays of 14028 *msbB*, where no significant difference was observed between the 14028 *msbB* mutant and 14028 wild type [33]. A possible explanation for our result is that we measured swim ring diameters after 12 hour, whereas in Frahm *et al.* [33], the measured time point was at 4 hour.

Since bacterial metabolism, chemotaxis, and motility are contributing to the swim ring phenotype, we determined the swimming speed of 14028, VNP20009 *cheY*⁺, and VNP20009 *cheY*⁺ *msbB*⁺. While VNP20009 *cheY*⁺ exhibited a 20% reduction in swimming speed compared to 14028, restoration of *msbB* increased swimming speed by 9%, but not to the level of 14028 (Figure 3.2). We therefore conclude that gene restoration increases motility, but this increase might not fully explain the phenomenon we observed on swim plates. We analyzed flagellation and found no difference between flagellar structures of VNP20009 *cheY*⁺ and 14028 (Figure 3.4) and similar levels of flagellin protein expression of 14028, VNP20009 *cheY*⁺, and VNP20009 *cheY*⁺ *msbB*⁺ (Figure 3.5). While flagella shearing was observed for fluorescently labeled VNP20009 *cheY*⁺, possibly due to the several centrifugation and resuspension steps involved in the experimental procedure, culture supernatants of VNP20009 strains had no elevated flagellin levels excluding flagella loss during cell culture growth.

Interestingly, we observed a considerably large subpopulation of non-motile VNP20009 *cheY*⁺ cells when compared to 14028 and the *msbB* restored VNP20009 *cheY*⁺ derivative (Figure 3.3). Restoration of *msbB* in VNP20009 *cheY*⁺ increased the motile cell population by 20%. The consequences of the presence of a non-motile VNP20009 *cheY*⁺ population was most apparent in the microfluidic device experiment. At the optimum concentration gradient, the chemotaxis response to the attractant increased by 47% when only the motile population was accounted for in the CPC calculation (Figure 3.6). It has been described for *Escherichia coli* that an *msbB* (*lpxM*) deletion results in outer membrane stress and σ^E release [120]. In *Salmonella*, σ^E regulates 62 genes, governing roles in pathogenicity, oxidative stress resistance, and stationary-phase survival [121]. It is therefore feasible to conceive that global regulatory

changes are occurring upon restoring *msbB* in VNP20009 *cheY*⁺, which could affect the motility of a population.

Our results revealed that complete restoration of VNP20009 chemotaxis cannot be achieved by replacing mutated genes of *cheY* and *msbB* with their parental copies. However, significant increases in overall performance can be obtained. Although the lipid A modification by MsbB is essential for attenuation of VNP20009, it is not ideal for the downstream application of exploring the role of bacterial chemotaxis in tumor colonization. Research questions on utilizing bacterial chemotaxis for improved tumor targeting might be better suited in strains that have been attenuated by other means, such as auxotrophy or modifications of LPS with a less detrimental effect as described by Frahm *et al.* [33]. However, gene targets for auxotrophy should be chosen carefully. An *S. Typhimurium aroA* deletion strain, which is auxotroph for aromatic amino acids, was reported to exhibit altered flagellar phase variation [122]. It has already been suspected that VNP20009 is over-attenuated due to its lipid A modification, which could prevent a maintained, high cytokine TNF- α release or induction of an inflammatory response. Depletion of TNF- α has been shown to retard tumor blood influx by the vasculature and delay bacterial tumor colonization [123]. Together, these results might explain the Phase 1 Clinical Trial outcome using VNP20009 [123], where significantly elevated TNF- α concentrations were detected in peripheral blood, however high enough levels were not maintained over the course of the study [102].

We discovered VNP20009 *cheY*⁺ to have reduced chemotaxis compared to the parental strain. The reduction is at least in part due to the disruption of *msbB*, the gene providing VNP20009 with an attenuated state. Prior to the present study, MsbB function has not been associated with chemotactic performance. Our objective was to maximize chemotaxis, in hopes of testing VNP20009 *cheY*⁺ for future efficacy as a biotherapeutic. We achieved this goal without manipulating any characteristic features of VNP20009, in particular tumor targeting and its

safety profile. Future studies utilizing VNP20009 *cheY*⁺ will bear in mind potentially unknown phenotypes associated with not only the *msbB* encoded lipid A modification, but other genomic alterations present in the strain, which have given it the reputation as an anticancer therapeutic.

3.6 Acknowledgments

This study was supported by seed funds from the Fralin Life Science Institute at Virginia Tech to Birgit E. Scharf and National Science Foundation CAREER award (CBET-1454226) to Bahareh Behkam. We are grateful to Timofey Arapov for his assistance in fluorescent image acquisition and processing.

Chapter 4. Robust Biomanufacturing of the Nanoscale Bacterial Enabled Autonomous Delivery Systems (NanoBEADS) and Bacterial Chemotaxis Enabled Autonomous Sorting of NanoBEADS⁴

Goal: To optimize the construction of the NanoBEADS with respect to various biomanufacturing parameters and to develop a microfluidic platform to sort NanoBEADS from unattached nanoparticles.

4.1 Introduction

Recent advances in nanotechnology have enabled in the field to propose a new cancer treatment approach using drug-delivery agents for various procedure. Limited transport of the drug-delivery vectors remains unresolved, however. Only a small fraction of the intravenously injected initial dose of a chemotherapeutic drug accumulates in tumors due to low selectivity of drugs [2]. In fact, reported accumulation of chemotherapeutic drugs in tumors is below 5% [124]. Even after the chemotherapeutic drugs reach the tumors sites, elevated interstitial pressure and other factors that impeded passive transport inside tumors [17]. Bacteria-mediated drug delivery systems possess unique characteristics that address many of the shortcomings of conventional drug-delivery approaches including bacterial preferential tumoral colonization and an inherent therapeutic effect on cancer [7], [31]. Nanoparticle-bacteria complexes (i.e. NanoBEADS) are an optimum such approach, as they will enable a more effective multimodal drug delivery approach by combining strengths of particle and bacteria-based drug delivery systems. NanoBEADS (Nanoscale Bacteria Enabled Autonomous Drug Delivery

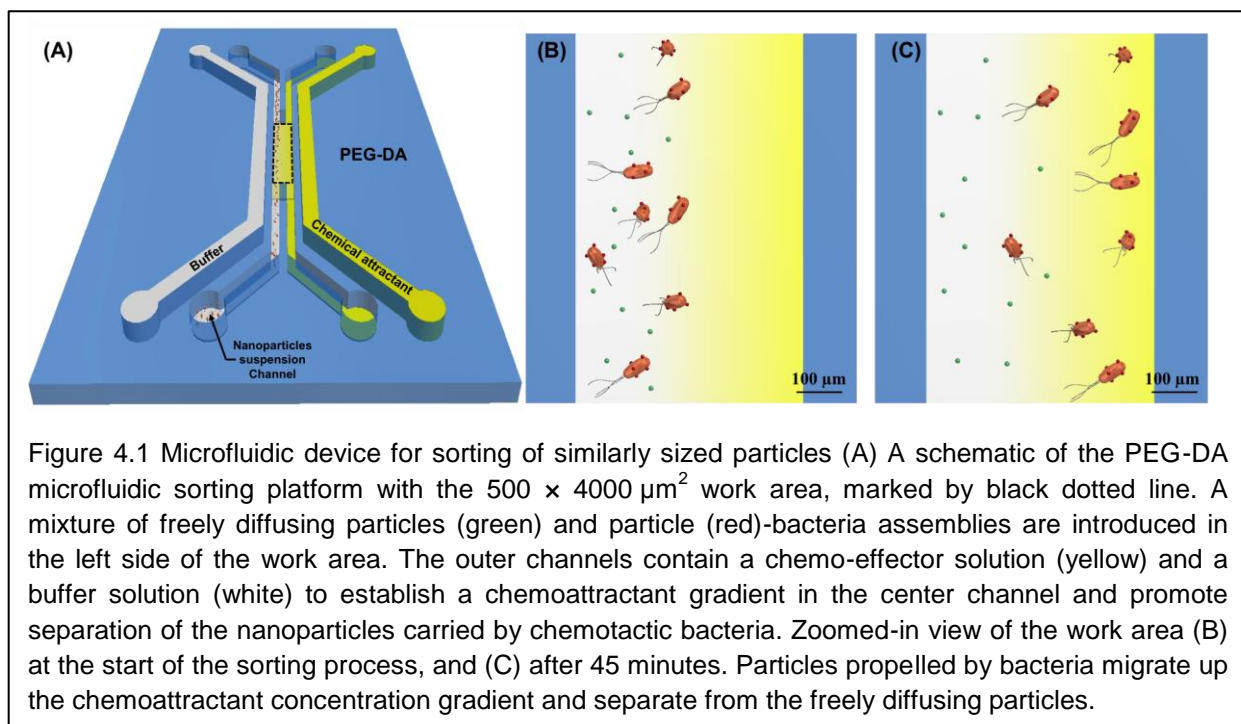
⁴ The part describing the sorting of nanoparticles of comparable sizes within a microfluidic platform was published in Lab on Chip [59]. SeungBeum Suh and Mahama A. Traore contributed equally to this work and the corresponding author was Bahareh Behkam.

Systems) is the drug delivery system platform coupled between *Salmonella* Typhimurium VNP20009 and biodegradable copolymer, poly(lactic-co-glycolic acid) nanoparticles. The biomanufacturing procedure of NanoBEADS was optimized, defined here as maximizing the nanoparticle load of each bacterium, by systematically exploring the effects of experimental parameters including the ratio of the particles to the bacteria, the zeta potential of streptavidin coated nanoparticles, and the antibody concentration and coating time.

Biomanufacturing the NanoBEADS with the optimized experimental parameters shows consistent and robust outcomes of fraction of bacteria conjugated with particles and the number of attached particles. A major drawback in the biomanufacturing of NanoBEADS using a large ratio of number of nanoparticles compared to the number of bacteria (i.e. 100 to 1) is that unattached nanoparticles are inadvertently present in the final suspension, which makes it difficult to estimate the actual dosage of drug delivered. To overcome this issue, we propose the exploitation of bacterial chemotaxis to sort the NanoBEADS from the unattached particles as an alternative to traditional centrifugation and affinity-based separation techniques, which are not compatible with “live” NanoBEADS due to the extended processing time and the potential damage to the flagella and negatively impact system efficacy.

Efficient and cost-effective micro/nanoparticle sorting and separation is fundamentally important in biological and chemical analyses such as cell separation, pathogen filtration, and drug screening [125], [126]. At the micro/nanoscale, sorting is achieved through a variety of passive and active techniques or a combination of both [126]. Active techniques are based on external recognition of particle properties (e.g. electrical charge) and subsequent force application (e.g. electrostatic force) to collect the particle into the desired location [127]. Examples include fluidic, optical, dielectrophoretic, and magnetic separation. Passive methods are based on one or more particle properties (e.g. size and

density) that result different behaviour of particles when placed in the sorting platform and are exploited for separation in absence of any active recognition step [127]. Examples include particle filtering and centrifugation. As such, the separation efficiency of active sorting techniques is usually higher than that of passive techniques. However, active sorting generally demands more complex set-ups operated by skilled user. On the other hand, conventional passive sorting methods are often inertia-based [128]–[130] which leads to limitations for sorting particles of comparable sizes and density, as well as unintended aggregation and compromise of the stability of nanoparticle suspension. Recent progress in multiplex microfluidics have enabled miniaturization and increased parallelism of micro/nano-particle manipulation and sorting. Active and passive micro-sorting devices based on several techniques including dielectrophoresis, [131] acoustophoresis, [132] hydrophoresis, [133] hydrodynamic flow control, [134] electrokinetic flow, [134] and optical force switching [135] have been developed. However, sorting particles of similar sizes and densities remains a challenge. Therefore,



there is substantial need for new, simple and cost-effective methodologies to be developed in order to sort particles of similar bulk physical properties (size, density, rigidity, etc.) at high efficiency.

Over the past decade, whole-cell actuators have been implemented in microscale-engineered systems for applications such as load transport and mixing [136]–[138]. It has been shown by us and others that flagellated bacteria can be used for controlled actuation, [138]–[141] directed transport, [142], [143] or manipulation and assembly of microscale objects [144]. In this work, to the best of our knowledge for the first time, we present a separation method that exploits chemotaxis (i.e. directed migration in response to a chemo-effector gradient) and selective adhesion in flagellated swimming bacteria for autonomous (passive) sorting of similarly sized nanoparticles of dissimilar surface properties. We have implemented an *Escherichia coli* chemotaxis activated microfluidic particle sorter and evaluated its performance in separating polystyrene particles of comparable sizes in the range of 320-390 nm and 1000-1040 nm. This platform can also be utilized for high throughput, inexpensive, and non-destructive separation of unattached nanoparticles from biomanufactured NanoBEADS.

Our method for sorting is based on selective adhesion of *E. coli* (or any other chemotactic) bacteria to one group of particles only and chemotactic transport of the adhered particles away from the mixture within a static body of fluid (Figure 4.1). The simple hydrogel-based microfluidic sorting platform reported here is fabricated in a one-step direct photopolymerization process, is robust to variation in operational conditions, does not require continuous flow of the immersion media, and obviates the need for additional external equipment (e.g. signal analysers, function generator, etc.). This platform offers substantial flexibility compared with other microfluidic-based techniques such as dielectrophoresis, magnetic sorting and acoustic sorting, wherein the strict requirements for particle properties and forces can add to the complexity of the task. In

contrast with probe-based systems such as atomic force microscope (AFM) or optical tweezers, this platform can easily achieve parallel operation as well as higher throughput autonomous separation and sorting. For isolating NanoBEADS made with non-chemotactic bacteria, we separated unattached nanoparticles from the suspension using a filter centrifugation technique with a selective pore size.

4.2 Materials and methods

a. Bacteria culture

Salmonella Typhimurium VNP20009 YS1646 (ATCC 202165), transformed with a plasmid encoding mRFP1 (BioBrick part BBa_J04450 in the plasmid standard backbone pSB1C3, iGEM foundation, Cambridge, MA), was used for NanoBEADS biomanufacturing. 10 ml of lysogeny broth (LB, 1% w/v of tryptone, 1% w/v of NaCl, and 0.5% w/v of yeast extract, supplemented with 35 µg/ml of chloramphenicol) was inoculated with a single colony and shaken overnight at 37°C and 100 rpm. Fresh cultures were started with 1 % v/v overnight culture in LB media supplemented with 35 µg/ml of chloramphenicol and shaken at 37°C and 100 rpm until the optical density at 600nm (OD₆₀₀) reached 1.0. A 1 ml aliquot of the liquid culture at OD₆₀₀ of 1.0 was then centrifuged at low speed (1,700 × g) for 5 minutes at room temperature and suspended in 1 ml of freshly prepared motility media (6.4 mM K₂HPO₄, 3.5 mM KH₂PO₄, 0.1 mM EDTA, 1 µM L-methionine, 10 mM DL-lactate, 2 mM MgSO₄, 2 mM CaCl₂, pH 7.0) and washed once more in motility media in prior to be used in the biomanufacturing of the NanoBEADS. *E. coli* MG1655m, a derivative of *E. coli* MG1655 from the K-12 family with increased motility was used in the proof of principle sorting experiments [143], [145]. *E. coli* RP437, a chemotaxis model strain from the same family, was used in all chemotaxis assays [146]. To facilitate microscopy imaging, *E. coli* RP437 was transformed with a plasmid encoding GFP (pHC60; Tet^R, constitutive expression of green fluorescent protein) [147] and *E. coli* MG1655m was transformed with a plasmid encoding RFP (p67TD1; Amp^R, expression of red

fluorescent protein in the presence of isopropyl- β -D-thiogalactopyranoside (IPTG)) [148]. *E. coli* RP437 culture from a single colony was incubated overnight in 10 ml of fresh T-broth (10 g/l tryptone, 5 g/l NaCl in deionized (DI) water) supplemented with 10 μ g/ml of tetracycline in a shaking incubator (30°C, 180 rpm). A 100 μ l aliquot of the overnight culture was inoculated in 10 ml of fresh T-broth supplemented with 0.04 g of the chemo-attractant (casamino acids) to promote a pronounced chemotactic response of the bacteria cells in all chemotaxis experiments [149]. A 1 ml aliquot of the liquid culture at OD₆₀₀ of 0.5 was then centrifuged at low speed (1,700 \times g) for 5 minutes at room temperature and suspended in 1 ml of freshly prepared chemotaxis buffer (150 mM NaCl, 2 mM Na₂HPO₄·7H₂O, 1.9 mM KH₂PO₄, 0.1 mM EDTA, 0.01 mM L-methionine, and 10 mM DL-lactate) [149] and was used in all chemotaxis assays. Similar culturing procedure was followed for *E. coli* MG1655m in 10 ml L-broth (10 g/l tryptone, 5 g/l NaCl, and 5 g/l yeast extract in DI water) supplemented with 10 μ g/ml of ampicillin, 0.5 mM of IPTG, and 0.04 g of casamino acids in a shaking incubator (30° C, 150 rpm). A 1 ml aliquot of the liquid culture at OD₆₀₀ of 0.5 was centrifuged at low speed (1,700 \times g) for 5 minutes at room temperature and suspended in 1 ml of freshly prepared motility media (0.01 M potassium phosphate, 0.067 M sodium chloride, 0.1 mM EDTA, 0.01 M glucose, and 0.002% Tween-20) [138] and was used in all sorting experiments.

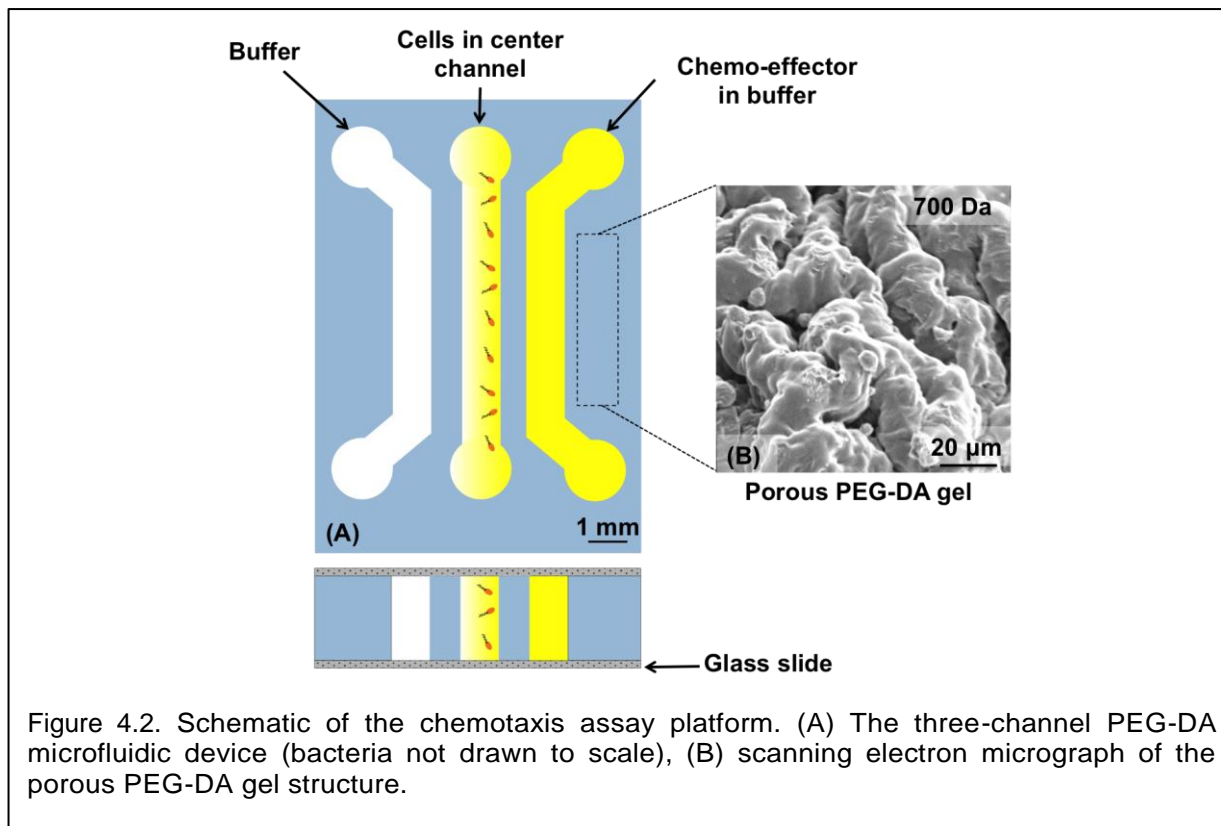
b. NanoBEADS construction

S. Typhimurium VNP20009 bacteria were suspended in 1 ml of motility media to a final concentration of 4.5×10^8 cfu/ml and were incubated with 10 μ g/ml of rabbit polyclonal anti-*S. Typhimurium* antibody conjugated with biotin (Thermo Scientific, Waltham, MA, USA) for 60 minutes at 500 rpm on a vortex mixer. Free antibody was removed by centrifugation at 1,700 \times g for 5 minutes, the bacterial suspension was concentrated (9.0×10^8 cfu/ml) with the total volume of 0.5 ml of motility media. 50 μ l of the bacterial suspension (4.5×10^7 cfu) in the motility

media was used for the conjugation with the nanoparticle per batch. Fabrication of TIPS pentacene-loaded Biodegradable copolymer, poly(lactic-co-glycolic acid), PLGA nanoparticles and surface functionalization by EDC coupling of Streptavidin-Cy3 were described in the supplementary information⁵. Briefly, 175 μ l of that nanoparticle ($\sim 4.5 \times 10^9$ NPs) suspension in PBS was spun down to a pellet using a centrifuge ($16,060 \times g$ for 10 minutes) and was re-suspended in 200 μ l of coupling buffer (Polysciences, Warrington, PA) with the 5 μ g/ml of Streptavidin-Cy3 (Sigma-Aldrich) and 1-ethyl-3-(3-dimethylaminopropyl) carbodiimide (EDAC) in order to coat the nanoparticles with the streptavidin. The carboxylate groups on the surface of the PLGA nanoparticles bind to the amine groups on the streptavidin to form a covalent bond. Once the streptavidin and nanoparticles were incubated for 3 hours to allow for sufficient coupling, the suspension was spun down again to a pellet (same conditions as above) to remove unbound streptavidin. The pellet (containing only streptavidin coupled nanoparticles) are then suspended in motility media (50 μ l per batch) for bacterial conjugation. The NanoBEADS was assembled through streptavidin-biotin binding via mixing the streptavidin-coated PLGA particles and biotinylated antibody coated bacteria. The NanoBEADS suspension was centrifuged through a 0.8 μ m sized centrifugal filter (Sartorius Vivaclear, Elk Grove, IL) at $1,700 \times g$ for 1 minute to selectively remove unattached nanoparticles. The NanoBEADS on the filter membrane was collected by re-suspending in the in specific cell growth media depending on the tumor cell line used for experiments. In order to avoid inadvertent interaction between cancer cells/tumors and unoccupied active binding sites of streptavidin present on the surface of nanoparticles, biotinylated-PEG (MW 5000, Laysan Bio, Arab, AL) at 0.8 μ g/ml was incubated with NanoBEADS in culturing media for 30 minutes.

c. Fabrication of the microfluidic platforms

⁵ PLGA nanoparticles were constructed by doctoral student Ami Jo and Professor Richey Davis, (VT Chemical Engineering)



The microfluidic chemotaxis assay device, shown in Figure 4.2, was used to characterize the chemotaxis behavior of *E. coli* over a wide range of chemical gradients of the chemo-effector casamino acids. This device has been described in a preceding work.[150] Briefly, a solution of polyethylene glycol diacrylate (PEG-DA, MW=700 Da, 10% (v/v) in PBS) hydrogel mixed with 0.5% (w/v) of the photoinitiator Irgacure® 2959 (Sigma-Aldrich, St. Louis, MO) was poured within a polydimethylsiloxane (PDMS) enclosure. A three-channel pattern was transferred into the hydrogel via UV photopolymerization (365 nm, 18W/cm², Omnicure S1000, Vanier, Quebec) for 15 seconds. A PDMS layer and two Plexiglas support layers were placed on top of the hydrogel device layer and one Plexiglas support layer was placed underneath the bottom glass slide. The top and bottom Plexiglas layers were clamped together to provide sufficient pressure to seal the device. Controllable, quasi-steady, and linear chemical concentration gradients were established by continuously flowing the buffer and the chemo-effector solution in the

outer channels at a flow rate of 5 $\mu\text{l}/\text{min}$ (PHD Ultra syringe pump, Harvard apparatus, Holliston, MA). The quasi-steady linear gradient was established in the center channel after 75 minutes as the chemo-effector diffused through the hydrogel wall into the buffer filled center channel.

Similar to the chemotaxis assay device, the sorting platform is comprised of a chemoattractant channel, a center channel (includes the sorting work area), and a buffer channel, as shown in Figure 4.1. The device layer is made of the same PEG-DA gel (MW = 700 Da). The inlet ports of the center channel in the sorting platform are designed such that the nanoparticles suspension, containing similarly sized particles, can be introduced in only one side of the work area. The chemo-attractant channel is filled with the chemo-effector casamino acid at a concentration of 0.004 g/ml to establish the optimum chemotactic response-inducing gradient. A 500 μl aliquot of the mixture of the particle-bacteria assemblies and unattached freely diffusing particles was infused through the left side of the center channel while motility buffer solution was simultaneously infused through right side of the central channel at the same flow rate. The two parallel stream introduction ensures that the nanoparticle mixture remains on the left side of the central channel before the bacteria carrying nanoparticles start migrating away (towards the chemo-attractant source) via chemotaxis

d. Selective bacteria adhesion to nanoparticles

This sorting technique exploits surface property differences between two groups of similarly sized nanoparticles to selectively attach bacteria to one group of particles. Specific attachment facilitated by biotin-streptavidin bond and non-specific attachment facilitated by electrostatic interactions were explored. For the specific adhesion experiments, a mixture of streptavidin coated 390 nm polystyrene particles (Bangs Laboratories, Fishers, IN) and 320 nm polystyrene particles (Bangs Laboratories, Fishers, IN) was prepared in advance to bacterial assembly. Briefly, *E. coli* MG1655m bacteria

were washed twice in motility media and incubated with 10 µg/ml biotin-conjugated goat polyclonal anti-Lipid A LPS antibody (Thermo Scientific, Waltham, MA) to enable attachment of 390 nm streptavidin coated nanoparticles on bacterial cell membrane.[151] The suspension was gyrated on a vortex shaker for one hour at 600 rpm to facilitate antibody attachment to the bacterial cell. The bacterial suspension was centrifuged at low speed ($1,700 \times g$) for 5 minutes at room temperature to remove the unbound antibody from the solution and was then suspended in 50 µl of motility buffer. The 320 nm and 390 nm particle mixture suspension was agitated with biotinylated antibody-coated bacteria at a 100:1 nanoparticle mixture to bacteria ratio for 30 minutes. Using the streptavidin-biotin complex, one of the strongest non-covalent bonds found in nature, the bacteria-390 nm particle assemblies were formed and the 320 nm particles remained unattached (Figures 4.6 (C) and 4.6 (D)). A similar procedure was followed to prepare a mixture of streptavidin coated 1040 nm polystyrene particles (Bangs Laboratories, Fishers, IN) and 1000 nm polystyrene particles (Thermo Scientific, Waltham, MA). The microparticle mixture was agitated with biotinylated antibody-coated bacteria at 2.5:1 bacteria to microparticle mixture ratio for 30 minutes. The bacteria-1040 nm particle assemblies were formed and the 1000 nm particles remained unattached (ESI† Figure 4.S1 (A)).

For non-specific adhesion experiments, a mixture of positively charged 1000 nm polystyrene particles (Polysciences, Warrington, PA) and 1000 nm neutrally charged polystyrene particles (Thermo Scientific, Waltham, MA) was first prepared. *E. coli* MG1655m bacteria were washed twice in motility media and agitated with particle suspension at 2.5:1 bacteria to particle mixture ratio for 30 minutes. The electrostatic interactions between the positively charged particles and negatively charged bacteria facilitated their assembly and the neutrally charged particles remained unattached (ESI† Figure 4.S1 (B)).

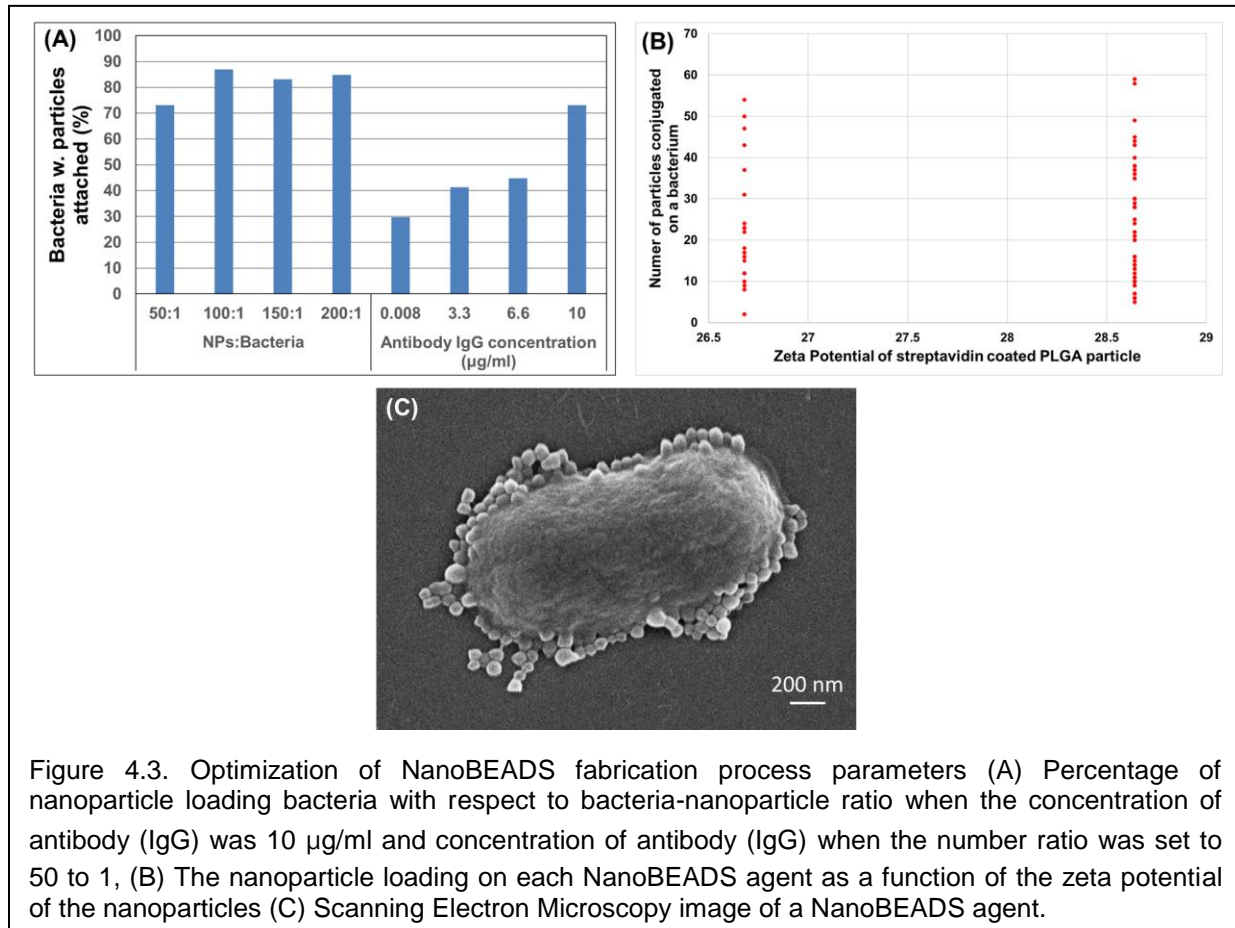


Figure 4.3. Optimization of NanoBEADS fabrication process parameters (A) Percentage of nanoparticle loading bacteria with respect to bacteria-nanoparticle ratio when the concentration of antibody (IgG) was 10 µg/ml and concentration of antibody (IgG) when the number ratio was set to 50 to 1, (B) The nanoparticle loading on each NanoBEADS agent as a function of the zeta potential of the nanoparticles (C) Scanning Electron Microscopy image of a NanoBEADS agent.

e. Imaging and data analysis

Spatiotemporal distribution of bacteria, nanoparticles, and bacteria-nanoparticle assemblies within the work area of both microfluidic devices was captured using a Zeiss AxioObserver Z1 inverted microscope equipped with an AxioCam MRm camera and a 10× objective. The recorded images were converted to binary images using Zen software (Zeiss Microscopy, Oberkochen, Germany). The binary images were then imported in ImageJ (NIH, Bethesda, MD) to obtain the spatiotemporal distribution information across the center channel. The chemotactic behaviour of the bacteria and bacteria-nanoparticle assemblies was quantified using the population-scale metrics of chemotaxis partition coefficient (CPC) and chemotaxis migration coefficient (CMC), which respectively represent the direction and strength of chemotaxis response[60]. The coefficients are defined by

$$CPC = \frac{N_r - N_l}{N_r + N_l} \quad (4.1)$$

$$CMC = \frac{\sum [N(x) \cdot (x)]}{[\sum N(x)] \cdot \left(\frac{w}{2}\right)} \quad (4.2)$$

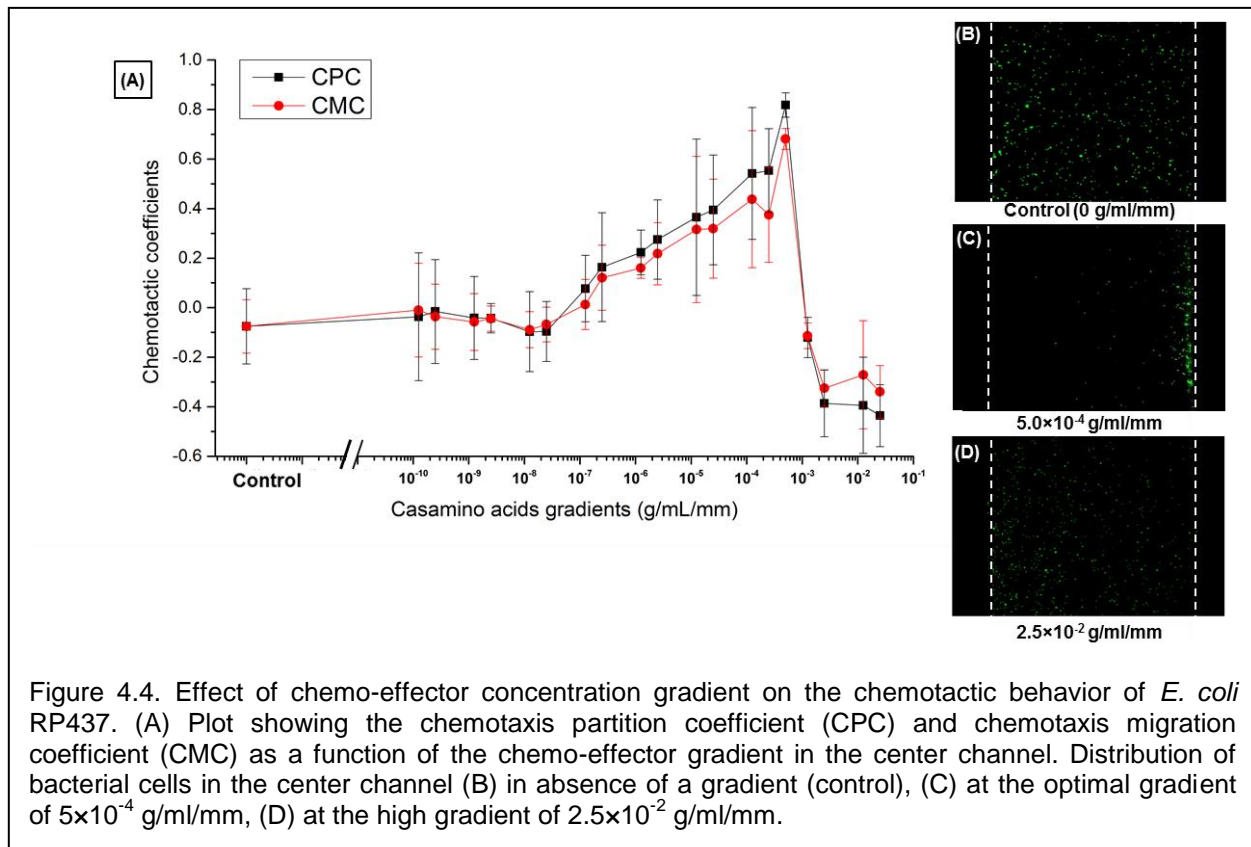
where N_r is the number of objects in the right side of the center channel, N_l is the number of objects in the left side of the center channel, $N(x)$ is the number of objects at a given position from the middle of the center channel ($x = 0$), and w is the width of the channel. Both coefficients range between -1 and 1, with 1 indicating the strongest attraction to a chemo-effector and -1, indicating the strongest repulsion. A coefficient value that is positive indicates that the cells respond positively to the chemo-effector present in the source channel.

4.3 Results and Discussion

a. Quantification of nanoparticle loading in NanoBEADS

The fabrication parameters such as the antibody concentration, particle to bacteria ratio, and filter pore size were investigated and chosen by quantifying the percentage of bacteria possessing attached nanoparticles via scanning electron microscopy images for each case, as shown in Figure 4.3. The parameters that yielded the highest number of attached particles were selected for the optimized NanoBEADS microfabrication procedure: 10 $\mu\text{g/ml}$ IgG antibody concentration, 100 to 1 particle to bacteria ratio, and 0.8 μm sized centrifugal filter for removing unattached nanoparticles. Quantifying the precise particle loading capacity of the NanoBEADS is crucial for estimating the drug delivery dosage because the amount of particles actually delivered within a tumor region determines the overall system efficacy. This was quantified by the analysis of scanning electron microscopy (SEM) images of NanoBEADS agents. To acquire the SEM images, the NanoBEADS was fixed overnight in a 2.5% (v/v) glutaraldehyde solution in PBS (Electron Microscopy Sciences, Hatfield, PA). Several 2 μl droplets of the fixed suspension was then transferred onto a glass slide. The droplets were washed with DI water after 10

minutes of drying to minimize the agglomeration induced by rapid dehydration. The glass slide was sputter coated with gold and imaged using a field emission scanning electron microscope (FESEM, LEO, Zeiss). A representative SEM image showing nanoparticles conjugated to a bacterium is shown in Figure 4.3 (C). In order to accurately quantify the number of particles attached on the bacterium, only particles that were actually contacting the bacterial surface were counted because the nanoparticle aggregation over multiple layers may be an artifact of the dehydration process. A positive correlation between zeta potential measurements of streptavidin coated PLGA particles and the average number of particles attached on a bacterium is shown in Figure 4.3. More positively charged particles indicate that more streptavidin molecules were available on the surface, which yields a higher probability of conjugation to the biotinylated antibody-coated bacteria. Thus, higher numbers of particles are expected to be conjugated. Even though there is variability in the number of particles attached



to a bacterium, the zeta potential measurements throughout the cell studies were consistent at around 30 mV. Thus, the number of particles attached to bacteria can be estimated as 23 ± 16 (n=80).

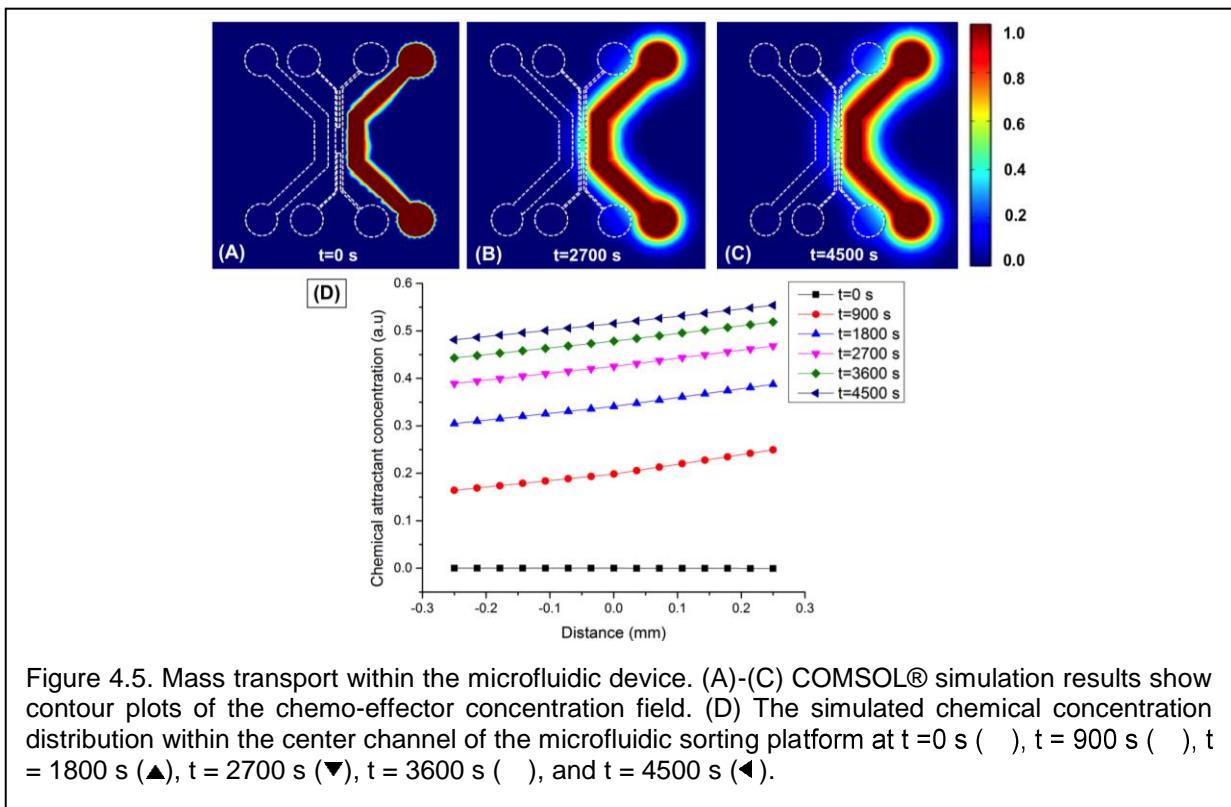
b. Quantification of the bacterial chemotactic response

Various linear concentration gradients, from 1.25×10^{-10} g/ml/mm to 2.5×10^{-2} g/ml/mm of casamino acids, were generated inside the center channel of the microfluidic chemotaxis device to fully characterize *E. coli* chemotaxis response in presence of this chemo-effector and identify the optimal gradient that induces the strongest chemotaxis response. To this end, a solution of casamino acids (of various concentrations) in the right outer channel and a buffer solution in the left outer channel were continuously flowed. Since the three channels were separated by porous PEG-DA hydrogel walls, this resulted in a quasi-steady linear concentration gradient of casamino acids in the center channel. The chemotactic partition coefficient (CPC) and chemotactic migration coefficient (CMC) were computed and plotted as a function of the chemical concentration gradients generated in the center channel (Figure 4.4 (A)). In a control experiment, with chemotaxis buffer continuously flowed in both outer channels, the bacteria distribution did not show any bias over time (shown in Figure 4.4 (B)). The threshold chemical concentration that elicits a chemotactic response was found to be 0.25×10^{-7} - 1.25×10^{-7} g/ml/mm, for which the chemotactic partition coefficient (CPC) value first became positive. The CPC value increased with increase in concentration gradient slope and reached a maximum of 0.82 ± 0.05 , at the chemical concentration gradient of 5.0×10^{-4} g/ml/mm, shown in Figure 4.4 (C). At higher concentration gradients the CPC begins to decrease. The bacteria exhibit a negative response towards the much higher gradient of 2.5×10^{-2} g/ml/mm, shown in Figure 4.4 (D). These results can be explained by the adverse effect of the high absolute chemical concentrations on bacterial motility and chemotaxis that prevents

the cells from performing chemotaxis towards the higher chemical concentration. This phenomenon where bacteria do not move up the gradient in a high chemical concentration environment has been discussed in previous works [152], [153]. Earlier investigations have also shown that bacteria have the ability to sense a chemo-effector as an attractant at low chemical concentrations and as a repellent at higher chemical concentrations [60], [154]. Based on the chemotaxis characterization results, the optimum concentration gradient of 5.0×10^{-4} g/ml/mm was selected for the chemotaxis-enabled sorting of nanoparticles.

c. Sorting of nanoparticles using bacterial chemotaxis

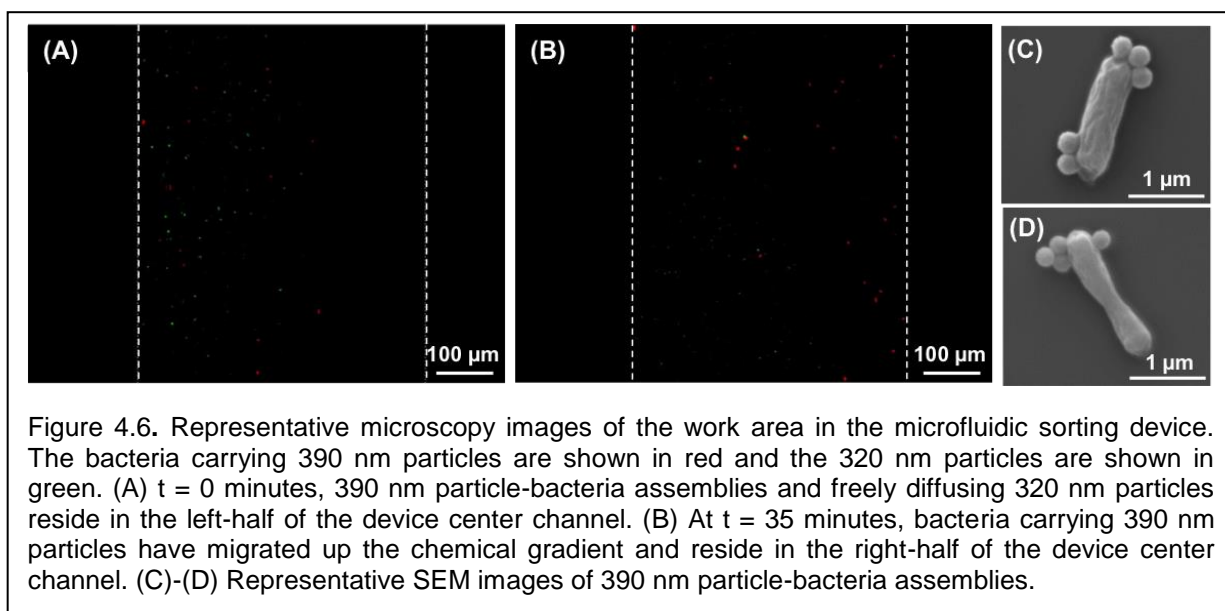
Well-characterized and repeatable performance of the sorting platform requires operation under steady-state conditions. To estimate the amount of time required to achieve a quasi-steady linear gradient across the work area of the sorting platform, a computational model of the chemoattractant casamino acid transport through the device



was carried out using finite element analysis software package COMSOL®. For this model, the diffusion coefficient of casamino acids through the hydrogel was taken to be $D=1.5 \times 10^{-6} \text{ cm}^2/\text{mm}$, as determined in a previous work using a Franz diffusion cell[150]. The diffusion coefficient and flux for transport of casamino acids through PDMS was assumed to be zero given its non-permeable nature to casamino acids. The chemical concentrations in both outer channels were assumed to be constant. As illustrated in Figure 4.5, our results show that the quasi-steady optimal chemical gradient of $5.0 \times 10^{-4} \text{ g/ml/mm}$, can be reached within 75 minutes (4500 s). As shown in Figure 4.6 and Figure 4.S2, this chemical attractant gradient across the work area of the sorting platform will prompt a strong chemotaxis response and chemotactic migration of the bacteria-particle assemblies towards the chemoattractant side of the work area while the freely diffusing particles will remain in close proximity to their initial location within the work area.

The diffusion length of the freely diffusing particles due to Brownian motion can be calculated from $L_d = \sqrt{(4Dt)}$, where $D=k_B T/6\pi\mu R$, k_B is the Boltzmann's Constant, T is the absolute temperature, μ is the dynamic viscosity, and R is the radius of the particle, and t is the time. Within the timeframe of the sorting experiment $t=45 \text{ min}$, the diffusion lengths of the 320 nm and 1000 nm particles are respectively approximated as $L_d = 120.61 \mu\text{m}$ and $L_d = 72.19 \mu\text{m}$, which are much smaller than the displacement of nanoparticles due to bacterial propulsion ($\sim 500 \mu\text{m}$), clearly demonstrating the feasibility of using the differential displacement of the diffusing particles and self-propelled particles for sorting.

The sorting performance was quantified using the CPC metric by measuring the number of particles in each half of the work area every 5 minutes over a total duration of 60 minutes as shown in Figure 4.7. The CPC of 390 nm and 1040 nm streptavidin-coated particle-bacteria assemblies formed via specific adhesion respectively increased from -0.58 ± 0.15 and -0.63 ± 0.01 to steady state values of 0.57 ± 0.10 and 0.62 ± 0.06 which were reached within 45 minutes. The CPC of 320 nm and 1000 nm uncoated freely diffusing particles remained negative and largely unchanged at -0.62 ± 0.06 and -0.66 ± 0.07 . Control experiments in which a chemical attractant gradient is not present showed that bacteria-propelled particles could not be separated from unattached particles (data not shown). The CPC values of 0.57 and 0.62 for the 390 nm and 1040 nm bacteria-propelled particles indicate that about 79% and 81% of these particles have been transported to the right side of the work area, respectively, where the chemical concentration of casamino acids is the highest. On the contrary, around 85% of 320 nm and 1000 nm unattached nanoparticles stayed near their initial location, on the buffer side of the work area. The sorting efficiency was not sensitive to the size of the nanoparticles, for the size range we explored. The CPC of 1000 nm bacteria-propelled



particles assembled via non-specific adhesion increased from -0.75 ± 0.07 to steady state value of 0.49 ± 0.02 , while the CPC of neutrally charged non-motile particles remained negative and largely unchanged at approximately -0.64 ± 0.10 , as shown in Figure 4.7. The small reduction in the sorting efficiency of the non-specific attachment method can be attributed to weaker attachment between bacteria and particles that may result reduced force transmission. The maximum CPC for the bacteria-propelled particles is somewhat smaller than the CPC obtained for free swimming bacteria subjected to the same chemical attractant gradient value (Figure 4.4). This can be attributed to disruption of flagella bundling and bacteria motility in a small fraction of bacteria due to the random nanoparticle attachment.

Upon the completion of sorting, the two parallel streams, each containing one type of the particles from the mixture can be purged into separate collectors on or off the chip. The separated particle-bacteria assemblies can be subjected to change in temperature or pH in order to break the bonds between the bacteria and the nanoparticles [155]–[157]. A density gradient centrifugation step can be implemented to retrieve nanoparticles from the suspension due to the size and density difference between the nanoparticles and the bacteria. The overall sorting yield of up to 80% can be improved through multiplexing and reintroducing unsorted particles propelled by bacteria in a similar sorting platform.

The strength of the sorting method presented here lies in its ability to separate micro/nanoscale objects with similar or even identical sizes and densities as long as their surface properties are different. Effective bacterial chemotaxis-enabled sorting requires careful selection of bacteria such that the surface energy difference between the bacteria and one set of the particles is minimized and selective adhesion is achieved [158]. We have previously demonstrated that the directed transport of 50 nm- 10 μm particles can be achieved through bacterial motility and chemotaxis [142], [143], [151]. Thus, this method will be suitable for sorting particles within the same size range. Furthermore, the current throughput of 2.4×10^5 particles/min can be enhanced by implementing bacteria with higher motility speed, stronger chemo-attractants and work areas with smaller width and larger length (ESI† section S.II). Moreover, different bacterial strains with specific

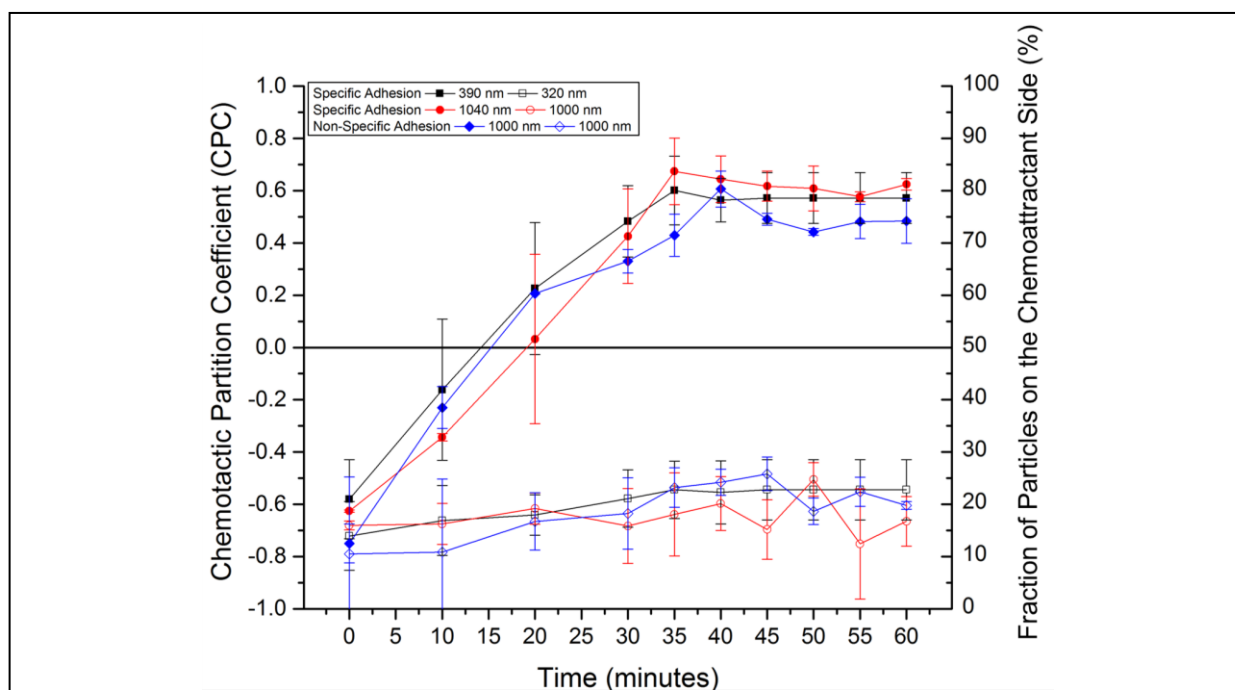


Figure 4.7. Sorting efficiency of the bacteria-enabled microfluidic sorting platform. The chemotactic partition coefficient (CPC) for the 390 nm (solid black rectangle) and 1040 nm (solid red circle) particle-bacteria complexes formed by specific biotin-streptavidin interactions reach steady-state values of 0.57 and 0.63, corresponding to a sorting efficiency of up to 81%. The CPC value for the 1000 nm positively charged particle-bacteria assemblies (solid blue diamond) formed through non-specific electrostatic interactions reaches a steady state value of 0.49, corresponding to a sorting efficiency of 75%. The CPC of the freely diffusing 320 nm (open black rectangle) and 1000 nm (open red circle and open blue circle) particles remain at around -0.7.

affinity to different chemoattractants can be used to sort more than two types of particles in terms of surface chemistries. Also, multiple sources of chemo-attractant activated in a pre-designed time controlled manner can be used to establish a spatiotemporal varying chemical gradient and achieve multi-dimensional particle manipulation. A limitation of the proposed method is that for the single chemoattractant design shown here, the width of the work area (width of center channel) cannot exceed 1500 μm , due to limited bacterial biased random walk distance (ESI† section S.III). If higher throughput is desired, a parallel array of the microfluidic sorting devices could be implemented.

4.4 Conclusions

In this chapter, we have described the fabrication of NanoBEADS (i.e. engineered bacteria coupled with surface-treated polymer nanoparticles) and characterized their physical properties such as particle loading capacities and zeta potential. For the extended work scope of separating unattached nanoparticles from NanoBEADS that are made with non-chemotactic bacteria with the filter centrifugation, we have introduced a passive sorting method for separating similarly sized nanoparticles by utilizing the motility and chemotaxis of bacteria for NanoBEADS that are made of chemotactic bacteria. This bacteria-enabled sorting method is simple and cost-effective and the sorted particles need not be modified or stained. The required chemoattractant gradient can be established using gravity driven flow, thus eliminating the need for a syringe pump. The predominantly attractive feature of the proposed system revolves around the fact that the biological manipulators and the microfluidic platforms can be generated cost-effectively and swiftly while being highly scalable in nature. This bio-hybrid manipulation platform is fabricated using a simple one-step microfabrication process and it does not require the electrical or magnetic energy sources generally required by active sorting systems. It mainly depends on chemical energy source for actuation and

chemical signalling for steering. Our previous efforts in bacteria-enabled propulsion of micro/nano-particles suggest that the presented method can be applied to sort objects 50 nm-10 μm in size.

The work presented here will serve as a stepping-stone for the development of inexpensive, self-directed, and chemically-based manipulation platforms which in the long run can contribute to reducing the complexity and costs associated with performance of these tasks at reduced length scales. In the future, we seek to engineer bio-hybrid autonomous factories for transport and delivery, sorting, or bottom-up programmed self-assembly of micro/nanoscale objects. Effective development of such assembly and manipulation workspaces could transform current practices and enable high throughput and high precision bottom-up assembly strategies.

4.5 Appendix

A. Selective attachment of bacteria to particles through specific and non-specific interactions

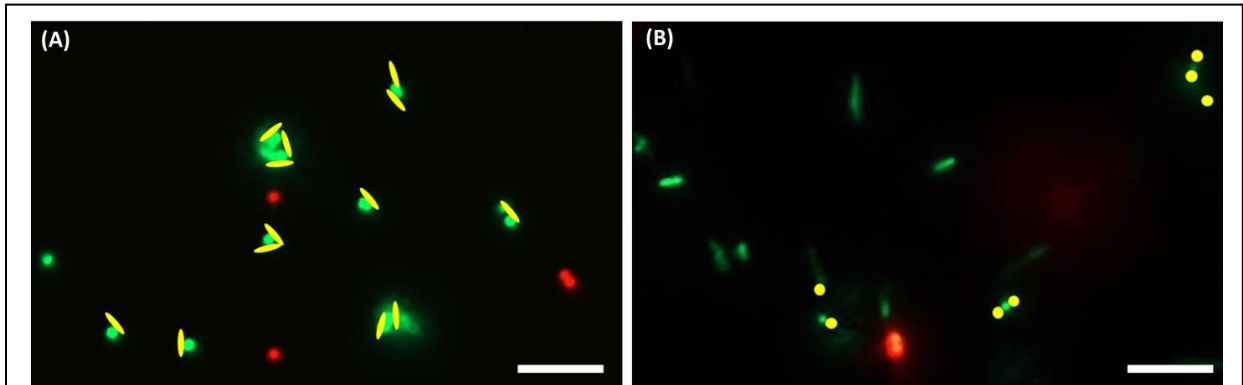


Figure 4.S1. (A) Representative micrograph images of 1040 nm streptavidin-coated particles (green), 1000 nm polystyrene particles (red), and biotinylated antibody coated *E. coli* MG1655m (false coloured in yellow). *E. coli* selectively attached on the surface of the 1040 nm particles via streptavidin-biotin binding. (B) Representative micrograph images of 1000 nm positively charged particles (yellow), 1000 nm neutrally charged polystyrene particles (red), and biotinylated antibody coated *E. coli* MG1655m (green). Negatively charged bacteria selectively attached on positively charged particle via electrostatic interactions, while neutrally charged particles remain unattached. All scale bars are 10 μm .

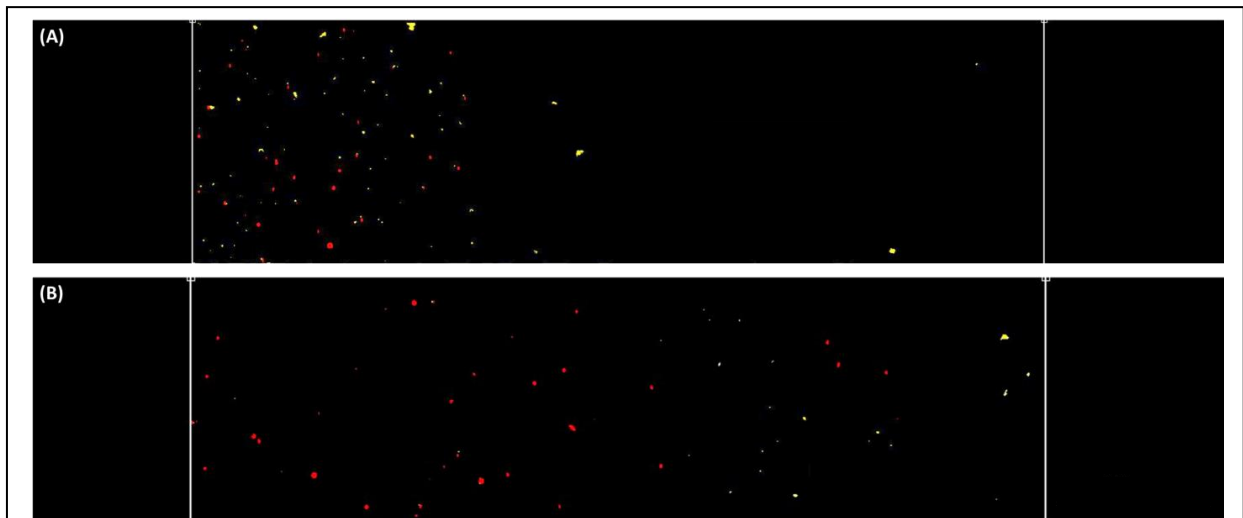


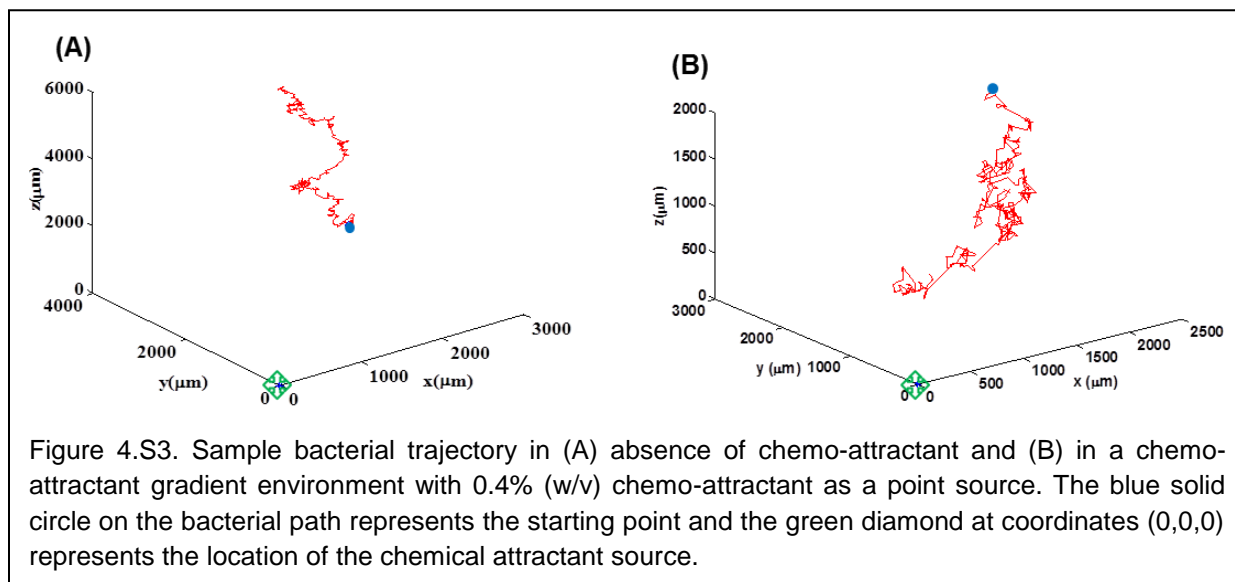
Figure 4.S2 Representative images of the work area in the microfluidic sorting device. (A) At $t = 0$ minutes, the 1000 nm particle-bacteria assemblies (yellow) and the freely diffusing neutrally charged 1000 nm particles (red) reside in the left-half of the device center channel. (B) At $t = 35$ minutes, bacteria carrying 1000 nm particles have migrated up the chemical gradient and reside in the right-half of the device center channel. All scale bars are 100 μm .

B. Design of the microfluidic sorting platform

To determine the maximum possible range of travel of a bacterium, bacterial movement in a 3D milieu both in presence and absence of a chemical attractant source was modelled over time to determine the maximum possible range of travel of the bacterium. The simulations conducted over 45 minutes suggest that a bacterium travels on average 2025 μm with a standard deviation of about 790 μm as depicted in Fig. S3. Through the experimentally validated computational modelling of 3D bacterial random walk in presence of a chemoattractant gradient, the limit of lateral dimension of the microfluidic device is found to be 1500 μm .

The motility of bacteria was modelled using two distinct states of run and tumble. In the run state, the flagellar motors of the bacterium rotate in the counter clockwise direction. This phenomenon induces the conjoining of the flagellar filaments, thus forming a bundle that leads to a propulsion force. The bacterium through this process propels itself forward at a constant speed ($\sim 20 \mu\text{m/s}$). In an isotropic environment, this bacterial run lasts on average for about 0.9 s followed by a tumble. Bacterial tumbling occurs when one or more of the bacterium's flagellar motors rotate in the clockwise direction. This process causes the disruption of the bundle that occurs during runs. During a tumble, under thermal diffusion effects, the bacterium randomly reorients itself before beginning a new run cycle. The duration of a tumble generally lasts for 0.1 s. The occurrence of runs and tumbles of a bacterium is termed bacterial random walk, which is a stochastic motion of bacteria in three dimensions. Random walks can be modelled as a two-state Markov chain with state duration distributions occurring based on an exponential distribution:

$$f(t, \lambda_i) = \lambda_i e^{-\lambda_i t}$$



In the presence of a chemical attractant gradient, the bacterium biases its random walk by extending its run state before tumbling. Through this mechanism, bacteria are able to direct their movement towards chemical attractant source.

C. Throughput of the bacteria chemotaxis-enabled microfluidic sorting platform

For the microfluidic device dimensions the throughput is calculated to be $\sim 3 \times 10^5$ particles/min. The maximum particulate concentration permissible for effective chemotaxis-based sorting was empirically determined to be 1.8×10^{10} /ml. Considering the work area volume ($500 \times 4000 \times 300 \mu\text{m}^3$) and the required sorting time of up to 45 minutes, the throughput was estimated to be:

$$\begin{aligned} \text{Throughput} &= \text{work area volume} \times \text{concentration of processed mixture} \times \text{process time} \\ &= 6.0 \times 10^{-4} \text{ml} \times 1.8 \times 10^{10} \left(\frac{\text{particles}}{\text{ml}} \right) \times \frac{1}{45 \text{ minutes}} = 2.4 \times 10^5 \frac{\text{particles}}{\text{min}} \end{aligned}$$

The throughput of our bacteria chemotaxis-enabled sorting method is within the range of other microfluidic based sorting techniques (10^3 - 10^9 cells/min)[125]. This throughput can further be improved by increasing the length of the work area or by multiplexing.

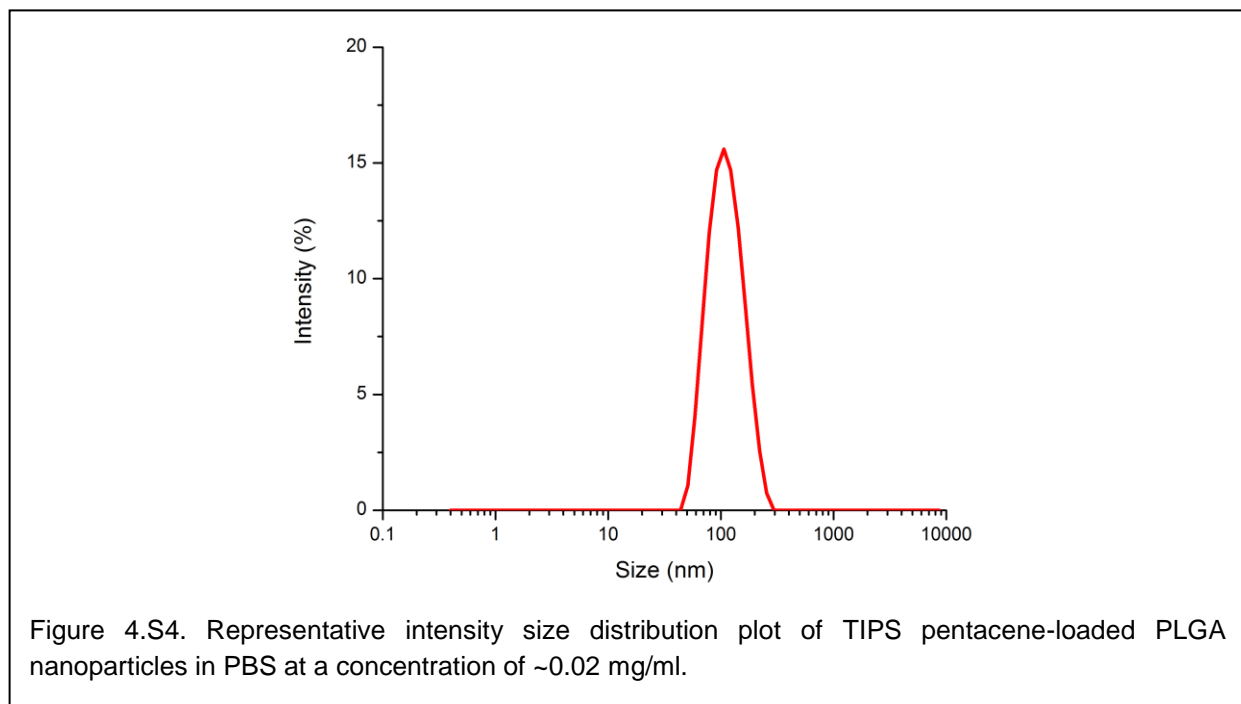
D. Fabrication of TIPS pentacene-loaded PLGA nanoparticle by nanoprecipitation⁶

The method used for nanoprecipitation of PLGA nanoparticles was modified from a method previously described by Niu *et al.* [159]. PLGA was dissolved in Dimethylformamide (DMF) (spectrophotometric grade) at a concentration of 22.22 mg/ml and left to sit, without any agitation, for 30 minutes to wet the polymer and partly dissolve it before being sonicated (Branson 2510 Ultrasonic Cleaner, 100 W output) for an additional 30 minutes. The temperature on the sonicator was set to room temperature although minor heating occurred during use, the temperature was typically below 30°C. During this time, the Pluronic F127 was dissolved in DI water at a concentration of 5 mg/ml by sonicating for 30 minutes first before being magnetically stirred at 600 rpm for an additional 30 minutes to reduce the bubbles that formed on the surface. TIPS pentacene was dissolved in tetrahydrofuran (THF) (anhydrous >99.9%) at a concentration of 3.05 mg/ml, by slight shaking by hand. The PLGA in DMF was then combined with the TIPS pentacene in THF at a volume ratio of 9:1 DMF:THF. This mixture had a PLGA concentration of 20 mg/ml and a 1.5 wt% TIPS pentacene targeted loading. To form the particles, 1 ml of an organic solution containing PLGA and TIPS pentacene was loaded in a 5 ml glass syringe. Using a syringe pump (New Era Pump Systems, Farmingdale, NY), the PLGA solution was added drop-wise (30 ml/hr) to the aqueous solution Pluronic® F-127 while magnetically stirred at 600 rpm. The combined solution was left stirring for 5 hours covered from exposure to light before being centrifuged at 4°C and 22,789 × *g* for 30 minutes. The pellet was then re-suspended in 20 ml of PBS by 30 minutes of sonication and then filtered through a 0.45 μm nitrocellulose membrane and stored in solution at room temperature and used within 4 days and will be referred to hereafter as the reserve suspension.

⁶ The contents in Appendix D, E, and F were provided by collaborator Ami Jo. (VT Chemical Engineering)

E. Nanoparticle functionalization by EDC coupling of Streptavidin-Cy3 onto surface

Streptavidin-Cy3 was bound to the surface of the nanoparticle using the PolyLink Protein Coupling Kit. First, Streptavidin-Cy3 was diluted from the 1 mg/ml stock solution to 100 $\mu\text{g/ml}$ using the coupling buffer in the kit. The 1-Ethyl-3-(3-dimethylaminopropyl) carbodiimide (EDAC) was dissolved separately at 200 mg/ml using the coupling buffer. The EDAC was weighed out per batch of nanoparticles to be prepared and was not stored in solution because EDC has been noted to be very labile in aqueous solutions especially in slightly acidic conditions as is the case for the coupling buffer (pH 5.2). EDC tends to hydrolyze and lose activity when stored in solution [160]. Each batch of nanoparticles ($\sim 4.5 \times 10^9$ nanoparticles) required 4 mg of EDAC powder suspended in 20 μl of coupling buffer. 10 μl of the diluted Streptavidin-Cy3 solution, 20 μl of the EDAC solution and an additional 170 μl of coupling buffer were mixed together to have 200 μl of coupling solution per batch of nanoparticles to be coated ($\sim 4.5 \times 10^9$ nanoparticles). Starting with 175 μl of the nanoparticle suspension in PBS placed into a 1.5 ml centrifuge tube, it was centrifuged down to a pellet at 13,000 RPM ($16,060 \times g$) for 10 minutes using the



Accuspin Microcentrifuge. The supernatant was removed by pipette and 200 μ l of the coupling solution was added. The pellet of nanoparticles was re-suspended by gentle pipetting up and down followed by short vortex mixing. The suspension was then left to incubate for 3 hours on a vortex mixer at 500 rpm. After incubation, the particles were spun down again at 13,000 rpm for 10 minutes and the supernatant again removed by pipette. This time the particles were re-suspended in 100 μ l motility media for invasion assays and NanoBEADS formation; otherwise, the particles were re-suspended in specific cell growth media depending on the tumor cell line and were used for nanoparticle-only control cases.

F. Characterization of the PLGA nanoparticles

Immediately after fabrication and before surface functionalization, the nanoparticles had an intensity average hydrodynamic diameter of \sim 117 nm with a zeta potential of -26 mV as measured by Dynamic Light Scattering (DLS) (Zetasizer NanoZS, Malvern Instruments). The polydispersity index (PDI) was very low, \sim 0.13, suggesting a narrow size distribution as shown

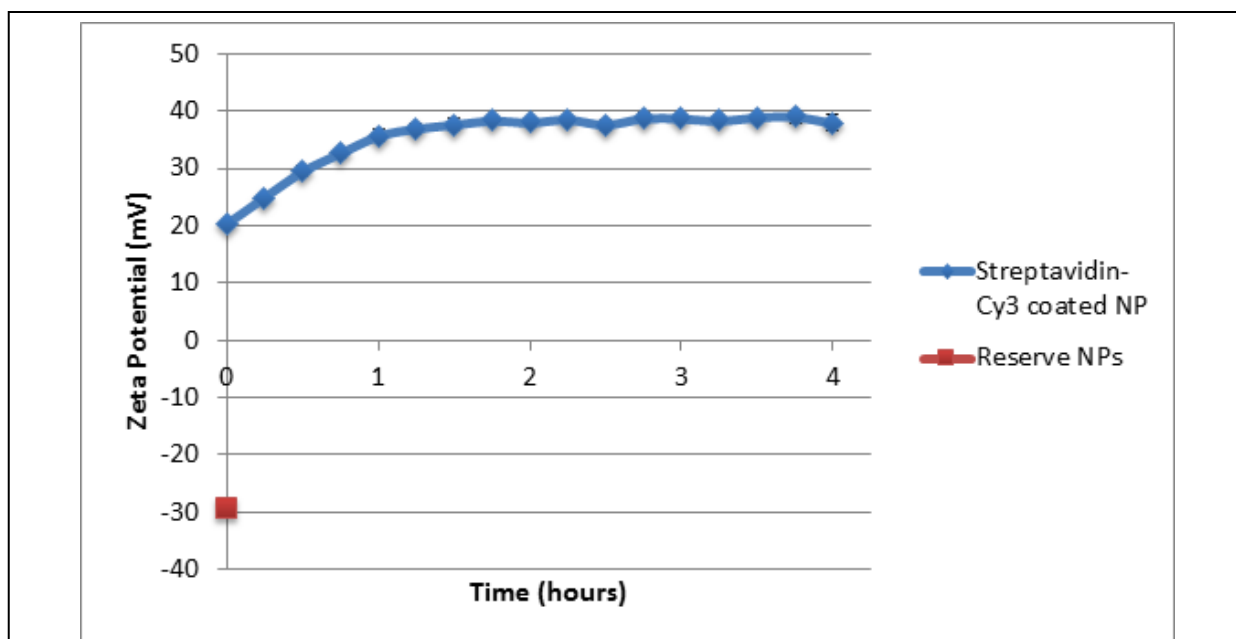


Figure 4.S5. Zeta potential versus time to track streptavidin-coating of nanoparticles for appropriate incubation period in coupling solution

by Figure 4.S4. These initial DLS and zeta potential measurements provided a baseline to compare stability and property changes of the particles throughout the NanoBEADS assembly process. The processing involved taking the nanoparticles in PBS reserve suspension and exchanging them into a coupling buffer containing EDAC (20 mg/ml) and Streptavidin-cy3 (5 μ g/ml) (Figure 4.S5). After incubation, the particles, now with Streptavidin attached, were then suspended in motility media for attachment to the cell surfaces.

Chapter 5. Intratumoral Transport of Nanoscale Bacteria-Enabled Autonomous Drug Delivery Systems (NanoBEADS)

Hypothesis: A bacteria-mediated drug delivery system enhances the transport of cancer chemotherapeutics into the tumor microenvironment comparing to the nanoparticle-mediated chemotherapy

5.1 Introduction

New cancer treatment strategies are presently needed in order to overcome the shortcomings of conventional treatments such as chemotherapy or radiation, both of which have limited efficacy and present significant risks to healthy tissue. Many years of research suggests that two primary factors account for the limitations of drug transport into solid tumor. First, only a small portion of the chemotherapeutic drug is transported to the tumor site through extravasation from blood vessels. In fact, more than 95% of nanoparticle-based chemotherapeutic drugs end up accumulating in organs such as the liver, spleen, and kidneys rather than the tumor for which the treatment is intended [6], [24]. Another major reason for poor drug delivery to tumors stems from the nature of tumor microenvironment [17], [161]. Elevated interstitial fluid pressure due to a dense extracellular matrix, an unusually high fraction of stromal cells, accumulated solid stress, and lack of lymphatic drainage significantly hinders the convective transport of macromolecular chemotherapeutic drugs inside of tumors, precluding deep penetration [21], [162]. Tortuous, elongated blood vessel, and relatively expanded intercapillary spaces in the tumor microenvironment contributes to geometric flow restriction, which further hinders intercapillary transport [5]. Overcoming the aforementioned challenges would significantly improve the efficacy of drug delivery to solid tumors.

Bacteria possess a host of factors that give them unique advantages as drug delivery vectors. Bacteria have long been known to have an inherent therapeutic effect on cancer. William Coley,

an early 20th century surgeon, intentionally infected cancer patients with bacteria after noting positive effects on a sarcoma patient. He later developed a bacteria-derived cancer drug termed “Coley’s toxin,” which showed actual tumor regression in over 47 patients [7], [8]. In addition, Bacillus Calmette-Guerin (BCG) vaccine, which utilizes a variant of *Mycobacterium bovis*, was shown to prevent bladder cancer relapse after surgical removal of the tumor [30].

Bacteria possess a variety of mechanisms through which they are believed to impart anti-tumor effects [34]–[36], [163]–[165]. One of these, particularly in the case of *Salmonella* Typhimurium, is the ability to invade and reside inside eukaryotic cells, which not only allows evasion of the host immune system, but also has negative effects on the infected cell. Although this behavior is normally pathogenic, it may be a distinct advantage in the context of cancer treatment. In *Salmonella*, cell invasion is mediated through a type-III secretion system (T3SS), which takes the form of a needle and syringe-like structure through which a bacterium secretes effector proteins, which help it to gain access to the cell [166], [167]. Additionally, *S. Typhimurium* is a facultative anaerobe and thus may preferentially colonize hypoxic tumor sites because bacteria can consume necrotic cell as the nutrients. *In vivo* animal studies have demonstrated more than 2000-fold higher accumulation of *S. Typhimurium* in tumor sites compared to normal tissue [31], [42], [63].

A genetically modified strain of *S. Typhimurium*, VNP20009, was developed for use as a cancer therapy vector through preferential tumoral colonization [46]. Random mutation of the wild-type strain of *S. Typhimurium* 14028 was carried out by incubating the bacteria with nitrosoguanidine and through UV irradiation at 254 nm [19], [23]. Hyperinvasive mutants were selected based on internalized bacteria within the mammalian cell after *in vitro* invasion assay [46], [168]. In an effort to attenuate the virulence of the bacteria, the *msbB* gene was deleted in order to modify lipid A synthesis, a highly immune-stimulatory component of the lipopolysaccharide (LPS) [42]. Deletion of the *purl* gene resulted in purine auxotrophy, a lack of

the ability to synthesize purines, which also aids in preferential bacterial colonization in tumor sites because tumor necrosis provides the metabolites (purines) exogenously, which are required for growth of the strain [169].

A Phase I clinical trial was carried out using this bacterial strain to study dose-related toxicity, selective replication within tumors, and antitumor effects [9]. The study found that the maximum-tolerated dose was 3×10^8 cfu/m². Colonization within metastatic lesions was detected in three out of 24 patients, but no tumor regression was observed. These results suggest that there is a need for an improved system to achieve more efficacious bacteria-mediated cancer treatment [9], [47].

In this work, we have developed a Nanoscale Bacteria Enabled Autonomous Drug Delivery Systems (NanoBEADS), to address the limiting factors of nanoparticle-only and bacteria-only cancer treatment approaches and enhance both the transport and the efficacy as shown in

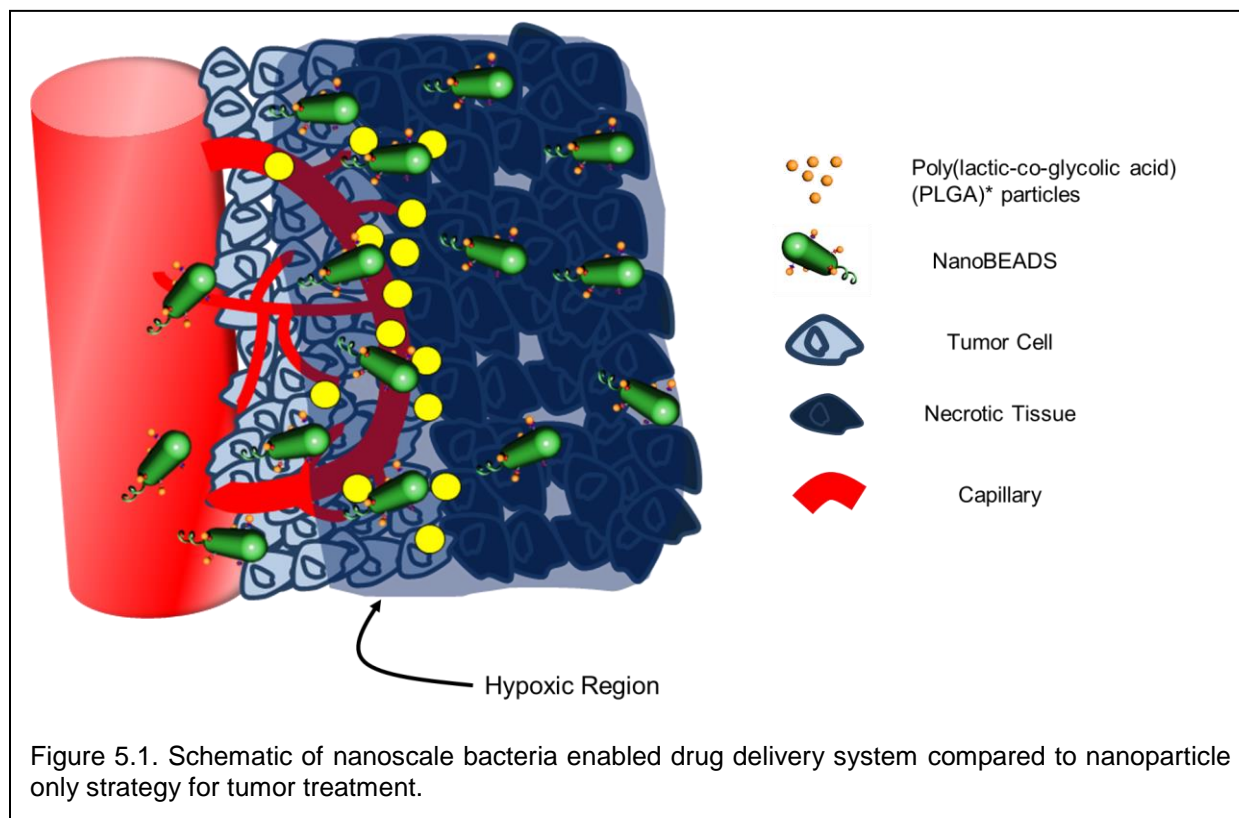


Figure 5.1. Each NanoBEADS agent is comprised of a bacterium conjugated with a number of biodegradable PLGA nanoparticles, as described in Chapter 4. The transport characteristics of the infecting agents, including NanoBEADS, bacteria, and nanoparticles, were investigated. The invasiveness of the infecting agents was quantified using the 2D cell invasion assay, and intratumoral transport efficacy within tumor spheroids was estimated through the intratumoral penetration experiment. Lastly, the dominant intratumoral penetration route was determined by measuring the numbers of intracellular and intercellular infecting agents within the tumor spheroids. The effect of surface property on infecting agents was also tested using PEGylated infecting agents.

5.2 Materials and methods

a. Mammalian cell culture

Three cell lines were used for the experiments; Human colon cancer (HCT-116, ATCC CCL-247), human brain cancer (U87MG, ATCC HTB-14), and murine breast cancer (4T1, ATCC CRL-2539). The culturing medium requirements for all cell lines are shown in Table 5.1. Briefly, cells were seeded in a T-25 flask with the corresponding culturing medium and incubated at 37°C with 5% CO₂. When the confluence of cell culture, estimated by the percentage of cell-covered area, became 80 % or higher, cells were lifted with 1 ml of 0.25% Trypsin-EDTA solution, 1x (ATCC, USA) and the cell density was estimated through the cell counting with a hemocytometer. The required number of the cell was transferred for each experiment as specified below.

b. Tumor spheroid formation

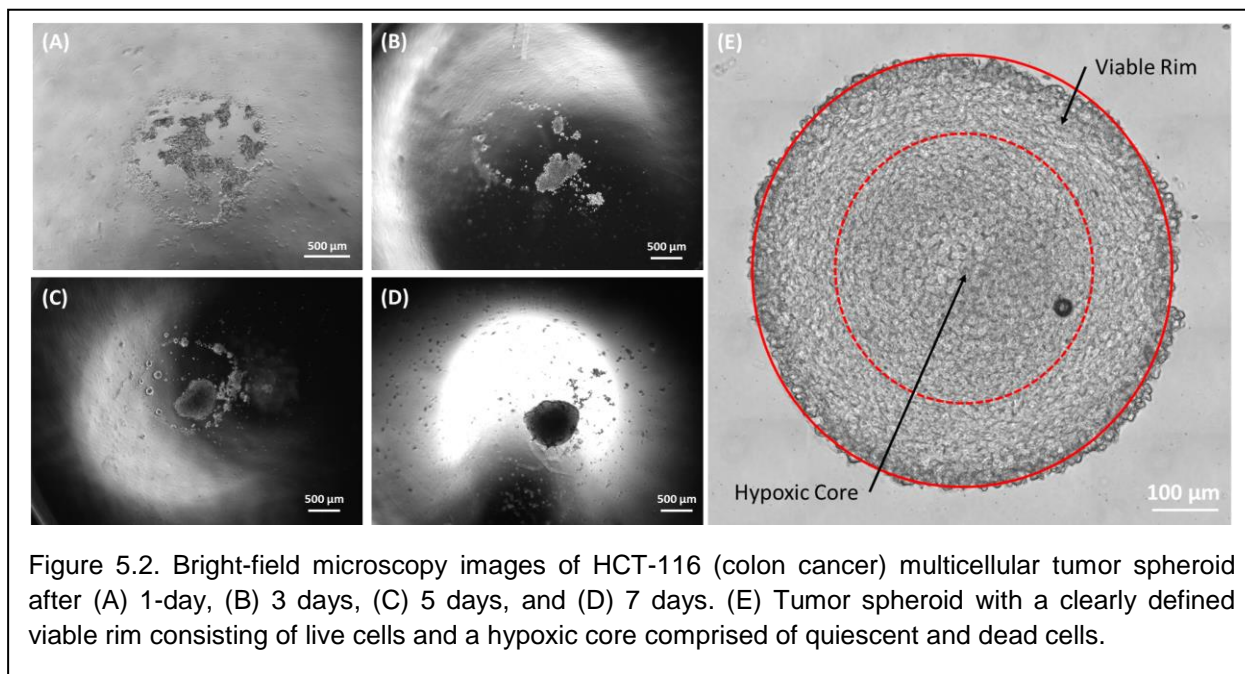
3D multicellular tumor spheroid model was selected as the model for the *in vitro* experiments as it recapitulates essential *in vivo* transport attributes such as highly dense ECM, and structural heterogeneity (proliferative, quiescent, and necrotic region) [170]–[172]. Methods originally developed by [171] and adapted in our lab by former lab member M. Traore [173] were used to form multicellular spheroids. Briefly, 15,000 cells in 200 μ l of culture medium were transferred into ultra-low adhesion round bottom 96 well plates (Corning Inc., Corning, NY, USA). In order to cluster the cells for better tumor spheroid formation, the well plate is centrifuged at 1000 \times g for 10 minutes and incubated at 37°C and 5% CO₂ until tumor spheroids grew to the maximum size, typically around 1 mm in diameter in 5-7 days, depending on the cell doubling time. The progression of the tumor spheroid formation is shown in Figure 5.2. Fresh culturing medium was changed every two days before use.

c. 2D *in vitro* invasion assay of bacteria and NanoBEADS through cancer cells

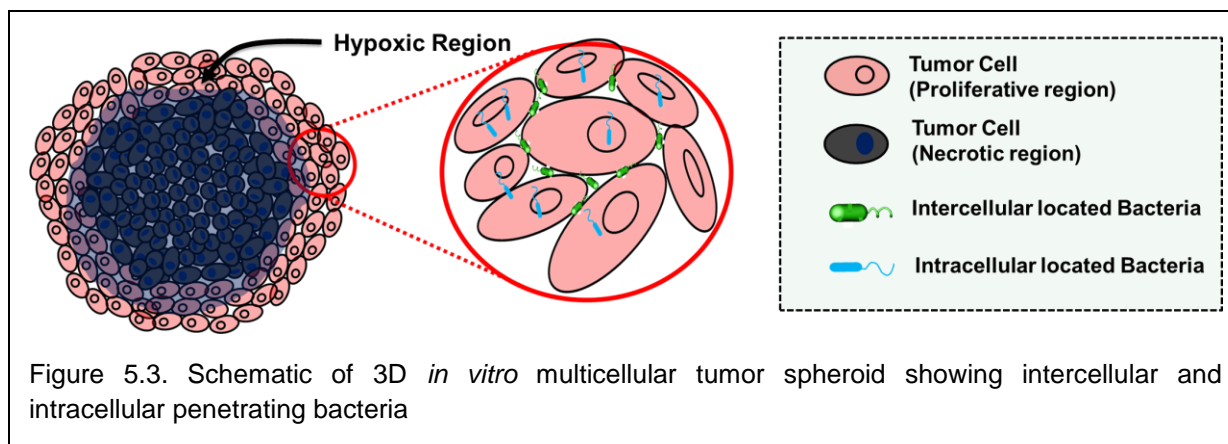
To investigate the invasiveness of the infecting agents into 2D tumor cell, *in vitro* invasion assay was executed. Briefly, 60,000 cells in 1 ml of cell culturing medium were transferred into each well of a tissue culture-treated 12-well plate (Fisher Scientific) and placed at 37°C with 5% CO₂ in a humidified incubator overnight. The infecting agents (bacteria without any treatment, mechanically treated bacteria, PEGylated bacteria, and PEGylated NanoBEADS) were diluted to 3.0 \times 10⁵ cfu/ml in cell culture media, which indicates that the multiplicity of infection (MOI) is

Table 5.1. Complete growth medium for the cancer cell culture

Cell line	ATCC Catalog #	Cell Type	Complete Growth Media	Doubling Time [Hours]
HCT-116	CCL-247	Colon Carcinoma	McCoy's 5a + 10% (v/v) FBS	21
U87MG	HTB-14	Brain Cancer	EMEM + 10% (v/v) FBS	34
4T1	CRL-2539	Breast Cancer	RPMI-1640 + 10% (v/v) FBS	23



set to 5:1. The adherent cancer cells were incubated with the infecting agents for 45 minutes at 37°C with 5% CO₂. Afterwards, the suspension is replaced with fresh cell culture medium with 50 μg/ml of gentamicin sulfate and incubated for 1 hour to kill extracellular bacteria, whereas phagocytosed bacteria were protected by the cell membrane. After a careful wash with Dulbecco's phosphate buffered saline (D-PBS), cells were treated with 0.25% trypsin-EDTA (ATCC, USA) for 10 minutes followed by 1% Triton X-100 (Fisher Scientific, Pittsburgh, PA) for 10 minutes to detach and lyse the cells, respectively. Subsequently, the suspension was sonicated for 30 seconds to break up the clumps of bacteria, and the bacteria suspension was diluted to be plated for colony counting. The experimental parameters such as the MOI, the antibiotic concentration, incubation period, cell-lysing media, volume of the suspension, and sonication were determined through series of assays with various process parameters until consistent plating results were established. As described in Chapter 4, NanoBEADS preparation involves several vortex-mixing steps, which subject the bacteria to mechanical shear. Furthermore, the coating layers on NanoBEADS alter the surface of the bacteria in regions that is not covered by nanoparticles. In order to provide a fair comparison of bacteria only to the



NanoBEADS case, two types of post-treatment were carried out for the bacteria-only case to delineate the effect of surface coating and shear forces due to vortex mixing. To determine the effect of shear forces experienced during NanoBEADS construction, bacteria were exposed to equivalent shear experience during the process of NanoBEADS construction and PEGylation without adding the actual chemical reagents. The surface treatment was comprised of a biotinylated antibody coating at 10 $\mu\text{g/ml}$ for 1 hour, streptavidin-cy3 (Sigma-Aldrich, St. Louis, MO) conjugation at 5 $\mu\text{g/ml}$ for 30 minutes, and biotinylated-polyethylene glycol (PEG) at 0.8 $\mu\text{g/ml}$ for 30 minutes. To determine the effect of shear forces experienced during NanoBEADS construction, bacteria were exposed to equivalent shear experience during the process of NanoBEADS construction and PEGylation without adding the actual chemical reagents.

d. Quantification of bacterial intra/inter-tumoral penetration through *in vitro* tumor spheroids

In order to elucidate the dominant route of tumor penetration, the number of infecting agents translocated intracellularly and intercellularly inside of the tumor spheroids was quantified, as shown in Figure 5.3. Fully-grown tumor spheroids (~1 mm diameter) were infected with 1.8×10^8 cfu of bacteria and equivalent number of NanoBEADS suspended in 100 μl of corresponding cell culturing medium and incubated at 37°C with 5% CO₂ on a vortex mixer set to 500 rpm for 12 hours. Subsequently, the tumors were rinsed with Dulbecco's phosphate buffered saline (D-PBS) at least three times to wash away the bacteria loosely associated on

the periphery of the tumor spheroid. Tumor spheroids were then dissociated within 500 μ l of Accumax (Accutase, San Diego, CA) treatment for 30 minutes. At this point, the cell suspension was divided into halves for quantifying either the total number of bacteria or the number of intracellular bacteria. For intracellular bacteria quantitation, the dissociated cells were incubated with 50 μ g/ml gentamicin sulfate for 1 hour to kill the extracellular bacteria. The suspension was centrifuged at 900 \times g for 2 minutes and the supernatant was discarded. The pellet was suspended in 1% Triton X-100 for 10 minutes to lyse the cell. Final suspension was sonicated for 15 seconds twice and plated on 1.5% LB agar plate. The total number of bacteria was quantified using a similar procedure except the antibiotic treatment. The number of intercellular bacteria was determined by subtracting the number of intracellular bacteria from the total number of bacteria.

e. Intratumoral penetration of particles, bacteria, and NanoBEADS through *in vitro* tumor spheroids

To quantify the intratumoral penetration of each agent, multicellular tumor spheroids were separately infected with bacteria, PLGA nanoparticles⁷, and NanoBEADS. PLGA nanoparticles were made using a nanoprecipitation method and were loaded with the fluorophore, 6,13-Bis(triisopropylsilylethynyl) (TIPS) pentacene, as described in Chapter 4. The estimated hydrodynamic diameter of the particles was 117 nm with the polydispersity index (PDI) of 0.13 and a zeta potential of -26 mV, whereas the zeta potential increased to +39 mV after the surface functionalization with streptavidin. The number of infecting agents was maintained constant for all experiments as 1.8×10^8 cfu for bacteria, 1.8×10^{10} for nanoparticles, and 1.8×10^8 cfu for NanoBEADS suspended in 100 μ l of corresponding cell culturing media. The tumor spheroids with infecting agents were incubated at 37°C with 5% CO₂ on a vortex mixer operated

⁷ PLGA nanoparticles were fabricated by Professor Richey Davis and doctoral student Ami Jo, (VT Chemical Engineering).

at 500 rpm to promote interactions of infecting agents and tumor regardless of motility of the infecting agents. Once the incubation period was completed, the tumors were rinsed with Dulbecco's phosphate buffered saline (D-PBS) three times and prepared for imaging.

f. Histology and image acquisition

The tumor spheroids were fixed in 4 % paraformaldehyde in PBS for 12 hours at 4 °C and gently rinsed with Dulbecco's phosphate buffered saline (D-PBS). The spheroids were transferred into cryomolds filled with a 1:1 (v/v) mixture of OCT compounds and sucrose solution (60% w/v of sucrose in DI water). The tumor spheroids deposited in cryomold was stored at -20 °C for at least 30 minutes before cryosectioning. Using a cryotome, 40 µm thick slices were sectioned and transferred on the poly-L-lysine coated glass slide. 10 µl of DI water was added onto each tumor slices and a coverslip was placed on top. A Zeiss LSM 880 confocal microscope was used for imaging the tissue slices. Series of images along different height within a tumor slice were acquired.

g. Image processing for data analysis

Intratumoral penetration performance was quantified through the image processing algorithm, '3DCONFO', developed in MATLAB (MathWorks, Natick, MA). 3DCONFO automates the detection of infecting agents located in a 3D sample, constructing a 3D map of agent distribution and assessing quantitative performance index such as the penetration and colonization indexes. Detailed descriptions of the 3DCONFO are presented in Chapter 2.

h. Structure Compactness Measurement of Multicellular Tumor Spheroids

One way to quantitatively estimate the tumor compactness is to measure the cell packing density, defined as the area fraction of cell nuclei [61]. To do this, the nuclei were fluorescently stained using NucBlue® Live (2 drops/ml in PBS), which was added onto a slice of a fixed tumor spheroid followed by 30 minutes of incubation at room temperature kept in the dark. The slices of tumor spheroids were then imaged using a Zeiss AxioObserver. Z1 inverted microscope

equipped with an AxioCam MRm camera and a 20× objective through a DAPI filter. The acquired fluorescent image was processed with the '3DCONFO' to quantify the area fraction of cell nuclei.

i. Animal experiment⁸

The institutional IACUC (International Animal Care and Use Committee) approved all experiments and the NIH guide for the Care and Use of Laboratory Animals were strictly observed for all experiments involving animals. Briefly, 8-10 week-old female BALB/c mice were purchased from The Jackson Laboratories and were acclimated in the cages for a week prior to tumor cell injection. Murine breast cancer (4T1) cells were grown in RPMI-1640 supplemented with 10% fetal bovine serum, 100 units/ml penicillin, and 100 µg/ml streptomycin at 37°C with 5% CO₂. A sample containing 1.2×10^6 cells suspended in 100 µl sterile phosphate-buffered saline was subcutaneously injected into the second mammary fat pad of anesthetized mice. Weights and tumor size were documented twice per week, where tumor size was estimated using two perpendicular diameter measurements [174]. The mice were euthanized under the following conditions: 1) weight loss was more than 10% of the initial body weight, 2) the tumor grew larger than 1.4 cm diameter, or 3) clearly clinically moribund.

PEGylated *S. Typhimurium* VNP20009 and PEGylated NanoBEADS were prepared as described in Section 4.2 to a final concentration of 8.0×10^5 CFU/ml in PBS whereas nanoparticles were prepared with a final concentration of 1.8×10^7 nanoparticles/ml in PBS. These concentrations were selected to such that comparable numbers of PLGA nanoparticles are injected in all cases (As described in Section 4.3, it was measured that an average of 23 PLGA particles were attached to a single NanoBEADS). These doses were administered through direct intratumoral (i.t.) injection of 100 µl the infecting agents 19 days after the tumor

⁸ Animal study was done in collaboration with Professor Irving C. Allen and doctoral students, Sheryl Coutermarsh-Ott and Veronica Ringel, (VT Veterinary Medicine)

cell injection. The same amount of PBS was injected for control cases. Mice were euthanized 48 hours post injection.

j. Tissue collection and processing

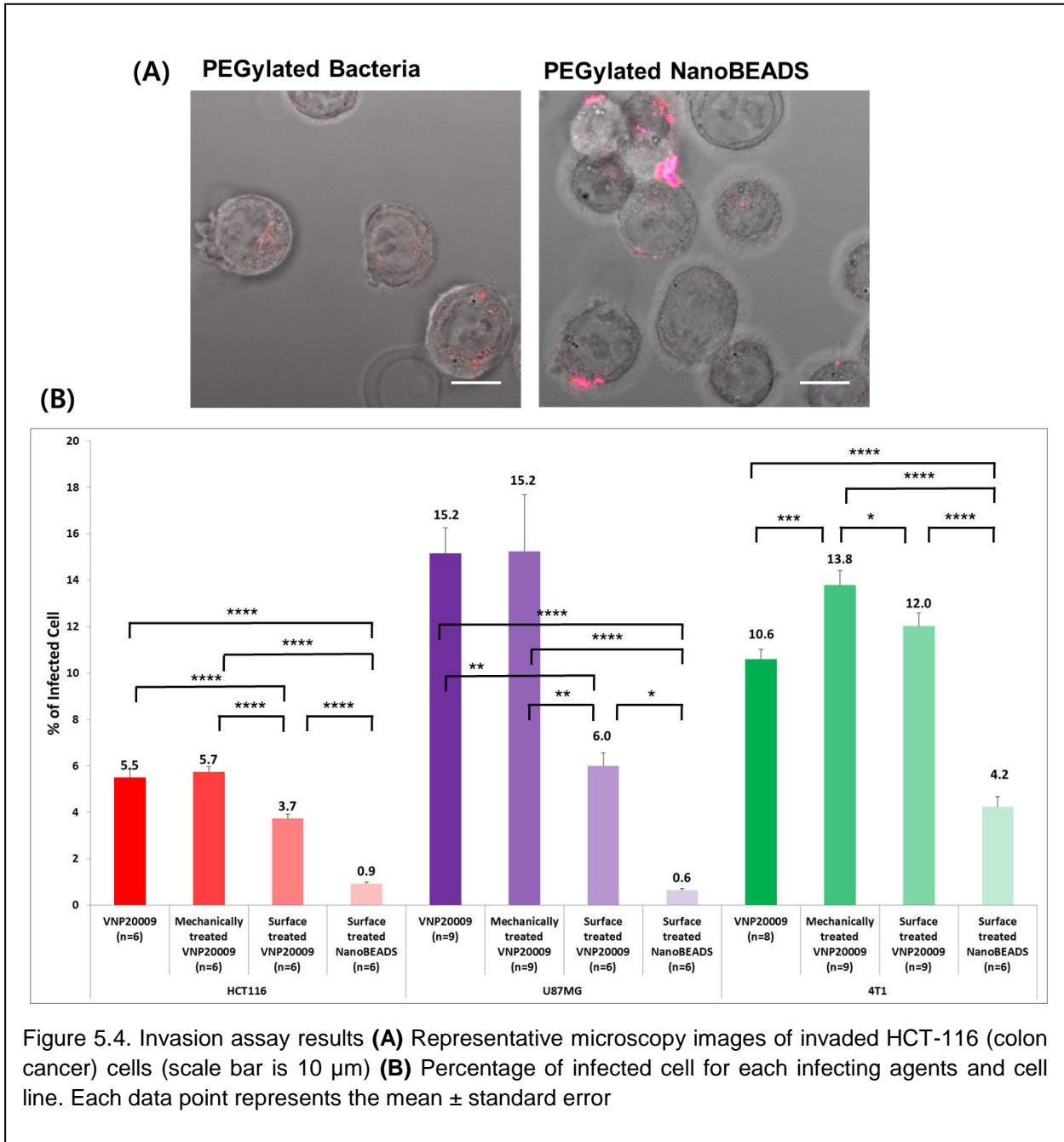
In experiments, harvested tumor, liver, and spleen tissues was split into two equally sized pieces: one piece was fixed in 4% paraformaldehyde prior to cryogenic slicing for confocal microscopy imaging and histopathology. One piece was weighed and homogenized with a disposable pestle system, and diluted in PBS prior to plating on LB agar plates for bacterial colony counting.

5.3 Results and discussions

a. Role of chemical and mechanical treatment and nanoparticle loading on bacteria invasiveness

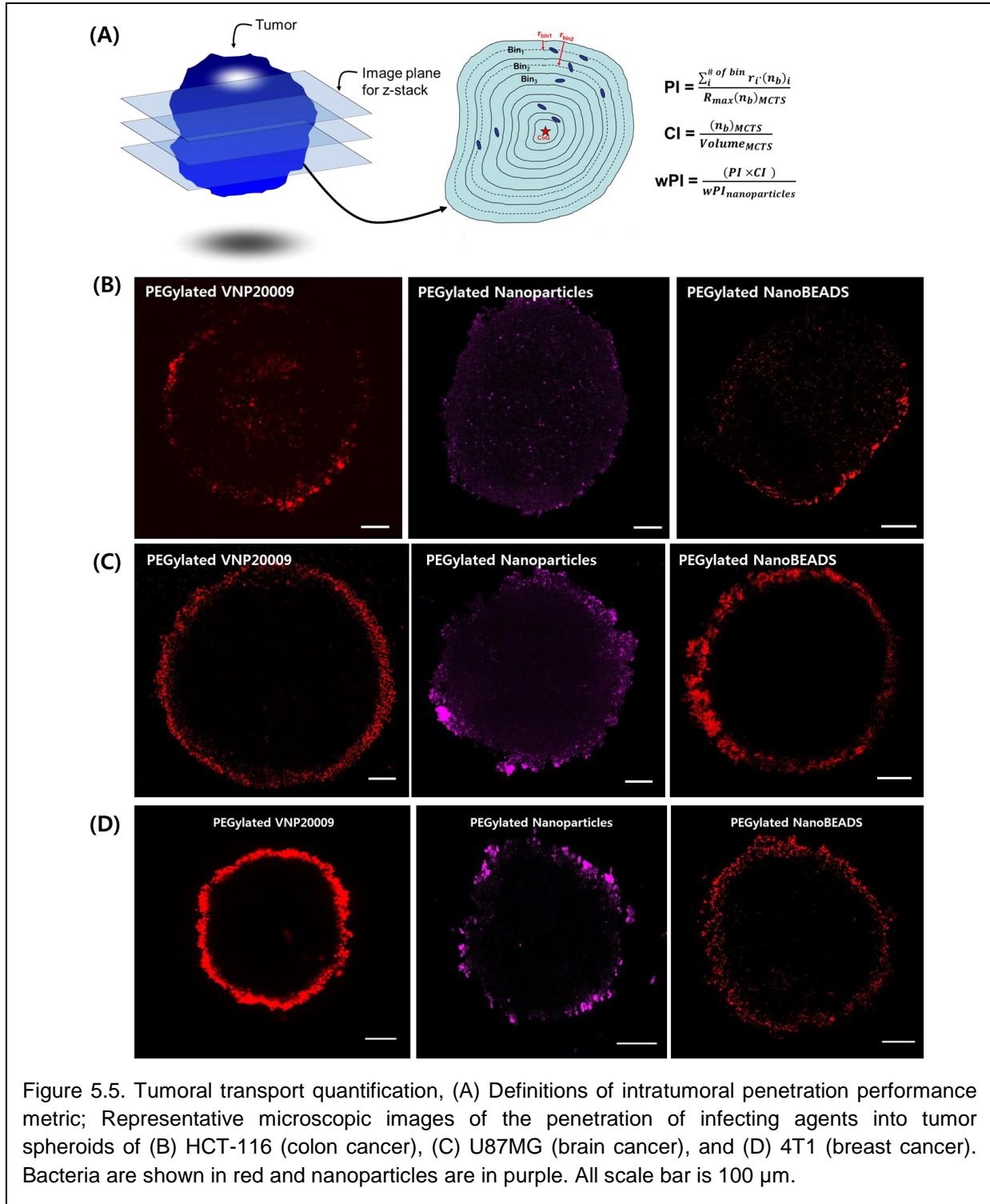
Infecting agents were chosen as *S. Typhimurium* VNP20009, mechanically treated *S. Typhimurium* VNP20009, PEGylated *S. Typhimurium* VNP20009, and PEGylated NanoBEADS. As shown in Figure 5.4, mechanical treatment did not have a statistically significant effect on the fraction of bacteria that resided intracellularly, whereas a smaller number of PEGylated bacteria were internalized. Even a smaller portion of the PEGylated NanoBEADS were internalized. The trend in the percentage of infected cell with respect to the various infecting agents was consistent for different cancer cell lines (HCT-116 colon cancer, U87MG brain cancer, and 4T1 breast cancer).

The mechanical shear that the bacteria experience during centrifugation and vortex mixing steps of NanoBEADS construction may cause the flagella to break [175]. In order to measure any potential change in invasiveness due to these processes, the mechanically-treated bacteria case was studied. It was found that mechanical treatment of the bacteria does not affect the fraction of internalized bacteria, suggesting that the mechanical shear force on the bacteria may



not be a detrimental factor for invasion (Fig. 5.4B). PEG coating is a commonly used surface treatment for reducing non-specific interactions between nanoparticles and tissue by increasing the steric distance, which leads to reduced reticuloendothelial system (RES) uptake and thus prolongs circulation times [176]. More than 35 US FDA-approved nanoscale therapeutics incorporate PEG use in imaging and therapy vector formulations [177]. Likewise, in order to inhibit non-specific interactions with the infecting agents, which are functionalized with positively charged streptavidin molecules, the active binding sites of streptavidin were capped with polyethylene glycol (PEG), referred to as PEGylated infecting agents. Thus, the case of PEGylated infecting agent was included in the invasion study. Although some studies demonstrate that PEGylated macromolecular therapeutics diffuse faster in the tumoral tissue compared to those that are not PEGylated, the PEG actually hinders uptake by the tumor cells; this phenomena has been named the PEG dilemma [178], [179]. The smaller number of internalized bacteria in the case of PEGylated bacteria compared to the mechanically treated bacteria can be attributed to the properties of the PEG coating. Increased hydrodynamic distance or spacing between the bacterial outer membrane and the tumor cell, due to the PEG chain length or particles attached on the bacteria, inhibits direct contact, which may lead to a lack of type III secretion system (T3SS) apparatus engagement, and thus a lower number of infecting agents end up internalized inside of cell [180].

b. Role of chemical and mechanical treatment and nanoparticle loading on intratumoral penetration of infecting agents through *in vitro* tumor spheroids



In vitro tumor spheroids were chosen as the tumor model for the transport efficacy assay as they have been shown to effectively recapitulate many aspects of the tumor microenvironment. Experimental parameters for the intratumoral penetration assay such as the tumor spheroid size,

agitation rate, infecting agent inoculant concentration and volume, and incubation duration were optimized through numerous experiments to identify the optimum parameters for effective demonstration of the penetration characteristics of the infecting agents without disintegrating the tumors by excessive bacterial colonization or shear force.

We developed a number of metrics to quantify various performance attributes of the infecting agents with tumors (Figure 5.5A). The *Penetration Index (PI)* provides a measure of the intratumoral penetration depth of the infecting agents towards the center of the tumor spheroids and is defined as

$$PI = \frac{\sum_{i=1}^N r_i \cdot (n_b)_i}{R_{max} \cdot (n_b)_{MCTS}}, \quad (5.1)$$

where r_i is the penetrating depth of each bin, $(n_b)_i$ is the number of the infecting agents within bin i , R_{max} is the maximum penetration distance (i.e. radius of the tumor spheroid), and $(n_b)_{MCTS}$ is the total number of the infecting agents detected within the entire tumor spheroid. The bin is donut-shaped subsection of the tumor spheroids determined by the equivalent penetrating distance increments. The PI ranges from 0 to 1, wherein a value of 1 indicates that all of the infecting agents travelled to the center of the tumor and 0 indicates that all of the infecting agents remained in the periphery of tumor. The *Colonization Index (CI)* quantifies the number of infecting agents that colonized a given tumor volume in units of number of agents/ μm^3 , as shown below.

$$CI = \frac{(n_b)_{MCTS}}{V_{MCTS}}, \quad (5.2)$$

where V_{MCTS} is the volume of the multicellular tumor spheroid. The weighted penetration index (wPI) represents an integrated index of penetration and colonization and is defined as

$$wPI = \frac{PI \times CI}{(PI \times CI)_b}, \quad (5.3)$$

The wPI provides a measure of general transport efficacy by compounding measurements of both the penetration depth and the colonization density. Confocal images of tumor slices infected with each of the three infecting agents were acquired (Figure 5.5B-D) and analyzed using the indexes described above. As shown in Figure 5.6, the weighted penetration index for NanoBEADS exceeds that of nanoparticles by 4.0-fold, 2.6-fold, and 3.0-fold for HCT-116 (colon cancer), U87MG (brain cancer), and 4T1 (breast cancer) respectively. Considering that 23 or more nanoparticles are being delivered with by each NanoBEADS agent, the transport efficacy

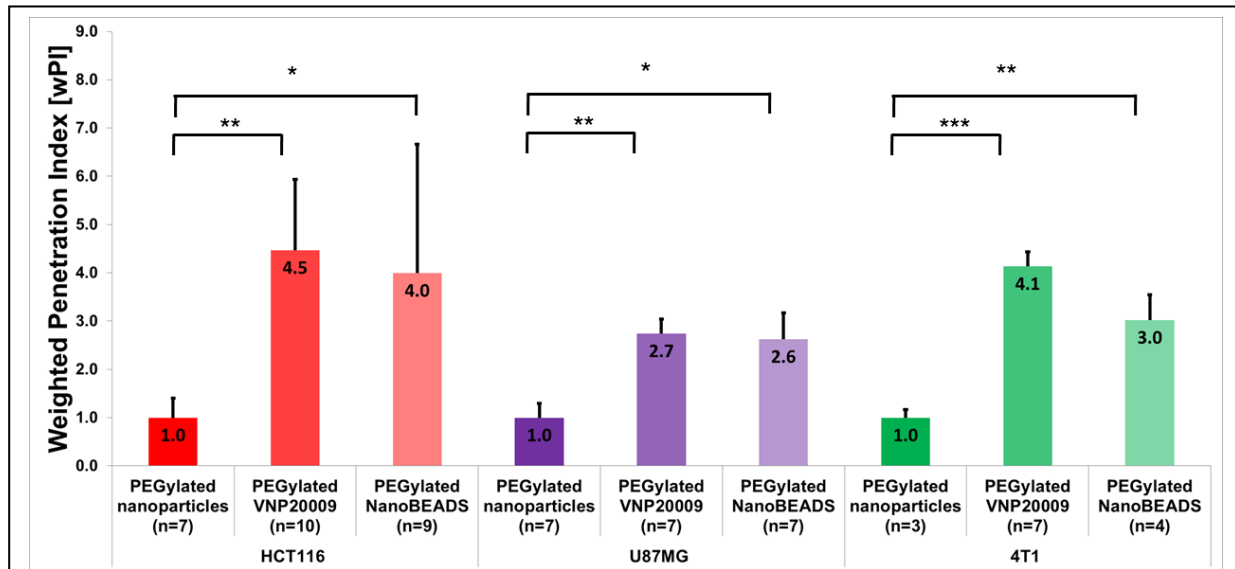


Figure 5.6. Intratumoral penetration results of infecting agents through *in vitro* tumor spheroids as indicated by the weighted penetration index

is enhanced significantly with the bacterial conjugation compared to the passively diffusing nanoparticle strategy. PEGylated bacteria showed the highest wPI for all tumors, whereas the increase in wPI from the nanoparticle case to PEGylated bacteria and PEGylated NanoBEADS within HCT-116 (colon cancer) and 4T1 (breast cancer) tumor spheroids is almost double that of the U87MG (brain cancer) tumor spheroid case. This may be attributed to the significantly denser microenvironment of the U87MG tumors [4], [181], [182]. Glioblastoma (U87MG brain cancer) is known to have a high amount of collagen, which inhibits macromolecular transport

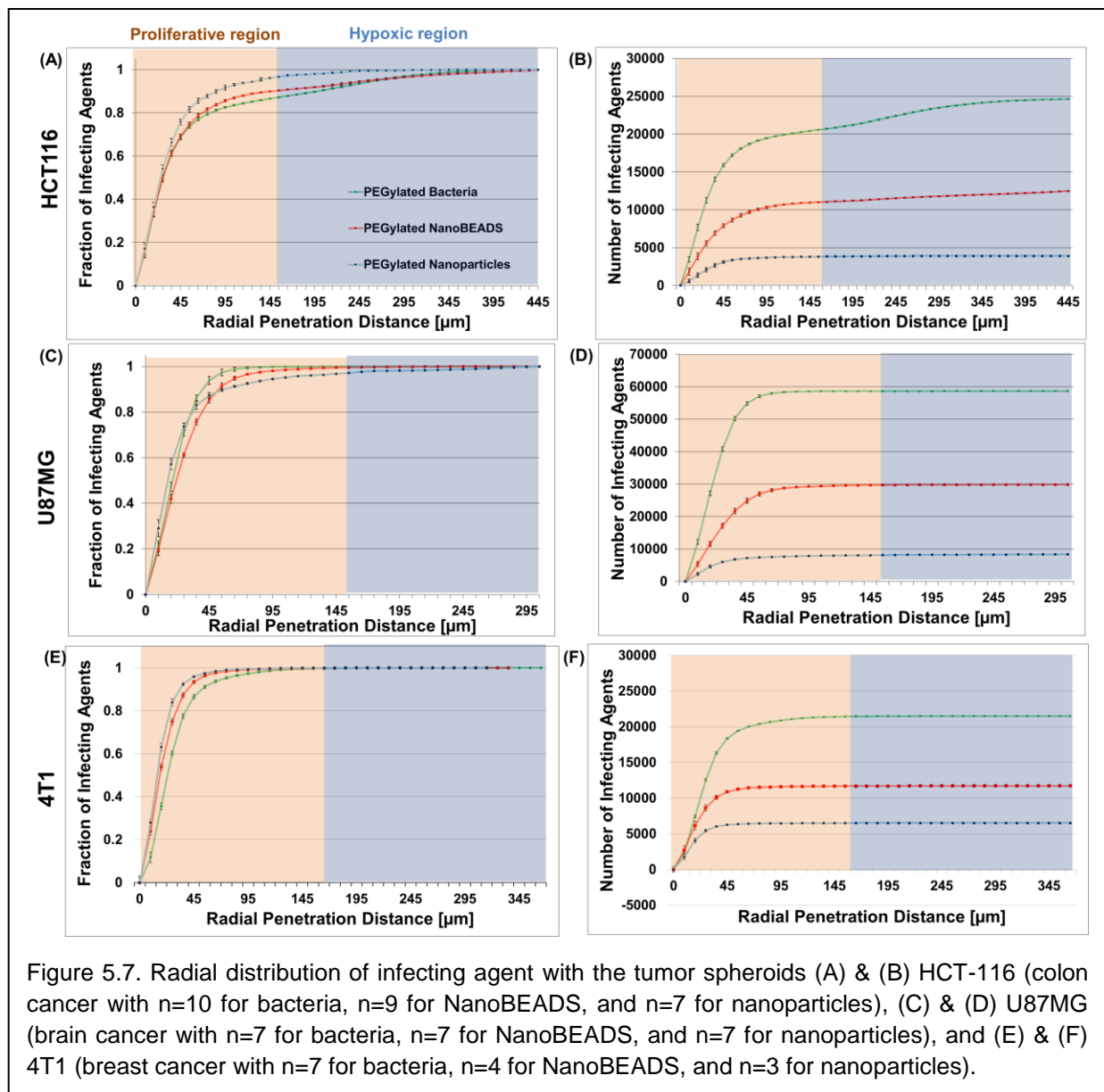


Figure 5.7. Radial distribution of infecting agent with the tumor spheroids (A) & (B) HCT-116 (colon cancer with $n=10$ for bacteria, $n=9$ for NanoBEADS, and $n=7$ for nanoparticles), (C) & (D) U87MG (brain cancer with $n=7$ for bacteria, $n=7$ for NanoBEADS, and $n=7$ for nanoparticles), and (E) & (F) 4T1 (breast cancer with $n=7$ for bacteria, $n=4$ for NanoBEADS, and $n=3$ for nanoparticles).

relative to colon adenocarcinoma (HCT-116) or murine mammary carcinoma (4T1) [4], [183], [184]. The penetration profiles depicted in Figure 5.7 show the radial density distribution of the infecting agents with the tumors. In the NanoBEADS case, compared to nanoparticles, as shown in Figure 5.7 (A), (C), and (E), less than 1% of all of infecting agents colonized the hypoxic region for the U87MG (brain cancer) tumor and 4T1 (breast cancer) tumor whereas larger portions of infecting agents colonized hypoxic regions for the HCT-116 (colon cancer) tumor: 14% for bacteria, 11% for NanoBEADS, and 3% for nanoparticles. The significantly higher number of agents for the bacteria and NanoBEADS case might be due to proliferation within the tumor spheroid during the incubation periods, which is a beneficial attribute for using bacteria as the means of carrying drug-loaded cargo. Binary fission facilitates bacterial intratumoral penetration and accumulative bacterial colonization over time makes tumor disintegrate faster. Even though the majority of agents colonized the proliferative region, there are distinct differences in the fraction of infecting agents colonized between different tumors, which again highlights the need to closely investigate physiological characteristics of different tumors. Tumoral resistance against therapeutic drugs is partially due to microenvironment-mediated resistance which is related to the 3D structure of tumor [41]. Differences in transport efficacy indexes between infecting agents demonstrate that substantial penetration differences might be due to dissimilar microenvironment properties (e.g. cell density, cell-cell junction strength, ECM density) between the tumors [42].

c. Intracellular and intercellular penetration of bacteria

Based on the results shown in the previous section, the bacterial penetration performances were considerably different between different tumors: the wPI of PEGylated bacteria in the denser U87MG (brain cancer) tumor was almost half of the wPI for PEGylated bacterial in HCT-116 (colon cancer) and in 4T1 (breast cancer). We thus hypothesize that the dominant mode of penetration is through intercellular bacterial translocation rather than intracellular bacterial

invasion. In order to test this hypothesis, the number of infecting agents translocating intracellularly and intercellularly in the tumor spheroids was quantified.

As shown in Figure 5.8, approximately 6.8 % and 12.8 % of the untreated bacteria and PEGylated bacteria population for HCT-116 (colon cancer) and 8.2 % and 10.9 % of the untreated bacteria and PEGylated bacteria population for 4T1 (breast cancer), respectively, penetrated into the tumor via intracellular translocation. An even smaller portion of NanoBEADS were determined to move through cells as opposed to around cells (1.4 % and 3.1 % for HCT-116 and 4T1, respectively), which indicates that intratumoral penetration primarily occurs via intercellular translocation. Considering the dominant mechanism of penetration is intercellular translocation, it is probable that the larger size of the NanoBEADS agents compared to the bacteria made it more difficult for the infecting agent to penetrate (Figure 5.6). The larger wPI value for bacterial penetration in HCT-116 (colon cancer) tumors and 4T1 (breast cancer) tumor compared to U87MG (brain cancer) tumors (Figure 5.6) also shows that a tumor with tighter cell junction is much harder for bacteria to penetrate due to the severely limited space between cells

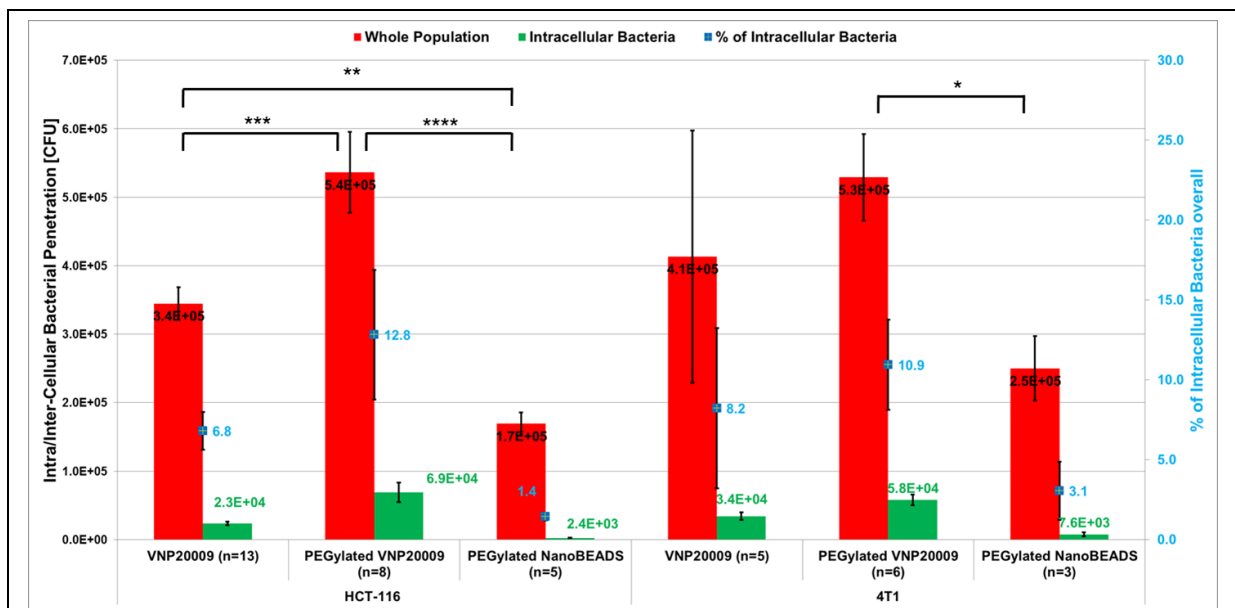
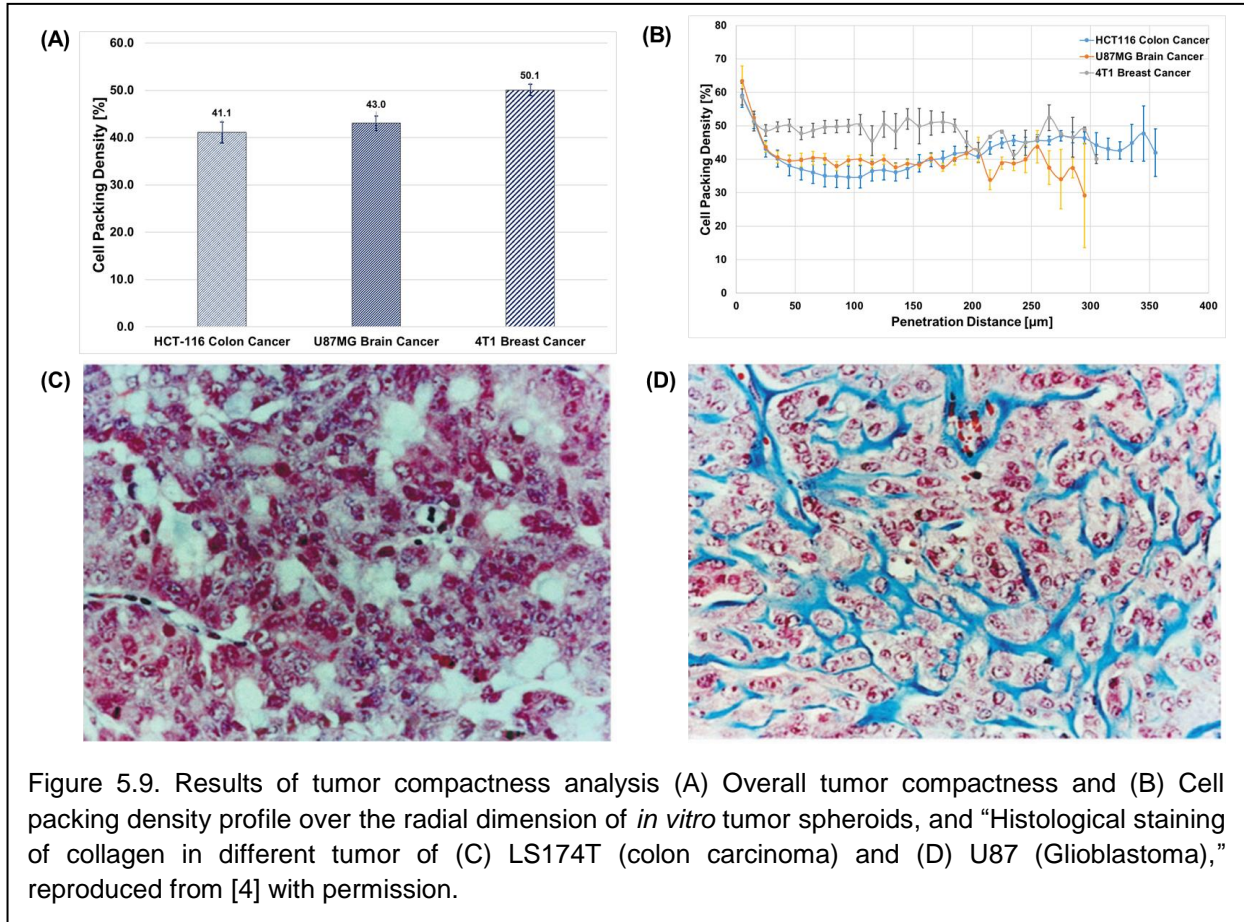


Figure 5.8. Fraction of infecting agents residing intra/intercellularly in HCT-116 (colon cancer) and 4T1 (breast cancer) tumor spheroids.

[4]. The lowest intracellular bacteria penetration of PEGylated NanoBEADS is also corroborated by the 2D invasion assay results (see Figure 5.4). On the other hand, using PEGylated bacteria led to higher overall colonization as well as a higher portion and increase in the number of intracellular bacteria compared to using untreated bacteria. There are several possible explanations for this observation. First, the infecting duration in the 2D invasion assay was set to 45 minutes, which is too short for the mechanically and chemically treated bacteria to recover their bio-activity with respect to motility, proliferation, and invasion, whereas intratumoral penetration experiments lasted for 12 hours, which is long enough for the bacteria to recuperate. Additionally, greater numbers of PEGylated bacteria translocated intercellularly compared to untreated bacteria due to the enhanced diffusion through the intercellular space facilitated by the PEG coating [187]. Bacteria located in between cells started to divide during the incubation period, which thus led to more colonization in the PEGylated bacteria case. Lastly, intratumoral penetration experiments allowed infecting agents to gather into tightly confined spaces between cells upon penetration, which significantly increased the number of infecting agents that were contacting the surrounding cells in the 3D space and thus a considerably greater probability of cell invasion by the infecting agents. Moreover, the concentration of infecting agents around seeded cells for the 2D invasion assay was relatively low, which further explains the different trends in invasion. Lastly, the newly divided bacteria within the tumor cells were exposed to an environment with limited oxygen, which possibly prompted elevated bacterial internalization compared to the 2D cell invasion assay, based on published results indicating that bacteria invasion is increased if the bacteria are grown in low oxygen conditions [188].

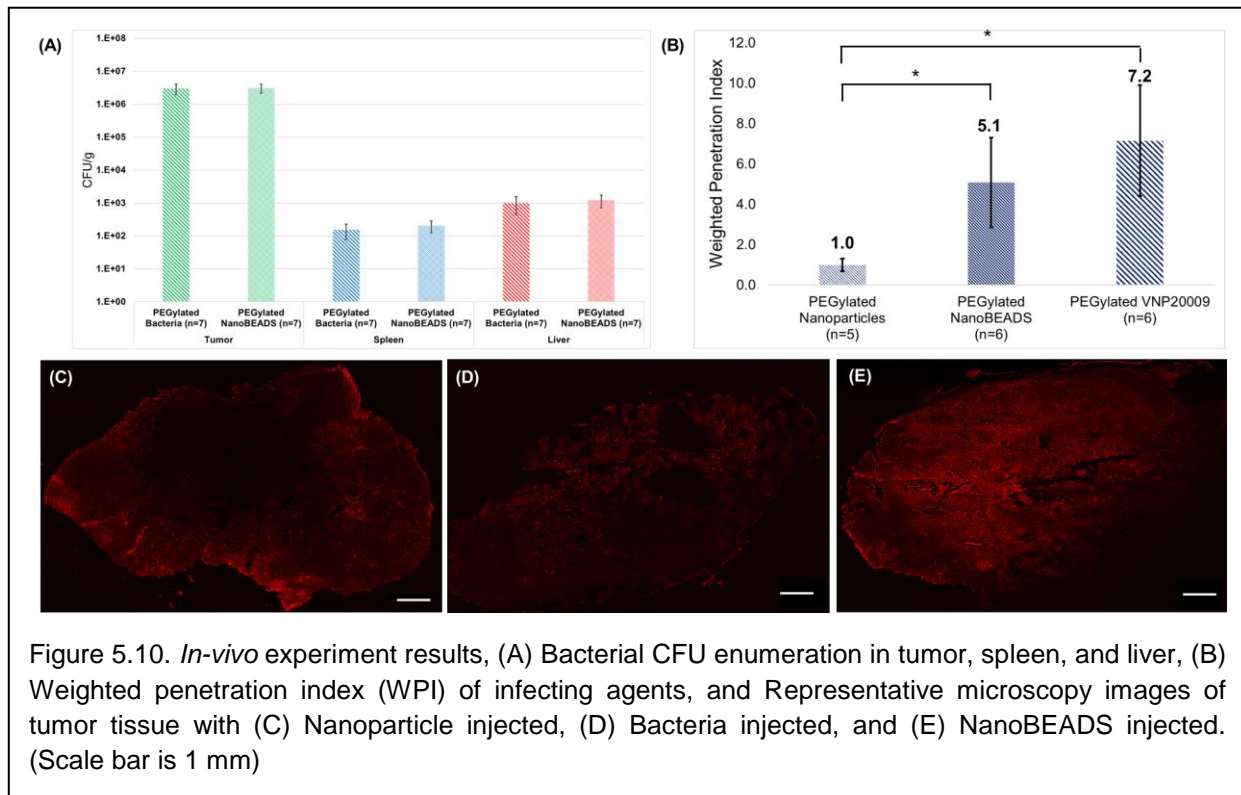
d. Cell Packing Density of Multicellular Tumor Spheroids

The measured cell packing densities of the tumor types, defined as by the area fraction of cell nuclei was $41.1 \pm 2.2 \%$, $43.0 \pm 1.5 \%$, $50.1 \pm 1.2 \%$ for HCT-116 colon cancer, U87MG brain cancer, and 4T1 breast cancer (Figure 5.9 (A)). The spatial cell packing density profile for each



tumor type was also quantified (Figure 5.9 (B)). Measured cell packing density differences between colon cancer and brain cancer was about 4.9%, which shows that the difference between the wPIs of colon cancer and brain cancer was greater than that of the difference between the two cell packing densities. The difference between the wPIs of carcinoma and glioma can be explained with the collagen contents as shown in Figure 5.9 (C) [4].

e. In-vivo experiment results



Colonization of the infecting agents was evaluated by the bacterial plating results. There were three orders of magnitude difference in numbers of bacteria colonized between tumor and liver. There was no significant difference between the bacteria case and NanoBEADS case (Figure 5.10). The weighted penetration index of each infecting agents analyzed through the image processing via confocal microscope images where the point of injection is considered as the center of the sliced tumor tissue. The weighted penetration index for NanoBEADS exceeds that of nanoparticles by 5.1-fold, which clearly shows transport enhancement for the bacteria conjugation strategy.

5.4 Conclusions

The tumor invasion of infecting agents (i.e. *S. Typhimurium* VNP20009, mechanically treated *S. Typhimurium* VNP20009, PEGylated *S. Typhimurium* VNP20009, and PEGylated NanoBEADS) was examined in an *in vitro* invasion assay. This work elucidated that mechanical treatment does not significantly impact invasiveness whereas increased hydrodynamic size of infecting

agents through PEGylation or particle conjugation particularly reduces invasiveness. The intratumoral transport efficacy of the infecting agents was characterized in an *in vitro* multicellular tumor spheroid model made from three tumor cell lines— HCT-116 (colon cancer), U87MG (brain cancer), and 4T1 (breast cancer). In spite of the reduced diffusivity due to the larger size of the NanoBEADS compared to the size of nanoparticles, its transport efficacy surpassed that of the nanoparticle, showing that using a bacteria-based penetration mechanism (binary fusion compared with remodeling of the tumor microenvironment) could improve intratumoral penetration of nanoparticles. Dissimilar intratumoral distribution patterns of infecting agents between different tumor types were hypothesized to be the results of structural variations. Intra/intercellular bacterial penetration investigation revealed that the dominant mode of penetration is intercellular translocation rather than intracellular invasion. Identifying the primary route of penetration reaffirms the important role of structural compactness of tumor on the bacteria-based infecting agent transport efficacy. Surface treatment with PEG coating also showed an enhancement in diffusive transport and thus promoted bacterial intercellular penetration. This combined with bacteria proliferation led to even higher colonization and thus greater bacterial intercellular penetration and intracellular uptake. We hypothesize that the structural compactness of the tumor may be a primary factor affecting the transport efficacy of infecting agents. Quantitative estimates of the compactness of tumors have been made using the cell packing density metric, which were then correlated with drug resistance [61]. Thereby, we measured the cell packing density in each of the tumor types tested using a custom image processing routine. As expected, the measured overall tumor compactness via cell packing density of tumor cells results showed HCT-116 colon cancer had the sparsest nucleus spatial density. However, defining tumor compactness based only on nucleus spatial density neglects structural differences due to differences in ECM make-up and density as well as cell-cell junction. Cell-cell adhesion in the process of tumor spheroids formation is primarily affected by cell adhesion molecules (CAMs), cadherin [181], integrin [189], and selectin [190]. Thus,

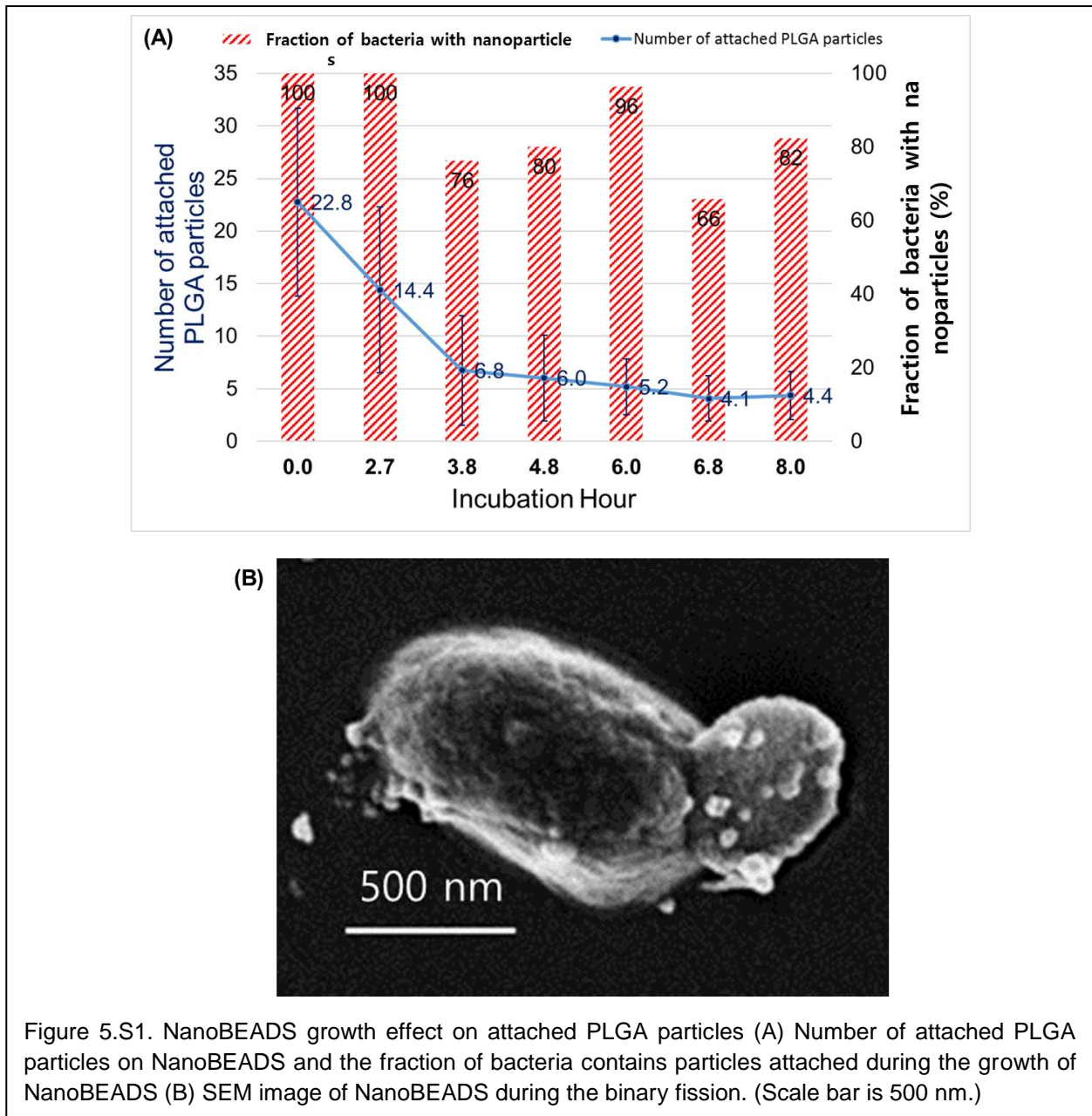
knowledge of the expression level of these proteins should also be considered to estimate the tightness of the tumor spheroids. Additionally, the extracellular matrix constituents, including fibronectin, laminin, glycosaminoglycans, and collagen, vastly influence the tumor tightness [191], leading to enhanced resistance to macromolecule interstitial transport [4]. Especially glioblastoma (U87MG brain cancer) is known to have a high amount of collagen, which inhibits macromolecular transport relative to colon adenocarcinoma (HCT-116) or murine mammary carcinoma (4T1) [4], [183], [184]. Considering both cell adhesion molecules expression level and the relative amounts of the constituents of the ECM would be necessary to accurately estimate the tumor compactness.

The animal study ensured that the chosen experimental parameters, namely the administration route, the inoculum concentration and volume, and the experiment duration of 48 hours, allow for the study of the interstitial transport efficacy *in vivo*. Bacterial plating results showed that tumor colonization is three orders of magnitude higher than liver colonization. Interestingly, the plating results of bacteria and NanoBEADS were equivalent throughout the organs which might imply there is no significant difference of the immune response initiated by them. The penetration performance results reaffirm that bacteria conjugation strategy enhanced the interstitial transport efficacy significantly compared to nanoparticle only approach.

5.5 Appendix

- Growth of infecting agent and PLGA loading capacity

As the proliferation of the infecting agents plays a crucial role in intratumoral penetration, the growth rate of each infecting agents, VNP20009, PEGylated VNP20009, and PEGylated NanoBEADS was evaluated. Mechanically or chemically treated bacteria need some time to recuperate in prior to proliferate. The doubling time based on the growth rate was measured



once the subject bounce back to grow from the dormant state. The evaluated doubling times are 43 minutes, 58 minutes, and 121 minutes for VNP20009, PEGylated VNP20009, and PEGylated NanoBEADS, respectively. PLGA particle loading over generation also needs to be quantified since the number of PLGA particles attached on the single NanoBEADS will decrease over course of treatment through the proliferation of bacteria. Particle loading capacity of NanoBEADS during proliferation was estimated by the analysis of scanning electron microscopy (SEM) images. Aliquot of NanoBEADS at each time point was fixed and imaged under a field emission scanning electron microscope (FESEM, LEO, Zeiss) to estimate the number of particle attached on the bacteria using manual counting. Even though the number of PLGA loading on NanoBEADS decreased over time, the fraction of bacteria contains PLGA particles sustained higher than 80% throughout the incubation duration (Figure 5.S1).

Chapter 6. Mathematical Modeling of NanoBEADS Penetration into *In vitro* Tumor Spheroids⁹

6.1 Introduction

Conventional chemotherapy remains the most common form of cancer therapy despite well-documented shortcomings that limit its effectiveness [19]. In particular, the systemic toxicity is induced through the limited selectivity of anti-cancer drug into the cancerous tissues. Conventional chemotherapeutic drug delivery rely on administration of free drug molecules, which exacerbates the problem of systemic toxicity [192]. There has thus been a push to introduce nanoparticle-based drug carriers such as liposomes, micelles, and dendrimers, among others to both enhance tumor selectivity and reduce toxic side effects [193]–[196]. On the other hand, after the chemotherapeutic drugs reach the tumors sites, elevated interstitial fluid pressure and a dense extracellular matrix, hallmarks of the tumor microenvironment, impeded passive transport of the freely diffusing nanotherapeutics inside tumors [17]. A potentially powerful bio-hybrid approach to actively target tumor sites is to utilize bacteria to carry and deliver the drug-loaded nanoparticles [197], [198]. Some bacterial strains have been genetically modified to evade the immune system resulting prolonged blood circulation allowing for larger tumor accumulation as well as tumor selective localization and preferential colonization [8], [9]. Certain bacterial strains have also shown an invasive phenotype in tumor tissue and are capable of intratumoral penetration, which can enhance the interstitial transport efficacy [10], [11].

⁹ Work done in collaboration with Eric J. Leaman (VT Mechanical Engineering). Eric J. Leaman constructed the computational framework and performed the modeling. SeungBeum Suh conducted the experiments. Eric J. Leaman, SeungBeum Suh, and Bahareh Behkam analyzed the experimental and computational results.

There have been many studies focused on formulating mathematical transport models of drug particles transport in tumor tissue with the goal of precisely predicting the effects of a variety of microenvironmental factors on drug penetration, thereby providing tools to comprehend the current drug delivery systems and possibly improve transport efficacy [199], [200]. Existing intratumoral drug transport models range from the intracellular drug uptake models [201], [202] to continuous models, which represent drug transport from a macroscopic view [200], [203]. A number of mathematical models of drug transport were developed to specifically study different modes of transport including, diffusion [204], [205] and advection [206], as well as the route of delivery, such as vascular transport, transvascular transport, and interstitial transport [17]. Mathematical models based on the transport of tumor targeting therapeutic antibody have also been formulated in order to investigate the role that physiological characteristics play in determining the therapeutic efficacy of macromolecular agents, such as blood circulation and clearance, diffusive and convective transport, and binding of the antigens [183], [207]–[209]. Nanoparticle-based drug delivery systems are suggested to take advantage of the enhanced permeability and retention (EPR) effect, which is the enhancement of the intratumoral accumulation of submicron-sized particles due to the leaky and fenestrated neovasculature, and lack of lymphatic drainage [22], [23]. Nanoparticle localization through the microvasculature was mathematically modelled using a convection-diffusion-reaction model [210]. Several published models have focused on physical aspects of intravenous delivery such as distribution in capillaries, interactions with red blood cells, adhesion with endothelial cells based on binding probability [211]–[214]. Goodman *et al.* [215] developed a mathematical transport model of nanoparticles in *in vitro* tumor spheroids and showed that physical properties such as particle size and rate of binding and porosity of the tissue critically influence delivery characteristics. Kim *et al.* [216] developed a mathematical model of gold nanoparticle-based drug transport *in vitro* experiments and showed that the positive charge of nanoparticles can

influence transport greatly because cellular uptake of nanoparticles is dominant compared to diffusive transport.

Although bacteria-mediated drug delivery systems have been extensively studied for their aforementioned advantages over conventional treatments, there have been few attempts to formulate a mathematical model of bacterial tumor colonization. On the other hand, a variety of mathematical models describing bacterial transport in porous media have been developed. Theoretical descriptions of bacteria transport are based on the passive diffusion of bacteria in porous media, bacterial motility and chemotaxis, and growth of bacteria [217]–[219]. Kasinskas *et al.* [49] proposed a mathematical model for bacteria transport in tumor cylindroids and fit its parameters to experimentally measured spatiotemporal bacterial distributions. The model suggested, based on the assumptions inherent in its formulation, that both chemotaxis and growth are crucial to effective tumor colonization.

In this work, we propose a simple model of bacterial colonization of *in vitro* tumor spheroids in order to help elucidate the mechanisms that facilitate bacterial penetration and colonization of tumors. Notably, we assume that the necrotic region of the tumor itself acts as a source of diffusing nutrients supporting bacterial growth. We show that this model can reproduce experimentally obtained characteristic intratumoral bacterial accumulation curves, manifesting as a ring of high bacterial concentration surrounding the tumor core in some experiments. Based on simulations, the model suggests that bacterial accumulation is primarily a function of an effective diffusivity and the growth rate of the bacteria. Moreover, we show that the effective diffusivity of bacteria and NanoBEADS is approximately two-fold higher than that of nanoparticles alone, thus demonstrating the advantage to using bacteria a nanoparticle carrier. This model can be used in the future to make predictions of bacterial tumor colonization, design therapeutic strategies, and estimate the drug delivery efficacy.

6.2 Methods

a. Computational Modeling of the Intratumoral Penetration

It is well established that bacterial transport in aqueous environments can be modeled as a diffusion-like process, even when transport is driven by chemotaxis and motility. While the specific mechanisms of bacterial transport in tissue are a matter of debate [49], [220], [221], we assumed that the transport of infecting agents in tumor spheroids can likewise be represented mathematically as a diffusive process. For PEGylated bacteria (PB) and PEGylated NanoBEADS (PNBs), we hypothesized that intratumoral growth is significant to the colonization process and occurs as a function of local nutrient availability. In general, these mechanisms are represented by a diffusion-reaction equation of the form

$$\frac{\partial C_i}{\partial t} = \nabla \cdot (D_i \nabla C_i) + R(\mathbf{x}) \quad (6.1)$$

where C_i is the local concentration of the species of interest, D_i is the diffusion coefficient of C_i , and $R(\mathbf{x})$ represents reaction terms ($\mathbf{x} = x, y, z$). In spherical coordinates, assuming symmetry in the angular dimensions and substituting the appropriate terms into Equation 6.1, tumor penetration and colonization is represented by a set of coupled partial differential equations (PDEs):

$$\frac{\partial B}{\partial t} = \frac{1}{r^2} \frac{\partial}{\partial r} \left(D_B r^2 \frac{\partial B}{\partial r} \right) + k_g B \left(g - \frac{B}{k_B} \right) \quad (6.2)$$

and

$$\frac{\partial s}{\partial t} = \frac{1}{r^2} \frac{\partial}{\partial r} \left(D_s r^2 \frac{\partial s}{\partial r} \right) + k_s - \frac{1}{Y} k_g g B. \quad (6.3)$$

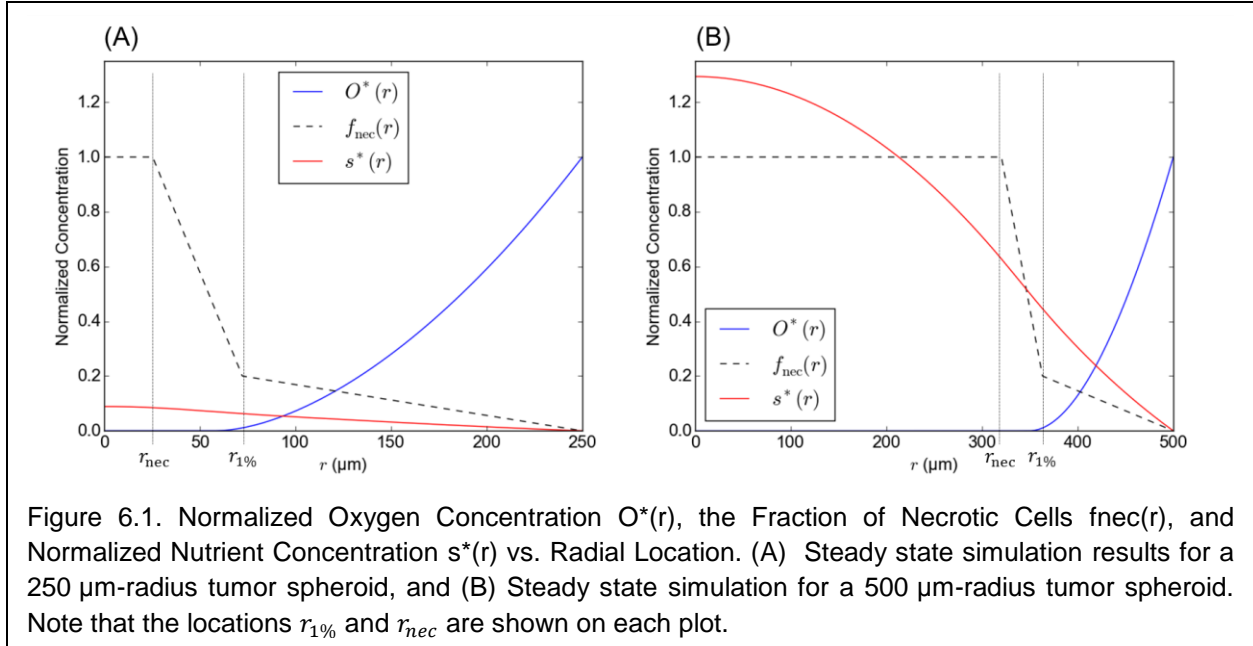
Equations 6.2 and 6.3 together govern the transport and growth of the infecting agent B (*i.e.* PB, PNBs, or PEGylated nanoparticles (PNPs)) and the transport and utilization of a nutrient species s (referred to generically as substrate from this point forward), respectively. The

effective local diffusion coefficients are given by $D_i = D_i(r)$, k_g is the maximum growth rate of B ($k_g = \ln(2) / \tau_{\min}$ where τ_{\min} is the doubling time in the nutrient rich medium), $k_B = k_B(r)$ is the local carrying capacity of the tumor (*i.e.* maximum concentration) [218], $k_s = k_s(r)$ is the local rate of release of substrate s from the tumor, Y is the bacterial yield (*i.e.* dry mass of bacteria per unit mass of substrate). The local growth rate is governed by the substrate availability according to Monod growth kinetics,

$$g = \frac{s}{K_m + s}, \quad (6.4)$$

where $s = s(r)$ is local substrate concentration, and K_m is the Monod constant (*i.e.* the concentration of s when the growth rate of B is one-half the maximum rate). Note that the transport of nanoparticles alone was assumed to be a passive, diffusion-only process, thus k_g was set to zero and solving Equation 6.3 was not needed when modeling this case.

Crucial to accurately modeling bacterial transport in the tumors is a determination of the source of nutrients that supports bacterial growth. It has been shown that mutant strains of *Salmonella* Typhimurium that are auxotrophic for (*i.e.* unable to synthesize) certain amino acids, such as VNP20009 or A1-R, can preferentially colonize tumor tissue over healthy tissue [42]–[44]. It is suspected that preferential growth is due in part to nutrients and metabolites in the tumor tissue, including the required amino acids among other substrates that support biosynthesis [44], [222], [223]. One of the hallmarks of avascular tumors, particularly of those grown *in vitro*, is the development of a hypoxic region beneath the tumor surface due to oxygen transport limitations. It is also known that hypoxia induces certain physiological attributes such as increased tumor progression and greater therapeutic resistance [226]. This lack of oxygen, among other factors, leads to cell death and the development of a necrotic core. We hypothesized that necrotic cells may secrete a variety of substances supporting preferential bacterial growth, lumped in our proposed model as a non-specific, diffusing species of nutrients (substrate).



Towards creating a physiologically-realistic simulation of tumor necrosis and location-dependent substrate release in the tumors, we adopted the model of oxygen transport and consumption proposed by Grimes *et al.* [227],

$$\frac{\partial O}{\partial t} = \frac{1}{r^2} \frac{\partial}{\partial r} \left(D_O r^2 \frac{\partial O}{\partial r} \right) - a, \quad (6.5)$$

where O is oxygen concentration, D_O is the diffusivity of oxygen in the tumor, and a is the rate of oxygen consumption by the cells. Note that a was taken to be a constant equal to $7.29 \times 10^{-7} \text{ m}^3/\text{kg}\cdot\text{s}$ based on the findings presented in [227], which included both experimental and computational results for tumor spheroids similar in size to those studied for this dissertation. The resulting steady state oxygen concentration profile was coupled with the results presented by Milotti and Chignola [228], who created a comprehensive computational simulation of tumor spheroid growth and metabolism, to define radially dependent tumor necrosis. Figure 6.1 shows the normalized concentrations of oxygen, necrotic cells, and substrate at steady state for tumor spheroids 250 μm and 500 μm in radii (note that the * symbol is used to denote normalized concentration variables). We noted that the authors found characteristically similar results for tumors of about 300 μm to 500 μm in diameter, wherein the

fraction of dead cells increased from 0% to about 20% from the outer tumor boundary to the point where the oxygen concentration had decreased by nearly 100% relative to the boundary. The fraction of dead cells was predicted to sharply increase to nearly 100% over approximately the next 50 μm (moving towards the tumor center) [228]. The fraction of necrotic cells (*i.e.* number dead cells/total number of cells) was simulated in the model according to

$$f_{\text{nec}}(r) = \begin{cases} 1 & \text{for } r < r_{\text{nec}} \\ 1 - \frac{0.8}{50 \mu\text{m}} (r - r_{\text{nec}}) & \text{for } r_{\text{nec}} \leq r < r_{1\%} \\ 0.2 - \frac{0.2}{R - r_{1\%}} (r - r_{1\%}) & \text{for } r \geq r_{1\%} \end{cases}$$

where $r_{1\%}$ is the radial value at which the simulated oxygen concentration is 1%, and $r_{\text{nec}} =$

Table 6.1. Constant Parameters and Boundary Conditions for All Simulations (* indicates normalized parameter)

Parameter	Value	Unit	Reference
k_B^*	1	dimensionless	N/A
D_S	1.0	$\mu\text{m}^2/\text{s}$	Estimated
D_O	2000	$\mu\text{m}^2/\text{s}$	[227]
a^*	0.24	s^{-1}	[227]
$s^* _{r=R}$	0	dimensionless	N/A
$O^* _{r=R}$	1	dimensionless	N/A
Simulated Time	12	hour	N/A

$r_{1\%} - 50 \mu\text{m}$ is the radial value 50 μm from $r_{1\%}$ (towards the tumor center). Using this result, the release of substrate by tumor cells is $k_s = \omega_s f(r)$, where ω_s is the rate of substrate release per unit volume of the necrotic tissue. To simplify analysis and facilitate comparison of simulations

run for tumors of varying size, the rate was chosen such that the steady state substrate concentration (without colonizing bacteria) at the center of a tumor 405 μm in radius was equal to unity, effectively normalizing its value. This same rate was used for all simulations. Since the volume of tumor spheroids used in experiments was much smaller than the volume of media they were submerged in ($V_{\text{media}}/V_{\text{tumor}} \approx 200$), the boundary condition for s was assumed as zero at the tumor surface. Because the tumors were constantly shaken during experiments, it was assumed that the media was saturated with oxygen at 30.0 m^3/kg (corresponding to a partial pressure of 100 mmHg). The oxygen model was normalized by dividing Equation 6.5 by 30.0 m^3/kg . Table 6.1 gives constant parameters used for each simulation.

b. Experimental Measurement of the Intratumoral Penetration of the Infecting Agents

Experimental data collection and protocols are described in Chapter 5. Briefly, HCT116 (human colon carcinoma) tumor spheroids were grown in ultra-low adhesion well plates. Once the tumors reached a diameter near 1 mm, infecting agents were suspended at high concentrations (i.e., 1.8×10^8 cfu for PB, 1.8×10^8 for PNBs, and 1.8×10^8 for PNPs) in cell culture media (McCoy's 5A supplemented with 10% FBS). Inoculated tumor spheroids were maintained in at 37° C and 5% CO_2 while being shaken constantly to prevent sedimentation of the infecting agents. After 12 hours of incubation period, the tumors were collected, washed, and fixed. Slices of tumors taken near the center of each spheroid were imaged to in order to quantify colonization by infecting agents using the custom image processing routine described in Chapter 2.

c. Experimental setup for Hypoxic study¹⁰

¹⁰ Work done in collaboration with Luke Onweller (VT Mechanical Engineering), Dr. Dwi Susanti (VT Biochemistry), and Professor Biswarup Mukhopadhyay (VT Biochemistry)

It should be noted that hypoxia has been shown to cause physiological changes in bacteria. Bacteria grown in different oxygen concentrations may have altered pathological characteristics such as invasiveness, growth rate, and anticancer efficacy [229]–[232]. Therefore, further research on bacterial physiological phenotypes within various oxygen concentrations would be valuable to better understand mechanisms facilitating colonization. To this end, we have developed a hypoxic gas infusion system to control oxygen concentration during invasion assays, cell viability assays, and growth rate measurements. Oxygen concentrations (1% and 5%) were chosen to represent the relevant physiological conditions of several various types of

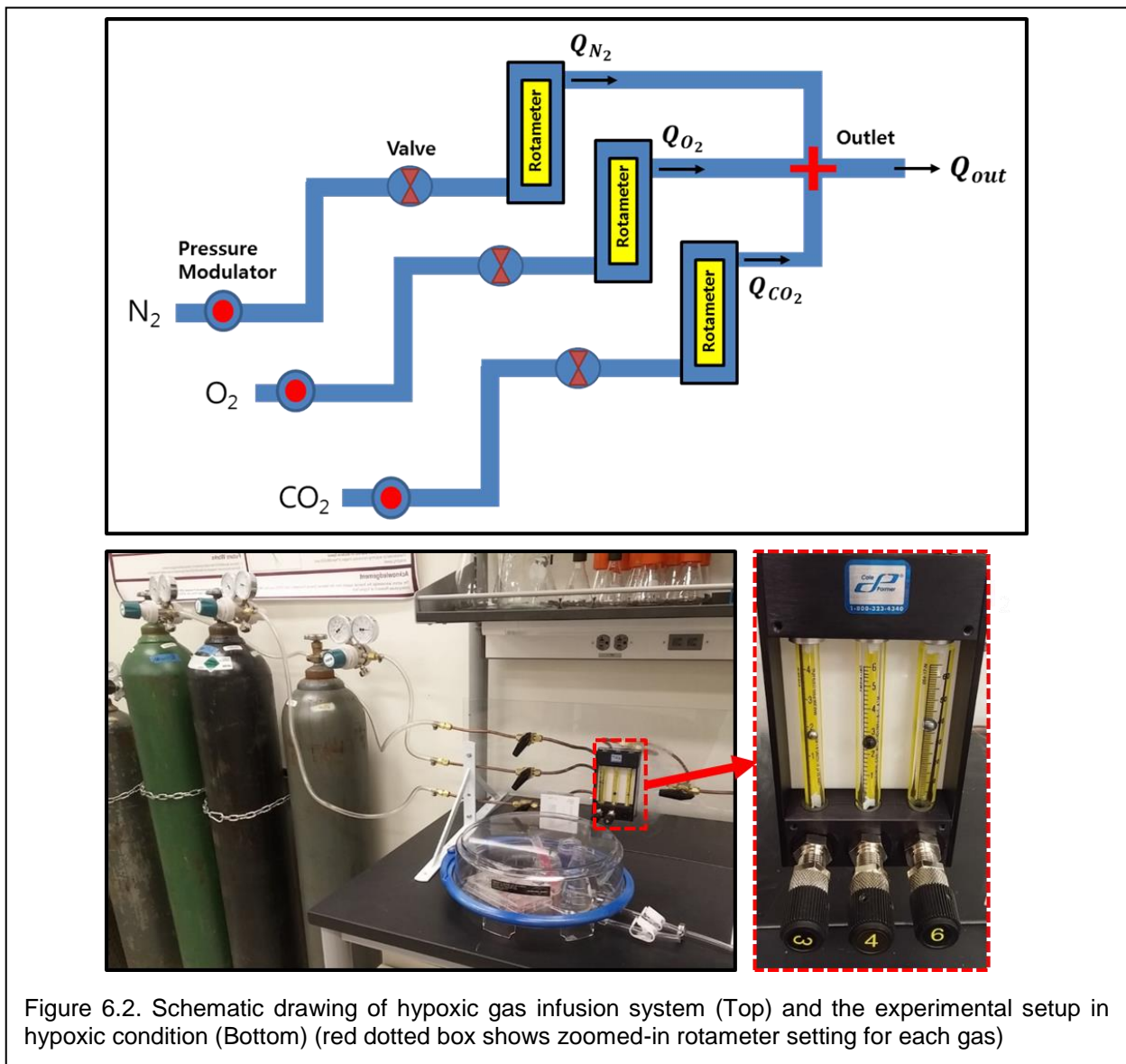


Figure 6.2. Schematic drawing of hypoxic gas infusion system (Top) and the experimental setup in hypoxic condition (Bottom) (red dotted box shows zoomed-in rotameter setting for each gas)

cancer (*i.e.*, 13mmHg in brain tumors = 1.78% oxygen). The partial pressure of oxygen (pO_2) in the hypoxic region varies between different types of tumors: the mean pO_2 value is 9.6 mmHg in renal carcinomas, 6 mmHg in liver tumors, and 13 mmHg in brain tumors [233].

In order to investigate the effect of oxygen concentration on the efficacy of the bacteria-mediated cancer treatment, we developed a hypoxic gas infusion system to control oxygen concentration during invasion assays, cell viability assays, and growth rate measurement experiments. The gas infusion system was designed to control the concentration of oxygen, carbon dioxide, and nitrogen, mixed by controlled volumetric flow rate measured via a rotameter (Figure 6.2). In order to realize the specific oxygen concentration of 1% and 5% with maintaining 5% CO_2 for the mammalian cell incubation, the nitrogen gas concentration was adjusted to 94% and 90% for the gas infusion system, respectively.

d. Bacterial growth rate assay in Hypoxia

The growth rates of *S. Typhimurium* VNP20009 in Lysogeny broth (LB, 1% w/v of tryptone, 1% w/v of NaCl, and 0.5% w/v of yeast extract), at limited oxygen concentrations was measured through temporal OD_{600} measurements of the bacterial culture in a crimp-sealed serum flask.

e. Bacterial Invasiveness in Hypoxia

The invasiveness of *S. Typhimurium* VNP20009 into HCT-116 (colon cancer) in limited oxygen concentration (1% and 5%) was examined through a 2D invasion assay within the hypoxic chamber (STEMCELL). The invasion assay methods were described in detail in Chapter 5.2. Briefly, 60,000 cells in 1 ml of cell culturing media were transferred into tissue treated 12-well plates, incubated at 37°C in a hypoxic chamber, injected with the gas mixture until the cells were adapted to the hypoxic condition for 6 hours. For the bacteria culture, 10 ml of LB was inoculated using a single colony and shaken overnight at 37°C and 100 rpm. Fresh cultures were started with 1 % v/v overnight culture in LB in the crimp-sealed serum flask injected with the mixed gas and shaken at 37°C and 100 rpm. Once the optical density at 600nm (OD_{600})

reached 1.0, the bacteria culture was washed twice by centrifugation at $1,700 \times g$ for 5 minutes, and suspended in McCoy's 5A supplemented with 10% FBS (HCT-116 cell culturing media) at a final concentration of 3.0×10^5 cfu/ml. After the monolayer of cells were infected with the 1 ml of the prepared bacteria for 45 minutes at 37°C within the hypoxic chamber, the suspension was discarded and the cells were incubated with antibiotic (50 $\mu\text{g/ml}$ of gentamicin sulfate) in culturing media for 1 hour to kill extracellular bacteria. After a careful wash with Dulbecco's phosphate buffered saline (D-PBS), cells were treated with 0.05% trypsin-EDTA for 10 minutes followed by 1% Triton X-100 for 10 minutes to detach and lyse the cells. Subsequently, the suspension was sonicated for 30 seconds to break up the clumps of bacteria, the bacteria suspension was diluted prior to plating for cfu counting.

f. Cell Viability assay in Hypoxia

In order to examine the cytotoxicity effect of bacterial invasion and exposure to the limited oxygen concentration, the cell viability assays at different oxygen concentrations (1% and 21%) in presence and absence of bacteria were tested. NucBlue® Live reagent (2 drops/ml) and NucGreen® Dead reagent (2 drops/ml) were added on the tumor cell (HCT-116 colon cancer)-seeded well plates after the bacterial invasion. The fraction of dead cells among the total population was quantified and found to be relatively small (less than 5%) in all of the cases, which implies that the bacteria do not affect the cell viability during the 45 minutes of incubation either in the normal condition or in limited oxygen concentration. The cytotoxicity of the limited oxygen concentration on bacteria was also examined by staining *S. Typhimurium* VNP20009 using the Live/Dead BacLight assay.

g. Statistical analysis

Error bars represent standard error and statistical significance was determined by a one-way ANOVA followed by Tukey-Kramer HSD test. A p-value of 0.05 was used as the threshold for significance.

6.3 Results

a. Model Validation

Parameters D_B , τ_{\min} (and thus k_g), K_m^* , and Y^* were fit using a differential evolution global optimization algorithm (`differential_evolution` function of the `scipy.optimize` module, SciPy v0.17) to stochastically select parameters within a user-defined set of ranges towards minimizing the sum of the squared error between experimental and simulated bacterial concentration profiles [234]. Since the tumors in experiments varied in size, thus affecting the physics of transport, the model was fit to individual data from each tumor with the simulated radius R determined from the experimental data. In order to compare fitted parameters between different slices, the infecting agent boundary condition $B|_{r=R}$ was taken as the outermost concentration measured in each slice, as this varied between samples. Likewise, the duration of each simulation was 12 hr based on the incubation time during experiments. Parameters derived directly from experimental data (*i.e.* not fit) are given in Table 6.2. The boundary condition at the center of spheroids was

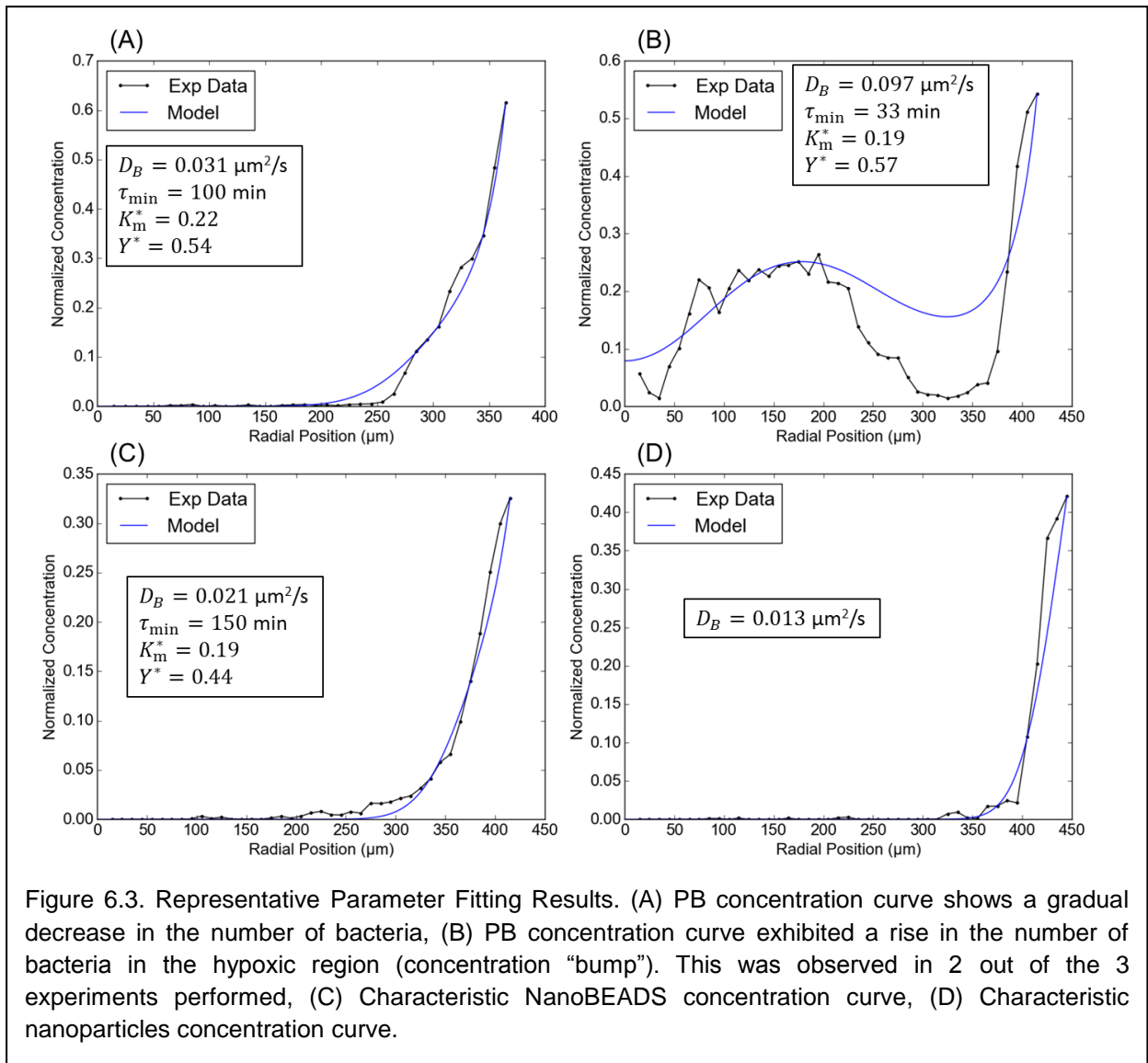
Table 6.2. Deterministic Parameters and Boundary Conditions Derived from Experimental Data (* indicates normalized parameter)

Parameter	Description	Unit
R	Radius of specific tumor sample	μm
$B^* _{r=R}$	Outermost bacterial concentration measured	dimensionless
Simulation Duration	The total amount of time tumors were incubated with infecting agents	hour

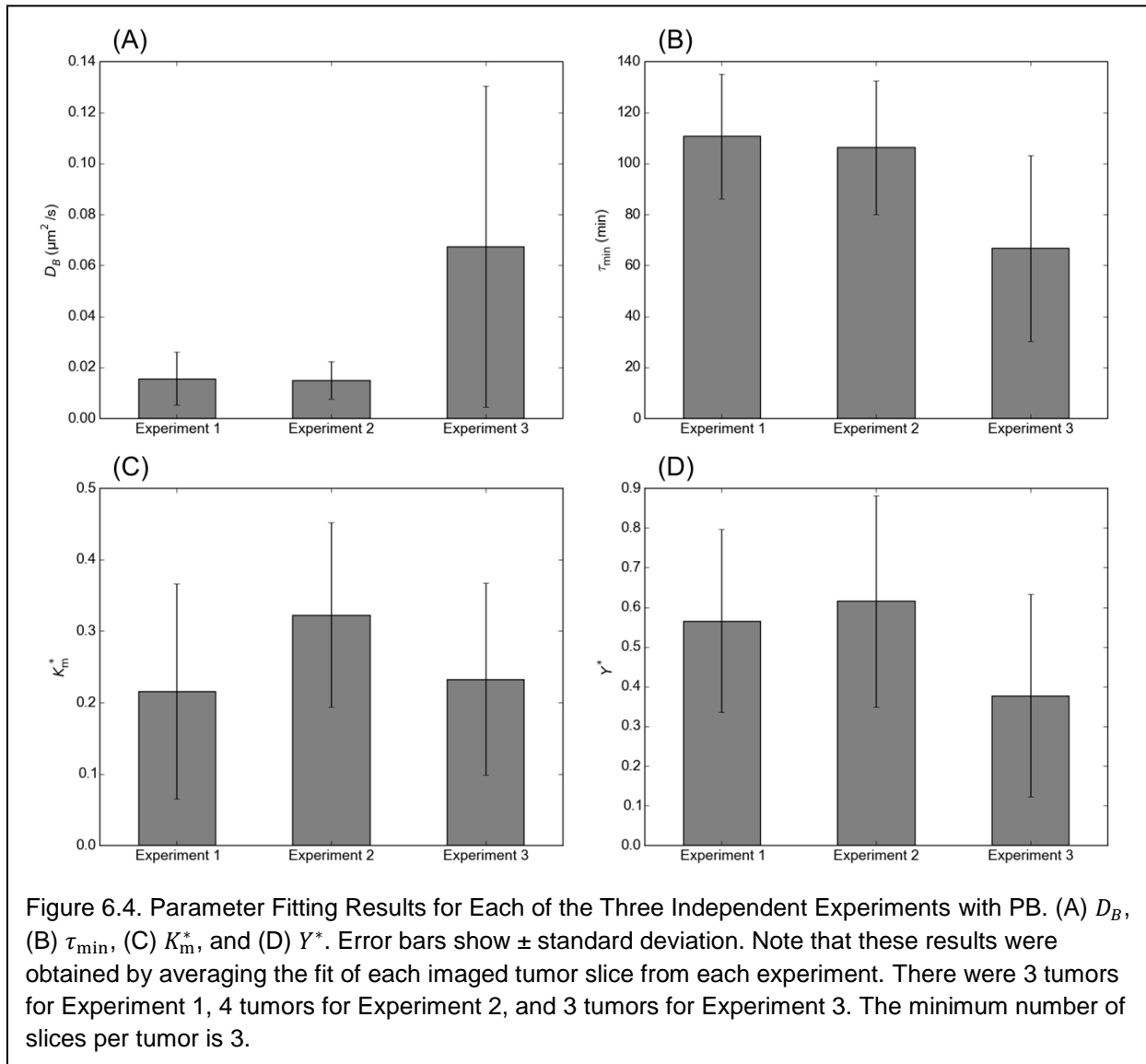
$$\left. \frac{\partial B}{\partial r} \right|_{r=0} = \left. \frac{\partial s}{\partial r} \right|_{r=0} = 0$$

based on the assumption of symmetry. Figure 6.3 shows example fitting results for PB, PNBs, and PNPs. Note that only the diffusion coefficient was fit for NP data, as growth parameters were not relevant.

Radial distribution of the agents for the case of tumor colonization by PB was highly variable. In two out of the three independent experiments, bacterial concentration curves, as measured from confocal images of several individual tumor slices, showed that bacterial concentration decreased rapidly towards zero from the outer boundary toward the tumor center. In contrast, all data from the third experiment showed a similar sharp decrease followed by an increase, before



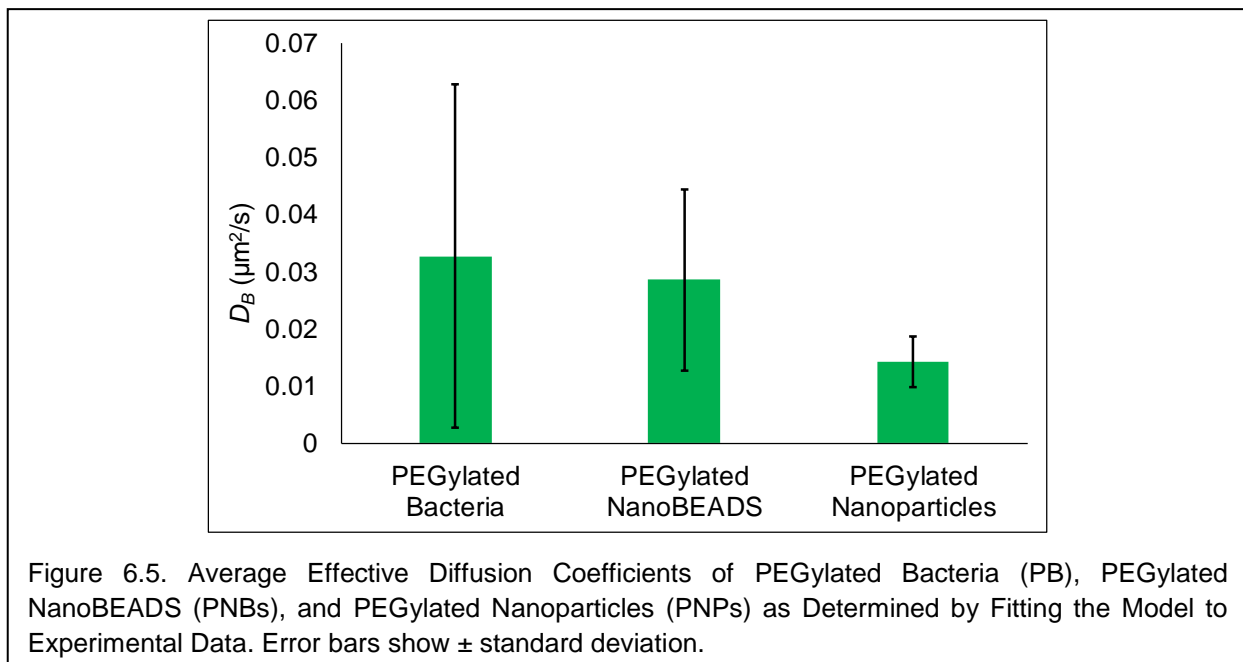
decreasing to near zero concentration at the tumor center (presenting a “bump” in the concentration profile). This resulted in best-fit parameters that deviated significantly from those optimized based on the first two experimental datasets. Figure 6.4 shows the average best-fit parameters for each independent experiment with PB. Note that the average diffusion coefficient and standard deviation for Experiment 3 was much higher on average than for the other two experiments. Additionally, the growth parameters τ_{\min} and Y^* were found to be smaller on average (leading to a greater overall growth rate) than for the other two experiments, while K_m^* was similar between all three. Notably, most samples not showing the “bump”



contained concentration curves that contained a nearly linear region (Fig. 6.3A).

Infecting agent concentration curves for both the NanoBEADS and the nanoparticles were similar among all data and experiments, following characteristic sharp decreases in concentration from the boundary towards the tumor center (Fig. 6.3C and D). From the experimental data shown in Chapter 5, it is clear that the overall amount of the PB and PNBs that colonized tumors was greater than the total amount of PNPs that diffused into tumors. This result is quantitatively reflected by differences between the fitted diffusion coefficients for each type of infecting agent, plotted in Figure 6.5. On average, the effective diffusivity of PB was found to be more than two-fold greater than that of PNPs, and about 15% higher than that of PNBs.

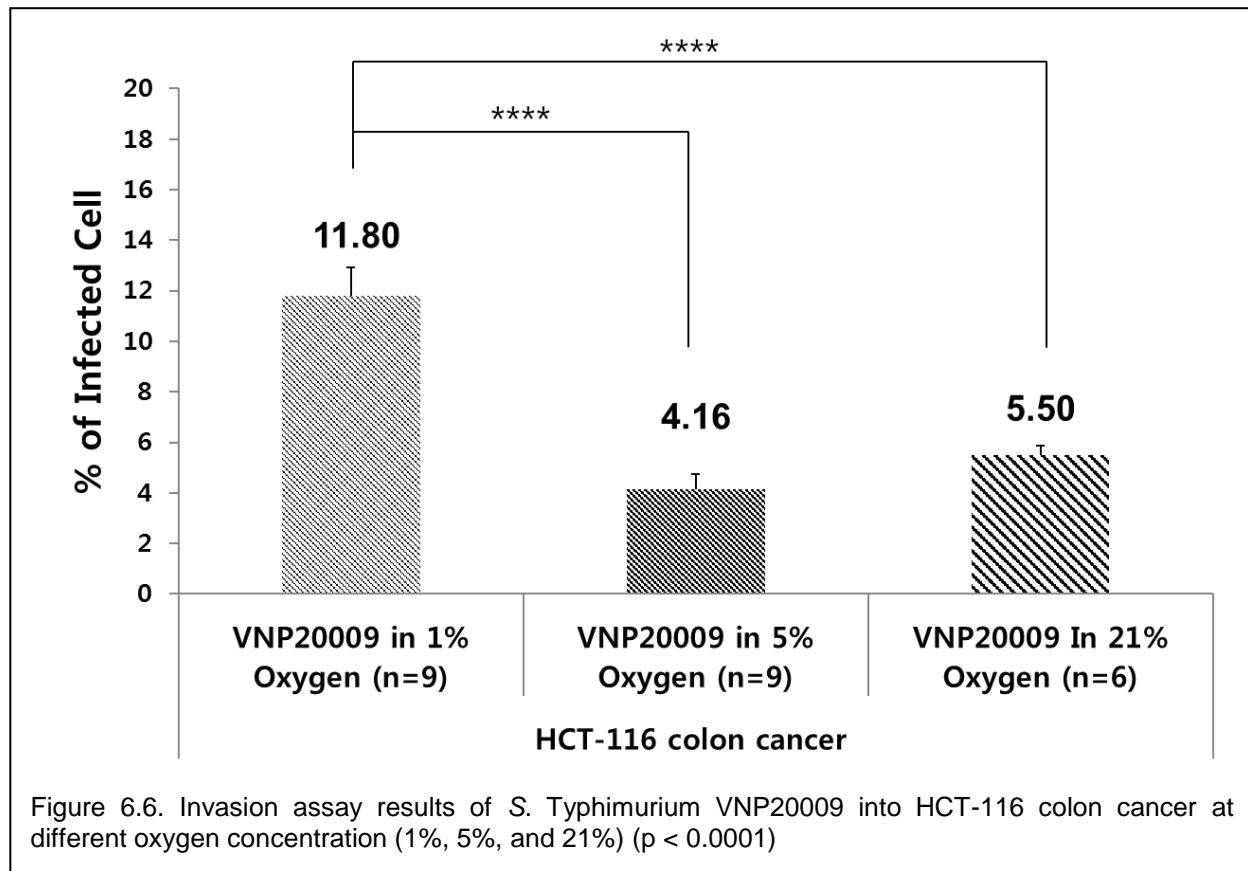
On average, the best-fit doubling times for PB and PNBs were 94.6 min and 137.7 min, respectively. A longer doubling time for PNBs in tumors was expected, as the doubling time for PNBs in culture media was approximately twice as long as for PB in culture media. The averages of the Monod constant K_m compared well between the two cases (0.25 for PB and



0.32 for PNBs), and the best-fit yield Y values were nearly identical (approximately 0.52 for both PB and PNBs).

b. Bacterial Phenotype Assay (Growth rate, Invasiveness, and Cell Viability) in Hypoxia

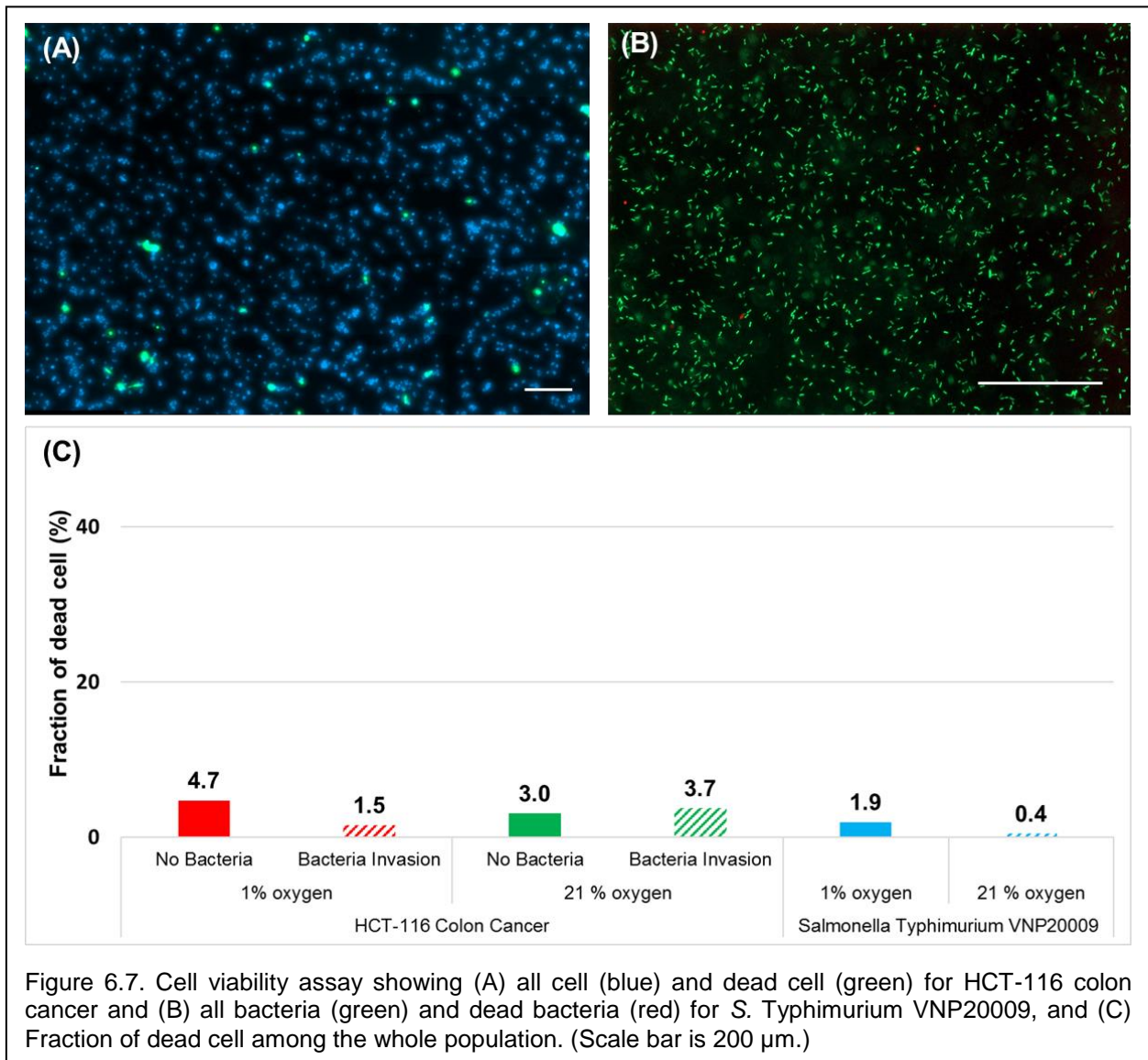
The doubling times for different oxygen concentrations were estimated as 43.9 ± 6.4 minutes, 51.7 ± 12.0 minutes, and 59.9 ± 28.6 minutes for 21% O₂, 5% O₂, and 1% O₂, respectively. The measurements of bacterial growth rate at 1%, 5%, and atmospheric oxygen concentrations were not found to be significantly different, thus we did not model bacterial growth as a function of oxygen concentration. On the other hand, the invasion assay results showed that there were no significant changes in invasiveness between experiments run at oxygen concentration greater than 5%, whereas the fraction of the internalized bacteria doubled when a 1% oxygen



concentration was used (Figure 6.6). The cell viability assay showed that the quantified fraction of dead bacteria among the total population was relatively small (less than 5%) for all of the cases, which implies that the limited oxygen concentration does not affect the viability of bacteria (Figure 6.7).

6.4 Discussion

We have developed a biophysical model to describe the transport and colonization of tumors by



bacteria by assuming that bacterial colonization can be modeled as a diffusion-like process with preferential intratumoral growth fueled by nutrients or growth factors that are released from the necrotic regions of tumors. Most notably, our results show that the effective diffusion coefficients of PB and PNBs are approximately two-fold higher than that of NPs alone, thereby demonstrating the potential for PNBs to improve upon conventional nanoparticle-based cancer therapies.

Our diffusion-reaction based continuum model is capable of reproducing the general trends

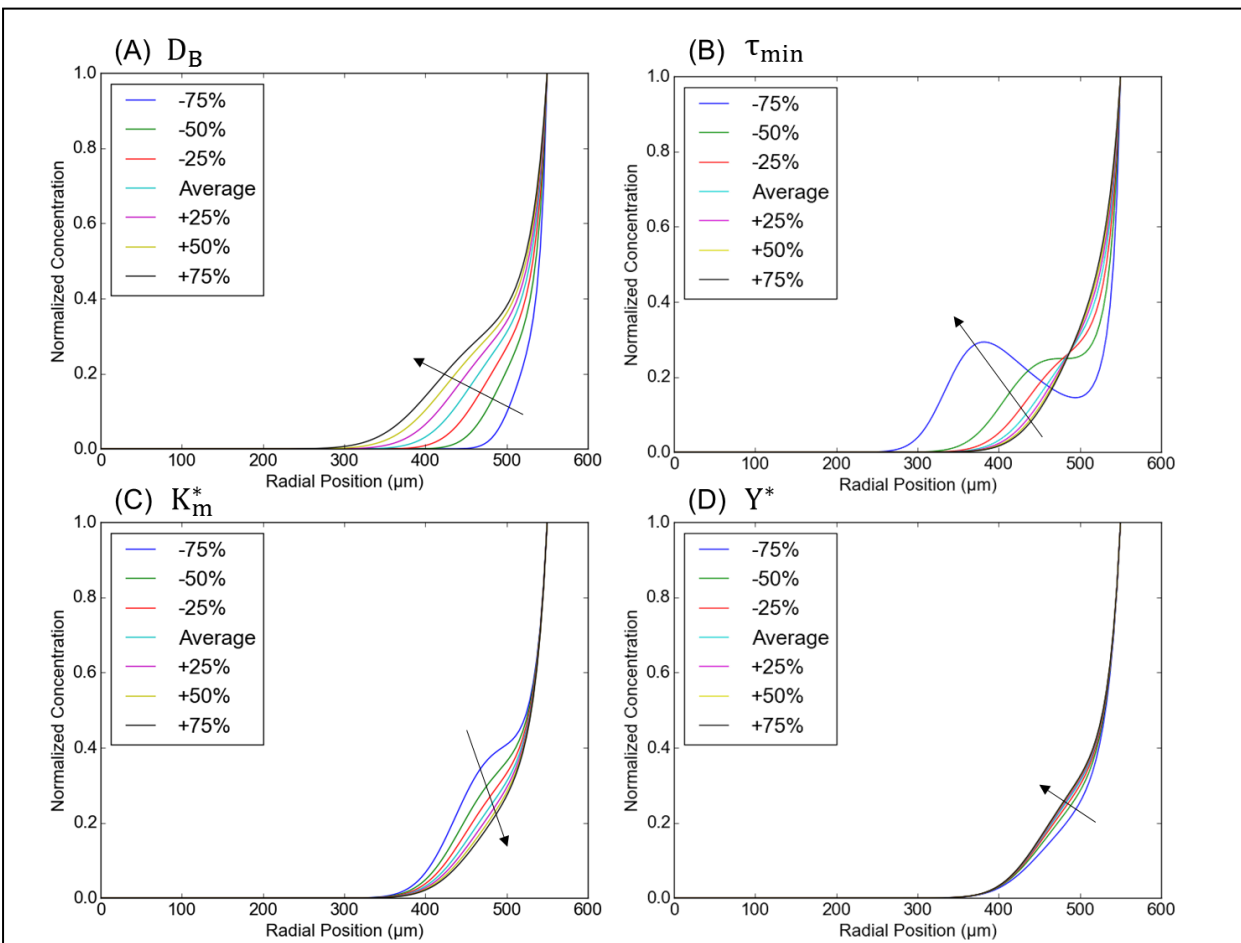


Figure 6.8. Sensitivity Analysis of the PB Colonization Profile with Respect to Fitted Parameters. (A) Sensitivity to D_B with $\bar{D}_B = 0.033 \mu\text{m}^2/\text{s}$, (B) Sensitivity to τ_{min} with $\bar{\tau}_{min} = 95 \text{ min}$, (C) Sensitivity to K_m^* with $\bar{K}_m^* = 0.26$, and (D) Sensitivity to Y^* with $\bar{Y}^* = 0.52$. Note that \bar{x} indicates the average value. The arrows shown on each plot indicate trending direction of the curves with increase in the parameter of interest.

captured in the data. The model fit data showing relatively low amounts of colonization particularly well. Qualitatively, the “bump” seen in approximately 25% of PB experiments was reproduced. The fitting results indicated that both enhanced growth and greater effective diffusivity in the tumor tissue was needed for this to occur. These results are plausible, as tumor morphology was observed to vary to an extent between experiments. Slight differences in media constituents, which include proteins and growth factors derived from animals, cell culture passage number, and handling of tumors, among other factors, could lead to differences in tumor microenvironment. Changes in these properties could affect both the “compactness” of the tumor and the chemicals released from dead cells.

A sensitivity analysis was performed in order to investigate the effect of changes in several parameters used in the proposed model (Figure 6.8). The nominal parameter values of effective diffusion coefficient (\bar{D}_B), bacterial doubling time ($\bar{\tau}_{\min}$), Monod constant (\bar{K}_m^*), and yield (Y^*), were determined by fitting the model to the experimental profiles. Two parameters that had the greatest effect on spatial distributions of bacteria were identified as the effective diffusion coefficient and the growth rate, which is dependent upon substrate availability. In other words, a small diffusion coefficient inhibits deep bacterial penetration, and relatively low substrate concentration at the boundary of the tumor negatively affects bacterial growth. The sensitivity analysis of the agent distribution to the diffusion coefficient (D_B) and doubling time (τ_{\min}) showed that an increase in the bacteria concentration within the hypoxic region can be produced when D_B is larger than $0.2 \mu\text{m}^2/\text{s}$ and the doubling time is short relative to the average. Agent localization is particularly sensitive to change in the diffusion coefficient in deeper intratumoral locations due to the higher substrate concentrations (due to the presence of a larger fraction of necrotic cells). A larger diffusion coefficient promotes greater colonization in the deeper region (Figure 6.8A), whereas bacterial colonization was not sensitive between the boundary and middle region where the substrate concentration is relatively lower. Parameters

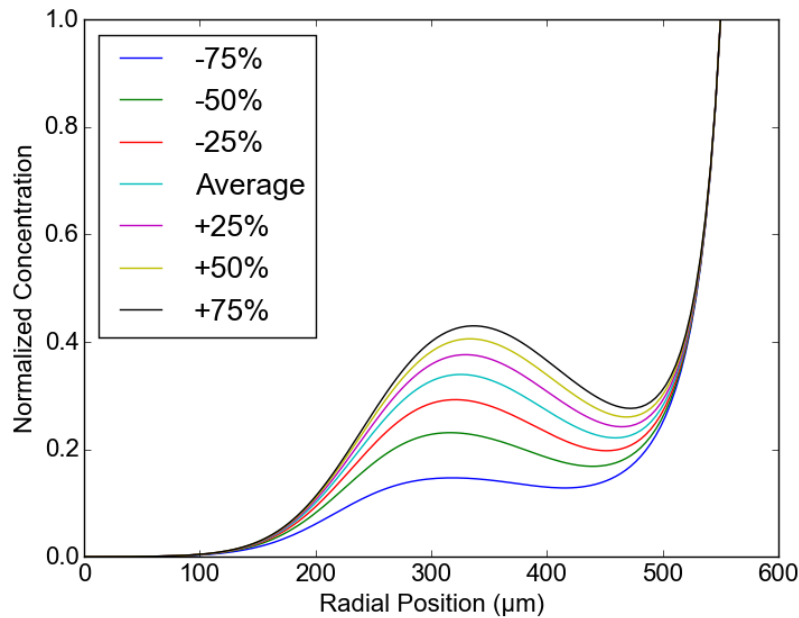
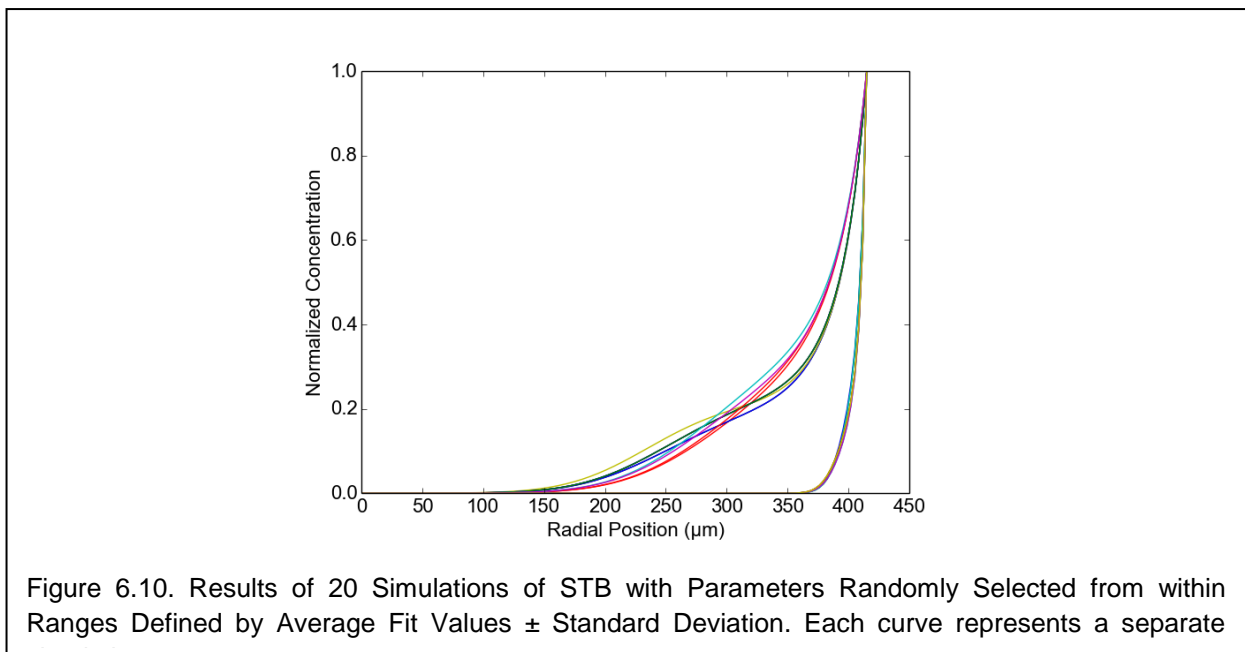


Figure 6.9. Sensitivity of the Colonization Profile to Yield Y with $D_B = 0.1 \mu\text{m}^2/\text{s}$, $\tau_{min} = 40 \text{ min}$, and $K_m^* = 0.519$

related to the growth of the bacteria (the doubling time τ_{min} and the Monod constant K_m^*) show similar trends in that the agents can penetrate more deeply as growth rate increases. Comparing these parameters, the system is more sensitive to the doubling time than to the Monod constant (Figure 6.8 (C)). Interestingly, changes in the yield, which defines how much of the substrate is required by the bacteria to grow, did not change the radial penetration distance but the amount of colonization (Figure 6.8 (D)). In contrast, running the same simulation but with a 3-fold greater diffusivity and the relatively short doubling time of 40 min shows that the results are highly sensitive to yield when bacteria are able to reach inner locations of the tumor compared to remaining only near the boundary (Fig. 6.9). This is due to the higher availability of substrate, meaning that preferential growth is enhanced compared to bacteria restricted to the outer tumor regions with lower substrate concentrations.

Despite capturing general trends, the model failed to reproduce the “valley” formed between the bump and the outer boundary (Fig. 6.3B) for all of the data with this characteristic “region of increased bacteria concentration within the hypoxic zone.” One potential reason for this is that the assumption of one constant effective diffusion coefficient throughout the tumor radius is inaccurate. It should be noted that the model did not reproduce the slope of the nearly linear portion of data near the outer boundary in Figure 6.3B, nor did the model capture the curves in this region for the representative data shown in Figure 6.3C and D. As the fraction of necrotic tissue increases moving from the boundary towards the center of the tumor, the effective diffusivity may increase due to shrinking tumor cells and an overall change in the mechanical properties of the tissue. Future work will include a time-course study of the bacteria concentration within the tumor to experimentally capture any spatial or temporal variation in the diffusion coefficient and growth rate. Nevertheless, the model developed in this work could be used to provide a first-order estimation of the amount of drug delivered by the NanoBEADS. This knowledge would be invaluable to the further development of NanoBEADS towards clinical application for determining appropriate dosages and administration strategies (*i.e.* frequency of



NanoBEADS injections).

To demonstrate the potential use of the model as a predictive tool, 20 simulations were run with each of the four fitted parameters randomly selected from the ranges (average \pm standard deviation) found by fitting the model to experimental data. The resulting curves (Fig. 6.10) well represent the characteristic curves obtained in experiments. It is evident that growth plays a key role in some, while others appear to represent primarily diffusion-based colonization alone. Note that none of these curves have a large “bump” as was obtained in one experimental dataset, likely because D_B and τ_{\min} fit to that data were very different than average values. It may be that such results represent outliers. Coupled with more experimental data, such stochastic simulations could be used to make predictions about tumor colonization and drug delivery with PNBs.

6.5 Conclusion

We propose a simple diffusion-reaction based continuum model of bacterial colonization of *in vitro* tumor spheroids in order to help elucidate the mechanisms that facilitate bacterial penetration and colonization of tumors. We show that this model can reproduce characteristic intratumoral bacterial accumulation curves consistent with the experimental results, based on the assumptions that the necrotic region of the tumor itself acts as a source of diffusing nutrients supporting bacterial growth. The proposed mathematical model suggests that bacterial accumulation is primarily a function of an effective diffusivity and the growth rate of the bacteria. The sensitivity analysis also shows that the agent distribution results are sensitive to changes in these two parameters. Moreover, we show that the effective diffusivity of bacteria and NanoBEADS is approximately two-fold higher than that of nanoparticles alone, thus demonstrating the advantage to using bacteria as nanoparticle carriers. This model can be used

in the future to make predictions of bacterial tumor colonization, design therapeutic strategies, and estimate the drug delivery efficacy.

Chapter 7. Conclusions and future directions

7.1 Concluding remarks

This research has focused on quantitatively investigating the intratumoral transport enhancement of *S. Typhimurium* VNP20009 coupled with a biodegradable copolymer, poly(lactic-co-glycolic acid) nanoparticles, referred to as NanoBEADS (Nanoscale Bacteria Enabled Autonomous Drug Delivery Systems), compared to the conventional passively diffusing nanoparticle-based approach and to identify the factors critically influencing intratumoral transport efficacy. The main accomplishments of this dissertation are: (1) the development of an image-processing algorithm to precisely analyze fluorescently labelled samples in 3D, (2) the investigation of the motility and chemotaxis of the *S. Typhimurium* VNP20009 bacteria used for biomanufacturing of NanoBEADS, (3) the optimization of the NanoBEADS biomanufacturing with development of the microfluidic sorting platform to separate unattached nanoparticles from NanoBEADS via chemotaxis, (4) the evaluation of the intratumoral transport of NanoBEADS compared to a nanoparticle-based approach, and (5) the development of a biophysical model for intratumoral transport of NanoBEADS. A brief description of each accomplishment is presented below:

- **Develop an image processing algorithm to precisely analyze fluorescently labelled samples**

We have developed a simple, semi-automated image processing paradigm for analyzing the distribution of fluorescent objects in microscopy images, particularly useful for z-stacked sets. By applying two calibration steps for the precise quantification regarding size and fluorescent intensity, the number of objects and 3D spatial distribution map were accurately quantified without the use of computationally expensive segmentation algorithms. When the number of

agents, bacteria on a coverslip (n=9), bacteria in tumor spheroids (n=9), or bacteria in a biofilm (n=9), detected by *3DCONFO* were compared with the manual enumeration results, the mean error was estimated to be 2.2 ± 0.9 %. We also demonstrated the robustness and accuracy of the method for analysis of bacterial colonization in tissue, bacterial chemotaxis in a microfluidic channel, the motile fraction of a bacterial population, and the compactness of tumor tissue. This processing routine is widely useful in biomedical research applications due to its simple operation and inexpensive computational cost. The method was implemented in computationally efficient MATLAB software.

- **Investigations of the motility and chemotaxis of the *S. Typhimurium* VNP20009**

The chemotaxis of *S. Typhimurium* VNP20009, recently discovered to be deficient in chemotaxis relative to the parental strain 14028s [56], was investigated to determine if it could be restored by reintroducing chemotaxis-related genes *cheY* and *msbB*, which were lost during construction of the *S. Typhimurium* VNP20009 strain [112]. By restoring the gene *msbB* in VNP20009 *cheY+*, the deletion of which confers attenuation by lipid A modification, we observed a 9% increase in swimming speed, 13% increase in swim plate performance, and 19% increase in chemotaxis performance, as evaluated by partitioning in a microfluidic channel by an optimized chemoattractant concentration gradient.

- **Develop a chemotaxis-based sorting platform for separation of NanoBEADS**

PEGylated biodegradable copolymer poly(lactic-co-glycolic acid) nanoparticles conjugated with VNP20009, called NanoBEADS (Nanoscale bacteria-enabled autonomous drug delivery system) was developed along with optimized fabrication parameters such as the particle-to-bacteria ratio, the zeta potential of streptavidin-coated nanoparticles, and the pore size for centrifugal filters used to separate unoccupied nanoparticles from NanoBEADS. The number of particles attached to bacteria was estimated as 23 ± 16 . For the extended work of separating unoccupied

particles from NanoBEADS, a high-throughput microfluidic sorting platform was developed for the separation of similarly-sized particles by utilizing the chemotaxis of bacteria for the first time through specific and non-specific types of nanoparticle attachment to bacteria. We demonstrate that at the optimum concentration gradient of 5.0×10^{-4} g/ml·mm, a sorting efficiency of up to 81% at a throughput of 2.4×10^5 particles per min can be achieved. The sensitivity of the sorting efficiency to the adhesion mechanism and particle size in the range of 320–1040 nm was investigated.

- **Evaluate the intratumoral transport of NanoBEADS**

The intratumoral transport efficacy of the infecting agents was characterized in an *in vitro* multicellular tumor spheroid models of three cell lines— HCT-116 (colon cancer), U87MG (brain cancer), and 4T1 (breast cancer) and on the tumors of 4T1 breast tumor-bearing mice *in vivo* using two performance indices: the penetration index and a colonization index. Despite the reduced diffusivity due to the larger size of the NanoBEADS compared to the size of nanoparticles, its transport efficacy surpassed that of the nanoparticle, showing that using a bacteria-based penetration mechanism could improve intratumoral penetration of nanoparticles. The weighted penetration index for NanoBEADS exceeded that of nanoparticles by 4.0-fold, 2.6-fold, and 3.0-fold for HCT116, U87MG, and 4T1, respectively. The primary route of intratumoral penetration was shown to be intercellular translocation rather than intracellular invasion, which increases the sensitivity of the intratumoral transport efficacy to the spatial compactness of the tumor, related to the density of ECM materials. Surface treatment with PEG coating enhanced the transport and thus promoted bacterial intercellular penetration. This combined with bacteria proliferation led to even higher colonization and thus greater bacterial intercellular penetration and intracellular uptake. The animal study reaffirmed that the interstitial transport efficacy *in vivo* was also enhanced through bacteria conjugation compared to nanoparticle only approach.

- **Develop a biophysical model for intratumoral transport of NanoBEADS**

We propose a simple diffusion-reaction based continuum model of bacterial colonization of *in vitro* tumor spheroids in order to help elucidate the mechanisms that facilitate bacterial penetration and colonization of tumors. We show that this model can reproduce characteristic intratumoral bacterial accumulation curves consistent with the experimental results, based on the assumptions that the necrotic region of the tumor itself acts as a source of diffusing nutrients supporting bacterial growth. The proposed mathematical model suggests that bacterial accumulation is primarily a function of the diffusivity properties of the tumor microenvironment and the growth rate of the bacteria. The parametric sensitivity analysis also shows that the agent distribution results are sensitive to changes in these two parameters. Moreover, we show that the effective diffusivity of bacteria and NanoBEADS is approximately two-fold higher than that of nanoparticles alone, thus demonstrating the advantage to using bacteria as nanoparticle carriers. This model can be used in the future to make predictions of bacterial tumor colonization, design therapeutic strategies, and estimate the drug delivery efficacy.

7.2 Future Directions

The work presented in this dissertation could be extended to propose possible solutions to pre-existing biological challenges. A few possible directions are outlined below:

1. Further exploration of the intratumoral penetration of NanoBEADS in tumor-bearing mice

The pilot study demonstrated that the chosen experimental parameters, namely the intratumoral administered method of direct injection into the core, dose, and experiment duration of 48 hours, allow for the study of the interstitial transport efficacy *in vivo*. This encourages further exploration of the intratumoral penetration of NanoBEADS in order to quantitatively estimate the enhancement of transport efficacy using the bacteria conjugation strategy over the nanoparticle-only approach.

2. Investigate the effect of the immune response against the linking mechanism between bacteria and particles

As discussed in Chapter 5, *in vivo* results showed that the vascular transport of the agents to the tumor site was not effective presumably due to efficient clearance via the immune response. The suspected key feature provoking the immune response was the linking mechanism, the streptavidin-biotin binding protocol utilized for conjugation between biotinylated antibody-coated bacteria and streptavidin-cy3-coated particles, as well as surface treatment with streptavidin-cy3 and biotinylated PEG. Knowledge of the immune response to the intravenous administration of NanoBEADS constructed using various linking mechanisms, including specific and non-specific adhesion of particles to bacteria, would aid in determining the most appropriate route of infection for studying the transport efficacy *in vivo*.

3. Investigate how the physiological tumor attributes impact bacterial intratumoral transport

The tumor study showed that the results, including bacterial invasion, intratumoral bacterial penetration, and intra/intercellular bacterial fraction, were influenced by the varying physiological traits of different tumor types. The different outcomes were not entirely explained by differences in the compactness based on the cell packing density. It would be tremendously beneficial to identify the underlying mechanisms of bacterial colonization dependencies on physiological features of a tumor, such as the tightness of the tumor, constituents of the tumor tissue, including cell adhesion molecules and the extracellular matrix, angiogenesis, acidosis, hypoxia, etc., in order to select bacteria with the attributes needed for optimal bacteria-enabled tumor treatment. The physiological features of different tumors could be compared with their associated bacterial penetration performances.

References

- [1] R. L. Siegel, K. D. Miller, and A. Jemal, "Cancer statistics, 2017," *CA. Cancer J. Clin.*, vol. 67, no. 1, pp. 7–30, Jan. 2017.
- [2] I. F. Tannock, C. M. Lee, J. K. Tunggal, D. S. M. Cowan, and M. J. Egorin, "Limited Penetration of Anticancer Drugs through Tumor Tissue : A Potential Cause of Resistance of Solid Tumors to Chemotherapy," *Clin. Cancer Res.*, vol. 8, no. March, pp. 878–884, Mar. 2002.
- [3] O. Trédan, C. M. Galmarini, K. Patel, and I. F. Tannock, "Drug resistance and the solid tumor microenvironment," *J. Natl. Cancer Inst.*, vol. 99, no. 19, pp. 1441–1454, Oct. 2007.
- [4] P. A. Netti, D. A. Berk, M. A. Swartz, A. J. Grodzinsky, and R. K. Jain, "Role of extracellular matrix assembly in interstitial transport in solid tumors.," *Cancer Res.*, vol. 60, no. 9, pp. 2497–503, May 2000.
- [5] P. Vaupel, F. Rallinoâ, and P. Okunieff, "Blood Flow , Oxygen and Nutrient Supply , and Metabolic Microenvironment Human Tumors : A Review," *Cancer Res*, vol. 49, no. 23, pp. 6449–6465, 1989.
- [6] Y. Han Bae, K. Park, Y. H. Bae, and K. Park, "Targeted drug delivery to tumors: Myths, reality and possibility," *J. Control. Release*, vol. 153, no. 3, pp. 198–205, Aug. 2011.
- [7] N. S. Forbes, "Profile of a bacterial tumor killer.," *Nat. Biotechnol.*, vol. 24, no. 12, pp. 1484–5, Dec. 2006.
- [8] N. S. Forbes, "Engineering the perfect (bacterial) cancer therapy.," *Nat. Rev. Cancer*, vol. 10, no. 11, pp. 785–94, Nov. 2010.
- [9] J. Toso Gill, V., Hwu, P., Marincola, F., Restifo, N, Schwartzentruber, D, Sherry, R, Topalian, S, Yang, J., Stock, F., Freezer, L., Morton, K., Seipp, C., Haworth, L., Mavroukakis, S., White, D., MacDonald, S., Mao, J., Sznol, M., and Rosenberg, S, "Phase I study of the intravenous administration of attenuated *Salmonella* typhimurium to patients with metastatic melanoma," *J Clin Oncol.*, vol. 20, no. 1, pp. 142–152, 2002.
- [10] S. Leschner and S. Weiss, "*Salmonella* -allies in the fight against cancer.," *J. Mol. Med. (Berl)*., vol. 88, no. 8, pp. 763–73, Aug. 2010.
- [11] S. Ganai, R. B. Arenas, J. P. Sauer, B. Bentley, and N. S. Forbes, "In tumors *Salmonella* migrate away from vasculature toward the transition zone and induce apoptosis.," *Cancer Gene Ther.*, vol. 18, no. 7, pp. 457–66, Jul. 2011.
- [12] American Cancer Society, "Cancer Facts & Figures 2016," *Cancer Facts Fig. 2016*, pp. 1–9, 2016.
- [13] R. Siegel, K. Miller, and A. Jemal, "Cancer statistics , 2015," *CA Cancer J Clin*, vol. 65, no. 1, p. 29, 2015.
- [14] D. Hanahan and R. A. Weinberg, "Hallmarks of cancer: The next generation," *Cell*, vol. 144, no. 5, pp. 646–674, 2011.
- [15] R. A. Gatenby and R. J. Gillies, "Why do cancers have high aerobic glycolysis?," *Nat. Rev. Cancer*, vol. 4, no. 11, pp. 891–899, 2004.
- [16] J. E. Moulder and S. Rockwell, "Tumor hypoxia: its impact on cancer therapy.," *Cancer Metastasis Rev.*, vol. 5, no. 4, pp. 313–41, 1987.

- [17] V. P. Chauhan, T. Stylianopoulos, Y. Boucher, and R. K. Jain, "Delivery of molecular and nanoscale medicine to tumors: transport barriers and strategies.," *Annu. Rev. Chem. Biomol. Eng.*, vol. 2, pp. 281–98, Jan. 2011.
- [18] M. Dean, T. Fojo, and S. Bates, "Tumour stem cells and drug resistance.," *Nat. Rev. Cancer*, vol. 5, no. 4, pp. 275–284, 2005.
- [19] B. a Chabner and T. G. Roberts, "Timeline: Chemotherapy and the war on cancer.," *Nat. Rev. Cancer*, vol. 5, no. 1, pp. 65–72, 2005.
- [20] A. I. Minchinton and I. F. Tannock, "Drug penetration in solid tumours.," *Nat. Rev. Cancer*, vol. 6, no. 8, pp. 583–92, Aug. 2006.
- [21] S. H. Jang, M. G. Wientjes, D. Lu, and J. L.-S. Au, "Drug Delivery and Transport to Solid Tumors," *Pharm. Res.*, vol. 20, no. 9, pp. 1337–1350, Sep. 2003.
- [22] J. Fang, H. Nakamura, and H. Maeda, "The EPR effect: Unique features of tumor blood vessels for drug delivery, factors involved, and limitations and augmentation of the effect.," *Adv. Drug Deliv. Rev.*, vol. 63, no. 3, pp. 136–51, Mar. 2011.
- [23] A. Z. Wang, "EPR or no EPR? The billion-dollar question," *Sci. Transl. Med.*, vol. 7, no. 294, p. 294ec112-294ec112, Jul. 2015.
- [24] H. F. Dvorak, J. A. Nagy, J. T. Dvorak, and A. N. N. M. Dvorak, "Identification and Characterization of the Blood Vessels of Solid Tumors That Are Leaky to Circulating Macromolecules," *Am. J. Pathol.*, vol. 133, no. 1, pp. 95–109, 1988.
- [25] R. H. THOMLINSON and L. H. GRAY, "The histological structure of some human lung cancers and the possible implications for radiotherapy.," *Br. J. Cancer*, vol. 9, no. 4, pp. 539–49, Dec. 1955.
- [26] M. Aspects and M. Ho, "Tumor Hypoxia : Definitions and Current Clinical, , biologic, and molecular aspects.," *J Natl Cancer Inst*, vol. 93, no. 4, 2001.
- [27] L. G. Griffith and M. A. Swartz, "Capturing complex 3D tissue physiology *in vitro*," *Nat. Rev. Mol. Cell Biol.*, vol. 7, no. 3, pp. 211–24, Mar. 2006.
- [28] G. Helmlinger, F. Yuan, M. Dellian, and R. K. Jain, "Interstitial pH and pO₂ gradients in solid tumors *in vivo*: High-resolution measurements reveal a lack of correlation," *Nat. Med.*, vol. 3, no. 2, pp. 177–182, Feb. 1997.
- [29] Deckert, P. M. "Current constructs and targets in clinical development for antibody-based cancer therapy." *Current drug targets* 10.2 (2009): 158-175.
- [30] J. M. Walker, *Bacterial Therapy of Cancer*, vol. 1409. New York, NY: Springer New York, 2016.
- [31] N. S. Forbes, L. L. Munn, D. Fukumura, and R. K. Jain, "Sparse initial entrapment of systemically injected *Salmonella typhimurium* leads to heterogeneous accumulation within tumors," *Cancer Res.*, vol. 63, no. 617, pp. 5188–5193, 2003.
- [32] J. M. Pawelek, K. B. Low, and D. Bermudes, "Bacteria as tumour-targeting vectors.," *Lancet Oncol.*, vol. 4, no. 9, pp. 548–56, Sep. 2003.
- [33] M. Frahm, S. Felgner, D. Kocijancic, M. Rohde, M. Hensel, C. Iii, M. Erhardt, and S. Weiss, "Efficiency of Conditionally Attenuated *Salmonella enterica serovar Typhimurium* in Bacterium-Mediated Tumor Therapy," *MBio*, vol. 6, no. 2, pp. 1–11, 2015.
- [34] N. P. Minton, "Clostridia in cancer therapy.," *Nat. Rev. Microbiol.*, vol. 1, no. 3, pp. 237–42, Dec. 2003.

- [35] K. Yazawa, M. Fujimori, T. Nakamura, T. Sasaki, J. Amano, Y. Kano, and S. Taniguchi, "Bifidobacterium longum as a delivery system for gene therapy of chemically induced rat mammary tumors.," *Breast Cancer Res. Treat.*, vol. 66, no. 2, pp. 165–70, Mar. 2001.
- [36] L. H. Dang, C. Bettegowda, D. L. Huso, K. W. Kinzler, and B. Vogelstein, "Combination bacteriolytic therapy for the treatment of experimental tumors.," *Proc. Natl. Acad. Sci. U. S. A.*, vol. 98, no. 26, pp. 15155–60, 2001.
- [37] D. Bermudes, M. Belcourt, M. Ittensohn, I. King, W. Lang, T. Le, Z. Li, S. L. Lin, X. Luo, J. Mao, J. Pike, J. D. Runyab, K. Troy, and L. Zheng, "Tumor-Targeted *Salmonella* Expressing Cytosine Deaminase as an Anticancer Agent." Mary Ann Liebert, Inc., 01-Jul-2012.
- [38] Y. Zhang, Y. Zhang, L. Xia, X. Zhang, X. Ding, F. Yan, and F. Wu, "*Escherichia coli* Nissle 1917 targets and restrains mouse b16 melanoma and 4T1 breast tumors through expression of azurin protein," *Appl. Environ. Microbiol.*, vol. 78, no. 21, pp. 7603–7610, 2012.
- [39] Z. K. Pan, L. M. Weiskirch, and Y. Paterson, "Regression of established B16F10 melanoma with a recombinant *Listeria monocytogenes* vaccine.," *Cancer Res.*, vol. 59, no. 20, pp. 5264–9, Oct. 1999.
- [40] G. V Gill, A. Holden, and J. C. Oncol, "A malignant pleural effusion infected with *Salmonella enteritidis*," *Thorax*, vol. 51, no. 1, pp. 104–105, Jan. 1985.
- [41] Strain, Genetically Stable Antibiotic-Sensitive. "Construction of VNP20009." *Suicide Gene Therapy: Methods and Reviews* 90 (2004): 47.
- [42] K. B. Low, M. Ittensohn, T. Le, J. Platt, S. Sodi, M. Amoss, O. Ash, E. Carmichael, a Chakraborty, J. Fischer, S. L. Lin, X. Luo, S. I. Miller, L. Zheng, I. King, J. M. Pawelek, and D. Bermudes, "Lipid A mutant *Salmonella* with suppressed virulence and TNFalpha induction retain tumor-targeting *in vivo*." *Nat. Biotechnol.*, vol. 17, no. 1, pp. 37–41, Jan. 1999.
- [43] M. Zhao, M. Yang, X.-M. Li, P. Jiang, E. Baranov, S. Li, M. Xu, S. Penman, and R. M. Hoffman, "Tumor-targeting bacterial therapy with amino acid auxotrophs of GFP-expressing *Salmonella typhimurium*." *Proc. Natl. Acad. Sci. U. S. A.*, vol. 102, no. 3, pp. 755–60, Jan. 2005.
- [44] M. Zhao, M. Yang, H. Ma, X. Li, X. Tan, S. Li, Z. Yang, and R. M. Hoffman, "Targeted therapy with a *Salmonella typhimurium* leucine-arginine auxotroph cures orthotopic human breast tumors in nude mice.," *Cancer Res.*, vol. 66, no. 15, pp. 7647–52, Aug. 2006.
- [45] Pawelek, John M., K. Brooks Low, and David Bermudes. "Tumor-targeted *Salmonella* as a novel anticancer vector." *Cancer research* 57.20 (1997): 4537-4544.
- [46] C. Clairmont, K. C. Lee, J. Pike, M. Ittensohn, K. B. Low, J. Pawelek, D. Bermudes, S. M. Brecher, D. Margitich, J. Turnier, Z. Li, X. Luo, I. King, and L. M. Zheng, "Biodistribution and genetic stability of the novel antitumor agent VNP20009, a genetically modified strain of *Salmonella typhimurium*." *J. Infect. Dis.*, vol. 181, no. 6, pp. 1996–2002, Jun. 2000.
- [47] J. Nemunaitis, C. Cunningham, N. Senzer, J. Kuhn, J. Cramm, C. Litz, R. Cavagnolo, A. Cahill, C. Clairmont, and M. Sznol, "Pilot trial of genetically modified, attenuated *Salmonella* expressing the *E. coli* cytosine deaminase gene in refractory cancer patients," *Cancer Gene Ther.*, vol. 10, no. 10, pp. 737–744, Oct. 2003.
- [48] J. Stritzker, S. Weibel, C. Seubert, A. Götz, A. Tresch, N. van Rooijen, T. a Oelschlaeger, P. J. Hill, I. Gentshev, and A. a Szalay, "Enterobacterial tumor colonization in mice

- depends on bacterial metabolism and macrophages but is independent of chemotaxis and motility.," *Int. J. Med. Microbiol.*, vol. 300, no. 7, pp. 449–56, Nov. 2010.
- [49] R. W. Kasinskas and N. S. Forbes, "Salmonella typhimurium specifically chemotax and proliferate in heterogeneous tumor tissue *in vitro*," *Biotechnol. Bioeng.*, vol. 94, no. 4, pp. 710–721, Jul. 2006.
- [50] K. Crull, M. Rohde, K. Westphal, H. Loessner, K. Wolf, A. Felipe-López, M. Hensel, and S. Weiss, "Biofilm formation by *Salmonella enterica* serovar Typhimurium colonizing solid tumours.," *Cell. Microbiol.*, vol. 13, no. 8, pp. 1223–33, Aug. 2011.
- [51] K. M. Broadway, E. a. P. Denson, R. V. Jensen, and B. E. Scharf, "Rescuing chemotaxis of the anticancer agent *Salmonella enterica* serovar Typhimurium VNP20009," *J. Biotechnol.*, vol. 211, pp. 117–120, 2015.
- [52] M. A. Traore and B. Behkam, "A PEG-DA microfluidic device for chemotaxis studies," *J. Micromechanics Microengineering*, vol. 23, p. 85014, 2013.
- [53] N. Bonnet, "Some trends in microscope image processing," *Micron*, vol. 35, no. 8, pp. 635–653, 2004.
- [54] G. Lin, U. Adiga, K. Olson, J. F. Guzowski, C. a Barnes, and B. Roysam, "A hybrid 3D watershed algorithm incorporating gradient cues and object models for automatic segmentation of nuclei in confocal image stacks.," *Cytometry. A*, vol. 56, no. 1, pp. 23–36, 2003.
- [55] C. Wahlby, I. M. Sintorn, F. Erlandsson, G. Borgefors, and E. Bengtsson, "Combining intensity, edge and shape informations for 2D and 3D segmentation of cell nuclei in tissue sections," *J. Microsc.*, vol. 215, no. January, pp. 67–76, 2004.
- [56] H. Daims, S. Lückner, and M. Wagner, "Daime, a Novel Image Analysis Program for Microbial Ecology and Biofilm Research," *Environ. Microbiol.*, vol. 8, no. 2, pp. 200–213, 2006.
- [57] E. Hodneland, T. Kögel, D. M. Frei, H.-H. Gerdes, and A. Lundervold, "CellSegm - a MATLAB toolbox for high-throughput 3D cell segmentation.," *Source Code Biol. Med.*, vol. 8, no. 1, p. 16, 2013.
- [58] V. Wiesmann, D. Franz, C. Held, C. Munzenmayer, R. Palmisano, and T. Wittenberg, "Review of free software tools for image analysis of fluorescence cell micrographs," *J. Microsc.*, vol. 257, no. 1, pp. 39–53, 2015.
- [59] S. Suh, M. A. Traore, and B. Behkam, "Bacterial chemotaxis-enabled autonomous sorting of nanoparticles of comparable sizes," *Lab Chip*, vol. 16, no. 7, pp. 1254–1260, 2016.
- [60] H. Mao, P. S. Cremer, and M. D. Manson, "A sensitive, versatile microfluidic assay for bacterial chemotaxis," *Proc. Natl. Acad. Sci. USA*, vol. 100, pp. 5449–5454, 2003.
- [61] R. Grantab, S. Sivananthan, and I. F. Tannock, "The penetration of anticancer drugs through tumor tissue as a function of cellular adhesion and packing density of tumor cells," *Cancer Res.*, vol. 66, no. 2, pp. 1033–1039, 2006.
- [62] S. C. Nallar, D.-Q. Xu, and D. V Kalvakolanu, "Bacteria and genetically modified bacteria as cancer therapeutics: Current advances and challenges.," *Cytokine*, Jan. 2016.
- [63] J. M. Pawelek, K. B. Low, and D. Bermudes, "Tumor-targeted *Salmonella* as a Novel Anticancer Vector," *Cancer Res.*, vol. 57, pp. 4537–4544, 1997.
- [64] M. Zhao, M. Yang, X. M. Li, P. Jiang, E. Baranov, S. Li, M. Xu, S. Penman, R. M. Hoffman, and D. L. Trump, "Tumor-targeting bacterial therapy with amino acid auxotrophs

- of GFP-expressing *Salmonella typhimurium*,” *Urol. Oncol. Semin. Orig. Investig.*, vol. 23, no. 5, p. 380, 2005.
- [65] M. Zhao, J. Geller, H. Ma, M. Yang, S. Penman, and R. M. Hoffman, “Monotherapy with a tumor-targeting mutant of *Salmonella typhimurium* cures orthotopic metastatic mouse models of human prostate cancer.,” *Proc. Natl. Acad. Sci. U. S. A.*, vol. 104, no. 24, pp. 10170–4, Jun. 2007.
- [66] Y. Hiroshima, M. Zhao, Y. Zhang, A. Maawy, M. Hassanein, F. Uehara, S. Miwa, S. Yano, M. Momiyama, A. Suetsugu, T. Chishima, K. Tanaka, M. Bouvet, I. Endo, and R. M. Hoffman, “Comparison of efficacy of *Salmonella typhimurium* A1-R and chemotherapy on stem-like and non-stem human pancreatic cancer cells,” *Cell Cycle*, vol. 12, no. 17, pp. 2774–2780, Sep. 2013.
- [67] R. M. Hoffman, “Tumor-Targeting *Salmonella typhimurium* A1-R: An Overview,” in *Methods in molecular biology (Clifton, N.J.)*, vol. 1409, 2016, pp. 1–8.
- [68] Y. Hiroshima, Y. Zhang, T. Murakami, A. Maawy, S. Miwa, M. Yamamoto, S. Yano, S. Sato, M. Momiyama, R. Mori, R. Matsuyama, T. Chishima, K. Tanaka, Y. Ichikawa, M. Bouvet, I. Endo, M. Zhao, and R. M. Hoffman, “Efficacy of tumor-targeting *Salmonella typhimurium* A1-R in combination with anti-angiogenesis therapy on a pancreatic cancer patient-derived orthotopic xenograft (PDOX) and cell line mouse models.,” *Oncotarget*, vol. 5, no. 23, pp. 12346–57, Dec. 2014.
- [69] S. Yano, Y. Zhang, M. Zhao, Y. Hiroshima, S. Miwa, F. Uehara, H. Kishimoto, H. Tazawa, M. Bouvet, T. Fujiwara, and R. M. Hoffman, “Tumor-targeting *Salmonella typhimurium* A1-R decoys quiescent cancer cells to cycle as visualized by FUCCI imaging and become sensitive to chemotherapy,” *Cell Cycle*, vol. 13, no. 24, pp. 3958–3963, Dec. 2014.
- [70] Murakami, Takashi, et al. "Tumor-targeting *Salmonella typhimurium* A1-R in combination with doxorubicin eradicate soft tissue sarcoma in a patient-derived orthotopic xenograft (PDOX) model." *Oncotarget* 7.11 (2016): 12783.
- [71] Kawaguchi, Kei, et al. "Tumor-targeting *Salmonella typhimurium* A1-R combined with temozolomide regresses malignant melanoma with a BRAF-V600E mutation in a patient-derived orthotopic xenograft (PDOX) model." *Oncotarget* 7.52 (2016): 85929.
- [72] W. Yoon, J. H. Choi, S. Kim, and Y. K. Park, “Engineered *Salmonella typhimurium* expressing E7 fusion protein, derived from human papillomavirus, inhibits tumor growth in cervical tumor-bearing mice,” *Biotechnol. Lett.*, vol. 36, no. 2, pp. 349–356, Feb. 2014.
- [73] B. K. al-Ramadi, M. J. Fernandez-Cabezudo, H. El-Hasasna, S. Al-Salam, G. Bashir, and S. Chouaib, “Potent anti-tumor activity of systemically-administered IL2-expressing *Salmonella* correlates with decreased angiogenesis and enhanced tumor apoptosis,” *Clin. Immunol.*, vol. 130, no. 1, pp. 89–97, Jan. 2009.
- [74] D. A. Saltzman, C. P. Heise, D. E. Hasz, M. Zebede, S. M. Kelly, R. Curtiss, A. S. Leonard, and P. M. Anderson, “Attenuated *Salmonella typhimurium* Containing Interleukin-2 Decreases MC-38 Hepatic Metastases: A Novel Anti-tumor Agent,” *Cancer Biother. Radiopharm.*, vol. 11, no. 2, pp. 145–153, Apr. 1996.
- [75] A. Eisenstark, R. A. Kazmierczak, A. Dino, R. Khreis, D. Newman, and H. Schatten, “Development of *Salmonella* Strains as Cancer Therapy Agents and Testing in Tumor Cell Lines,” in *Methods in molecular biology (Clifton, N.J.)*, vol. 394, 2007, pp. 323–354.
- [76] S.-N. Jiang, S.-H. Park, H. J. Lee, J. H. Zheng, H.-S. Kim, H.-S. Bom, Y. Hong, M. Szardenings, M. G. Shin, S.-C. Kim, V. Ntziachristos, H. E. Choy, and J.-J. Min,

- “Engineering of Bacteria for the Visualization of Targeted Delivery of a Cytolytic Anticancer Agent,” *Mol. Ther.*, vol. 21, no. 11, pp. 1985–1995, Nov. 2013.
- [77] J.-E. Kim, T. X. Phan, V. H. Nguyen, H.-V. Dinh-Vu, J. H. Zheng, M. Yun, S.-G. Park, Y. Hong, H. E. Choy, M. Szardenings, W. Hwang, J.-A. Park, S. Park, S.-H. Im, and J.-J. Min, “*Salmonella typhimurium* Suppresses Tumor Growth via the Pro-Inflammatory Cytokine Interleukin-1 β ,” *Theranostics*, vol. 5, no. 12, pp. 1328–42, 2015.
- [78] V. H. Nguyen, H.-S. Kim, J.-M. Ha, Y. Hong, H. E. Choy, and J.-J. Min, “Genetically engineered *Salmonella typhimurium* as an imageable therapeutic probe for cancer,” *Cancer Res.*, vol. 70, no. 1, pp. 18–23, Jan. 2010.
- [79] L. Zhang, L. Gao, L. Zhao, B. Guo, K. Ji, Y. Tian, J. Wang, H. Yu, J. Hu, D. V. Kalvakolanu, D. J. Kopecko, X. Zhao, and D.-Q. Xu, “Intratumoral Delivery and Suppression of Prostate Tumor Growth by Attenuated *Salmonella enterica serovar typhimurium* Carrying Plasmid-Based Small Interfering RNAs,” *Cancer Res.*, vol. 67, no. 12, pp. 5859–5864, Jun. 2007.
- [80] J. L. VanCott, S. N. Chatfield, M. Roberts, D. M. Hone, E. L. Hohmann, D. W. Pascual, M. Yamamoto, H. Kiyono, and J. R. McGhee, “Regulation of host immune responses by modification of *Salmonella virulence genes*,” *Nat. Med.*, vol. 4, no. 11, pp. 1247–1252, Nov. 1998.
- [81] H. Jia, Y. Li, T. Zhao, X. Li, J. Hu, D. Yin, B. Guo, D. J. Kopecko, X. Zhao, L. Zhang, and D. Q. Xu, “Antitumor effects of Stat3-siRNA and endostatin combined therapies, delivered by attenuated *Salmonella*, on orthotopically implanted hepatocarcinoma,” *Cancer Immunol. Immunother.*, vol. 61, no. 11, pp. 1977–1987, Nov. 2012.
- [82] S. Grille, M. Moreno, T. Bascuas, J. M. Marqués, N. Muñoz, D. Lens, and J. A. Chabalgoity, “*Salmonella enterica serovar Typhimurium* immunotherapy for B-cell lymphoma induces broad anti-tumour immunity with therapeutic effect,” *Immunology*, vol. 143, no. 3, pp. 428–437, Nov. 2014.
- [83] E. R. Manuel, C. A. Blache, R. Paquette, T. I. Kaltcheva, H. Ishizaki, J. D. I. Ellenhorn, M. Hensel, L. Metelitsa, and D. J. Diamond, “Enhancement of Cancer Vaccine Therapy by Systemic Delivery of a Tumor-Targeting *Salmonella*-Based STAT3 shRNA Suppresses the Growth of Established Melanoma Tumors,” *Cancer Res.*, vol. 71, no. 12, pp. 4183–4191, Jun. 2011.
- [84] X. Xu, W. A. H. Hegazy, L. Guo, X. Gao, A. N. Courtney, S. Kurbanov, D. Liu, G. Tian, E. R. Manuel, D. J. Diamond, M. Hensel, and L. S. Metelitsa, “Effective Cancer Vaccine Platform Based on Attenuated *Salmonella* and a Type III Secretion System,” *Cancer Res.*, vol. 74, no. 21, pp. 6260–6270, Nov. 2014.
- [85] G. Xiong, M. I. Husseiny, L. Song, A. Erdreich-Epstein, G. M. Shackelford, R. C. Seeger, D. Jäckel, M. Hensel, and L. S. Metelitsa, “Novel cancer vaccine based on genes of *Salmonella pathogenicity Island 2*,” *Int. J. Cancer*, vol. 126, no. 11, p. NA-NA, Jun. 2009.
- [86] R. Xiang, N. Mizutani, Y. Luo, C. Chiodoni, H. Zhou, M. Mizutani, Y. Ba, J. C. Becker, and R. A. Reisfeld, “A DNA vaccine targeting survivin combines apoptosis with suppression of angiogenesis in lung tumor eradication,” *Cancer Res.*, vol. 65, no. 2, pp. 553–61, Jan. 2005.
- [87] S.-H. Lee, N. Mizutani, M. Mizutani, Y. Luo, H. Zhou, C. Kaplan, S.-W. Kim, R. Xiang, and R. A. Reisfeld, “Endoglin (CD105) is a target for an oral DNA vaccine against breast cancer,” *Cancer Immunol. Immunother.*, vol. 55, no. 12, pp. 1565–1574, Dec. 2006.

- [88] B.-J. Qian, F. Yan, N. Li, Q.-L. Liu, Y.-H. Lin, C.-M. Liu, Y.-P. Luo, F. Guo, and H.-Z. Li, "MTDH/AEG-1-based DNA vaccine suppresses lung metastasis and enhances chemosensitivity to doxorubicin in breast cancer," *Cancer Immunol. Immunother.*, vol. 60, no. 6, pp. 883–893, Jun. 2011.
- [89] B. Chirullo, S. Ammendola, L. Leonardi, R. Falcini, P. Petrucci, C. Pistoia, S. Vendetti, A. Battistoni, and P. Pasquali, "Attenuated mutant strain of *Salmonella* Typhimurium lacking the ZnuABC transporter contrasts tumor growth promoting anti-cancer immune response," *Oncotarget*, vol. 6, no. 19, pp. 17648–17660, Jul. 2015.
- [90] E. Roeder, S. Jellbauer, B. Köhn, C. Berchtold, M. Partilla, D. H. Busch, H. Rüssmann, and K. Panthel, "Invasion and destruction of a murine fibrosarcoma by *Salmonella*-induced effector CD8 T cells as a therapeutic intervention against cancer," *Cancer Immunol. Immunother.*, vol. 60, no. 3, pp. 371–380, Mar. 2011.
- [91] C.-S. Lin, S.-H. Kao, Y.-C. Chen, C.-H. Li, Y.-T. Hsieh, S.-C. Yang, C.-J. Wu, R.-P. Lee, and K.-W. Liao, "Enhancement of anti-murine colon cancer immunity by fusion of a SARS fragment to a low-immunogenic carcinoembryonic antigen," *Biol. Proced. Online*, vol. 14, no. 1, p. 2, Feb. 2012.
- [92] C. Jin, Y. Liu, J. Zhu, T. Xia, B. Zhang, Y. Fei, B. Ma, J. Ye, and W. Chen, "Recombinant *Salmonella*-based CEACAM6 and 4-1BBL vaccine enhances T-cell immunity and inhibits the development of colorectal cancer in rats: *In vivo* effects of vaccine containing 4-1BBL and CEACAM6," *Oncol. Rep.*, vol. 33, no. 6, pp. 2837–44, Apr. 2015.
- [93] M. Jarosz, J. Jazowiecka-Rakus, T. Cichoń, M. Głowala-Kosińska, R. Smolarczyk, A. Smagur, S. Malina, A. Sochanik, and S. Szala, "Therapeutic antitumor potential of endoglin-based DNA vaccine combined with immunomodulatory agents," *Gene Ther.*, vol. 20, no. 3, pp. 262–273, Mar. 2013.
- [94] Z. Li, P.-H. Yin, S.-S. Yang, Q.-Y. Li, T. Chang, L. Fang, L.-X. Shi, and G.-E. Fang, "Recombinant attenuated *Salmonella* typhimurium carrying a plasmid co-expressing ENDO-VEG151 and survivin siRNA inhibits the growth of breast cancer *in vivo*," *Mol. Med. Rep.*, vol. 7, no. 4, pp. 1215–22, Feb. 2013.
- [95] L. Shi, B. Yu, C.-H. Cai, W. Huang, B.-J. Zheng, D. K. Smith, and J.-D. Huang, "Combined prokaryotic–eukaryotic delivery and expression of therapeutic factors through a primed autocatalytic positive-feedback loop," *J. Control. Release*, vol. 222, pp. 130–140, Jan. 2016.
- [96] E. Berger, R. Soldati, N. Huebener, O. Hohn, A. Stermann, T. Durmus, S. Lobitz, A. C. Zenclussen, H. Christiansen, H. N. Lode, and S. Fest, "*Salmonella* SL7207 application is the most effective DNA vaccine delivery method for successful tumor eradication in a murine model for neuroblastoma," *Cancer Lett.*, vol. 331, no. 2, pp. 167–173, May 2013.
- [97] C.-X. Li, B. Yu, L. Shi, W. Geng, Q.-B. Lin, C.-C. Ling, M. Yang, K. T. P. Ng, J.-D. Huang, and K. Man, "'Obligate' anaerobic *Salmonella* strain YB1 suppresses liver tumor growth and metastasis in nude mice.," *Oncol. Lett.*, vol. 13, no. 1, pp. 177–183, Jan. 2017.
- [98] B. Yu, L. Shi, B.-Z. Zhang, K. E. Zhang, X. Peng, H.-B. Niu, and J.-L. Qu, "Obligate anaerobic *Salmonella* typhimurium strain YB1 treatment on xenograft tumor in immunocompetent mouse model.," *Oncol. Lett.*, vol. 10, no. 2, pp. 1069–1074, Aug. 2015.
- [99] K. B. Low, M. Ittensohn, X. Luo, L.-M. Zheng, I. King, J. M. Pawelek, and D. Bermudes, "Construction of VNP20009: a novel, genetically stable antibiotic-sensitive strain of tumor-targeting *Salmonella* for parenteral administration in humans.," *Methods Mol. Med.*, vol. 90, pp. 47–60, 2004.

- [100] K. C. Lee, L.-M. Zheng, X. Luo, C. Clairmont, J. Fischer, D. Margitich, J. Turnier, B. Almassian, D. Bermudes, and I. King, "Comparative Evaluation of the Acute Toxic Effects in Monkeys, Pigs and Mice of a Genetically Engineered *Salmonella* Strain (VNP20009) Being Developed as an Antitumor Agent," *Int. J. Toxicol.*, vol. 19, no. 1, pp. 19–25, Jan. 2000.
- [101] D. H. Thamm, I. D. Kurzman, I. King, Z. Li, M. Sznol, R. R. Dubielzig, D. M. Vail, and E. G. MacEwen, "Systemic administration of an attenuated, tumor-targeting *Salmonella* typhimurium to dogs with spontaneous neoplasia: phase I evaluation.," *Clin. Cancer Res.*, vol. 11, no. 13, pp. 4827–34, Jul. 2005.
- [102] J. F. Toso, V. J. Gill, P. Hwu, F. M. Marincola, N. P. Restifo, D. J. Schwartzentruber, R. M. Sherry, S. L. Topalian, J. C. Yang, F. Stock, L. J. Freezer, K. E. Morton, C. Seipp, L. Haworth, S. Mavroukakis, D. White, S. MacDonald, J. Mao, M. Sznol, and S. a Rosenberg, "Phase I study of the intravenous administration of attenuated *Salmonella* typhimurium to patients with metastatic melanoma.," *J. Clin. Oncol.*, vol. 20, no. 1, pp. 142–52, Jan. 2002.
- [103] K. Crull, D. Bumann, and S. Weiss, "Influence of infection route and virulence factors on colonization of solid tumors by *Salmonella enterica* serovar Typhimurium," *FEMS Immunol. Med. Microbiol.*, vol. 62, no. 1, pp. 75–83, 2011.
- [104] P. Chorobik, D. Czaplicki, K. Ossysek, and J. Bereta, "*Salmonella* and cancer: from pathogens to therapeutics.," *Acta Biochim. Pol.*, vol. 60, no. 3, pp. 285–97, 2013.
- [105] R. W. Kasinskas and N. S. Forbes, "*Salmonella* typhimurium lacking ribose chemoreceptors localize in tumor quiescence and induce apoptosis.," *Cancer Res.*, vol. 67, no. 7, pp. 3201–9, Apr. 2007.
- [106] Silva-Valenzuela, Cecilia A., et al. "Solid tumors provide niche-specific conditions that lead to preferential growth of *Salmonella*." *Oncotarget* 7.23 (2016): 35169.
- [107] K. M. Broadway, E. A. P. Denson, R. V Jensen, and B. E. Scharf, "Rescuing chemotaxis of the anticancer agent *Salmonella enterica* serovar Typhimurium VNP20009," *J. Biotechnol.*, vol. 211, pp. 117–120, 2015.
- [108] "[https://www.cancer.gov/publications/dictionaries/cancer-drug?cdrid=37800.](https://www.cancer.gov/publications/dictionaries/cancer-drug?cdrid=37800)" [Online]. Available: [https://www.cancer.gov/publications/dictionaries/cancer-drug?cdrid=37800.](https://www.cancer.gov/publications/dictionaries/cancer-drug?cdrid=37800) [Accessed: 14-Apr-2017].
- [109] S. R. Murray, D. Bermudes, K. S. de Felipe, and K. B. Low, "Extragenic suppressors of growth defects in msbB *Salmonella*," *J. Bacteriol.*, vol. 183, no. 19, pp. 5554–61, Oct. 2001.
- [110] J. E. Karlinsey, "λ-Red Genetic Engineering in *Salmonella enterica* serovar Typhimurium," *Methods Enzymol.*, vol. 421, pp. 199–209, 2007.
- [111] K. A. Datsenko and B. L. Wanner, "One-step inactivation of chromosomal genes in *Escherichia coli* K-12 using PCR products.," *Proc. Natl. Acad. Sci. U. S. A.*, vol. 97, no. 12, pp. 6640–5, 2000.
- [112] K. M. Broadway, T. Modise, R. V. Jensen, and B. E. Scharf, "Complete genome sequence of *Salmonella enterica* serovar Typhimurium VNP20009, a strain engineered for tumor targeting," *J. Biotechnol.*, vol. 192, no. Part A, pp. 177–178, 2014.
- [113] G. BERTANI, "Studies on lysogenesis. I. The mode of phage liberation by lysogenic *Escherichia coli*," *J. Bacteriol.*, vol. 62, no. 3, pp. 293–300, Sep. 1951.

- [114] L. Turner, W. S. Ryu, and H. C. Berg, "Real-time imaging of fluorescent flagellar filaments.," *J. Bacteriol.*, vol. 182, no. 10, pp. 2793–801, May 2000.
- [115] K. B. Low, S. R. Murray, J. Pawelek, and D. Bermudes, "Isolation and Analysis of Suppressor Mutations in Tumor-Targeted *msbB* *Salmonella*," in *Methods in molecular biology (Clifton, N.J.)*, vol. 1409, 2016, pp. 95–123.
- [116] U. Attmannspacher, B. E. Scharf, and R. M. Harshey, "FliL is essential for swarming: Motor rotation in absence of FliL fractures the flagellar rod in swarmer cells of *Salmonella enterica*," *Mol. Microbiol.*, vol. 68, no. 2, pp. 328–341, 2008.
- [117] "A Phase 1 Study of an IL-2 Expressing, Attenuated *Salmonella* Typhimurium in Patients With Unresectable Hepatic Spread From Any Non-Hematologic Primary," *NCT01099631*. [Online]. Available: <https://clinicaltrials.gov/ct2/show/NCT01099631>. [Accessed: 14-Apr-2017].
- [118] J. E. Somerville, L. Cassiano, B. Bainbridge, M. D. Cunningham, R. P. Darveau, and R. P. Darveau, "A novel *Escherichia coli* lipid A mutant that produces an antiinflammatory lipopolysaccharide.," *J. Clin. Invest.*, vol. 97, no. 2, pp. 359–65, Jan. 1996.
- [119] S. R. Murray, K. S. de Felipe, P. L. Obuchowski, J. Pike, D. Bermudes, and K. B. Low, "Hot spot for a large deletion in the 18- to 19-centisome region confers a multiple phenotype in *Salmonella enterica* serovar Typhimurium strain ATCC 14028.," *J. Bacteriol.*, vol. 186, no. 24, pp. 8516–23, Dec. 2004.
- [120] C. Tam and D. Missiakas, "Changes in lipopolysaccharide structure induce the σ E-dependent response of *Escherichia coli*," *Mol. Microbiol.*, vol. 55, no. 5, pp. 1403–1412, Jan. 2005.
- [121] H. Skovierova, G. Rowley, B. Rezuchova, D. Homerova, C. Lewis, M. Roberts, and J. Kormanec, "Identification of the E regulon of *Salmonella enterica* serovar Typhimurium," *Microbiology*, vol. 152, no. 5, pp. 1347–1359, May 2006.
- [122] S. Felgner, M. Frahm, D. Kocijancic, M. Rohde, D. Eckweiler, A. Bielecka, and E. Bueno, "aroA -Deficient *Salmonella enterica* serovar Typhimurium Is More Than a Metabolically Attenuated Mutant," vol. 7, no. 5, pp. 1–12, 2016.
- [123] S. Leschner, K. Westphal, N. Dietrich, N. Viegas, J. Jablonska, M. Lyszkiewicz, S. Lienenklaus, W. Falk, N. Gekara, H. Loessner, and S. Weiss, "Tumor invasion of *Salmonella enterica* serovar Typhimurium is accompanied by strong hemorrhage promoted by TNF-alpha.," *PLoS One*, vol. 4, no. 8, p. e6692, Jan. 2009.
- [124] You Han Baea. Kinam Parkb, "Targeted drug delivery to tumors: Myths, reality and possibility," *J Control Release*, vol. 153, no. 3, pp. 198–205, 2011.
- [125] D. R. Gossett, W. M. Weaver, A. J. Mach, S. C. Hur, H. T. K. Tse, W. Lee, H. Amini, and D. Di Carlo, "Label-free cell separation and sorting in microfluidic systems.," *Anal. Bioanal. Chem.*, vol. 397, no. 8, pp. 3249–67, Aug. 2010.
- [126] P. Sajeesh and A. K. Sen, "Particle separation and sorting in microfluidic devices: a review," *Microfluid. Nanofluidics*, vol. 17, no. 1, pp. 1–52, Nov. 2013.
- [127] P. Jákł, T. Čižmár, M. Šerý, and P. Zemánek, "Static optical sorting in a laser interference field," *Appl. Phys. Lett.*, vol. 92, no. 16, p. 161110, 2008.
- [128] S. S. Kuntaegowdanahalli, A. A. S. Bhagat, G. Kumar, and I. Papautsky, "Inertial microfluidics for continuous particle separation in spiral microchannels.," *Lab Chip*, vol. 9, no. 20, pp. 2973–80, Oct. 2009.

- [129] M. Masaeli, E. Sollier, H. Amini, W. Mao, K. Camacho, N. Doshi, S. Mitragotri, A. Alexeev, and D. Di Carlo, "Continuous Inertial Focusing and Separation of Particles by Shape," *Phys. Rev. X*, vol. 2, no. 3, p. 31017, Sep. 2012.
- [130] T. Morijiri, S. Sunahiro, M. Senaha, M. Yamada, and M. Seki, "Sedimentation pinched-flow fractionation for size- and density-based particle sorting in microchannels," *Microfluid. Nanofluidics*, vol. 11, no. 1, pp. 105–110, Mar. 2011.
- [131] S. Fiedler, S. G. Shirley, T. Schnelle, and G. Fuhr, "Dielectrophoretic Sorting of Particles and Cells in a Microsystem," *Anal. Chem.*, vol. 70, no. 9, pp. 1909–1915, May 1998.
- [132] T. Laurell, F. Petersson, and A. Nilsson, "Chip integrated strategies for acoustic separation and manipulation of cells and particles.," *Chem. Soc. Rev.*, vol. 36, no. 3, pp. 492–506, 2007.
- [133] S. Choi and J.-K. Park, "Continuous hydrophoretic separation and sizing of microparticles using slanted obstacles in a microchannel.," *Lab Chip*, vol. 7, no. 7, pp. 890–897, 2007.
- [134] A. Y. Fu, C. Spence, A. Scherer, F. H. Arnold, and S. R. Quake, "A microfabricated fluorescence-activated cell sorter.," *Nat. Biotechnol.*, vol. 17, no. 11, pp. 1109–11, Nov. 1999.
- [135] M. M. Wang, E. Tu, D. E. Raymond, J. M. Yang, H. Zhang, N. Hagen, B. Dees, E. M. Mercer, A. H. Forster, I. Kariv, P. J. Marchand, and W. F. Butler, "Microfluidic sorting of mammalian cells by optical force switching," *Nat. Biotechnol.*, vol. 23, no. 1, pp. 83–87, Dec. 2004.
- [136] J. Xi, J. Schmidt, and C. Montemagno, "Self assembled microdevices driven by muscle," *Nat. Mater.*, vol. 4, pp. 180–184, 2005.
- [137] D. B. Weibel, P. Garstecki, D. Ryan, W. R. DiLuzio, M. Mayer, J. E. Seto, G. M. Whitesides, and D. Weibel Garstecki, P., Ryan, D., DiLuzio, W.R., Mayer, M., Seto, J.E., and Whitesides, G.M., "Microoxen: Microorganisms to move microscale loads," *Proc. Natl. Acad. Sci. USA*, vol. 102, pp. 11963–11967, 2005.
- [138] N. Darnton, L. Turner, K. Breuer, and H. Berg, "Moving Fluid with Bacterial Carpets," *Biophys. J.*, vol. 86, pp. 1863–1870, Mar. 2004.
- [139] B. Behkam and M. Sitti, "Bacterial flagella-based propulsion and on/off motion control of microscale objects," *Appl. Phys. Lett.*, vol. 90, p. 23902, 2007.
- [140] M. Steager, E., Kim, C., Patel, J., Bith, S., Naik, C., Reber, L. and Kim, "Control of microfabricated structures powered by flagellated bacteria using phototaxis," *Appl. Phys. Lett.*, vol. 90, p. 263901, 2007.
- [141] G. Martel, S. Tremblay, C., Ngakeng, S., Langlois, "Controlled manipulation and actuation of micro-objects with magnetotactic bacteria," *Appl. Phys. Lett.*, vol. 89, p. 233804, 2006.
- [142] M. A. Traoré, A. Sahari, and B. Behkam, "Computational and experimental study of chemotaxis of an ensemble of bacteria attached to a microbead.," *Phys. Rev. E*, vol. 84, no. 6, p. 61908, Dec. 2011.
- [143] A. Sahari, M. A. Traore, B. E. Scharf, and B. Behkam, "Directed transport of bacteria-based drug delivery vehicles: bacterial chemotaxis dominates particle shape.," *Biomed. Microdevices*, vol. 16, pp. 717–725, Jun. 2014.
- [144] S. Martel and M. Mohammadi, "Using a Swarm of Self-propelled Natural Microrobots in the Form of Flagellated Bacteria to Perform Complex Micro-assembly Tasks," in *IEEE International Conference on Robotics and Automation*, 2010, pp. 500–505.

- [145] C. S. Barker, B. M. Prüss, and P. Matsumura, "Increased motility of *Escherichia coli* by insertion sequence element integration into the regulatory region of the *flhD* operon.," *J. Bacteriol.*, vol. 186, no. 22, pp. 7529–37, Nov. 2004.
- [146] J. S. Parkinson and S. E. Houts, "Isolation and behavior of *Escherichia coli* deletion mutants lacking chemotaxis functions.," *J. Bacteriol.*, vol. 151, no. 1, pp. 106–113, 1982.
- [147] H. P. Cheng and G. C. Walker, "Succinoglycan is required for initiation and elongation of infection threads during nodulation of alfalfa by *Rhizobium meliloti*," *J. Bacteriol.*, vol. 180, no. 19, pp. 5183–5191, 1998.
- [148] J. T. Singer, R. T. Phennicie, M. J. Sullivan, L. a Porter, V. J. Shaffer, and C. H. Kim, "Broad-host-range plasmids for red fluorescent protein labeling of gram-negative bacteria for use in the zebrafish model system.," *Appl. Environ. Microbiol.*, vol. 76, no. 11, pp. 3467–74, Jun. 2010.
- [149] D. L. Englert, M. D. Manson, and A. Jayaraman, "Investigation of bacterial chemotaxis in flow-based microfluidic devices," *Nat. Protoc.*, vol. 5, pp. 864–872, 2010.
- [150] M. A. Traore and B. Behkam, "A PEG-DA microfluidic device for the chemotaxis study of prokaryotic and eukaryotic cells," *J. Micromechanics Microengineering*, vol. 23, no. 8, p. 85014, 2013.
- [151] M. A. Traore, C. M. Damico, and B. Behkam, "Biomufacturing and self-propulsion dynamics of nanoscale bacteria-enabled autonomous delivery systems," *Appl. Phys. Lett.*, vol. 105, p. 173702, 2014.
- [152] D. E. Koshland, "Biochemistry of sensing and adaptation in a simple bacterial system.," *Annu Rev Biochem*, vol. 50, pp. 765–82, Jan. 1981.
- [153] R. Mesibov, G. W. Ordal, and J. Adler, "The range of attractant concentrations for bacterial chemotaxis and the threshold and size of response over this range. Weber law and related phenomena.," *J. Gen. Physiol.*, vol. 62, no. 2, pp. 203–23, Aug. 1973.
- [154] C. Li, a J. Boileau, C. Kung, and J. Adler, "Osmotaxis in *Escherichia coli*," *Proc. Natl. Acad. Sci. USA*, vol. 85, pp. 9451–5, Dec. 1988.
- [155] A. Holmberg, A. Blomstergren, O. Nord, M. Lukacs, J. Lundeberg, and M. Uhlén, "The biotin-streptavidin interaction can be reversibly broken using water at elevated temperatures.," *Electrophoresis*, vol. 26, no. 3, pp. 501–10, Feb. 2005.
- [156] R. Faibish, M. Elimelech, and Y. Cohen, "Effect of Interparticle Electrostatic Double Layer Interactions on Permeate Flux Decline in Crossflow Membrane Filtration of Colloidal Suspensions: An Experimental Investigation.," *J. Colloid Interface Sci.*, vol. 204, no. 1, pp. 77–86, Aug. 1998.
- [157] U. A. Gurkan, S. Tasoglu, D. Akkaynak, O. Avci, S. Unluisler, S. Canikyan, N. Maccallum, and U. Demirci, "Smart interface materials integrated with microfluidics for on-demand local capture and release of cells.," *Adv. Healthc. Mater.*, vol. 1, no. 5, pp. 661–8, Sep. 2012.
- [158] X. Zhang, Q. Zhang, T. Yan, Z. Jiang, X. Zhang, and Y. Y. Zuo, "Quantitatively Predicting Bacterial Adhesion Using Surface Free Energy Determined with a Spectrophotometric Method," *Environ. Sci. Technol.*, vol. 49, no. 49, pp. 6164–6171, 2015.
- [159] X. Niu, W. Zou, C. Liu, N. Zhang, and C. Fu, "Modified nanoprecipitation method to fabricate DNA-loaded PLGA nanoparticles," *Drug Dev. Ind. Pharm.*, vol. 35, no. 11, pp. 1375–1383, Nov. 2009.
- [160] G. T. Hermanson, *BIOCONJUGATE TECHNIQUES*. 2013.

- [161] R. K. Jain and T. Stylianopoulos, "Delivering nanomedicine to solid tumors.," *Nat. Rev. Clin. Oncol.*, vol. 7, no. 11, pp. 653–64, Nov. 2010.
- [162] H. T. Nia, H. Liu, G. Seano, M. Datta, D. Jones, N. Rahbari, J. Incio, V. P. Chauhan, K. Jung, J. D. Martin, V. Askoxylakis, T. P. Padera, D. Fukumura, Y. Boucher, F. J. Hornicek, A. J. Grodzinsky, J. W. Baish, L. L. Munn, and R. K. Jain, "Solid stress and elastic energy as measures of tumour mechanopathology," *Nat. Biomed. Eng.*, vol. 1, no. 1, p. 4, 2016.
- [163] F. Liu, L. Zhang, R. M. Hoffman, and M. Zhao, "Vessel destruction by tumor-targeting *Salmonella typhimurium* A1-R is enhanced by high tumor vascularity," *Cell Cycle*, vol. 9, no. 22, pp. 4518–4524, 2010.
- [164] C. H. Lee, C. L. Wu, and A. L. Shiau, "*Salmonella choleraesuis* as an anticancer agent in a syngeneic model of orthotopic hepatocellular carcinoma," *Int. J. Cancer*, vol. 122, no. 4, pp. 930–935, 2008.
- [165] Y. A. Yu, S. Shabahang, T. M. Timiryasova, Q. Zhang, R. Beltz, I. Gentshev, W. Goebel, and A. A. Szalay, "Visualization of tumors and metastases in live animals with bacteria and vaccinia virus encoding light-emitting proteins.," *Nat. Biotechnol.*, vol. 22, no. 3, pp. 313–20, Mar. 2004.
- [166] R. Rajashekar and M. Hensel, "The Intracellular Lifestyle of *Salmonella enterica* and Novel Approaches to Understand the Adaptation to Life within the *Salmonella*-containing Vacuole," in *Salmonella : From Genome to Function*, S. Porwollik, Ed. Norfolk: Caister Academic Press, 2011.
- [167] D. White, J. Drummond, and C. Fuqua, *The Physiology and Biochemistry of Prokaryotes*, 4th Ed. New York: Oxford University Press, 2012.
- [168] D. Bermudes, B. Low, and J. M. Pawelek, "Tumor-Targeted *Salmonella*: Strain Development and Expression of the HSV-tk Effector Gene.," *Methods Mol. Med.*, vol. 35, pp. 419–36, 2000.
- [169] M. Sznol, S. L. Lin, D. Bermudes, L. M. Zheng, and I. King, "Use of preferentially replicating bacteria for the treatment of cancer.," *J. Clin. Invest.*, vol. 105, no. 8, pp. 1027–30, Apr. 2000.
- [170] G. Mehta, A. Y. Hsiao, M. Ingram, G. D. Luker, and S. Takayama, "Opportunities and challenges for use of tumor spheroids as models to test drug delivery and efficacy.," *J. Control. Release*, vol. 164, no. 2, pp. 192–204, 2012.
- [171] F. Hirschhaeuser, H. Menne, C. Dittfeld, J. West, W. Mueller-Klieser, and L. A. Kunz-Schughart, "Multicellular tumor spheroids: an underestimated tool is catching up again.," *J. Biotechnol.*, vol. 148, no. 1, pp. 3–15, Jul. 2010.
- [172] T. Liu, C. T. Yang, L. Dieguez, J. A. Denman, and B. Thierry, "Robust and flexible fabrication of chemical micropatterns for tumor spheroid preparation," *ACS Appl. Mater. Interfaces*, vol. 6, no. 13, pp. 10162–10171, 2014.
- [173] M. A. Traore, "Bacteria-Enabled Autonomous Drug Delivery Systems: Design, Modeling, and Characterization of Transport and Sensing," 2014.
- [174] B. A. Pulaski and S. Ostrand-Rosenberg, "Mouse 4T1 breast tumor model.," *Curr. Protoc. Immunol.*, vol. Chapter 20, p. Unit 20.2, May 2001.
- [175] L. Turner, A. S. Stern, and H. C. Berg, "Growth of flagellar filaments of *Escherichia coli* is independent of filament length," *J. Bacteriol.*, vol. 194, no. 10, pp. 2437–2442, 2012.

- [176] F. Alexis, E. Pridgen, L. K. Molnar, and O. C. Farokhzad, "Factors affecting the clearance and biodistribution of polymeric nanoparticles," *Mol. Pharm.*, vol. 5, no. 4, pp. 505–515, 2008.
- [177] J. V. Jokerst, T. Lobovkina, R. N. Zare, and S. S. Gambhir, "Nanoparticle PEGylation for imaging and therapy.," *Nanomedicine (Lond.)*, vol. 6, no. 4, pp. 715–28, Jun. 2011.
- [178] E. Nance, C. Zhang, T. Shih, and Q. Xu, "Brain-Penetrating Nanoparticles Improve Paclitaxel Efficacy in Malignant Glioma Following Local Administration," *ACS Nano*, vol. 8, no. 10, pp. 10655–10664, 2014.
- [179] H. Hatakeyama, H. Akita, K. Kogure, and H. Harashima, "Development of a novel systemic gene delivery system for cancer therapy with a tumor-specific cleavable PEG-lipid," *Yakugaku Zasshi*, vol. 127, pp. 1549–1556, 2007.
- [180] J. M. Pawelek, S. Sodi, A. K. Chakraborty, J. T. Platt, S. Miller, D. W. Holden, M. Hensel, and K. B. Low, "*Salmonella* pathogenicity island-2 and anticancer activity in mice," *Cancer Gene Ther.*, vol. 1646, no. 9, pp. 813–818, 2002.
- [181] A. Ivascu and M. Kubbies, "Diversity of cell-mediated adhesions in breast cancer spheroids," *Int. J. Oncol.*, vol. 31, no. 6, pp. 1403–1413, 2007.
- [182] M. Vinci, S. Gowan, F. Boxall, L. Patterson, M. Zimmermann, W. Court, C. Lomas, M. Mendiola, D. Hardisson, and S. a Eccles, "Advances in establishment and analysis of three-dimensional tumor spheroid-based functional assays for target validation and drug evaluation.," *BMC Biol.*, vol. 10, no. 1, p. 29, Jan. 2012.
- [183] C. P. Graff and K. D. Wittrup, "Theoretical analysis of antibody targeting of tumor spheroids: importance of dosage for penetration, and affinity for retention.," *Cancer Res.*, vol. 63, no. 6, pp. 1288–96, 2003.
- [184] M. A. Clauss, R. K. Jain, and N. Tissues, "Interstitial Transport of Rabbit and Sheep Antibodies in Normal and Neoplastic Tissues," *Cancer Res.*, vol. 50, no. 14, pp. 3487–3492, 1990.
- [185] H. B. Frieboes, E. S. Han, V. Cristini, and J. P. Fruehauf, "Modeling breast cancer tumor morphology to predict drug response," *Cancer Res.*, vol. 65, no. 9 Supplement, pp. 1403–1403, 2005.
- [186] F. B., D. R.N., C. M.a., G. I., L. L., and M. a.a., "Tumor vascular normalization as a strategy to potentiate effectiveness of therapeutic vaccines," *J. Immunother. Cancer*, vol. 2, no. Suppl 3, p. no pagination, 2014.
- [187] N. J. Boylan, J. S. Suk, S. K. Lai, R. Jelinek, M. P. Boyle, M. J. Cooper, and J. Hanes, "Highly compacted DNA nanoparticles with low MW PEG coatings: *in vitro*, *ex vivo* and *in vivo* evaluation.," *J. Control. Release*, vol. 157, no. 1, pp. 72–9, Jan. 2012.
- [188] D. A. Schiemann, "Anaerobic growth of *Salmonella typhimurium* results in increased uptake by Henle 407 epithelial and mouse peritoneal cells *in vitro* and repression of a major outer membrane protein," *Infect. Immun.*, vol. 59, no. 1, pp. 437–440, 1991.
- [189] N. S. Waleh, J. Gallo, T. D. Grant, B. J. Murphy, R. H. Kramer, and R. M. Sutherland, "Selective down-regulation of integrin receptors in spheroids of squamous cell carcinoma.," *Cancer Res.*, vol. 54, no. 3, pp. 838–43, Feb. 1994.
- [190] S. Chandrasekaran, Y. Geng, L. A. DeLouise, and M. R. King, "Effect of homotypic and heterotypic interaction in 3D on the E-selectin mediated adhesive properties of breast cancer cell lines," *Biomaterials*, vol. 33, no. 35, pp. 9037–9048, 2012.

- [191] G. Hamilton, F. Hirschhaeuser, H. Menne, C. Dittfeld, J. West, W. Mueller-Klieser, and L. A. Kunz-Schughart, "Multicellular spheroids as an *in vitro* tumor model.," *Cancer Lett.*, vol. 131, no. 1, pp. 29–34, Sep. 1998.
- [192] C. Y. Chou, C. K. Huang, K. W. Lu, T. L. Horng, and W. L. Lin, "Investigation of the Spatiotemporal Responses of Nanoparticles in Tumor Tissues with a Small-Scale Mathematical Model," *PLoS One*, vol. 8, no. 4, 2013.
- [193] K. Kataoka, A. Harada, and Y. Nagasaki, "Block copolymer micelles for drug delivery: design, characterization and biological significance," *Adv. Drug Deliv. Rev.*, vol. 47, no. 1, pp. 113–131, 2001.
- [194] E. Blanco, H. Shen, and M. Ferrari, "Principles of nanoparticle design for overcoming biological barriers to drug delivery," *Nat. Biotechnol.*, vol. 33, no. 9, pp. 941–951, Sep. 2015.
- [195] V. P. Torchilin, "Recent advances with liposomes as pharmaceutical carriers," *Nat. Rev. Drug Discov.*, vol. 4, no. 2, pp. 145–160, Feb. 2005.
- [196] A. Quintana, E. Raczka, L. Piehler, I. Lee, A. Myc, I. Majoros, A. K. Patri, T. Thomas, J. Mulé, and J. R. Baker, "Design and function of a dendrimer-based therapeutic nanodevice targeted to tumor cells through the folate receptor.," *Pharm. Res.*, vol. 19, no. 9, pp. 1310–6, Sep. 2002.
- [197] D. Akin, J. Sturgis, K. Ragheb, D. Sherman, K. Burkholder, J. Robinson, A. Bhunia, S. Mohammed, and R. Bashir, "Bacteria-mediated delivery of nanoparticles and cargo into cells," *Nat. Nanotechnol.*, vol. 2, pp. 441–449, 2007.
- [198] B. Huang, W. D. Abraham, Y. Zheng, S. C. B. López, S. S. Luo, and D. J. Irvine, "Active targeting of chemotherapy to disseminated tumors using nanoparticle-carrying T cells," *Sci. Transl. Med.*, vol. 7, no. 291, 2015.
- [199] M. Kim, R. J. Gillies, and K. A. Rejniak, "Current Advances in Mathematical Modeling of Anti-Cancer Drug Penetration into Tumor Tissues," *Front. Oncol.*, vol. 3, no. November, pp. 1–10, 2013.
- [200] C. M. Groh, M. E. Hubbard, P. F. Jones, P. M. Loadman, N. Periasamy, B. D. Sleeman, S. W. Smye, C. J. Twelves, and R. M. Phillips, "Mathematical and computational models of drug transport in tumours," *J. R. Soc. Interface*, vol. 11, no. 94, pp. 20131173–20131173, 2014.
- [201] N. D. Evans, R. J. Errington, M. Shelley, G. P. Feeney, M. J. Chapman, K. R. Godfrey, P. J. Smith, and M. J. Chappell, "A mathematical model for the *in vitro* kinetics of the anti-cancer agent topotecan," *Math. Biosci.*, vol. 189, no. 2, pp. 185–217, 2004.
- [202] C. J. Evans, R. M. Phillips, P. F. Jones, P. M. Loadman, B. D. Sleeman, C. J. Twelves, and S. W. Smye, "A mathematical model of doxorubicin penetration through multicellular layers," *J. Theor. Biol.*, vol. 257, no. 4, pp. 598–608, 2009.
- [203] R. J. Shipley and S. J. Chapman, "Multiscale Modelling of Fluid and Drug Transport in Vascular Tumours," *Bull. Math. Biol.*, vol. 72, no. 6, pp. 1464–1491, Aug. 2010.
- [204] R. Venkatasubramanian, M. A. Henson, and N. S. Forbes, "Integrating cell-cycle progression, drug penetration and energy metabolism to identify improved cancer therapeutic strategies," *J. Theor. Biol.*, vol. 253, no. 1, pp. 98–117, Jul. 2008.
- [205] R. Rockne, J. K. Rockhill, M. Mrugala, A. M. Spence, I. Kalet, K. Hendrickson, A. Lai, T. Cloughesy, E. C. Alvord, and K. R. Swanson, "Predicting the efficacy of radiotherapy in

- individual glioblastoma patients *in vivo*: a mathematical modeling approach,” *Phys. Med. Biol.*, vol. 55, no. 12, pp. 3271–3285, Jun. 2010.
- [206] D. Y. Arifin, K. Y. T. Lee, and C.-H. Wang, “Chemotherapeutic drug transport to brain tumor,” *J. Control. Release*, vol. 137, no. 3, pp. 203–210, 2009.
- [207] R. K. Banerjee, W. W. Van Osdol, P. M. Bungay, C. Sung, and R. L. Dedrick, “Finite element model of antibody penetration in a prevascular tumor nodule embedded in normal tissue,” *J. Control. Release*, vol. 74, no. 1–3, pp. 193–202, 2001.
- [208] L. E. Gerlowski and R. K. Jain, “Microvascular permeability of normal and neoplastic tissues,” *Microvasc. Res.*, vol. 31, no. 3, pp. 288–305, 1986.
- [209] K. Fujimori, D. G. Covell, J. E. Fletcher, and J. N. Weinstein, “Modeling Analysis of the Global and Microscopic Distribution of Immunoglobulin G, F(ab')₂, and Fab in Tumors,” *Cancer Res.*, vol. 49, no. 20, 1989.
- [210] X. Yu, I. Trase, M. Ren, K. Duval, X. Guo, and Z. Chen, “Design of Nanoparticle-Based Carriers for Targeted Drug Delivery,” *J. Nanomater.*, vol. 2016, 2016.
- [211] J. Siepmann and F. Siepmann, “Mathematical modeling of drug delivery,” *Int. J. Pharm.*, vol. 364, no. 2, pp. 328–343, 2008.
- [212] G. Fullstone, J. Wood, M. Holcombe, G. Battaglia, and K. Hori, “Modelling the Transport of Nanoparticles under Blood Flow using an Agent-based Approach,” *Sci. Rep.*, vol. 5, no. 1, p. 10649, Sep. 2015.
- [213] W. M. Saltzman and M. L. Radomsky, “Drugs released from polymers: diffusion and elimination in brain tissue,” *Chem. Eng. Sci.*, vol. 46, no. 10, pp. 2429–2444, 1991.
- [214] R. Langer and N. Peppas, “Chemical and Physical Structure of Polymers as Carriers for Controlled Release of Bioactive Agents: A Review,” *J. Macromol. Sci. Part C*, vol. 23, no. 1, pp. 61–126, Jan. 1983.
- [215] T. T. Goodman, J. Chen, K. Matveev, and S. H. Pun, “Spatio-temporal modeling of nanoparticle delivery to multicellular tumor spheroids,” *Biotechnol. Bioeng.*, vol. 101, no. 2, pp. 388–99, Oct. 2008.
- [216] B. Kim, G. Han, B. J. Toley, C.-K. Kim, V. M. Rotello, and N. S. Forbes, “Tuning payload delivery in tumour cylindroids using gold nanoparticles,” *Nat. Nanotechnol.*, vol. 5, no. 6, pp. 465–72, Jun. 2010.
- [217] A. K. Sarkar, G. Georgiou, and M. M. Sharma, “Transport of bacteria in porous media: II. A model for convective transport and growth,” *Biotechnol. Bioeng.*, vol. 44, no. 4, pp. 499–508, 1994.
- [218] O. A. Croze, G. P. Ferguson, M. E. Cates, and W. C. K. Poon, “Migration of chemotactic bacteria in soft agar: Role of gel concentration,” *Biophys. J.*, vol. 101, no. 3, pp. 525–534, 2011.
- [219] N. A. Licata, B. Mohari, C. Fuqua, and S. Setayeshgar, “Diffusion of Bacterial Cells in Porous Media,” *Biophys. J.*, vol. 110, no. 1, pp. 247–257, 2016.
- [220] D. N. Thornlow, E. L. Brackett, J. M. Gigas, N. Van Dessel, and N. S. Forbes, “Persistent enhancement of bacterial motility increases tumor penetration,” *Biotechnol. Bioeng.*, vol. 112, no. 11, pp. 2397–2405, 2015.
- [221] J. Stritzker, S. Weibel, C. Seubert, A. Götz, A. Tresch, N. van Rooijen, T. a Oelschlaeger, P. J. Hill, I. Gentshev, and A. a Szalay, “Enterobacterial tumor colonization in mice

- depends on bacterial metabolism and macrophages but is independent of chemotaxis and motility.," *Int. J. Med. Microbiol.*, vol. 300, no. 7, pp. 449–56, Nov. 2010.
- [222] Y. A. Yu, Q. Zhang, and A. A. Szalay, "Establishment and characterization of conditions required for tumor colonization by intravenously delivered bacteria.," *Biotechnol. Bioeng.*, vol. 100, no. 3, pp. 567–78, Jun. 2008.
- [223] A. T. St Jean, M. Zhang, and N. S. Forbes, "Bacterial therapies: completing the cancer treatment toolbox," *Curr. Opin. Biotechnol.*, vol. 19, no. 5, pp. 511–517, 2008.
- [224] M. Höckel and P. Vaupel, "Tumor hypoxia: definitions and current clinical, biologic, and molecular aspects.," *J. Natl. Cancer Inst.*, vol. 93, no. 4, pp. 266–276, 2001.
- [225] J. a Bertout, S. a Patel, and M. C. Simon, "The impact of O₂ availability on human cancer.," *Nat. Rev. Cancer*, vol. 8, no. 12, pp. 967–975, 2008.
- [226] A. L. Harris, "Hypoxia — a Key Regulatory Factor in Tumour Growth," *Nat. Rev. Cancer*, vol. 2, no. 1, pp. 38–47, 2002.
- [227] D. R. Grimes, C. Kelly, K. Bloch, and M. Partridge, "A method for estimating the oxygen consumption rate in multicellular tumour spheroids," *J. R. Soc. Interface*, vol. 11, no. 92, pp. 20131124–20131124, 2014.
- [228] E. Milotti and R. Chignola, "Emergent properties of tumor microenvironment in a real-life model of multicell tumor spheroids," *PLoS One*, vol. 5, no. 11, 2010.
- [229] N. Yamamoto and M. L. Droffner, "Mechanisms determining aerobic or anaerobic growth in the facultative anaerobe *Salmonella typhimurium*," *Proc. Natl. Acad. Sci. U. S. A.*, vol. 82, no. 7, pp. 2077–2081, 1985.
- [230] S. C. Liu, N. P. Minton, A. J. Giaccia, and J. M. Brown, "Anticancer efficacy of systemically delivered anaerobic bacteria as gene therapy vectors targeting tumor hypoxia/necrosis.," *Gene Ther.*, vol. 9, no. 4, pp. 291–6, Feb. 2002.
- [231] A. Castan, A. Näsman, and S.-O. Enfors, "Oxygen enriched air supply in *Escherichia coli* processes: production of biomass and recombinant human growth hormone," *Enzyme Microb. Technol.*, vol. 30, pp. 847–854, 2002.
- [232] C. A. Lee and S. Falkow, "The ability of *Salmonella* to enter mammalian cells is affected by bacterial growth state.," *Proc. Natl. Acad. Sci. U. S. A.*, vol. 87, no. 11, pp. 4304–8, 1990.
- [233] A. Carreau, B. El Hafny-Rahbi, A. Matejuk, C. Grillon, and C. Kieda, "Why is the partial oxygen pressure of human tissues a crucial parameter? Small molecules and hypoxia," *J. Cell. Mol. Med.*, vol. 15, no. 6, pp. 1239–1253, 2011.
- [234] R. Storn and K. Price, "Differential Evolution – A Simple and Efficient Heuristic for Global Optimization over Continuous Spaces," *J. Glob. Optim.*, vol. 11, no. 4, pp. 341–359, 1997.
- [235] K. M. Broadway, S. Suh, B. Behkam, and B. E. Scharf, "Optimizing the restored chemotactic behavior of anticancer agent *Salmonella enterica* serovar Typhimurium VNP20009," *J. Biotechnol.*, 2017.